TECHNISCHE UNIVERSTITÄT MÜNCHEN

Lehrstuhl für Anorganische Chemie mit Schwerpunkt Neue Materialen

Alloy-Based Anodes with Inverse Opal Structure for Lithium Ion Batteries

Sebastian Geier

Vollständiger Abdruck der von der Fakultät für Chemie der Technischen Universität München zur Erlangung des akademischen Grades eines

Doktors der Naturwissenschaften (Dr. rer. nat.)

genehmigten Dissertation.

Vorsitzender: Univ.-Prof. Dr. T. Nilges

Prüfer der Dissertation:

1. Univ.-Prof. Dr. T. F. Fässler
2. Univ.-Prof. Dr. H. Gasteiger

Die Dissertation wurde am 22.11.2018 bei der Technischen Universität München eingereicht und durch die Fakultät für Chemie am 13.12.2018 angenommen.

„The best way to predict your future is to create it.“

ABRAHAM LINCOLN

Danksagung

Mein besonderer Dank gilt meinem Doktorvater

Prof. Dr. Thomas F. Fässler

für die Möglichkeit am Lehrstuhl für Anorganische Chemie mit Schwerpunkt Neue Materialien meine Promotion durchzuführen und die tatkräftige Unterstützung dabei.

Außerdem möchte ich danken

Prof. Dr. Hubert Gasteiger

für die Möglichkeit an seinem Lehrstuhl für Technische Elektrochemie zahlreiche elektrochemische Messungen durchzuführen

Prof. Dr. Dina Fattakhova-Rohlfing

für die Bereitstellung einer Vielzahl von Messgeräten zur Probencharakterisierung

Prof. Dr. Paolo Lugli

für die Bereitstellung von Spin- und Spray-Coater sowie eines UV/Vis-Messgeräts

Prof. Dr. Peter Müller-Buschbaum

für die Bereitstellung des UV/Vis-Messstandes

Manuela Donaubauer

für die Hilfe bei organisatorischen Problemen aller Art und das meist klaglose Hinnehmen diverser organisatorischer Versäumnisse meinerseits

Dem **Arbeitskreis Prof. Dr. Thomas Bein**

für die Unterstützung bei diversen Messungen und das angenehme Klima im Labor und auf zahlreichen, gemeinsam besuchten Konferenzen

Dr. Steffen Schmidt

für die Aufnahme von REM-Bildern und der EDX-Spektren

Dr. Wilhelm Klein und **Dr. Viktor Hlukhyy**

für die Hilfe bei Problemen mit dem Diffraktometer

Dr. Roland Jung

für die sehr konstruktive und produktive Kooperation auf dem Gebiet der Batterieforschung und die großartige Hilfestellung bei Problemen elektrochemischer Natur

M. Sc. Marius Loch

für die Unterstützung bei Spin- und Spray-Coating Versuchen

M. Sc. Nuri Hohn

für die Durchführung zahlreicher Messungen zur Bandlückenbestimmung

Dr. Kristina Peters und **M. Sc. Daniel Böhm**

für REM/EDX-Messungen und Unterstützung bei Problemen bezüglich PMMA oder des Dip-Coaters

M.Sc. Fabian Linsenmann

für Hilfestellung bei elektrochemischen Zyklisierungsmessungen sowie der Zellkonstruktion

M. Sc. Tim Kratky, M.Sc. Bernhard Böller und **Dr. Patrick Zeller**

für die Messung von XPS-Spektren

Meinen Forschungspraktikanten **Fabian Linsenmann** und **Korbinian Huber**

Ganz besonders meinen Laborkollegen **Benedikt Witzel**, **Sabine Frischhut**, **Michael Giebel** und **Lorenz Schiegerl** für die sehr angenehme Zusammenarbeit, die fruchtbaren Diskussionen und die kleinen Ablenkungen vom manchmal frustrierenden Laboralltag.

Besonders hervorzuheben **Sabine „Dudli" Frischhut** für eine schöne Zeit in Labor und Büro, das Herausziehen aus dem ein oder anderen Stimmungstief im Laufe dieser Arbeit, die konstruktiven Diskussionen und die erfolgreichen Kooperationen auch außerhalb der Mauern der Universität.

Außerdem dem gesamten **Arbeitskreis Prof. Dr. Thomas F. Fässler**, besonders **Felix Geitner**, **Christoph Wallach**, **Thomas Wylezich** und **Stefan Strangmüller** für die angenehme Zusammenarbeit, das gute Klima am Lehrstuhl und die zahlreichen fachfremden Aktivitäten nach Dienstschluss.

Mein besonderer Dank gilt meiner Freundin **Marina** und meinen **Eltern**

für ihren Rückhalt, das offene Ohr bei Problemen aller Art und die bedingungslose Unterstützung während dieser Promotion.

Zusammenfassung

Mit steigendem Interesse an erneuerbaren Energien und Elektromobilität in der heutigen Gesellschaft wird mehr und mehr Fokus auf neue Technologien im Bereich der Energiespeichersysteme gelegt. Lithium-Ionen-Batterien haben in den letzten Jahren zunehmend Aufmerksamkeit auf sich gezogen und spielen eine zentrale Rolle in öffentlichen Diskussionen. Besonders der Aufstieg der Elektromobilität und die Notwendigkeit von transportablen Speichersystemen in mobilen Geräten und deren unstillbares Verlangen nach höheren Kapazitäten und Energiedichten sowie Anforderungen an die Sicherheit treiben die Forschung im Bereich der Lithium-Ionen-Batterien voran. Um alle Anforderungen, die an zukünftige Batterietechnologien gestellt werden, zu erfüllen müssen neue Materialen entwickelt werden. Diese Arbeit fokussiert sich dabei auf die Untersuchung von so genannten Legierungsanoden basieren auf Germanium und Zinn für Lithium-Ionen-Batterien. Verglichen mit konventionellen Graphitanoden bieten diese Systeme sehr hohe Kapazitäten während die notwendigen Sicherheitsaspekte gewahrt werden. Das Hauptproblem aller Legierungsanoden ist deren Instabilität gegenüber dem Ladungs-Entladungs-Zyklisieren, verursacht durch massive Volumenänderungen im Prozess der Legierungsbildung. Um dieses Problem zu beheben werden poröse und mechanisch stabile Strukturen benötigt. Diese Arbeit konzentriert sich auf Dünnfilme mit einer inversen Opalstruktur, ähnlich zu Honigwaben. Diese haben die Voraussetzungen, die Anforderungen erfüllen, die nötig sind, um Legierungsanoden mit höherer Zyklisierungsstabilität zu konstruieren.

Der erste Teil dieser Arbeit beschreibt den Prozess der Templataufbringung und Germaniumanodenpräparation auf Kupfersubstraten. Vier verschiedene Beschichtungsmethoden wurden untersucht und das Dip-Coating-Verfahren erwies sich als die am besten geeignetste Methode für die nasschemische Dünnfilmpräparation. Im nächsten Schritt wurden invers Opal strukturierte Germaniumfilme, basierend auf Ethylendiamin-Lösungen der Zintl-Phase K_4Ge_9, produziert und als Anoden in Lithium-Ionen-Halbzellen getestet. Die Elektroden zeigten hohe Kapazitäten und Zyklenstabilität, vielversprechend für Anwendung in Systemen mit langer Lebensdauer.

Im zweiten Kapitel wurde die Einführung von Phosphor durch verschiedene Dotierungsreagenzien untersucht. Einbringung von Phosphor wurde dabei erfolgreich durch den Einsatz von NaP_7, rotem Phosphor und der ternären Phase $K_2Ge_2P_2$ durchgeführt. Gemischte Germanium/Phosphor-Anoden wurden anschließend als Elektroden in Lithium-Ionen-Batterien eingesetzt. Diese wiesen gute Kapazitäten und Kapazitätserhaltung auf, waren aber den reinen Germaniumanoden in dieser Arbeit unterlegen.

Weiterhin wurde die eingeführte Präparationsmethode für invers opalstrukturierte Dünnfilme auf Zinn, Zinn/Germanium sowie Selen-, Tellur- und Phosphor-dotierte Zinnfilme übertragen. Ausgehend von den Zintl-Phasen K_4Sn_9, K_4Ge_9 und $K_4Ge_5Sn_4$ wurden reine Zinn- und gemischte Zinn/Germanium-Filme erfolgreich hergestellt, wobei die gewünschte Honigwabenstruktur erhalten wurde. Diese Filme wurden auch als Anoden in Lithium-Ionen-Halbzellen getestet. Sie weisen allerdings sehr niedrige Kapazitäten und eine schlechte Zyklenstabilität auf. Einzig gemischte Zinn/Germanium-Filme, basierend auf der ternären Phase $K_4Ge_5Sn_4$, wiesen Kapazitäten und Kapazitätserhaltung vergleichbar mit Literaturdaten für Zinn/Germanium-Anoden auf. Selen-dotierte Zinnfilme mit inverser Opalstruktur konnten nicht erhalten werden. Gemischte Zinn/Tellur-Filme wurden im Gegensatz dazu erfolgreich hergestellt. Auch Phosphor-dotierte Zinnfilme konnten hergestellt werden, hier ist aber noch mehr Arbeit notwendig um die erhaltenen Dünnfilme vollständig zu charakterisieren.

Das abschließende Kapitel dieser Arbeit befasst sich mit der Herstellung von Phosphorfilmen mit inverser Opalstruktur. Ausgehend von einer Lösung von K_3P_7 in Ethylendiamin wurden homogene Filme mit der gewünschten Honigwabenstruktur erhalten. Durch Variation des Reagenz zur Clusterverknüpfung wurde versucht Fremdatome einzubringen. $SiCl_4$, $GeCl_4$ und $SnCl_4$ wurden als Verknüpfungsreagenzien eingesetzt. Silizium und Zinn konnten dadurch erfolgreich auf den Filmen nachgewiesen werden, Germanium dagegen konnte nicht detektiert werden. Zuletzt wurden reine Phosphorfilme als Anoden für Lithium-Ionen-Halbzellen getestet. Diese zeigten gute Kapazitätswerte, jedoch fielen die Kapazitäten mit steigender Zyklenzahl rapide ab. Generell konnten die hier verwendeten Phosphorelektroden nicht mit literaturbekannten Kompositsystemen bestehend aus rotem Phosphor und Kohlenstoff mithalten.

Abstract

With increasing interest in renewable energy and electromobility in today's society, more and more focus is put on new technologies in the field of energy storage systems. Lithium ion batteries attracted increasing attention in recent years and play a central role in public discussions. Especially the rise of electromobility and the need for transportable storage systems in mobile devices with its insatiable demand for higher capacities and energy densities as well as requirements regarding safety keeps pushing lithium ion battery research forward. However, to fulfill all needs imposed on future battery technologies, new materials have to be developed. This work focusses on the investigation of so called alloy-anodes based on germanium and tin for lithium ion batteries. Compared to conventional graphite anodes, these systems offer very high capacities while still maintaining system safety. The main issue of all alloy-based anodes is their instability towards charge-discharge cycling, caused by immense volume changes during alloying and dealloying. To overcome this problem, porous and mechanically flexible structures are needed. This work centers upon thin films with a honeycomb-like inverse opal structure which should match the requirements to create alloy-anodes with higher cycling stability.

The first part of this work describes the process of template coating and germanium-anode preparation. Four different coating methods were investigated and dip-coating was figured out to be the most suitable method for our wet-chemical thin film preparation. In the next step, inverse opal structured germanium thin films, based on solutions of the Zintl precursor K_4Ge_9 in ethylenediamine, were fabricated and tested as anodes in lithium ion half-cells. The electrodes showed high capacities and capacity retentions promising for application in long-lifetime systems.

In the second chapter, introduction of phosphorus by utilizing various different doping agents was investigated. Phosphorus introduction was performed successfully using NaP_7, red phosphorus and the ternary phase $K_2Ge_2P_2$. Mixed germanium/phosphorus anodes were then used as electrodes in lithium ion half-cells. They exhibited good capacities and capacity retentions, but were generally outperformed by pure germanium anodes reported in this work.

Another part of this work was the transfer of the invented preparation method for inverse opal structured thin films to tin, tin/germanium as well as selenium, tellurium, and phosphorus doped tin films. Starting from the Zintl phases K_4Sn_9, K_4Ge_9, and $K_4Ge_5Sn_4$, pure tin and mixed tin/germanium thin films were successfully prepared and the desired honeycomb structure was achieved. These films were also tested as anodes in lithium ion half-cells. However, the electrodes delivered very low capacities and insufficient cycling stability was observed. Only mixed tin/germanium electrodes prepared from the ternary phase $K_4Ge_5Sn_4$ yielded capacities and capacity retentions comparable to

literature data for mixed tin/germanium anodes. Mixed selenium/tin films with inverse opal structure could not be achieved, while introducing tellurium was done successfully. Phosphorus doped tin films were obtained, but more work has to be done to fully characterize the resulting thin films.

The final chapter of this work focusses on the preparation of phosphorus thin films with inverse opal structure. Starting from a solution of K_3P_7 in ethylenediamine, homogenous films with the desired honeycomb structure could be obtained. By variation of the cross-linking agent, introduction of impurity atoms was attempted. Therefore, $SiCl_4$, $GeCl_4$, and $SnCl_4$ were utilized as linkers. While silicon and tin could be found on the phosphorus thin films, germanium could not be detected. Pure phosphorus films were also used as anodes in lithium ion batteries. They delivered good capacities but showed rapid capacity fading and were outperformed by literature known systems based on red phosphorus/carbon composite materials.

Table of Contents

Abbreviations and Symbols

%	percentage
°	degree, angle
°C	degree celcius
Å	Angström
A	ampere
A	alkali metal
a	amorphous
α	crystalline
a.u.	arbitrary unit
Ah kg^{-1}	amperehour per kilogram
at.%	atomic percentage
BTS	copper oxide catalyst for gas regeneration
C	charge
cm	centimeter
cm^{-1}	reciprocal centimeter, wavenumber
CNT	carbon nanotube
C-rate	charging rate
CVD	chemical vapor deposition
dmf	N,N-dimethylformamide
DEC	diethyl carbonate
DLS	dynamic light scattering
DMC	dimethyl carbonate
E	tetrel element
EC	ethylene carbonate
EDX	energy dispersive X-ray analysis
E_G	energy gap
e.g.	*exempli gratia*, for example
EMC	ethyl-methyl carbonate
en	ethylenediamine

eV	electronvolt
fcc	face-centered cubic close packing
FEC	fluoroethylene carbonate
g cm^{-3}	gram per cubic centimeter
g m^{-2}	gram per square meter
g mol^{-1}	gram per mole
h	hour(s)
K	Kelvin
K min^{-1}	Kelvin per minute
kJ mol^{-1}	kilojoule per mole
LIB	lithium ion battery
M	molar
mAh g^{-1}	milliamperhour per gram
mbar	millibar
Me	methyl
min	minute(s)
mg	milligram
mL	mililitre
mm	millimeter
mmol	millimole
mol	mole
mV	millivolt
mV s^{-1}	millivolt per second
mW	milliwatt
µ	micro
µL	microliter
µm	micrometer
nm	nanometer
NMP	N-methyl-pyrrolidone
NMR	nuclear magnetic resonance spectroscopy
OCV	open circuit voltage

PEO	poly(ethylene oxide)
PMMA	poly(methyl methacrylate)
ppm	part per million
PVDF	polyvinylidene fluoride
PXRD	powder X-ray diffraction
rpm	rounds per minute
RT	room temperature
SDS	sodium dodecyl sulfate
SEI	solid-electrolyte interphase
SEM	scanning electron microscopy
theo.	theoretically
Tt	tetrel element
sec	second(s)
thf	tetrahydrofurane
UV	ultra violet
V	volt
Vis	Visible light
VLS	vapor-liquid-solid
vol.%	volume percentage
wt.%	weight percentage
XPS	X-ray photoelectron spectroscopy
XRD	X-ray diffraction
Z	number of formula units per unit cell
2θ	diffraction angle
λ	wavelength

Table of Figures

List of Tables

1. Introduction

The following chapter points out the motivation and aim of this thesis and gives an overview of the literature background of the research topics covered by this work.

1.1 Motivation

So called green energy sources such as solar power, wind power or tidal and geothermal power are on the rise in the light of becoming more and more independent of fossil fuel and nuclear energy and fighting global warming. Not only new energy sources, but also new technologies in the field of energy storage systems have to be invented for both large-scale stationary as well as portable power applications, especially against the backdrop of the advent of electromobility and the demand for transportable storage systems in mobile devices.

In recent years, Lithium ion batteries attracted increasing attraction as they are assumed to be one of the most promising candidates when it comes to future's energy storage systems. Lithium ion batteries combine high capacities and energy densities as well as high safety during operation, making them highly attractive for either mobile or stationary devices. Particularly recent progress in the scope of electromobility and automotive applications lead to intense research in the field of lithium ion batteries in the last years. While investigations have been done covering all aspects of lithium ion batteries such as electrolytes, anode and cathode materials, battery design, theoretical simulations and implementation in the energy grid, research of new battery materials has become of outstanding importance. New materials have to be developed to cope with the demands of modern applications regarding capacities, energy densities and capacity retention. In the scope of this research, alloy-based anodes such as silicon, germanium and tin containing materials have attracted a lot of attention. Compared to conventional graphite anodes, these systems offer very high capacities while still maintaining operating safety. However, all alloy-based anodes suffer from one main flaw, their instability towards charge-discharge cycling. This is caused by immense volume changes during alloying and de-alloying. Therefore many studies focused on developing new porous and mechanically flexible structures to overcome the problem of volume changes.

This work was done within this context and aims at the introduction of a highly porous and mechanically stable, inverse opal structured thin films for alloy-based anodes, prepared by a simple, wet-chemical process involving so called Zintl clusters containing the tetrel elements germanium and tin, as well as further adjusting the thin films properties by impurity doping.

1.2 General Principles of Lithium Ion Batteries

Lithium Ion Batteries (LIBs) show high energy densities and good cycle life while fulfilling high safety standards for everyday applications such as mobile phones or laptops. Starting from 1991, where SONY commercialized the first rechargeable LIB,[1] LIBs have become more and more established as energy storage system in small and medium-sized electronics. By introduction of LIBs in the automotive field, research in electromobility experienced a huge boost. Due to their high energy and power density, LIBs are the most promising candidate regarding battery technologies to meet the requirements of the automotive industry.[2]

Figure 1.1 shows a schematic depiction of a LIB. Generally speaking, a LIB consists of three main parts; anode, cathode, and electrolyte. Anode and cathode are the negative and positive electrodes where insertion and storage of Li ions takes place during a charge-discharge cycle. In case of SONY's battery from 1991, graphite was used as anode and $LiCoO_2$ was used as cathode material.[1] Li ions migrate across the third part of a LIB, the electrolyte, which is located between the two electrodes and has to provide sufficient Li ion conductivity. The electrolyte can either be a liquid or solid medium. In the case of a liquid electrolyte, an additional separator membrane is used to avoid a short circuit, usually consisting of glass fiber or polymeric fiber.

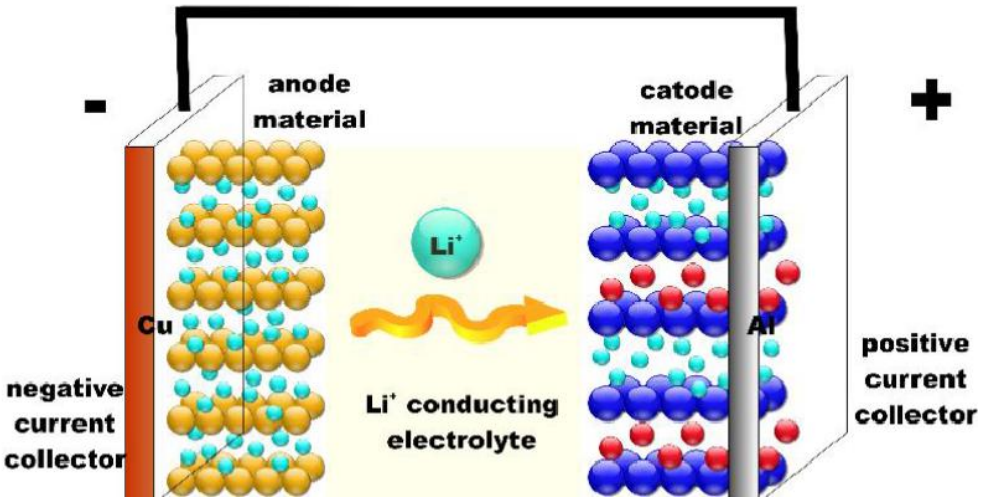

Figure 1.1. Schematic presentation of a lithium ion battery (LIB). Image obtained with kind permission by Dr. I. Kurylyshyn.

Liquid electrolytes typically consist of Li salts dissolved in water-free, aprotic solvents such as ethylene carbonate (EC), dimethyl carbonate (DMC), ethyl methyl carbonate (EMC), or diethyl carbonate (DEC). The two electrodes are connected to metal current collectors, typically copper for the anode and aluminum for the cathode. Current collector materials are chosen based on their passivity towards Li

at low and high potentials. The current collectors are necessary to connect anode and cathode to an external circuit. Mechanical and electrical contact is needed between the current collectors and the electrodes. Therefore, the electrodes usually consist of several compounds, an active material, a conductive additive, and a binder. The active material is the main compound, it provides the capacity of the battery and allows for Li^+ insertion and extraction. A conductive additive (*e.g.* carbon black) is used if the electrode material itself is not conductive and ensures electrical contact with the current collector, while the electrochemically inactive binder ensures mechanical contact. Typical binders are polyvinylidene fluoride (PVDF) or poly(ethylene oxide) (PEO). Binder-free electrodes are also possible if mechanical contact can be assured without an additional binder. This type of electrodes will be discussed in more detail later in this work.

Research has been made and is still going on regarding all different components of LIBs. The search for higher capacities and energy densities is of immense importance, as the demand of modern and future applications is nearly insatiable. New materials are needed to cope with the constantly increasing requirements. A big factor in nowadays research is the transition to so called all-solid-state-batteries, where not only the electrodes but also the electrolyte is a solid compound, providing higher stability and safety.[3] A large variety of transition metal oxides have been studied as possible cathode materials in LIBs.[2b] Search for new anode materials with higher capacities and energy densities has also attracted a lot of attention in recent years. The different types of anode materials and recent developments in this field of studies will be discussed in more detail in the following chapters, since this work focusses on the investigation of new materials and systems as anodes for LIBs.

1.3 Anodes for Lithium Ion Batteries

Anodes for LIBs can be divided in three different categories, regarding their reaction mechanism upon Li insertion and extraction during charge-discharge cycling: Intercalation, conversion, and alloying materials. The next sections of this work will discuss the three different types of anodes and present the most important materials of each type. Short overviews can be found at the end of each chapter.

1.3.1 Intercalation Anodes

Intercalation anodes for LIBs provide host matrices where Li ions are accommodated between layers or in channels with very little mechanical strain during lithiation. This usually leads to high cycling stability. The classic example for an intercalation anode is graphite with a theoretical gravimetric specific capacity of 372 mAh g^{-1} for Li_6C as lithiated species.[4] Here, Li ions intercalate between graphene sheets without changes in the backbone structure. While achieving good cycling stability, the specific capacity of this material is comparably low. Carbon based materials are separated in two different categories, soft carbon and hard carbon. In soft carbon materials (*e.g.* carbon nanotubes (CNT), nanofibers, and graphene), the crystallites are oriented in the same direction, while they are disordered in hard carbons. Hard carbons deliver higher reversible capacities but suffer from poor rate capacities due to random alignment of graphene sheets.[4]

Apart from carbon based materials, metal-oxides have been considered promising candidates for intercalation anodes for LIBs. They offer high volumetric energy densities, safety, and high power performance during cycling. A typical example for this type of materials are titanium based oxides such as TiO_2 or $Li_4Ti_5O_{12}$. Their characteristic advantages are low toxicity, low volume changes during cycling, good cycling stability and cheap prize.[5] However, their theoretical gravimetric specific capacities are very low, 330 mAh g^{-1} for TiO_2 and only 175 mAh g^{-1} for $Li_4Ti_5O_{12}$.[4] Regarding TiO_2, the anatase form attracted the most attention in research, but there are also studies on the rutile and the brookite form of TiO_2.[6] Nevertheless, all of these materials suffer from low energy densities, and low electronic conductivity. The spinel $Li_4Ti_5O_{12}$ exhibits the so-called “zero strain” property, with only very little structural changes during Li intercalation and deintercalation. However, it features the same problems for application in LIBs as TiO_2 based materials.

Recent studies report on the intercalation of Li ions in $Li_{1+x}V_{1-x}O_2$ at a potential of about 0.1 V vs. Li^+/Li. Kim *et al*. reported on $Li_{1.1}V_{0.9}O_2$ as anode material for LIBs with a gravimetric specific capacity of 345 mAh g^{-1}.[7] Another group tested $Li_{1+x}VO_2$ (x = 0.00-0.35) as anode material and achieved a discharge capacity of 294 mAh g^{-1}.[8] O’Dwyer *et al.* prepared $NiVO_3$ fused oxide nanoparticles *via*

thermal reduction of Ni-doped vanadium oxide nanotubes.[9] The fact that intercalation of Li ions in $Li_{1+x}V_{1-x}O_2$ takes place at a potential similar to graphite (about 0.1 V vs. Li^+/Li) is of high importance, especially when compared to the relatively high potential of about 1.6 V vs. Li^+/Li for titanates. This allows for much higher theoretical volumetric capacities (1360 mAh cm^{-3}) which is, in theory, a main advantage of dense metal oxides as anodes compared to graphite (790 mAh cm^{-3}).[10] This advantage is mostly negated for titanate based materials due to their high potential. However, vanadium-based anodes exhibit issues in terms of toxicity and high electronic resistivity, which are main hindrances when it comes to actual application.

Another type of metal-oxide intercalation anodes is based on MoO_2, a material that is more commonly used as conversion anode in LIBs. Dahn *et al*. studied the structure and electrochemistry of Li_xMoO_2 (x = 0-1) in 1987.[11] They figured out that Li/Li_xMoO_2 is stable in the regions of the monoclinic and the orthorhombic phase but cycles poorly through the M-O and O-M transitions. Since then, not much research has been done on this material as intercalation anode for LIBs. However, in 2014, Mitra *et al*. fabricated nanobelts of MoO_2 and applied them as intercalation anodes. With a theoretical gravimetric specific capacity of 209 mAh g^{-1},[11] they received up to 139 mAh g^{-1} after 200 cycles at a specific current rate of 50 mA g^{-1} in a potential window of 0.01 V to 3 V.[12] Not only MoO_2, but also MoS_2 received attention regarding its usage as anode material in LIBs. Zhao *et al*. introduced a N-doped graphene/MoS_2/N-doped graphene heterostructure with a reversible capacity of 522 mAh g^{-1} after 600 cycles.[13] Huo *et al*. investigated oriented MoS_2 nanoflakes on N-doped carbon nanosheets and obtained a reversible capacity of 722 mAh g^{-1} after 100 cycles.

Table 1.1 gives an overview of the before mentioned intercalation anodes for LIBs.

Table 1.1. Overview of intercalation anodes for LiBs.

Material	**Theoretical Gravimetric Capacity [mAh g^{-1}]**	**Reference**
Li_6C	372	Capiglia *et al.*[4]
TiO_2	330	Capiglia *et al.*[4]
$Li_4Ti_5O_{12}$	175	Capiglia *et al.*[4]
$Li_{1.1}V_{0.9}O_2$	345	Kim *et al.*[7]
$Li_{1+x}VO_2$ (x = 0.00-0.35)	294	Kim *et al.*[8]
MoO_2	209	Dahn *et al.* & Mitra *et al*.[11-12]
MoS_2	670	Zhao *et al.* & Huo *et al*.[13-14]

1.3.2 Conversion Anodes

Conversion anodes for LIBs are typically transition metal compounds such as oxides, phosphides, sulfides, and nitrides. Their electrochemical behavior is based on reduction of the respective transition metal and formation of Li compounds during lithiation.[4]

A well-known type of material used as conversion anode in LIBs are iron based oxides. γ-Fe_2O_3 and α-Fe_3O_4 are considered to be promising candidates for application in LIBs, due to their high theoretical gravimetric specific capacities of 926 and 1007 mAh g^{-1}, respectively.[15] However, they exhibit poor cycling performance due to high volume expansion and iron aggregation during cycling.[4] To fight these issues, preparation of porous nanomaterials or introduction of carbon based composite materials have been studied. In 2005, Kanno *et al*. investigated nano-sized γ-Fe_2O_3 as conversion anode material for LIBs and observed reversible Li intercalation without spinel-rocksalt phase transformation, allowing for good cycling stability.[16] Cho *et al*. fabricated spindle-like porous α-Fe_3O_4 from on an iron-based metal organic framework template.[17] Their electrodes demonstrated that good cycling stability can be achieved with this type of material.

Similar studies have been performed on cobalt oxides. CoO shows a theoretical gravimetric specific capacity of 715 mAh g^{-1}, while Co_3O_4 theoretically reaches 890 mAh g^{-1}.[18] Huang *et al*. managed to obtain ultrathin CoO/graphene nanosheets with high reversible capacities.[19] McNulty *et al*. utilized a polystyrene template to produce inverse opal structured Co_3O_4. Applied as conversion anode in LIBs, this material exhibited an initial capacity of 1655 mAh g^{-1}. The authors assumed that cation vacancies with lithiated oxygen sites were introduced, which served as additional charge-storage sites.[20]

Many other types of metal oxides such as CrO_x, MoO_x, MnO_x, NiO, CuO_x, and SnO_2 have been studied regarding their application as conversion anodes in LIBs. All of these materials delivered high capacities but suffered from low cycling stability.[21] They will not be described in more detail in this work for reasons of clarity.

Apart from oxides, metal phosphides, sulfides, nitrides, and hydrides have also investigated regarding their application as conversion anodes for LIBs.

Metal phosphides can act as both, intercalation and conversion anodes. If used as conversion anodes, Li phosphides and metal particles are formed during lithiation. Typical metals are Fe, Co, Ni, Cu, Ge and Sn. Stevenson *et al*. prepared amorphous FeP_2 by reacting $Fe(N(SiMe_3)_2)_3$ with PH_3.[22] Shin *et al*. electroplated FeP_x (x = 0.85-0.91) films on Cu substrates and tested them as anodes in LIBs.[23] Yan *et al*. developed a thermal decomposition method to obtain Co_xP nanostructures.[24] Tatsumisago *et al*. prepared cubic NiP_2 crystals *via* a mechanical milling technique from a mixture of Ni and red P.[25] The

group of Guo *et al*. fabricated monodispersed carbon-coated NiP_2 nanoparticles anchored on CNTs. Used as conversion anodes in LIBs, these particles exhibited extremely high cycling stability.[26] Falqui *et al*. fabricated Cu_3P nanoplates with hexagonal morphology in a one-pot approach and suggested that they could be attractive for application in LIBs due to their cyclability properties during charge-discharge cycling.[27] Another group utilized a CuP_3/reduced graphene oxide composite as anode in LIBs.[28] Zitoun *et al.* synthesized a Cu_3P membrane with faster kinetics during cycling.[29] Zhou *et al*. utilized high energy mechanical ball milling to synthesize GeP_5 which they then used as anode material in LIBs. By using a GeP_5/C nanocomposite, a high capacity retention could be achieved. The group figured out that a combination of a conversion and an alloying reaction took place during lithiation, as Li_3P as well as Li_xGe alloys were formed, explaining the high capacity of those anodes.[30] Tuan *et al*. prepared mesoporous GeP_x microspheres by mixing tri-*n*-octylphosphine, diphenylgermanium, and toluene in a titanium reactor.[31] Tin phosphide anodes show a similar reaction mechanism, combining conversion and alloying. Fu *et al*. fabricated Sn_4P_3 anodes for LIBs applying a pulsed-laser-deposition technique starting from Sn and P powders.[32] Park *et al*. prepared a layered SnP_3/C composite by high energy ball milling of the elements.[33] Chen *et al*. synthesized Sn_4P_3 *via* a solvothermal method with the possibility to control the particle size by adjusting the solvent ratio.[34]

Conversion anodes based on metal sulfides and metal nitrides will not be discussed in detail in this work as they are of only minor importance for the studies performed during this thesis. Their Li insertion reaction mechanisms are analogous to metal phosphides, forming Li sulfides and Li nitrides. Regarding metal sulfides, Mo, W, Mn, Fe, Co, Ni, Sn, and Sb have been in the spotlight of recent research.[35] Concerning metal nitrides as conversion anodes for LIBs, SiN_x, VN, CrN, Mn_4N, Fe_3N, Co_3N, Ni_3N, and Cu_3N have been excessively studied.[36] Hydrides of these mentioned metals have also been investigated in regard of their application in LIBs, however their conversion reaction with lithium suffers from low reversibility at room temperature.[37]

Newer studies also focus on hybrid organic/inorganic materials as anodes for LIBs. Yamauchi *et al*. report on mesoporous iron phosphonate electrodes. They offer a large contact area with the electrolyte, high structural stability, and short transport pathways for Li^+ ions, resulting in high specific capacities and good cycling stability.[38] Villevieille *et al.* investigated lithium iron methylenediphosphonate *via operando* X-ray absorption spectroscopy and pronounced a methodology to verify the predicted P co-cycling of other conversion-type materials.[39]

Table 1.2 gives an overview of the before mentioned conversion anodes for LIBs.

Table 1.2. Overview of conversion anodes for LIBs.

Material	**Initial Capacity [mAh g^{-1}]**	**Capacity after X Cycles [mAh g^{-1}]**	**Reference**
γ-Fe_2O_3	926 (theo.)	-	Zhu *et al.*[15]
α-Fe_3O_4	1007 (theo.)	-	Zhu *et al.*[15]
Spindle-like porous α-Fe_3O_4	-	911 after 50	Cho *et al*.[17]
CoO	715 (theo.)	-	Tondello *et al.*[18a]
Co_3O_4	890 (theo.)	-	Xia *et al.*[18b]
CoO/graphene nanosheets	-	1018 after 520	Huang *et al*.[19]
Inverse opal structured Co_3O_4	1655	230 after 50	McNulty *et al*.[20]
Amorphous FeP_2	1258	906 after 10	Stevenson *et al*.[22]
FeP_x (x = 0.85-0.91) films	-	420 after 30	Shin *et al*.[23]
Hollow CoP nanoparticles	-	630 after 100	Yan *et al*.[24]
Cubic NiP_2 crystals	1100	600 after 5	Tatsumisago *et al*.[25]
Monodispersed carbon-coated NiP_2 nanoparticles	-	816 after 1200	Guo *et al*.[26]
CuP_3/reduced graphene oxide composite	1578	954 after 80	Yan *et al*.[28]
Cu_3P membrane	419	250 after 20	Zitoun *et al.*[29]
GeP_5	2406	250 after 40	Zhou *et al*.[30]
Mesoporous GeP_x microspheres	2126	1400 after 150	Tuan *et al*.[31]
Sn_4P_3	1076	553 after 10	Fu *et al*.[32]
Layered SnP_3/C	1306	1000 after 20	Park *et al*.[33]
Mesoporous Fe phosphonate	790	355 after 30	Yamauchi *et al*.[38]

1.3.3 Alloy-Based Anodes

Alloy-based anodes for LIBs are a promising candidate for future applications. Typical examples for this type of anodes are based on Al, Si, Ge, Sn, and P. Their Li insertion mechanism is based on the formation of Li-rich alloy compounds, leading to extremely high theoretical gravimetric specific capacities. While providing high capacities, all these materials have in common that they suffer from drastic volume changes (around 300% for Si and Ge)[40] which they undergo during Li alloying and dealloying. These volume changes lead to contact losses and therefore poor cycling performances as the capacities fade rapidly with increasing cycle number. Another general disadvantage of alloy-based anodes are relatively high irreversible capacities during the first cycles due to solid-electrolyte interphase (SEI) formation.

As this work focusses on the fabrication of alloy-based anodes from elements of the main-groups IV and V of the periodic table, their most prominent representatives regarding LIBs will be discussed in more detail in the following. An overview can be found in Table 1.3 at the end of this chapter.

Si is probably the most attractive material for actual application in LIBs. It shows the highest theoretical gravimetric specific capacity of all tetrel elements, can be found in high abundance which leads to low costs, and Si based anodes are safe for use.[41] Theoretically, a capacity of up to 4056 mAh g^{-1} could be achieved for $Li_{17}Si_4$, which is the Li-richest compound in the Li-Si system. However, $Li_{17}Si_4$ could only be obtained by cycling at high temperatures and therefore $Li_{15}Si_4$ with a theoretical specific capacity of 3579 mAh g^{-1} is seen as the Li-richest phase that can be electrochemically achieved in LIBs.[42] Lithiation and delithiation of Si in LIBs have been well studies by groups of Christensen and Dahn.[41a, 43] During lithiation, crystalline Si becomes amorphous and forms an amorphous Li_xSi phase. Upon further lithiation, crystalline $Li_{15}Si_4$ is formed at 30 mV. By lithium extraction, the $Li_{15}Si_4$ again forms amorphous Li_xSi, which then undergoes a two-phase reaction to amorphous Si. Grey *et al*. suggested a phase width of the $Li_{15}Si_4$ phase, since more Li can be inserted into the crystalline phase by lowering the voltage down to 0 V.[44] As mentioned before, alloy-based anodes show high irreversible capacities during the first cycles due to SEI formation. Usually, SEI composition is based on the used electrolyte in the cell. However, the SEI formed on Si surfaces during cycling also contains Li_xSiF_y and Li_xSiO_y species, with the latter most likely originating from a native SiO_2 layer on Si particles, as shown by Lucht *et al*.[45] The main issue for practical application of Si anodes in LIBs are volume changes of up to 310% during lithiation and delithiation. Therefore, many studies investigated porous Si materials, which are supposed to be a possible solution to overcome that problem.

Cui *et al*. prepared hollow Si nanospheres by utilizing chemical vapor deposition (CVD) of SiH_4 onto a SiO_2 template.[46] Lee *et al*. fabricated hollow porous Si nanoparticles by magnesiothermic reduction of

hollow porous SiO_2 nanoparticles which were previously formed by a templating method involving a polysterene template.[47] Chen *et al.* prepared Si particles sandwiched in a 3D polyacrylonitrile matrix.[48] Tu *et al.* encapsulated Si nanoparticles into mesoporous carbon and applied the resulting pomegranate-structured electrodes as anodes in LIBs.[49] Liang *et al*. obtained nest-like Si nanospheres *via* a solvothermal method, utilizing NaSi and NH_4Br.[50] Guo *et al.* fabricated watermelon-inspired Si/C microspheres with hierarchical buffer structures.[51] Nanowires were also extensively studied as possibly desired morphology of Si anodes. Lieber *et al*. demonstrated the preparation of Si nanowires by vapor-liquid-solid (VLS) growth and implemented size-control by formation of nanometer-diameter catalyst clusters by laser ablation.[52] The group of Cui prepared Si nanowires by a VLS growth method directly onto stainless steel current collectors.[53] Cho *et al*. focused on the fabrication of 3D porous Si particles by thermal annealing and etching starting from butyl-capped Si gels and SiO_2 nanoparticles.[54] Fultz *et al*. prepared two different nanostructured Si materials as electrodes for LIBs. Nanocrystalline Si clusters were formed *via* gas-phase condensation and ballistic consolidation on Cu. Nanostructured Si films were prepared by evaporating elemental Si on Ni current collectors.[55] Ozin *et al*. synthesized hydrogenated amorphous Si inverse opals, nanocrystalline Si inverse opals, nanocrystalline Si-C inverse opal composites, and inverse opal composites consisting of carbon and amorphous Si. The inverse opal structure was fabricated with the intention to create a mechanically flexible framework, able to cope with the volume changes during cycling. Their electrodes showed promising capacity retentions and rate capabilities.[56]

SiO is also seen as viable candidate for anodes in LIBs. SiO consists of random mixtures of amorphous Si and amorphous SiO_2 domains.[57] During lithiation, Li-Si alloys, Li_2O, and lithium silicates are formed.[58] The alloying and dealloying reactions in the amorphous Si domains are reversible and mainly contribute to the capacity, while the reactions in the SiO_2 domains seem to be irreversible.[59] The problem of volume changes during charge-discharge cycles remains with this material, as well as low electrical conductivity and poor Li insertion/de-insertion rates. To overcome these problems, among other approaches, mainly carbon coating and particle size reduction have been studied.[45a, 60]

The heavier analogue germanium is also considered to be a promising candidate for alloy-based anodes in LIBs. Its theoretical gravimetric specific capacity is with 1385 mAh g^{-1} (for $Li_{15}Ge_4$) lower than for Si, but still much higher than for commercial graphite anodes.[61] Ge shows a volumetric capacity of 7366 A h L^{-1}, which is close to that of Si (8334 A h L^{-1}), making Ge an attractive alternative for Si in porous electrodes.[62] Additionally, the Li ion diffusivity of Ge is approximately 15 times higher than for Si at 360 °C ($2.14 \cdot 10^{-7}$ cm^2 s^{-1} vs. $1.48 \cdot 10^{-8}$ cm^2 s^{-1}) and about 400 times higher at room temperature. It also exhibits an electronic conductivity four orders of magnitude higher than Si.[63] Similar to Si, the volume changes are the main hindrance for practical application of Ge anodes in LIBs.[40b] Recent

research focused on the formation of highly porous materials to optimize Ge anodes for usage in LIBs.[64]

Mitlin *et al*. prepared Ge nanowires with distinct mass loading with adjustable diameters, lengths, and thicknesses utilizing a VLS process.[65] Tuan *et al*. used a gold-seeded supercritical fluid-liquid-solid method to prepare Ge nanowires. The nanowires were subsequently passivated by functionalization with dodecanethiol.[66] Korgel *et al*. fabricated Ge nanowires by an Au nanocrystal-seeded solution-liquid-solid growth, starting from diphenylgermane.[67] Zhang *et al*. prepared Ge nanoparticles starting from $GeBr_2$ and oleylamine. The obtained material was then added to graphene oxide sheets and ultrasonicated. By addition of CNTs and H_2 driven reduction, a Ge-graphene-CNT composite was achieved which was further used as anode material.[68] Furthermore, Ge nanoparticles attracted a lot of attention in recent studies. Landi *et al*. utilized a CVD process to synthesize Ge nanoparticles which were then introduced in single-wall CNT electrodes.[69] Maier *et al*. encapsulated Ge nanoparticles with carbon by a solid-state pyrolysis of thermally polymerized tetraallylgermane.[70] Zhou *et al*. synthesized nanoscale Ge-grains by reduction of GeO_2 using H_2.[71] Mullins *et al*. report on slurry-cast anodes utilizing commercially available Ge nanopowder.[72] Cho *et al*. prepared Ge nanoparticles by mixing $GeCl_4$ and 1,2-dimethoxyethane and adding the solution to a sodium naphtalide solution. After addition of butyllithium, Ge nanoparticles were obtained.[73] Bao *et al*. mixed graphene oxide and polyvinylpyrrolidone in ethanol and added $GeCl_4$. After precipitation and annealing, a Ge nanoparticle/reduced graphene oxide composite material was obtained.[74] Zitoun *et al*. fabricated Ge nanoparticles *via* oxidation of the Zintl precursor $Na_{12}Ge_{17}$ by addition of alcohols.[75] Wu *et al*. prepared mesoporous Ge *via* a mechanochemical reaction involving GeO_2 and Mg powder, including a subsequent etching process using HCl.[76] Winter *et al*. report on 3D macroporous Ge particles, produced by heating a GeO_2 template and Mg powder in a mixed Ar/H_2 atmosphere.[77] Park *et al.* synthesized mesoporous Ge materials by a zincothermic reduction of GeO_2.[78] Porous Ge films are another promising morphology due to their mechanical stability and flexibility such films could provide. Paik *et al*. prepared inverse opal structured Ge films with dense and porous walls by CVD of GeH_4 onto a silica opal template. The template was removed by etching with hydrofluoric acid.[79]

Ge oxides have also been studied regarding their application as anodes in LIBs. The group of Cho synthesized a GeO_2/Ge/C nanocomposite anode material. In a first step, they synthesized GeO_2 nanoparticles by a hydrolysis method starting from $GeCl_4$. By heating in an acetylene/Ar atmosphere, a carbon coating layer was formed on the particles. *Via* increasing of the heating temperature, a partial reduction of the GeO_2 particles was achieved and the desired composite material was obtained.[80] Lee *et al*. fabricated mesoporous GeO_2-based carbon composites. They used PEO-*b*-PS as structure directing agent, a phenolformaldehyde resin as carbon precursor, and $Ge(OEt)_4$ as Ge source in an

acidic tetrahydrofuran (THF)/H_2O solution. During solvent evaporation, a phase-separation between hydrophobic and hydrophilic phase takes place and the mixture self-assembles into wormhole-like mesoporous structures. Thermal carbonization formed a mesoporous GeO_2/C composite which was then thermally reduced in an Ar/H_2 atmosphere to the desired mesoporous Ge/GeO_2/C composite.[81] Prikhodchenko *et al.* deposited a GeO_2 thin film onto graphene oxide and tested the obtained material as anode in LIBs.[82]

Moving further in the periodic table, the heavier homologue Sn has also been considered as potential candidate for anodes in LIBs. Sn exhibits a lower theoretical gravimetric specific capacity than Si and Ge (991 mAh g^{-1}), but is shows a much higher electric conductivity ($9.17 \cdot 10^6$ S m^{-1} compared to 2.17 S m^{-1} for Ge and $1.56 \cdot 10^{-3}$ S m^{-1} for Si).[83] As for all alloy-based anodes, volume changes during lithiation and delithiation are the main problem of Sn electrodes. Different strategies were pursued to overcome this issue.

The group of Kovalenko prepared monodisperse colloidal Sn nanocrystals with tunable sizes by introducing $LiN(SiMe_3)_2$ into a hot oleylamine solution containing $SnCl_2$ or $Sn[N(SiMe_3)_2]_2$ at 180-200 °C. Subsequent reduction with diisobutylaluminium hydride and mixing in amorphous carbon and polymer binder yielded an electrode material which exhibited reversible discharge capacities of 700 mAh g^{-1} during 100 cycles.[84] Li *et al*. prepared metallic Sn nanocrystals embedded into graphitic mesoporous carbon walls by a one-step solid-liquid grinding/templating route. A mesoporous silica template, soybean oil and $SnCl_2$ were ball milled together and the mixture was heated to 900 °C for carbonization. Template removal was carried out by using NaOH.[85] Su *et al.* fabricated porous Sn-C composites. Industrial porous acrylic ion-exchange resin spheres were ground into a powder and immersed in a $SnCl_2$ solution. After washing and drying, a vacuum carbonization process was performed at 600 °C for 6 h. The resulting composite then underwent a CVD process utilizing a N_2/C_2H_4 gas flow to achieve surface carbon encapsulation.[86] Maier *et al.* fabricated metallic Sn particles encapsulated in porous multichannel carbon microtubes using an electrospinning technique based on Sn-octoate-poly(methyl meth-acrylate)-polyacrylonitrile emulsion in dimethyl formamide (DMF). The obtained fibers were stabilized in air at 250 °C, where encapsulated SnO_2 nanoparticles formed. The SnO_2 nanoparticles were finally reduced in an Ar/H_2 atmosphere.[87] They also report on the preparation of Sn@carbon nanoparticles encapsulated in hollow carbon nanofibers. Two solutions, a mixture of tributyltin and a mineral oil solution as well as a polyacrylonitrile solution were used for electrospinning. The nanofibers were then immersed in *n*-octane and subsequently pyrolyzed at 1000 °C to form the desired Sn@carbon nanoparticles.[88] Deng *et al.* embedded well-dispersed Sn nanoparticles in a porous N-doped graphene-like carbon network by a facile one-step thermal reaction.[89] The group of Bai prepared carbon-fiber supported Sn materials by a two-step process. In the first step, viscose carbon

fibers were impregnated with $SnCl_4$ for 24 h. In the second step they were heated under Ar/H_2 gas flow at 400 °C and then further to 800 °C for 2 h.[90] Zhang *et al*. reported on Sn nanopillar arrays embedded between graphene sheets. Graphite powders were exfoliated and dispersed in N-methyl-2-pyrrolidone. The solution was filtrated through an anodic aluminum oxide membrane, resulting in a graphene film on the membrane. A Sn film was then deposited on the graphene film by thermal evaporation of Sn powder. They also fabricated pure Sn films and tested them as anodes, they achieved an initial discharge capacity of 756 mAh g^{-1} and a capacity retention of 20% after 30 charge-discharge cycles.[91] Li *et al.* fabricated graphene networks anchored with Sn nanoparticles encapsulated with graphene shells using an *in situ* CVD technique. Citric acid, $SnCl_2$, and NaCl were dissolved in water and frozen at -20 °C for 24 h. The resulting gel was ground to a powder and used for the CVD synthesis. Prepared electrodes exhibited an initial discharge capacity of 1805 mAh g^{-1} and retained a reversible capacity of 1089 mAh g^{-1} after 100 cycles. Also tested pure Sn nanoparticles delivered a reversible capacity of 30 mAh g^{-1} after 50 cycles.[92] Wang *et al.* prepared 3D porous Sn thin films by electroless plating on Cu foam, using $SnCl_2$, NaH_2PO_2, and $CS(NH_2)_2$. Deposition took place at 60 °C for 30, 60, and 90 s.[93] Chung *et al.* synthesized a porous Ni-Sn foam by an electrodeposition process. A mixture of $NiCl_2$, $SnCl_2$, and H_2SO_4 in water was used for electrodeposition at a cathodic overpotential of -4 V on a Cu foil. The deposition process was accompanied by a hydrogen evolution reaction at room temperature on a three-electrode system. Two different foam compositions were synthesized, $Ni_{20}Sn_{80}$ and $Ni_{50}Sn_{50}$.[94]

The group of Miyasaka from Fuji Photo Film were the first to introduce a Sn metal oxide composite material as anode for LIBs.[95] Lithiation of SnO_2 is a two-step process. In a first partially irreversible step, Sn and Li_2O are formed. The second step is the reversible Sn-Li alloying reaction.[96] Taking the full two-step process into account, a theoretical gravimetric specific capacity of 1491 mAh g^{-1} could be reached. However, due to the irreversibility of the first step, a specific capacity of 783 mAh g^{-1} is considered to be the maximum gravimetric capacity of SnO_2.[4] Volume changes of more than 200% during lithiation and delithiation are the main problem of SnO_2-based anodes in LIBs. Similar to what has been mentioned before for Si and Ge, a wide variety of porous morphologies and nanostructures have been investigated in order to reduce the volume changes and to improve cycle life of SnO_2 anodes.[84, 97]

The elements P, As, Sb, and Bi from the fifth main group of the periodic table are also promising candidates for application as alloy-anodes in LIBs. Since a part of this work focused on the preparation of P-based anodes, research done on the element P as anode material will be described in more detail in the following.

Orthorhombic Black P is an attractive material for Li accommodation. It shows a layered structure, comparable to the graphite structure. It exhibits a high capacity of 2595 mAh g^{-1}, due the formation of the Li-rich Li_3P alloy phase during lithiation.[98] Sohn *et al*. prepared black P by high energy mechanical milling of red P under Ar atmosphere for 54 h. Black P/carbon composites were prepared similarly by milling for 12 h. Synthesized black P showed an initial charge capacity of 1279 mAh g^{-1}, while the black P/carbon composite delivered an initial charge capacity 1814 mAh g^{-1}.[98b] Bonaccorso *et al*. utilized a liquid-phase exfoliation process of black P to achieve few-layer black P to increase the available surface area for enhancement of the electrochemical activity of black P. Size control of the black P flakes was done by solvent variation.[99] Tang *et al*. gained a composite material consisting of black P and carbon paper by a thermal annealing process of red P and carbon paper.[100] However, due to the difficulty of the synthesis of black P, not many studies have been performed on this material regarding its application as anode in LIBs.

Many reports on red P as anode material for LIBs can be found in literature. Qian *et al.* applied a wet solvothermal method to prepare hollow P nanospheres with porous shells. PCl_5 in toluene solution was reduced by NaN_3 at 280 °C for 12 h. [101] Tuan *et al.* prepared iodine-doped red P nanoparticles. PI_3 in a solution of iodobenzene was reduced in a solution-phase process by ethylene glycol. Cetyltrimethylammonium bromide was used as surfactant for size control of the formed P particles.[102] Mei *et al.* homogeneously distributed red P nanoparticles in cigarette filter-derived porous carbon by a vaporization-condensation method. Cigarette filters were heated up to 850 °C under Ar atmosphere for 2 h to obtain porous carbon. The so-prepared porous carbon was mixed with red P and heated to 500 °C under Ar atmosphere for 12 h and then cooled to 300 °C for 24 h.[103] Zhang *et al.* fabricated a red P/CNT composite material. Previously ball milled red P was dispersed in water and heated at 200 °C for 12 h in an autoclave. After purification, the red P was dispersed in a water/ethanol mixture and ultrasonicated together with multi-walled CNTs.[104] Sakurai *et al*. prepared P-encapsulated CNTs with nanopores on the sidewalls by gas-phase synthesis. Red P and purified multi-walled CNTs were heated at 550 °C for 10 h and then cooled down to room temperature.[105] Yu *et al.* utilized a vaporization–condensation–conversion process to integrate red P into a mesoporous carbon matrix. Red P and a mesoporous carbon matrix were heated over the sublimation temperature of red P to achieve diffusion of P vapor into the pores of the carbon matrix. The obtained white P was further converted to red P by heating at 260 °C.[106] Wang *et al.* fabricated red P-graphene nanosheet hybrids by ball-milling of red P and graphene stacks.[107] Chang *et al.* investigated a red P/carbon cloth composite as anode material. Cotton cloth was carbonized at 900 °C and then mixed with red P. The mixture was heated to sublimate red P. Transformation to white P was prevented by applying an additional thermal treatment at 300 °C.[108] Zheng *et al.* synthesized red P/carbon films with embedded red P particles in a cross-linked-structural carbon film by vapor phase polymerization followed by a pyrolysis process.

Ball milled red P was added to a solution of ferric *p*-toluenesulfonate in *n*-butanol. After ultrasonication, the mixture was applied onto a glass substrate and exposed to pyrrole vapor to obtain the desired composite film.[109] Tian *et al.* fabricated a composite material consisting of nanoconfined red P films on interconnected multi-walled CNT networks by a wet ball-milling process. Red P, multi-walled CNTs, and water were ball-milled together and then dried by a freeze-drying step at -50 °C for 24 h.[110] Feng *et al.* prepared red P/pyrolyzed bacterial cellulose free-standing films *via* thermal carbonization followed by a vaporization-condensation process. Red P and a film of pyrolyzed bacterial cellulose were heated together to 450 °C for 24 h, then the temperature was decreased to 260 °C for another 24 h. The obtained films were washed with CS_2 and dried.[111]

As already described in Chapter 1.3.2, metal phosphides can act as conversion and alloying anodes. While during the conversion mechanism Li_3P and the elemental metal are formed, an alloying reaction leads to the formation of Li_xMP_y species. Formation of Li_xMP_y delivered high capacities and stable crystalline structures, but suffered heavily from rapid capacity fading after a few cycles, due to collapsing of the phosphides. The group of Nazar reported on MnP_4 as anode material, which formed Li_7MnP_4 during Li insertion.[112] This attracted new attention to the research field of phosphide based alloying anodes. Sohn *et al*. investigated the reaction mechanism of VP_4 in LIBs. They described the reaction in four steps. In the first step, a topotactic Li insertion takes place and Li_3VP_4 is formed. Secondly, a phase transformation of the monoclinic Li_3VP_4 to the cubic phase Li_6VP_4 takes place. Then the structure decomposes and Li_3P as well as VP are formed and finally Li is inserted into VP to form LiVP. Formation of Li_6VP_4 results in a volume expansion of 270% when compared with the initial VP_4, which leads to disintegration of the active anode material and therefore to very low cycling stability.[113] Sohn *et al*. and Tarascon *et al*. also performed similar studies on VP and VP_2 as possible anode materials for LIBs.[114] However, due to much better cycle life, most research on metal phosphides focused on their usage as conversion anodes which have been discussed before in Chapter 1.3.2.

Table 1.3 gives an overview of the before mentioned alloy-based anodes for LIBs.

Table 1.3. Overview of alloy-based anodes for LIBs.

Material	**Initial Capacity [mAh g^{-1}]**	**Capacity after X Cycles [mAh g^{-1}]**	**Reference**
Silicon based			
$Li_{15}Si_4$	3579 (theo.)	-	Fässler *et al.*[42b, 42c]
Hollow Si nanospheres	2725	2180 after 700	Cui *et al*.[46]
Hollow porous Si nanoparticles	3762	3499 after 100	Lee *et al*.[47]
Si particles in a 3D matrix	3081	1423 after 500	Chen *et al.*[48]
Nest-like Si nanospheres	3052	1095 after 48	Liang *et al*.[50]
Si/C microspheres	620	496 after 250	Guo *et al.*[51]
Si nanowires	3124	-	Cui *et al.*[53]
3D porous Si particles	3138	3107 after 100	Cho *et al*.[54]
Nanocrystalline Si clusters	1100	550 after 50	Fultz *et al*.[55]
Nanostructured Si films	3500	2000 after 50	Fultz *et al*.[55]
Germanium based			
$Li_{15}Ge_4$	1385 (theo.)	-	Grey et al.[61]
Ge nanowires	1405	1377 after 100	Mitlin *et al*.[65]
Ge nanowires	1332	1130 after 100	Tuan *et al*. [66]
Ge nanowires	1050	800 after 20	Korgel *et al.*[67]
Ge nanoparticles	1602	864 after 100	Zhang *et al*.[68]
Ge nanoparticles	850	-	Landi *et al*.[69]
Ge nanoparticles	1190	774 after 50	Maier *et al*.[70]
nanoscale Ge-grains	1920	1500 after 40	Zhou *et al*.[71]
Ge nanopowder	-	700 after 500	Mullins *et al*.[72]
Ge nanoparticles	1470	-	Cho *et al*.[73]
Ge nanoparticle/reduced graphene oxide composite	1475	700 after 200	Bao *et al*.[74]
Ge nanoparticles	900	540 after 10	Zitoun *et al*.[75]
3D macroporous Ge particles	1508	890 after 200	Winter *et al*.[77]
Mesoporous Ge	1450	1449 after 100	Park *et al.*[78]
Inverse opal structured Ge films	1375	1224 after 100	Paik *et al*.[79]
GeO_2/Ge/C nanocomposite	2293	1650 after 50	Cho *et al.*[80]

GeO_2-based carbon composites	2250	1710 after 90	Lee *et al.*[81]
GeO_2 film on graphene oxide	2067	1798 after 50	Prikhodchenko *et al.*[82]
Tin based			
$Li_{22}Sn_5$	991 (theo.)	-	Huggins *et al.* [108]
$Li_{17}Sn_4$	960 (theo.)	-	Nazar *et al.*[115]
Colloidal Sn nanocrystals	-	700 after 100	Kovalenko *et al.*[84]
Metallic Sn nanocrystals	691	560 after 100	Li *et al.*[85]
Porous Sn-C composites	692	496 after 100	Su *et al.*[86]
SnO_2 nanoparticles	774	648 after 140	Maier *et al.*[87]
Sn nanoparticles	1129	595 after 100	Deng *et al.*[89]
Carbon-fiber supported Sn	1168	740 after 160	Bai *et al.* [90]
Sn nanopillars	945	879 after 30	Zhang *et al.*[91]
Sn films	756	151 after 30	Zhang *et al.*[91]
Sn nanoparticles	1805	1089 after 100	Li *et al.* [92]
3D porous Sn thin films	676	311 after 100	Wang *et al.*[93]
Porous Ni-Sn foam	361	530 after 50	Chung *et al.* [94]
Phosphorus based			
Li_3P	2595 (theo.)	-	Cao *et al.* Sohn *et al.* [98]
Black P	1279	-	Sohn *et al.* [132]
Black P/carbon composite	1814	600 after 100	Sohn *et al.* [132]
Few-layer black P	1732	480 after 100	Bonaccorso *et al.*[99]
Black P/ carbon paper composite	2169	1677 after 200	Tang *et al.*[100]
Hollow P nanospheres	2799	1655 after 80	Qian *et al.*[101]
Iodine-doped red P nanoparticles	2519	1562 after 150	Tuan *et al.* [102]
Red P nanoparticles	1744	1244 after 50	Mei *et al.*[103]
Red P/CNT composite	2166	960 after 120	Zhang *et al.*[104]
P-encapsulated CNTs	1819	834 after 50	Sakurai *et al.*[105]
Red P integrated in a mesoporous carbon matrix	2250	1150 after 100	Yu *et al.*[106]
Red P-graphene nanosheet hybrids	2517	1283 after 300	Wang *et al.*[107]

Red P/carbon cloth composite	1100	910 after 200	Chang *et al.*[108]
Red P/carbon films	1511	903 after 640	Zheng *et al.*[109]
Nanoconfined red P films on interconnected multi-walled CNT networks	1981	1397 after 50	Tian *et al.*[110]
Red P/pyrolyzed bacterial cellulose free-standing films	1742	1040 after 100	Feng *et al.*[111]

1.4 Tetrel Zintl Anions

Zintl phases are intermetallic phases, formed from alkaline and earth alkaline metals with the exception of Be and elements from the groups 13-16 of the periodic table, with the exception of the second period.[83b] They are named after the German chemist Eduard Zintl due to his merits on the research of these phases.[116] Zintl phases comprise polyanions forming chains, two or three dimensional networks, or molecule-like entities.[117] Based on the Zintl-Klemm-concept, electrons get formally transferred from the more electropositive alkaline or earth alkaline metal to the more electronegative element. Between elements of group 13 and group 14 a hypothetical boundary, the Zintl line, is drawn. Elements from the 14th group can form salts with polymeric anions. The structure of the polyanions has to be considered on the basis of the electronic state as they adopt structures of isovalence electronic species in accordance to the 8-N rule.[116, 118] Typical examples for such Zintl phases are NaTl and KSb.[118-119] NaTl consists of the $[Tl^-]_x$ polyanion with a covalent diamond-type structure, while KSb exhibits chain like $[Sb^-]_x$ polyanions. As predicted, their structures match the element structures of the isovalance electronic C and Te, respectively.

However, this thesis focused on Zintl anions from the group 14 elements Ge and Sn. Tetrel elements form Zintl phases with the nominal compositions A_4Tt_4 (A = K, Rb; Tt = Si-Pb), A_4Tt_9 (A = K-Cs; Tt = Ge-Pb), and $A_{12}Tt_{17}$ (A = K-Cs; Tt = Si-Pb) by heating of stoichiometric mixtures of the elements.[120]

A_4Tt_4 phases contain isolated $[Tt_4]^{4-}$ tetrahedrons (Figure 1.1a). They are isovalence electronic to P_4 in white phosphorus and can be described by the 8-N rule.[121]

A_4Tt_9 contain $[Tt_9]^{4-}$ polyanions.[122] They are described by the Wade rules for electron deficient clusters. A $[Tt_9]^{4-}$ polyanion formally contains two electrons from each tetrel vertex and four electrons from the charge of the polyanion, adding up to 22 skeleton bonding electrons. According to the Wade rules, $[Tt_9]^{4-}$ polyanions are therefore classified as *nido*-clusters.[123] The *nido*-cluster can be described as mono-capped square antiprism with C_{4v} symmetry (Figure 1.1b). $[Tt_9]^{4-}$ can also form D_{3h} symmetric tricapped trigonal prism with elongated prism heights (Figure 1.1c). However, Tt_9 clusters do not only form $[Tt_9]^{4-}$ polyanions, but also $[Tt_9]^{3-}$ and $[Tt_9]^{2-}$. While the $[Tt_9]^{4-}$ clusters can be found in both, the solid state and solution, $[Tt_9]^{3-}$ and $[Tt_9]^{2-}$ clusters are only accessible in solution. $[Tt_9]^{2-}$ contain 20 skeleton bonding electrons according to the Wade rules and can be described as *closo*-deltahedra with the structure of a tricapped trigonal prism (Figure 1.1c). $[Tt_9]^{3-}$ clusters possess 21 skeleton bonding electrons and form structures between those of the *nido*- and the *closo*-clusters.

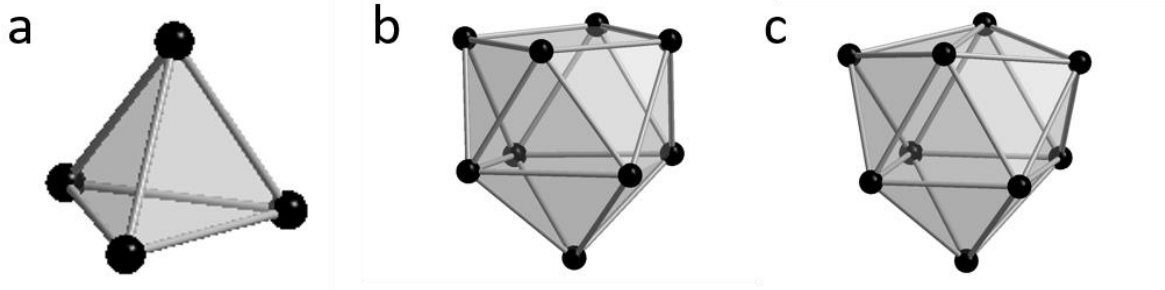

Figure 1.2. Schematic representation of a) $[Tt_4]^{4-}$,[124] b) nido-$[Tt_9]^{4-}$ with C_{4v} symmetry,[122b] and c) *closo*-$[Tt_9]^{2-}$ with D_{3h} symmetry.[125]

This work was based on the accessibility of $[Tt_9]^{4-}$ Zintl anions in solution. It can be achieved by extraction of A_4Tt_9 (Tt = Ge-Pb) phases with polar solvents such as ethylene diamine (*en*), dimethyl formamide (*dmf*), acetonitrile, and liquid ammonia.[120b, 120c] Solubility of A_4Tt_9 phases can be further enhanced by addition of sequestering agents such as cryptand[2.2.2], 18-crown-6, 15-crown-5, or other crown ethers.[126] While Tt_9 clusters in solution extracted from A_4Tt_9 phases consisting of the elements Ge, Sn, and Pb are well studied and reported in literature,[122g] A_4Si_9 phases are not known. Si_9 clusters in solution can be obtained from $A_{12}Si_{17}$ phases.[127] $A_{12}Tt_{17}$ phases in general consist of mixtures of $[Tt_4]^{4-}$ and $[Tt_9]^{4-}$ clusters with a ratio of 2 : 1.[120a, 122a]

The focus in this work was mainly centered on K_4Ge_9 and K_4Sn_9, due to the fact that $[Ge_9]^{4-}$ and $[Sn_9]^{4-}$ Zintl anions can be obtained in stable and highly concentrated solutions.

1.5 Inverse Opal Structured Tetrel Thin Films

Porous thin films of tetrel elements have been studied extensively in the last years as they offer promising properties for applications such as solar cells, batteries, or optical components.

Several studies focused on the fabrication of thin films *via* electrochemical methods or by template-assisted methods, mostly utilizing SiO_2 opals as template structure. Endres *et al*. performed electrodeposition to achieve 3D ordered macroporous Ge. $GeCl_4$ was added to the commercially available ionic liquids 1-methyl-3-methylimidazolium tris(pentafluoroethyl)trifluorophosphate ([HMIm]FAP) or 1-ethyl-3-methylimidazolium bis(trifluoromethylsulfonyl)amide ([EMIm]Tf_2N). ITO-coated glass covered with a multilayer polystyrene colloidal crystal was used as working electrode, an Ag wire as quasi-reference electrode, and a Pt ring as counter electrode. Electrodeposition was achieved by applying a constant potential. After THF supported template removal a macroporous Ge structure was obtained.[128] The same group also prepared Ge/Al and Ge/Si bilayer films and Si_xGe_{1-x} films *via* electrodeposition from ionic liquids.[129] Paik *et al.* deposited a Ge layer on a SiO_2 opal template using a CVD method, utilizing GeH_4 as Ge source. The SiO_2 template was removed by etching with HF.[79] Van Driel *et al.* applyied a very similar CVD method to form inverse Ge opals.[130] Fornés *et al.* created a face-centered cubic inverse opal Ge structure utilizing SiO_2 opals as template. The porous template was infiltrated by $Ge(OCH_3)_4$ which was then hydrolyzed to form GeO_2. The GeO_2 was further reduced in H_2 atmosphere resulting in Ge. Template removal was done by etching with HF.[131]

The groups of Kanatzidis and Tolbert were the first to introduce group 14-16 clusters as precursors for nanostructured non-oxide semiconductors. Zintl clusters offer a broad spectrum of possibilities for material synthesis, allowing for compositional variety, shape and size control, and elemental mixing on a molecular level.[120c, 132] They provide excellent solubility in organic solvents and can be oxidized to the respective elements, enabling fabrication of nanostructures with tunable composition and electronic properties. Kanatzidis *et al.* used Ga^{3+} and In^{3+} as linking agents of $[Ge_4S_{10}]^{4-}$ clusters and cetylpyridinium bromide in formamide as surfactant to form ordered mesostructured sulfidic solids with hexagonal frameworks.[133] Frameworks based on K_4SnSe_4 were prepared in the same way.[134] More literature can be found on mesostructures based on $[M_4Q_{10}]^{4-}$ (M = Ge, Sn; Q = S, Se, Te).[135] Tolbert *et al.* reported on the fabrication of periodic surfactant-templated nanostructured semiconductors. They were prepared *via* solution-phase self-assembly of $SnTe_4^{4-}$ clusters, linked by Pt salts and utilizing cetyltriethylammonium as structure directing agent.[136] In similar manner, the same group fabricated thin films with nanometer-scale periodicity based on the clusters $[Ge_4Se_{10}]^{4-}$, $[Sn_4Se_{10}]^{4-}$, and $SnSe_4^{4-}$. The different formed structures were described as partly disordered wormlike phase, periodic, hexagonal, honeycomb structure and highly ordered cubic geometry.[137]

Sevov and coworkers reported on the preparation of Ge films *via* anodic deposition of $[Ge_9]^{4-}$. The precursor K_4Ge_9 was dissolved in ethylene diamine (*en*). B-doped Si wafers were used as anodes and a Cu wire was used as counter electrode. Constant-current electrodeposition was carried out in a Teflon cuvette under N_2-atmosphere.[138]

Bentlohner *et al*. achieved inverse opal structured Ge thin films utilizing a facile wet-chemical synthesis route based on the K_4Ge_9 as Zintl precursor.[139] Poly(methyl methacrylate) spheres were utilized as template structure. They were dispersed in water and dip-coated onto a variety of substrates, such as Si, SiO_2, Al_2O_3, and tin oxides. Solutions of K_4Ge_9 in *en* were drop casted onto the PMMA coated substrates. After solvent assisted or thermal template removal, thin Ge films with inverse opal structure were obtained.

Inverse opal structures based on SnO_2 are also well known in literature. Deki *et al.* prepared inverse opal structured SnO_2 by a liquid phase deposition method. SnF_2 was dissolved in water and oxidized by H_2O_2, resulting in precipitating SnO_2 which was then dissolved in HF. H_3BO_3 was added and the solution was used to infiltrate a polystyrene colloidal crystal template. Inverse SnO_2 opals were obtained after thermal template removal.[140] Meng *et al.* combined a similar liquid phase deposition with a doctor-blading technique, also utilizing a polystyrene template to achieve highly ordered SnO_2 inverse opal films.[141] Variations based on the preparation of solutions of $SnCl_4 \cdot 5H_2O$ and citric acid in ethanol which were then used to infiltrate polystyrene templates to achieve inverse opal structured SnO_2 are also reported in literature.[142]

Inverse opal structured thin films of tetrel elements provide high mechanical stability and flexibility as well as high porosity and represent a material morphology which allows for potentially easy up-scaling, making it a very attractive candidate for several applications. Therefore the main focus of this work was the investigation of such honeycomb structured tetrel films and their potential applications.

1.6 Scope and Outline

This thesis builds up on the previously described work by Bentlohner *et al.*, the preparation of inverse opal structured Ge thin films utilizing a facile wet-chemical method revolving around the Zintl phase K_4Ge_9.[139] The main aim of this thesis is to utilize and modify the process to prepare anodes for LIBs. The honeycomb structure provides essential electron and Li ion pathways, needed for application as electrode in Li ion batteries. Its three-dimensional macroporous network should also be sufficiently mechanically stable to overcome the problem of significant volume changes during the charge-discharge process which are a main issue of alloy anodes. Other goals of this work are to expand the invented procedure to Sn and mixed Sn/Ge films, and to introduce P, Se, and Te to the framework systems.

In the following, PMMA synthesis, size variation, and coating techniques are described (Chapter 2.1). The parameters suitable for anode preparation are highlighted in this chapter.

The next part describes the synthesis of Ge thin films on Cu substrates (Chapter 2.2.1). Furthermore, XPS studies on the oxidation of the obtained films (Chapter 2.2.2) and electrochemical measurements performed with the prepared anodes are presented and discussed (Chapter 2.2.3).

The third part focuses on mixed Ge/P thin films (Chapter 2.3). The selection of suitable P sources (Chapter 2.3.1) as well as the usage of the doping agents PPh_3, NaP_7, and red P are described (Chapters 2.3.2 – 2.3.5). Strategies involving the ternary phases "$K_2Ge_2P_2$" and "$K_2Ge_7P_2$" are presented (Chapter 2.3.6). Finally, electrochemical measurements are shown (Chapter 2.3.7).

The fourth part describes the preparation of Sn and mixed Sn/Ge films (Chapter 2.4). Synthesis (Chapter 2.4.1), investigations on precursor solutions (Chapter 2.4.2) and obtained films (Chapter 2.4.3) as well as electrochemical measurements (Chapter 2.4.4) are presented.

The fifth part focuses on mixed Sn/Se films (Chapter 2.5.1), Sn/Te films (Chapter 2.5.2), and Sn/P films (Chapter 2.5.3).

P thin films are described in Chapter 2.6. Their synthesis is presented in Chapter 2.6.1 and electrochemical measurements are shown in Chapter 2.6.2.

The final part, experimental techniques (Chapter 4.1), analytical methods (Chapter 4.2), and syntheses (Chapter 4.3) are described.

2. Results and Discussion

In the following chapter the results of this thesis are presented and discussed.

2.1 PMMA Synthesis and Coating Techniques

As reported by Bentlohner *et al.*, PMMA opals were used as template for thin film fabrication.[139] PMMA opals were synthesized by emulsion polymerization according to Smarsly *et al.*,[143] starting from methyl methacrylate (MMA) in water and using sodium dodecyl sulfate (SDS) as structure directing agent. By variation of the amount of SDS added to the reaction mixture, particle size could be controlled. A higher amount of SDS in the mixture resulted in smaller PMMA particles. Particle size was monitored by dynamic light scattering. Detailed information on PMMA synthesis can be found in Chapter 4.3.8.

Different applications require different thin film properties (e.g. films with high mass loading for batteries, extremely thin films for solar cells). Because of this reason, various PMMA coating techniques have been investigated, aiming for optimal adjustment of the inverse opal structured thin films regarding their potential field of applications.

Bentlohner *et al.* utilized a dip-coating method to generate a homogenous PMMA coating on various substrates (silicon, silica, sapphire, FTO, and ITO).[139] Dip-coating onto Cu substrates without any previous surface treatment did not work out as the PMMA solution did not stick to the substrates and no coating could be achieved. Therefore, different surface treatments known as industrial standards were tested and compared regarding the homogeneity of the PMMA coating performed afterwards. Four different surface treatments were tested, they are shown in Table 2.1.

Table 2.1. Cu substrate surface treatments.

Method	Mixture A	Temperature	Mixture B	Temperature	Rinsing
A	9.8 mg $Na_2S_2O_8$ + 3.6 mL H_2SO_4 (96%) in 180 mL H_2O	35 °C (1 min)	-	-	H_2O
B	5.6 g $Na_2S_2O_8$ + 0.44 mL C_3H_8O in 70 mL H_2O	45 °C (1 min)	-	-	H_2O
C	H_2O_2 (30%) + NH_3 (conc.) in H_2O (1.3 : 2.2 : 100 wt%)	30 °C (ultrasonication, 2 min)	HCl in H_2O (1 : 100 wt%)	30 °C (ultrasonication, 2 min)	H_2O
D	EtOH + Acetone	RT (ultrasonication, 5 min)	2.5 g $FeCl_3$ + 5 mL HCl (conc.) in 50 mL H_2O	RT (ultrasonication, 5 min)	H_2O

Method C delivered the best results, here the most homogeneous coating could be obtained. The Cu substrates are placed in Mixture A and ultrasonicated at 30 °C for 2 min. After washing with water, another ultrasonication step with Mixture B is added. The substrates are finally washed with water and dried under vacuum. It was clearly visible to the unaided eye that the methods A, B, and D resulted in much more inhomogeneous Cu surfaces and therefore in worse PMMA coatings. Figure 2.1 shows photos of a Cu substrate before and after cleaning *via* method C. The surface is much smoother, allowing for better wetting by the PMMA solution.

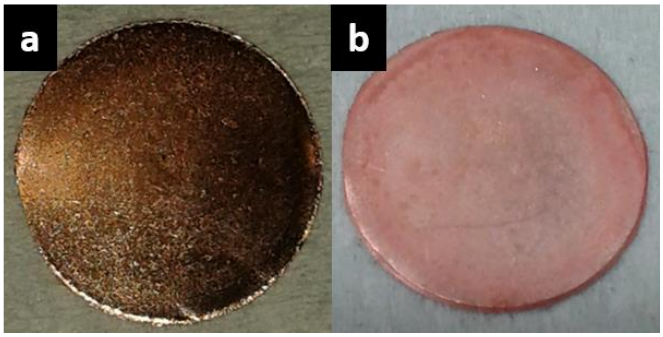

Figure 2.1. Cu substrates, a) before cleaning and b) after cleaning by applying method C.

PMMA-Dip-Coating (described in more detail in Chapter 4.1.3) served as standard procedure for thin film preparation in this work. It could be transferred to Cu substrates without any changes to the coating process. It allows for relatively thick coatings, usually around 2.5 – 3.0 µm (determined by profilometry by default, see Chapter 4.2.9), over a surface area of around 1.0 x 1.5 cm. Due to it being able to be easily transferred to copper substrates and resulting in a high film thickness, it also was the method of choice for electrode preparation.[144] Its downsides are the relatively high inhomogeneity and the lack of adjustable parameters. The achieved film thickness is solely dependent on the wetting of the substrate surface and cannot easily be controlled. Slight adjustments can only be done by varying the concentration of the PMMA solution and the dipping speed. The homogeneity of the coating can also not be controlled and is rather random, it suffers highly if the PMMA beads are clumped together. Therefore, the PMMA dispersion in water had to be ultrasonicated at least 2 d prior to the coating process, for at least 5 h per day.

Another method for PMMA coating is spin-coating (Figure 2.2). Here, the PMMA solution is directly given on a spinning substrate, which leads to a homogenous surface coating over larger areas (up to 9 cm^2 were tested). Different parameters were tested during the spin-coating experiments. The concentration of PMMA in water was varied between 15% and 25%. Additionally, different rotations speeds (750, 770, 800, 1000, 1500, 1600, 1750, 2000, and 3000 rpm) and spinning times (10 s, 30 s, and 45 s) were applied. PMMA concentrations of 25% were needed, with lower concentrations no

coating could be achieved. Rotation speeds of 750 rpm were too slow for the solvent to dry, resulting in extremely inhomogeneous coatings. Rotation speeds above 1750 rpm were too high, the PMMA dispersion did not stay on the substrate. The best parameters were found to be a 5 s ramp up to 770 rpm, holding that speed for 10 s, then followed by another 5 s ramp up to 1750 rpm and holding that speed for 30 s. However, the resulting films are extremely thin (< 0.5 µm). Film thickness cannot be controlled, since repeating the coating step leads to removal of the initially coated film. A minor downside of this technique is the high waste of PMMA solution, most of it gets slung away due to the rotation during the process.

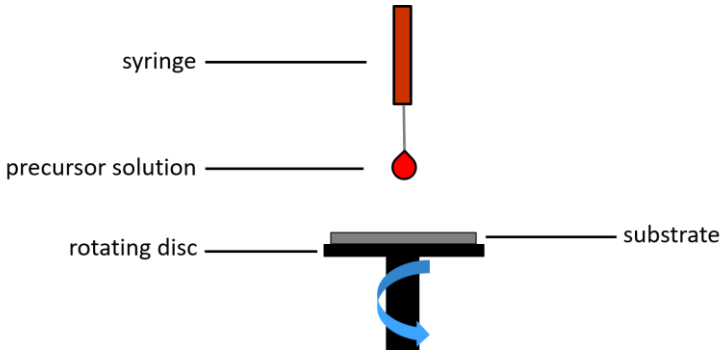

Figure 2.2. Schematic depiction of PMMA spin-coating.

A different possible PMMA coating technique is vertical deposition (Figure 2.3). Applying this method, the substrate is vertically placed in a highly diluted PMMA solution (0.001 wt%). Concentrations of 0.001 wt%, 0.005 wt%, 0.01 wt%, and 0.1 wt% were tested, with 0.001 wt% resulting in the most homogenous coatings. The solution gets evaporated at 60 °C in a dry oven and a homogenous thin film remains on the substrate. This procedure leads to very homogenous coatings over potentially large areas and consumes very little PMMA. However, this method did only work out for Si and glass substrates, but not for Cu substrates. The coatings on Cu substrates were completely random and extremely inhomogeneous. The film thickness is again not adjustable and very thin (< 1.0 µm) using this technique.

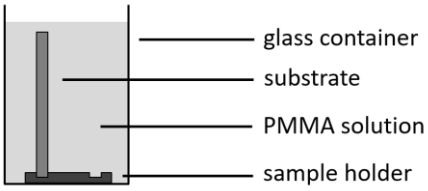

Figure 2.3. Schematic depiction of vertical disposition of a PMMA solution.

For preparation of homogenous films with controllable thickness over larger areas, spray-coating was investigated (Figure 2.4 & 2.5). Using this method, the PMMA solution is sprayed onto a substrate which is placed on a heating plate. The heating plate serves the purpose of immediately evaporating the PMMA solution, as soon as it hits the substrate surface. This allows for repeated coating without washing away previous layers and thus for adjusting the film thickness. The downsides of this method are very high PMMA consumption and the sheer amount of adjustable parameters (e.g. PMMA concentration, temperature, pressure, spray nozzle opening), making it very hard to create reproducible system configurations. Slight changes in one of the many parameters already have a big impact on the outcome which makes this technique less convenient for research lab applications.

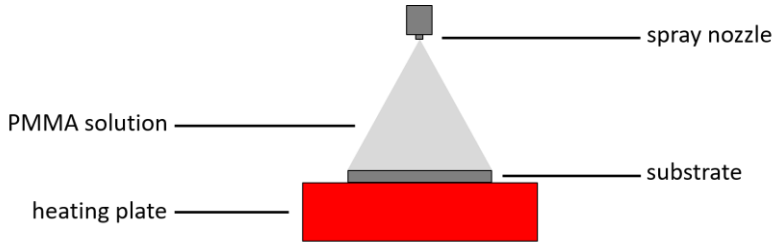

Figure 2.4. Schematic depiction of PMMA spray-coating.

All of the mentioned coating techniques have specific advantages and disadvantages. As explained before, dip-coating was chosen as standard method. It can be applied to all used substrates and results in the highest film thickness of all coating procedures. This is desirable for electrochemical applications to achieve high loadings of active material. Coating techniques resulting in thinner films are more suited for e.g. solar cell or applications or optical components. Spray-coating allows for easy up-scaling and potentially industrial application. Once the parameters are adjusted according to the desired product properties, the process can be highly automatized and applied to large surface areas.

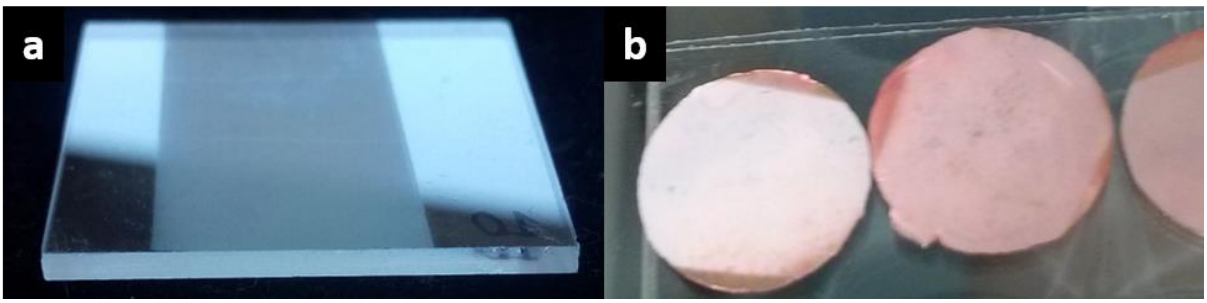

Figure 2.5. Photos of spray-coated PMMA. a) On a TiO_2 substrate, b) on Cu substrates.

2.2 Germanium Thin Films

The following chapter focuses on the synthesis and characterization of germanium thin films with inverse opal structure. Analytical methods applied to these films are summarized in Table 2.2.

Table 2.2. Analytical methods applied to Ge thin films.

Sample	SEM	XPS	Raman	Electrochemical Methods
Ge thin film	x	x	x	x
PMMA coating	x	-	-	-

2.2.1 Synthesis

Germanium thin films with inverse opal structure have already been published by Fässler *et al.*[139] In the scope of this work, the known synthesis protocol has been transferred to copper substrates for battery applications and PMMA size variation was done to further adjust the properties of the resulting thin films. After coating the PMMA template on the desired substrate, the cavities in between the PMMA opals got infiltrated by a K_4Ge_9/*en* solution (0.06 mmol L^{-1}, details on solution preparation can be found in Chapter 4.3.9). After thermal removal of the solvent, the $[Ge_9]^{4-}$clusters were cross-linked by impregnation with $GeCl_4$. The template was thermally removed and the thin films were washed for solvate assisted KCl removal (Figure 2.6).

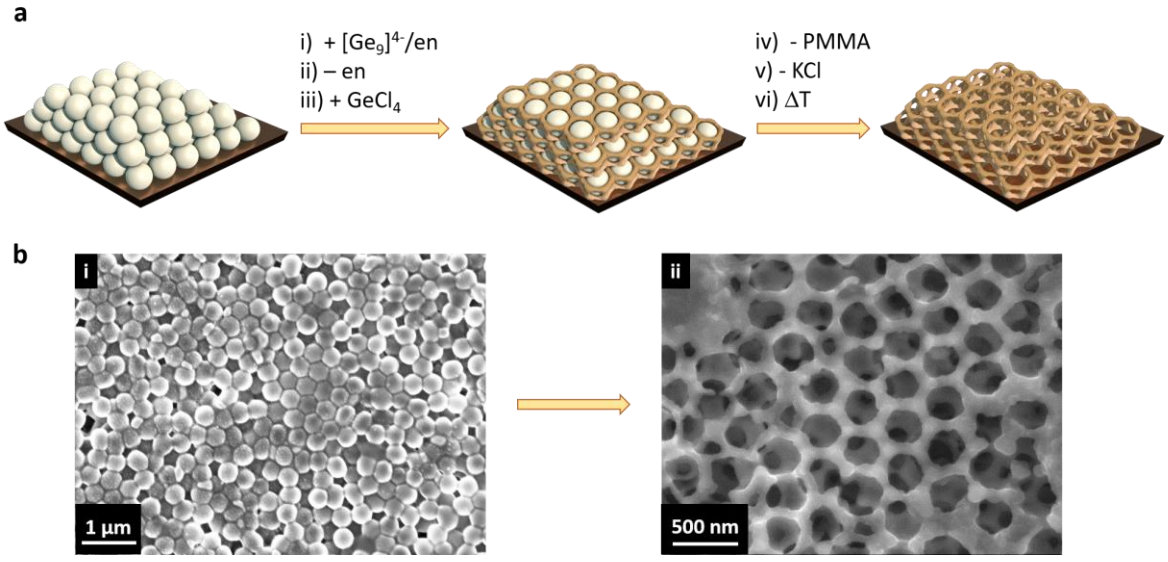

Figure 2.6. a) Synthesis route to inverse Ge opals using a PMMA template.[139, 144] i) Infiltration of the PMMA beads (grey spheres) with a solution of K_4Ge_9 in *en*, ii) solvent removal via evaporation, iii) impregnation with $GeCl_4$, iv) thermal removal of the PMMA template, v) removal of KCl *via* washing with dimethyl sulfoxide (DMSO) and tetrahydrofuran (THF) leaving an inverse opal structure of *a*-Ge, vi) optional crystallization step to obtain α-Ge. b) SEM images of i) PMMA template coated on a Cu substrate, and ii) an inverse opal structured Ge film on Cu (thickness 2.75 µm). The figure was modified on the basis of ref.[144]

During PMMA synthesis, size variation could be done by varying the amount of SDS, with a higher amount of SDS leading to smaller PMMA particles (Figure 2.7). Size distribution of PMMA particles was monitored by dynamic light scattering (DLS) by default. Smaller PMMA spheres then result in smaller pore openings in the final thin film, influencing its mechanical stability. The larger the pores, the more mechanically flexible the films should be, while smaller pores lead to a denser network, causing higher tension. PMMA spheres below a diameter of 100 nm could not be obtained. For subsequent thin film preparation, PMMA particles with a size of 250 – 300 µm were used. This specific size resulted in the most homogenous coating during dip-coating while being sufficiently mechanically stable for electrode applications.

Figure 2.7 shows the results of a combined spray-coating/drop-casting technique, where the PMMA opals were spray-coated onto Cu substrates followed up by drop-casting the K_4Ge_9/*en* solution. Figures 2.7a and 2.7c demonstrate that this combined procedure was successfully applied to create inverse opal structured Ge thin films. This further illustrates that spray-coating allows for potential up-scaling, as already mentioned in Chapter 2.1. However, Ge thin film preparation using PMMA opals with a size of 125 nm as template did not result in the desired inverse opal structure. No ordered porosity could be observed, the material forms randomly distributed bulks with large cracks where blank substrate can be seen (Figure 2.7d).

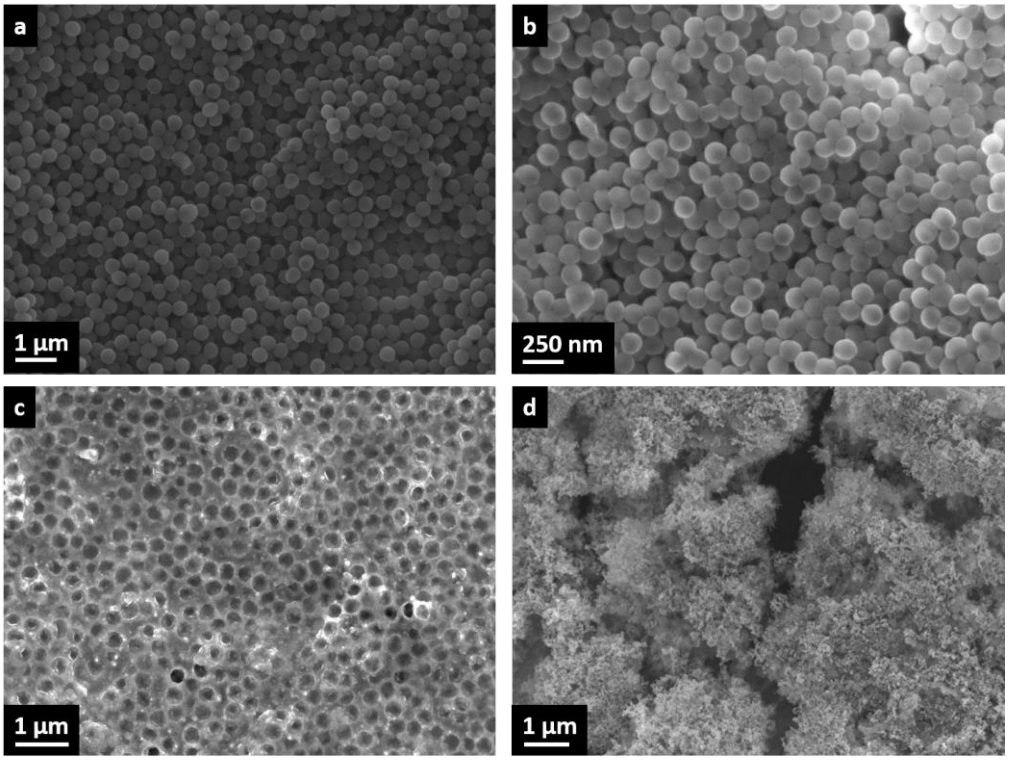

Figure 2.7. a) SEM micrograph of PMMA opals with 360 nm diameter. b) SEM micrograph of PMMA opals with 125 nm diameter. c) Ge thin film prepared from 360 nm opals. d) Ge thin film prepared from 125 nm opals. All samples obtained *via* spray-coating of the PMMA dispersion and drop-casting of the Zintl precursor solution on Cu substrates.

2.2.2 XPS studies on oxidation

For further studies, air sensitivity of the prepared germanium thin films was a critical question. To investigate this, XPS studies on thin films have been performed. Inverse opal structured Ge thin films were prepared on Si substrates as described in Figure 2.6 (solution concentration 0.06 mmol L^{-1}). After preparation, the Ge films have been exposed to air for a certain amount of time. After air exposure, the samples got transferred into the vacuum chamber of the XPS device so that no further oxidation due to air exposure could take place. Figure 2.8 shows the measured Ge 3d signals after 0.5 h, 1 h and 24 h air exposure. After 0.5 h air exposure (Figure 2.8a), a large signal of Ge(IV) can be observed before sputtering the sample surface. The germanium sample already got partially oxidized. While this being the case for the sample surface; after sputtering with Ar^+, the Ge(0) signal is of much higher intensity as the signals of Ge(II) and Ge(IV). Therefore it can be concluded that mainly the surface of the thin film got oxidized after 0.5 h, while deeper layers within the film still remain mainly non-oxidized. After 1 h of air exposure (Figure 2.8b), a very dominant Ge(IV) signal can be observed before sputtering. Even after sputtering, the Ge(IV) signal is of higher intensity than the Ge(0) signal. This shows that already after 1 h significant oxidation of the Ge film has taken place. After 24 h (Figure 2.8c) the Ge(II) and Ge(IV) signals gained intensity as the thin film gets more and more oxidized. These studies clearly demonstrate that the prepared inverse opal structured Ge thin films are highly sensitive towards oxidation. Even after only 0.5 h the film surface is mostly oxidized. Deeper layers inside the film are only slightly more stable towards oxidation. Bentlohner *et al.* conducted similar experiments without air exposure, leading to non-oxidized Ge films.[139]

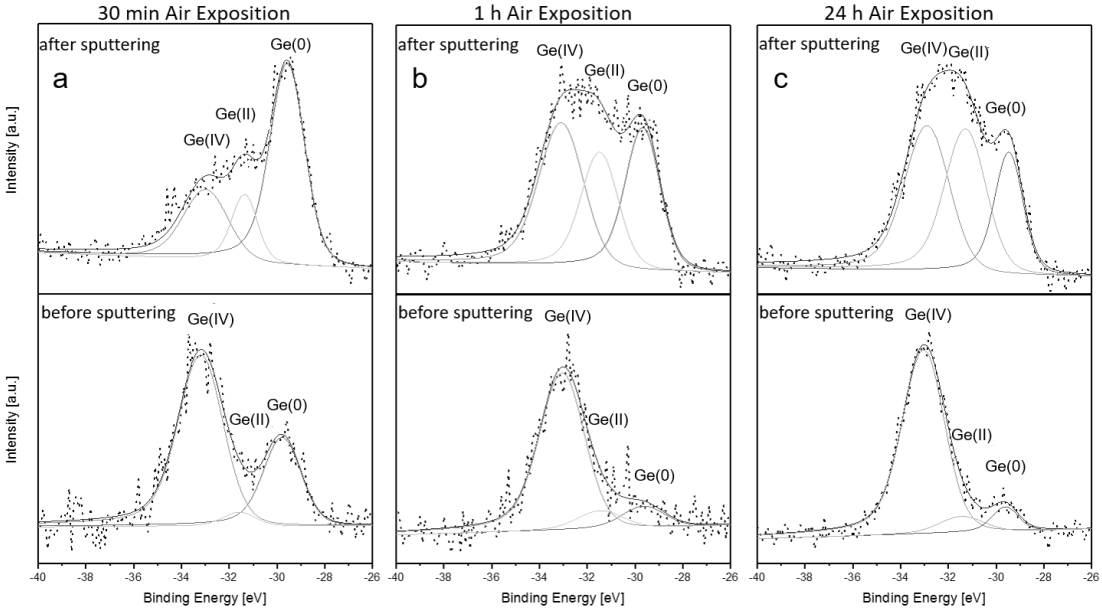

Figure 2.8. XPS spectra of inverse opal structured Ge thin films on Si substrates after a) 0.5 h, b) 1 h, and c) 24 h air exposition; before and after Ar^+ sputtering.

This leads to the conclusion that all following measurements on the prepared thin films should be carried out under inert gas atmosphere. This is also highly important for battery cell construction where changes of the active material have a potentially high impact on the cell performance.

2.2.3 Electrochemical measurements

For electrochemical measurements inverse opal Ge thin films were prepared on Cu substrates (see Chapters 4.1.4 and 4.3.11). A cross-section of a Ge film coated (solution concentration 0.06 mmol L^{-1}) on a copper substrate is shown in Figure 2.9. The film thickness is around 2.75 µm, resulting in a maximum loading of 313 µg (determination of the loading is described in Chapter 4.1.6).

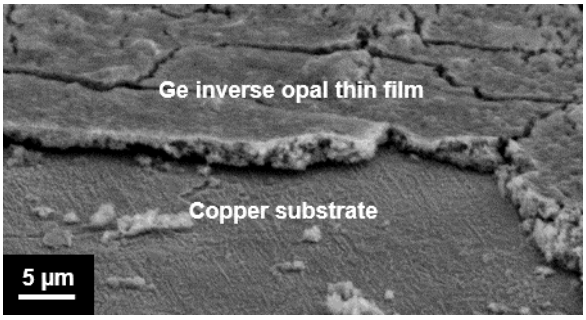

Figure 2.9. SEM cross-section of an inverse opal structured Ge thin film on a Cu substrate. The figure was modified on the basis of ref.[144]

First experiments were performed on *a*-Ge as well as α-Ge thin films. To distinguish between *a*-Ge and α-Ge Raman measurements were executed (Figure 2.10). The Raman spectrum of *a*-Ge shows a characteristic signal at 270 cm^{-1} which often appears to be rather broad due to the amorphous character of the sample. Crystalline α-Ge shows a signal at 300 cm^{-1}. According to the literature, no other Raman signals could be expected for *a*-Ge and α-Ge.[130] The spectra obtained from samples on Cu substrates are identical to reported signals on Si substrates.[139] Sample purity was further checked by EDX measurements (see Appendix Chapter 5.1, Figure 5.1).

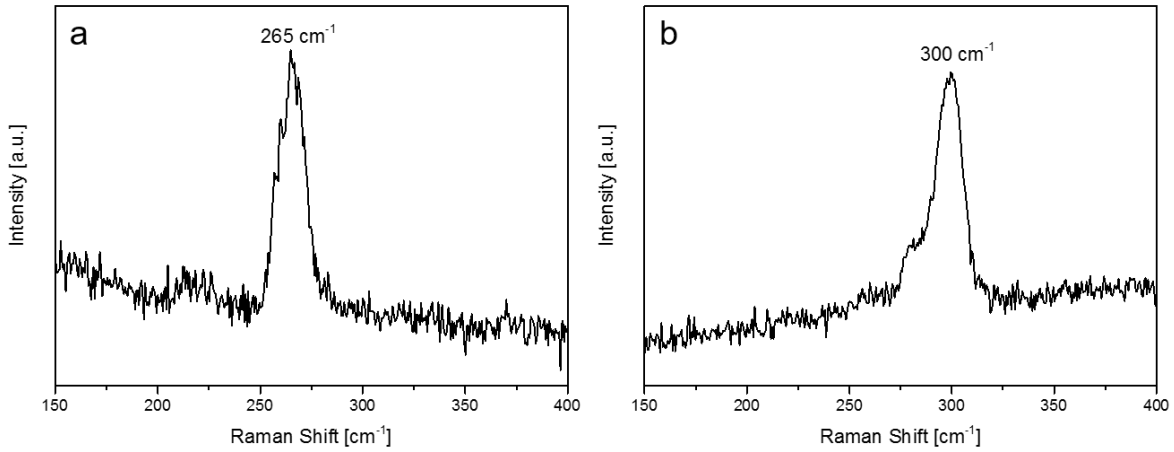

Figure 2.10. Raman spectra of a) *a*-Ge and b) α-Ge on Cu substrates. The figure was modified on the basis of ref.[144]

The prepared thin films were directly used for electrochemical measurements, without addition of a binder (for details on cell preparation, see Chapter 4.1.6). All capacities mentioned in the following are referred to a theoretical capacity of 1385 mAh g^{-1} for $Li_{15}Ge_4$ which is the Li-richest phase that can be formed during electrochemical measurements in standard Li ion battery systems.[61, 72, 145] However, $Li_{17}Ge_4$ with a gravimetric capacity of 1564 mAh g^{-1} is known to be the Li-richest phase in the Li-Ge system, but the mentioned phase cannot be observed in Li ion batteries.[146] Firstly, the performances of *a*-Ge and α-Ge electrodes were investigated to check if crystallization of the Ge thin films is necessary to obtain high performances during electrochemical cycling. To do so, voltage profiles of respective inverse opal structured electrodes were analyzed (Figure 2.11). If not mentioned differently, voltage profiles of the fourth charge-discharge cycle were used for analysis and entitled as initial capacities. Otherwise the formation of the solid electrolyte interface (SEI) could lead to misinterpretations. However, in the case of α-Ge in Figure 2.11 the first and second cycle are depicted due to the already huge performance drop. The α-Ge electrode performs significantly worse than the *a*-Ge electrode and shows a very low reversible capacity. This is mainly caused by flaws in the inverse opal structure of the thin film which lead to connectivity issues. These flaws are caused by the more invasive temperature treatment which is needed to crystallize the Ge film. Due to the low cycling performance of α-Ge electrodes, all further studies were performed on *a*-Ge electrodes. The *a*-Ge electrode shows plateaus of lithiation and delithiation reactions at 0.25 V and 0.4 – 0.5 V, respectively. The small linear region at the end of the discharge process is caused by the constant voltage (CV) step which is performed at the end of each discharge cycle at 20 mV. The difference in lithiation and delithiation capacity is due to the SEI formation.

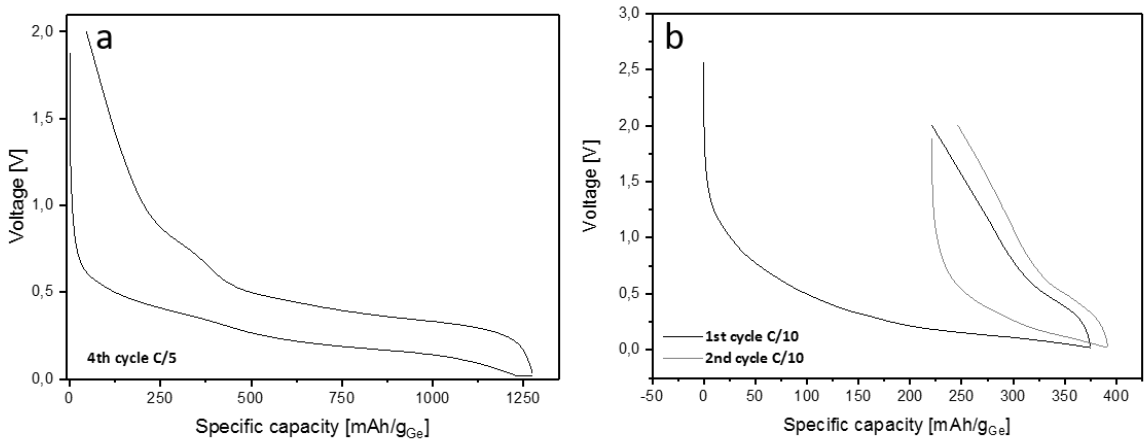

Figure 2.11. Voltage profiles of an *a*-Ge electrode (a) and an α-Ge electrode (b). The figure was modified on the basis of ref.[144]

Figure 2.12a shows the course of the specific delithiation capacities for inverse opal structured *a*-Ge electrodes over 100 charge-discharge cycles. It has been reported in the literature that the addition of small amounts of fluoroethylene carbonate (FEC) to the electrolyte has a beneficial influence on the cycling stability of the silicon electrodes.[147] Therefore, experiments with and without addition of FEC to the electrolyte were performed in this work.

As can be seen in Figure 2.12a, an electrode without FEC shows a different cycling behavior than an electrode with the addition of 5 wt% FEC to the electrolyte. The initial delithiation capacity is at around 1420 mAh g^{-1}. After 100 cycles, the capacity retention is at 47% with a rapid fading after about 60 cycles. The coulombic efficiency is at 91% after the second cycle. After the first few cycles a strong decrease from 98% to 95% efficiency can be observed. Electrodes measured including FEC show highly improved cycling performances. Without an extra CV step at the end of the discharge process the initial capacity is at 1360 mAh g^{-1} with a capacity retention of 67% after 100 cycles. The relatively low capacity retention is mainly caused by a fast capacity fading during the first cycles. For the last 80 cycles, the retention is at 88%, while for the last 20 cycles a capacity retention of 98.3% is obtained. As can be seen, capacity retention and coulombic efficiencies of FEC containing cells are much higher than of cells without FEC.

The coulombic efficiency after the second cycle for the electrode with FEC is 89.1% and averaged from the 4th to the 100th cycle 99.5%. These values are higher compared to those of literature known Ge inverse opal electrodes and much higher than those of differently fabricated Ge thin film electrodes.[40b, 79] They also compare well to electrodes prepared in more complex procedures like Ge nanowires with coulombic efficiencies of 99.9% after the 50th cycle,[148] macroporous Ge particles (99.5% after 200 cycles) and Ge nanoparticles (98.6% after 90 cycles).[149] Electrodes made from inverse

opal structured Ge have been reported before. However, the synthesis procedure described in this work is very simple and can be done with ordinary lab equipment, other than e.g. applying chemical vapor deposition (CVD) using GeH_4 as Ge source. The electrodes presented in this work stick out regarding the very slow capacity fading towards the last cycles, making them attractive candidates for long-lifetime applications.[79] They also perform well compared to Ge nanowires retaining ip to 98% of their initial capacity after 100 cycles, three-dimensional macroporous Ge particles with up to 96% after 200 cycles and Ge nanoparticles with up to 86% after 90 cycles.[65, 77, 150] While Zitoun *et al.* created Ge nanoparticles starting from the Zintl phase $Na_{12}Ge_{17}$, they only were able to obtain 60% of their initial capacity after 10 charge-discharge cycles.[75] Hybrid materials such as Ge@C core-shell particles and graphene oxide nanosheets receive capacity retentions of up to 96.5% after 600 cycles.[151]

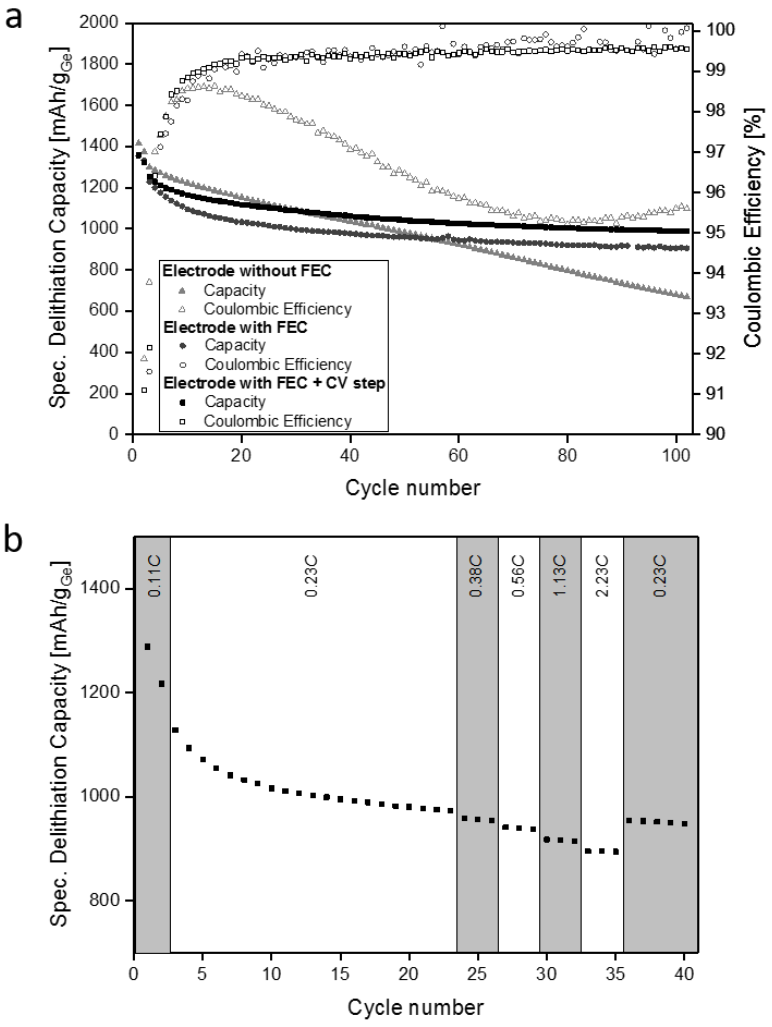

Figure 2.12. a) Specific delithiation capacity over extended cycling at a rate of 0.23*C* with the first two cycles at 0.11*C*. b) Specific delithiation capacity at various *C*-rates of an electrode with FEC and an extra CV step at the end of the discharge process. The figure was modified on the basis of ref.[144]

Including a CV step at the end of each discharge process enhances the cycling performance of the here presented electrodes, as it is shown in Figure 2.12a. The depicted electrode exhibits an initial delithiation capacity of 1360 mAh g^{-1} and receives a capacity retention of 73% after 100 cycles. Its coulombic efficiency is 91.6% after the second cycle, while averaged from cycles 4-100 it is 99.3%. Comparable to the before mentioned electrode without CV step, the course of the capacity fading behaves similar. There is almost no capacity fading after an initial drop, which can be documented by calculating capacity retentions for higher cycle numbers. From cycle 20 to cycle 100, the capacity retention is 89%, while its even 99% from cycle 80 to cycle 100. As expected, the capacity values are higher than the ones for the electrode without CV step. After 100 cycles a capacity of 990 mAh g^{-1} is achieved whilst the electrode measured without CV step only delivers 905 mAh g^{-1} after 100 cycles.

Rate test were also performed on cells containing FEC and applying the before mentioned additional CV step (Figure 2.12b). *C*-rates were increased from 0.23*C* up to 2.23*C* and after three cycles at 2.23*C* another five cycles at 0.23*C* were measured. An approximately linear decrease in capacity could be observed with increasing *C*-rates. At 0.56*C*, 96.3% of the capacity shown at 0.23*C* is obtained. At 2.23*C*, 91.8% of the capacity at 0.23*C* is received. This means that a more than ten times higher *C*-rate translates in a very low capacity loss of only 8.2%. The tested electrodes show outstanding intrinsic rate capabilities and can be charged and discharged relatively fast.

Since it was assumed that the good cycling performances of the tested electrodes are based on the inverse opal structure of the Ge thin films, allowing for mechanical flexibility during the drastic volume changes, SEM images of cycled electrodes were taken (Figure 2.13). The inverse opal structure could not be retained after 100 charge-discharge cycles. Nevertheless, the material still offers high porosity. Randomly distributed vertical channels can still be observed. Due to their pores with diameters of 200 – 300 nm it can be assumed that they are remnants of the pores in the initial honeycomb structure. Even though no ordered structure is existent anymore, the high porosity and the vertical channels still offer Li ion pathways and thus allow for high reversible capacities.

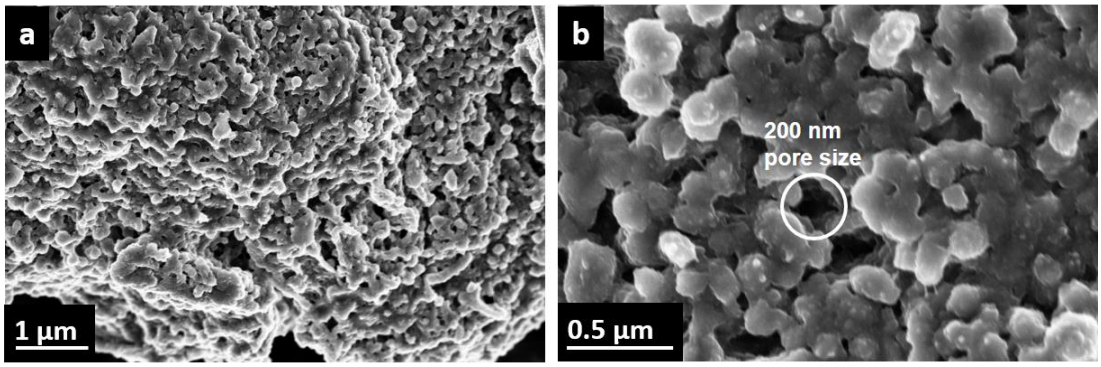

Figure 2.13. SEM images of Ge electrodes after 100 charge-discharge cycles. a) 25000x magnification, b) 80000x magnification. The figure was modified on the basis of ref.[144]

While the loading of active material for the electrodes shown in Figure 2.12 was rather low (313 µg) due to a film thickness of about 2.75 µm, tests were also performed on electrodes with higher loading. Due to the preparation method, higher electrode loadings could only be achieved at the cost of losing the desired inverse opal structure, as shown in Figure 2.14a. The electrode depicted in Figure 2.14 exhibits a loading of 5.5 mg of active material (for loading determination see Experimental Part Chapter 4.1.6). Due to the excess of precursor solution needed to achieve such high loadings, no inverse opal structure can be observed. Nevertheless, the coating offers a porous surface which could be sufficient for receiving a good cycling performance. As shown in Figure 2.14b, the electrode performs poorly during charge-discharge cycling. Starting from an initial capacity of 555 mAh g^{-1}, only 66% could be retained after 100 cycles. The low initial capacity can be explained by connectivity issues, caused by the rather inhomogeneous coating due the missing ordered inverse opal structure. The trend of the capacity in Figure 2.14b also decreases in a steeper way than for electrodes with lower loading, making the here tested electrode less attractive for long-lifetime applications. Even though it has to be taken into account that electrodes with lower loading always show a less rapid capacity fading when compared to higher loaded electrodes, the much lower specific capacities demonstrated in Figure 2.14b are a clear disadvantage of the here prepared higher loaded electrodes.

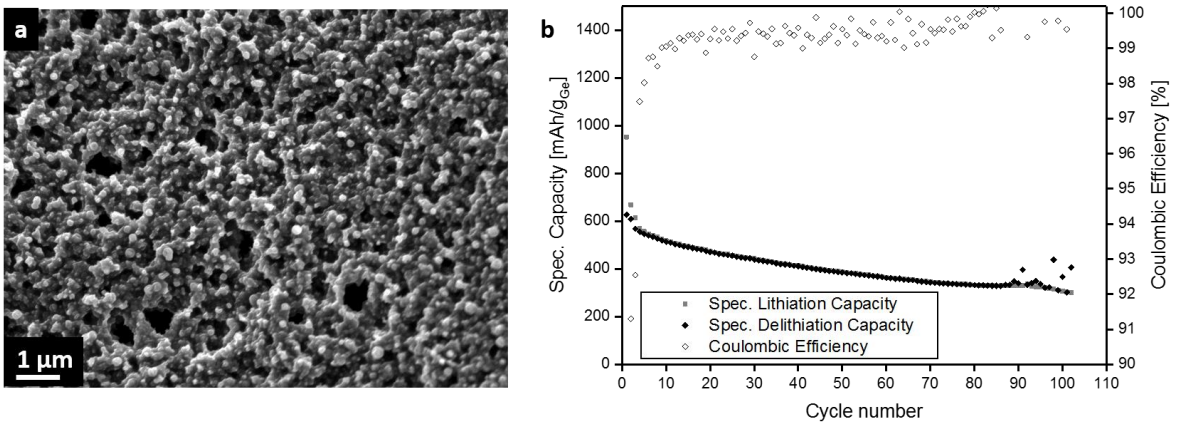

Figure 2.14. a) SEM image of a Ge electrode with high loading, b) specific capacities over extended cycling at a rate of 0.23*C* with the first two cycles at 0.11*C* of an electrode with higher loading. A loading of 5.5 mg of active material was used.

To further prove that the achieved inverse opal structure is the main reason for the good cycling performance of the presented cells, electrodes without the mentioned structure were prepared. Here, the K_4Ge_9/*en* solution was directly drop-casted onto the copper substrate, without usage of a PMMA template. Figure 2.15 shows the performance of a cell using an unstructured electrode during charge-discharge cycling for 100 cycles. The loading of the used electrode was 1.70 mg (see Chapter 4.1.6). As it can be seen, the initial capacity is already very low (617 mAh g^{-1}) and after 100 cycles a capacity retention of only 42% could be achieved. This cell definitely performs much worse during cycling than

the cells with inverse opal structured electrodes and in terms of capacity retention even worse than the cells with high loading. This clearly demonstrates that Ge electrodes without inverse opal structure perform significantly worse in electrochemical cycling experiments. The ordered honeycomb structure offers high mechanical flexibility which helps overcome the issue of drastic volume changes during charging and discharging of the used material.

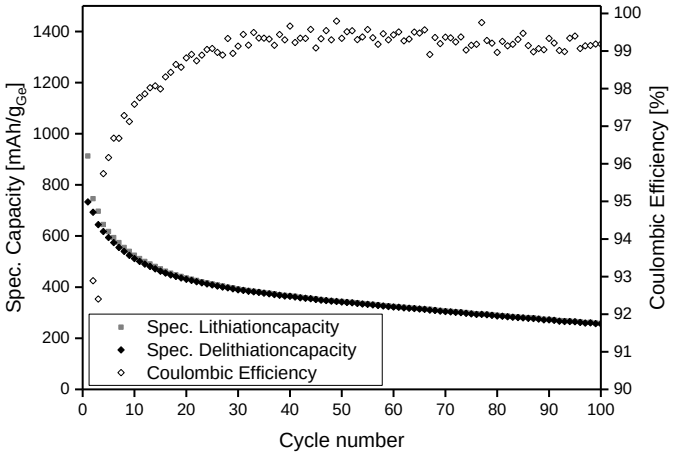

Figure 2.15. Specific capacities over extended cycling at a rate of 0.2*C* with the first two cycles at 0.1*C* of an electrode prepared without using a PMMA template (loading 1.70 mg).

Additionally to the binder-free electrodes with inverse opal structured Ge, electrodes prepared from more conventional inks were prepared and tested. Ink preparation is described in Chapter 4.3.10. Two different types of electrodes are distinguished. The first type, shown in Figure 2.16a, is prepared by drop-casting a K_4Ge_9/*en* solution on a copper substrate which has been coated with ink free of active material beforehand. In this case the ink replaces the PMMA spheres and has a template-like function. The second type (Figure 2.16b) is prepared from an ink which already contains the active material. This ink gets directly coated on the copper substrate, without any form of template.

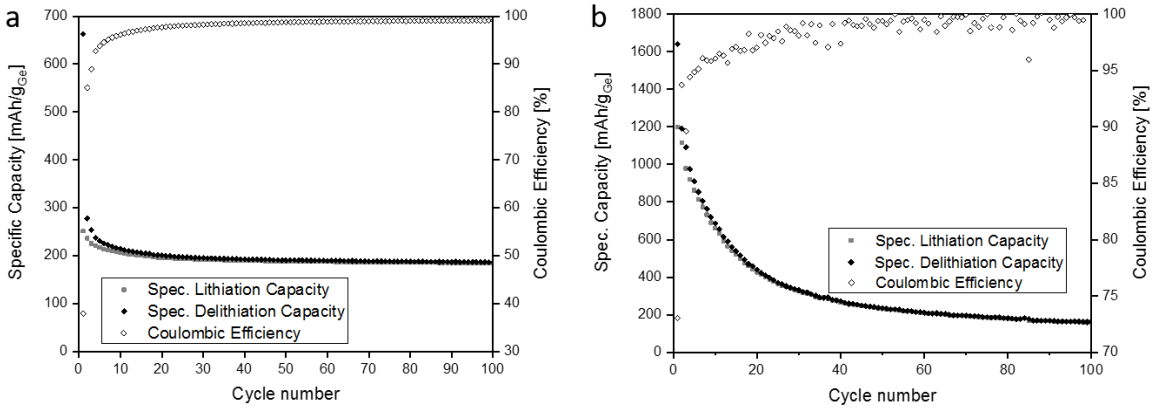

Figure 2.16. Specific capacities over extended cycling at a rate of 0.2*C* with the first two cycles at 0.1*C* of a) an electrode prepared from an ink not containing the active material (loading: 321 µg), and b) an electrode prepared from an ink containing the active material (loading: 2.35 mg).

The cell shown in Figure 2.16a shows a very low capacity but good cycling stability and high coulombic efficiency. Most likely no Ge but carbon black is cycled during this measurement. Capacities for Ge would be much higher and some form of capacity fading should be observable, as shown for the other cells. Adding a K_4Ge_9/*en* solution to an ink covered copper substrate does not yield the desired result. For the electrode prepared using an ink which already contains the active material different results are obtained. As can be seen in Figure 2.16b, the initial capacity is very high, it is in the range of the theoretical capacity of $Li_{15}Ge_4$ (1385 mAh g^{-1}). However, after the high initial capacity a rapid capacity fading during the following charge-discharge cycles can be observed. Similar to the unstructured cell shown in Figure 2.15, the long-time performance is very low. This again is due to the fact that Ge goes through immense volume changes during the cycling experiment. This material cannot compensate those volume changes due to the lack of a mechanically flexible, porous structure.

Concluding, Ge electrodes with great long-time cycling performances were prepared by a simple wet-chemical process starting from the Zintl phase K_4Ge_9 as precursor and the necessity of the inverse opal structure was demonstrated.

2.3 Germanium/Phosphorus Thin films

In order to adjust the thin films' properties according to desired applications, introduction of phosphorus was investigated. The following chapter presents the applied techniques and showcases the achieved results. Analytical methods applied to the samples in this chapter are summarized in Table 2.3.

Table 2.3. Analytical methods applied to Ge/P samples.

Sample	SEM	EDX	Raman	XRD	Raman/Fano	XPS	Electrochemical methods
Ge + PPh_3 film	x	-		-	x	x	-
Ge + PPh_3 dried residue	-	-	x	x	-	-	-
Ge + NaP_7 film	x	-	x	-	x	x	x
Ge + NaP_7 dried residue	-	-	x	x	-	-	-
Ge + P_{red} film	x	x	x	-	-	x	x
Ge + P_{red} dried residue	-	-	-	-	-	-	-
"$K_2Ge_2P_2$"	x	x	x	-	-	-	-
"$K_2Ge_7P_2$"	x	x	x	-	-	-	-

2.3.1 Selection of phosphorus sources

To obtain mixed Ge/P thin films, several different phosphorus sources were investigated. Bentlohner *et al*. already reported on the utilization of PCl_3 which was used for cluster cross-linking instead of $GeCl_4$.[139] This allows for a very elegant way of adding P to the inverse opal structured Ge thin films by only slightly adjusting the synthesis procedure. The boiling point of PCl_3 is at 76.1 °C which makes it a suitable candidate for cross-linking by keeping the substrates in an atmosphere saturated with the cross-linking agent. It was demonstrated that introduction of heteroatoms by varying the cross-linking agent can successfully be executed which opens up further doping possibilities by e.g. utilizing $SiCl_4$, $SnCl_4$ or other potential candidates for cross-linking.

The P sources used in this work are PPh_3, NaP_7 and red P. They were directly solved in *en*, together with K_4Ge_9. However, red phosphorus was treated slightly different. Tests were done by mixing P_{red} directly with K_4Ge_9 in *en*, but also by preliminary mixing K with P_{red} in a molar ratio of 3:7 in a glass flask and subsequently adding *en* to obtain a K_3P_7/*en* solution. This solution was then added to a K_4Ge_9/*en* solution. For more details on the composition of the different solutions, see Chapter 4.3.9.

2.3.2 PPh_3 as phosphorus source

One possibility to achieve inverse opal structured mixed Ge/P thin films was investigated by using PPh_3 as P source. Sevov *et al.* reported on the possibility of obtaining mono- and disubstituted cluster species through reactions of $[Ge_9]^{4-}$ with EPh_3.[152] Following this approach, the good solubility of PPh_3 in *en* was utilized. Based on this property, mixed solutions of K_4Ge_9 and PPh_3 in *en* could be easily prepared by adding the solvent to a mixture of a desired K_4Ge_9/PPh_3 ratio in a glass flask (for details on the compositions of the prepared solutions see Chapter 4.3.9). The concept of this procedure was that varying the K_4Ge_9/PPh_3 ratio in the solutions should allow for adjustable degrees of doping in the final thin films, according to the required thin film properties. Cross-linking agents like $GeCl_4$ were not used for this method.

Figure 2.17 shows inverse opal structured thin films prepared using two different mixed K_4Ge_9/PPh_3/*en* solutions (Figure 2.17a: 100 mg/0.12 mmol K_4Ge_9, 1 mg/4 µmol PPh_3 in 2 mL *en*; Figure 2.17b: 25 mg/0.03 mmol K_4Ge_9, 36.4 mg/0.15 mmol PPh_3 in 1 mL *en*). The depicted films have not been crystallized at 600 °C. The desired honeycomb structure could be obtained for both films, the SEM images also show several layers of the porous structure. However, the structure is broken up in multiple areas which could possible provide more “breathing space”, allowing for more physical stability.

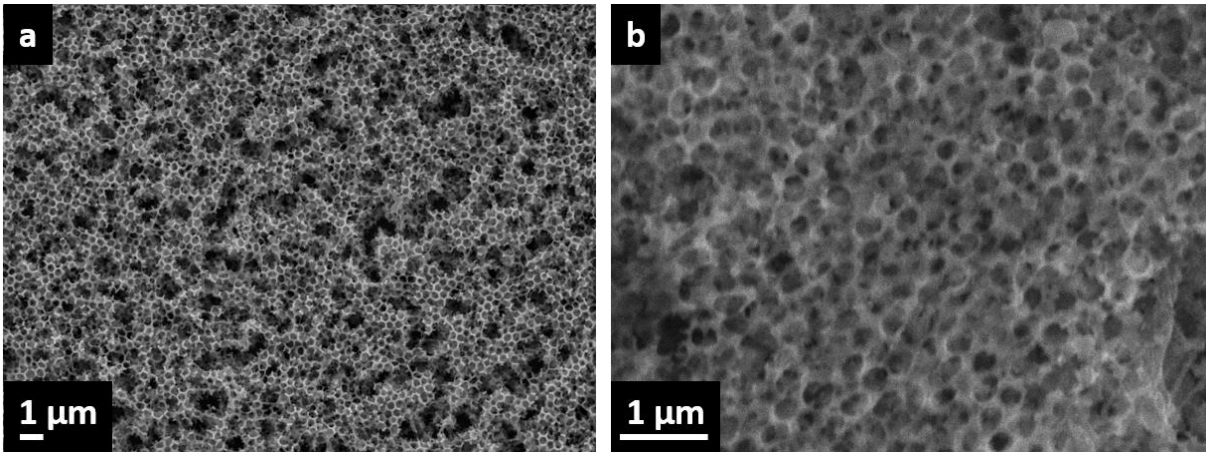

Figure 2.17. SEM images of inverse opal structured Ge thin films prepared by using mixed K_4Ge_9/PPh_3/*en* solutions (K_4Ge_9 : PPh_3 100:1 mg). a) Film prepared on sapphire using a solution with a very high excess of Ge; 5000x magnification. b) Film prepared on Cu using a solution with a molar ratio of Ge : P 2:1; 15000x magnification.

To investigate the influence of the added PPh_3, Raman measurements on dried residues of precursor/*en* solutions were performed. Prior to the measurements, the respective solutions were filtrated under argon atmosphere and the solvent was removed *in vacuo*. The remaining residues were filled into glass capillaries which were sealed afterwards. This was done to make sure that the samples were not exposed to oxygen prior or during the measurements. Figure 2.18 compares the Raman spectra of dried residues of K_4Ge_9/*en* and K_4Ge_9/PPh_3/*en* solutions (Figures 2.18a and 2.18b). The mixed solutions contained K_4Ge_9 and PPh_3 in a molar ratio of Ge : P 1:1 (0.03 mmol K_4Ge_9 / 0.30 mmol PPh_3 in 1 mL *en*). A high amount of P was used in order to be able to easier detect the influence of the dopant compared to the dopant free samples.

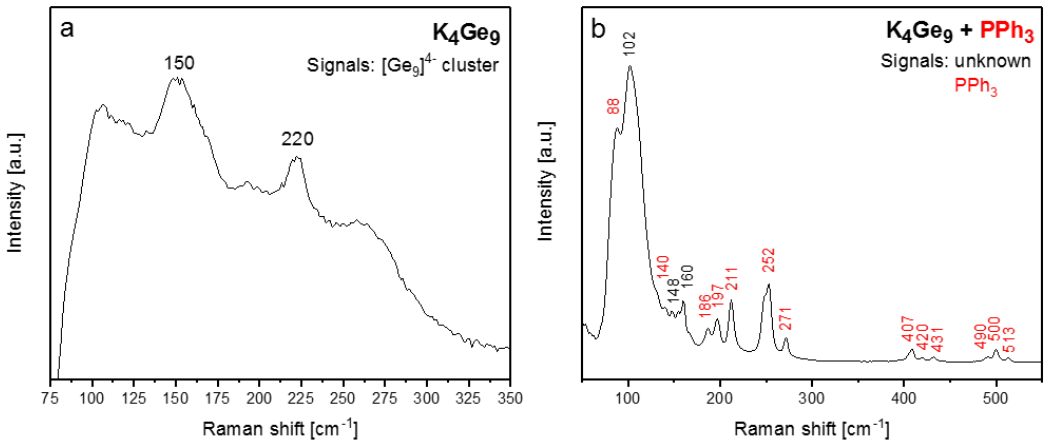

Figure 2.18. Raman spectra of dried residues of a) a K_4Ge_9/*en* solution and b) a K_4Ge_9/PPh_3/*en* solution. Molar ratios of Ge : P were 2:1.

The spectrum in Figure 2.18a shows signals of the $[Ge_9]^{4-}$ cluster, as expected.[122a] Due to the amorphous nature of the sample after solvent removal only the main signals can be observed, including significant signal broadening when compared to the cluster signals of the Zintl phase after solid state synthesis, similar to what can be found in the literature.[139] Figure 2.18b however mainly displays signals of PPh_3 and three signals at 102, 148, and 160 cm^{-1} which cannot be distinctively assigned to a certain species; the characteristic cluster signals cannot be found.[153] . Snyder *et al.* observed a signal at 350 cm^{-1} when studying doped Ge nanowires and assigned it to P in a Ge nanowire.[154] Bentlohner *et al*. reported a broad Ge/P signal at 345 cm^{-1} when using PCl_3 as dopant for Ge films on Si substrates.[139] However, other than for PCl_3, no Ge/P signal at around 350 cm^{-1} can be detected in Figure 2.18b. It seems that no Ge/P species has formed, all expected signals for PPh_3 are depicted in the spectrum.

Similar to the Raman studies mentioned above, P-XRD measurements of dried residues of K_4Ge_9/PPh_3/*en* solutions were conducted (Figure 2.19). The solutions contained the precursors K_4Ge_9 and PPh_3 in a molar ratio of Ge : P 2:1. Diffractograms were recorded after drying the residue, and after each individual heating step (100 °C, 500 °C, and 600 °C). Analogous to the Raman spectrum in Figure 2.18b, the powder pattern of the dried residue without any further temperature treatment shows reflections of K_4Ge_9 and PPh_3 (Figure 2.19a). All detected reflections can be assigned to the two educts, again indicating that no reaction took place in solution. After 1 h at 100 °C the diffractogram still shows the same reflections, no changes can be observed (Figure 2.19b). The diffractogram measured after 5 min at 500 °C shows a different pattern (Figure 2.19c). No reflections of PPh_3 can be observed anymore and the intermetallic clathrate-I K_8Ge_{44} has formed. Grin *et al.* already reported on the oxidation of Na_4Ge_9 and K_4Ge_9 to Ge with the clathrate-II structure and also on the oxidation of M_4Si_4 (M = Na, K) to clathrate-I compounds of the composition $M_{8-x}Si_{46}$.[155] Reflections of the precursor K_4Ge_9 can still be detected. Since the boiling point of PPh_3 is at 377 °C under standard conditions it can be assumed that it evaporated during the heating step. Figure 2.19d shows a diffractogram measured after 1 h at 600 °C. As expected, α-Ge has formed. Additionally, small amounts of K_8Ge_{44} can still be found as impurity phase. The reflections of α-Ge are not shifted towards lower or higher angles. This in addition with the Raman results in Figure 2.18b leads to the assumption no phosphorus doping took place. P inherits a smaller ionic radius than Ge, so a shift to lower angles due to an increase in lattice parameters should be detectable. A shift to higher angles could be explained by substitutional doping. In this case the lattice parameters would decrease due to the lower covalent radius of P compared to Ge.[156] However, since the reflections of crystalline α-Ge in the measured sample are not shifted, PPh_3 does not seem to be suitable for preparation of mixed Ge/P samples.

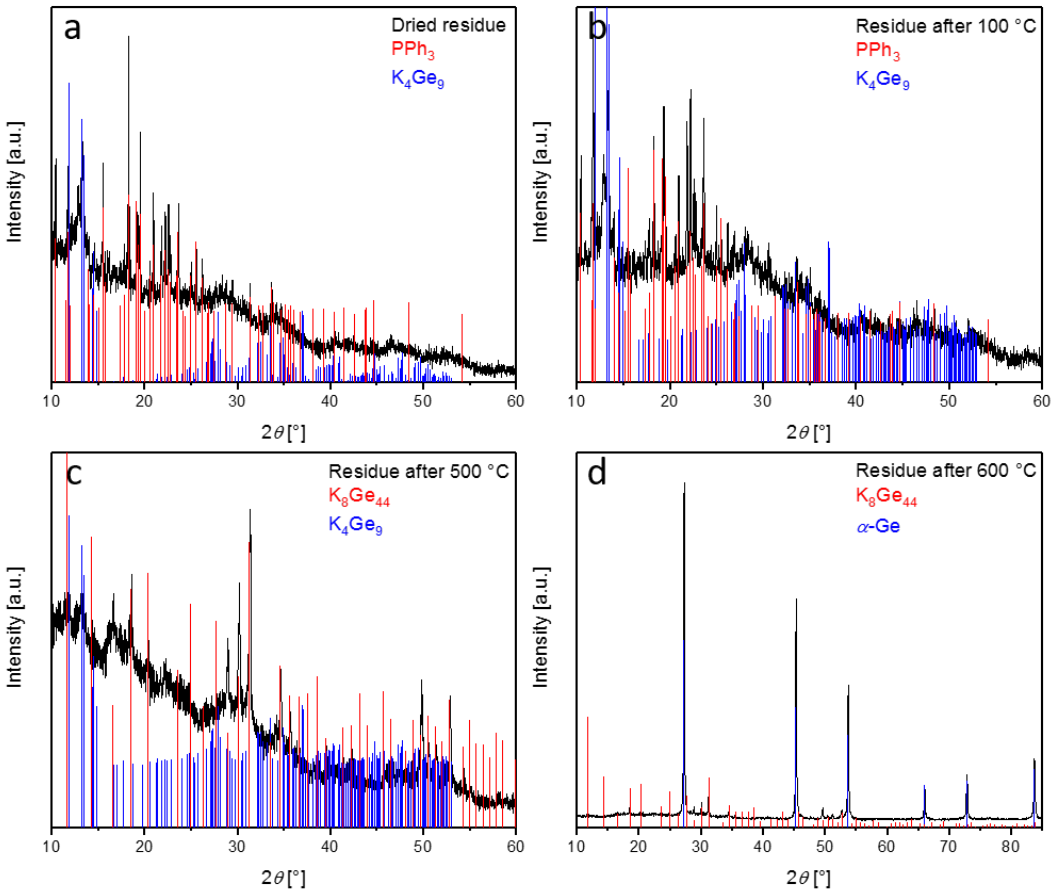

Figure 2.19. P-XRD patters of dried residues of $K_4Ge_9/PPh_3/en$ solutions. a) Measured after solvent removal, b) measured after 1 h at 100 °C under vacuum, c) measured after 5 min at 500 °C under vacuum, d) measured after 1 h at 600 °C under argon atmosphere. The calculated diffractograms are based on single crystal data.[122b, 157] Diffractograms were measured using Cu-$K_{\alpha1}$ radiation.

Another method for checking for possible phosphorus doping is utilizing the Fano effect when measuring Raman spectra of crystalline samples. Raman spectra of highly doped crystalline α-Ge are dependent on the dopant concentration.[158] This is based on the asymmetric broadening of the Raman signal, which was discovered by U. Fano *via* electron energy loss spectroscopy of helium.[159] At high doping densities a continuum of states of free charge carriers exists close to the Fermi level. This continuum of states is able to interact with either discrete vibrational modes or local vibrational modes. The overlap between the electronic continuum and discrete states causes interference effects which leads to asymmetric or inverted line-shapes in optical spectroscopy, dependent on excitation wavelength and free charge carrier concentration. This resonant scattering phenomenon is called Fano resonance.[160]

The Fano effect can be utilized to determine the charge carrier concentration in highly doped germanium.[161] The asymmetric broadening of the Raman signals increases with decreasing frequency of the Raman laser.[162]

This can be described using the Breit-Wigner-Fano fit function:

$$y = y_0 + \frac{H \cdot (1 + \frac{x - x_c}{w \cdot q})^2}{1 + (\frac{x - x_c}{w})^2} \quad (1)$$

Where y_0 is the linear background, H the signal amplitude, q the inverse coupling strength, w the Fano line width, x the Raman shift and x_c the signal position. For increasing dopant concentration, w is increasing, while $|q|$ is decreasing.[159]

For proper determination of the aforementioned Fano effect, samples were measured with two different laser wavelengths (514 nm and 633 nm). The resulting spectra and obtained values for the parameters q and w are shown in Figure 2.20. The spectra on the left hand side (Figure 2.20a, c, e) are measured at λ = 514 nm, the spectra on the right hand side (Figure 2.20b, d, f) at λ = 633 nm. Prior to the measurements, all thin films have been crystallized by temperature treatment at 600 °C for 1 h.

As expected, the films containing pure α-Ge show sharp and highly symmetrical Raman signals at 300 cm^{-1} (Figures 2.20a, b). Applying the Breit-Wigner-Fano fit function yields low values for w and high values for $|q|$, indicating no impurity doping. Figures 2.20c-f show spectra of thin films prepared from K_4Ge_9/PPh_3/*en* solutions with different Ge/P ratios. As stated before, $|q|$ is expected to decrease while w should increase with increasing dopant concentration. These effects can be observed for the samples measured at λ = 514 nm. $|q|$ is decreasing with a higher amount of phosphorus in the starting precursor solution (77.68 > 12.66 > 9.04) and w is increasing (2.19 < 3.35 < 5.44). Additionally, a significant asymmetric line shape can be observed for the samples prepared from mixed Ge/P solutions. However, even though these results are hinting towards successful phosphorus doping, the progression of the BWF fit parameters needs to be confirmed for a different laser wavelength. If that is not the case, the observed effect on the fit parameters could also be caused by grain boundary effects instead of dopant concentration. Therefore the same samples were additionally measured at λ = 633 nm. Again, a decrease of $|q|$ can be seen (34.11 > 7.05 > 6.32). But in this case, w is not increasing with increasing dopant concentration (2.35 < 3.66 > 3.54). The samples prepared from mixed Ge/P solutions show higher values for w than the pure α-Ge thin film, but the sample with higher phosphorus concentration exhibits a lower w value than sample with lower phosphorus concentration (3.54 vs. 3.66). Both mixed Ge/P samples show asymmetric peak broadening. The inconsistency in the behavior of the BWF fit parameters makes it impossible to make a clear statement about successful phosphorus doping using mixed K_4Ge_9/PPh_3/*en* solutions. Furthermore it has to be recognized that, other than for PCl_3 as phosphorus source, no Ge/P signal at around 350 cm^{-1} can be detected for any of the measured samples. These factors lead to the assumption that phosphorus introduction was not successful.

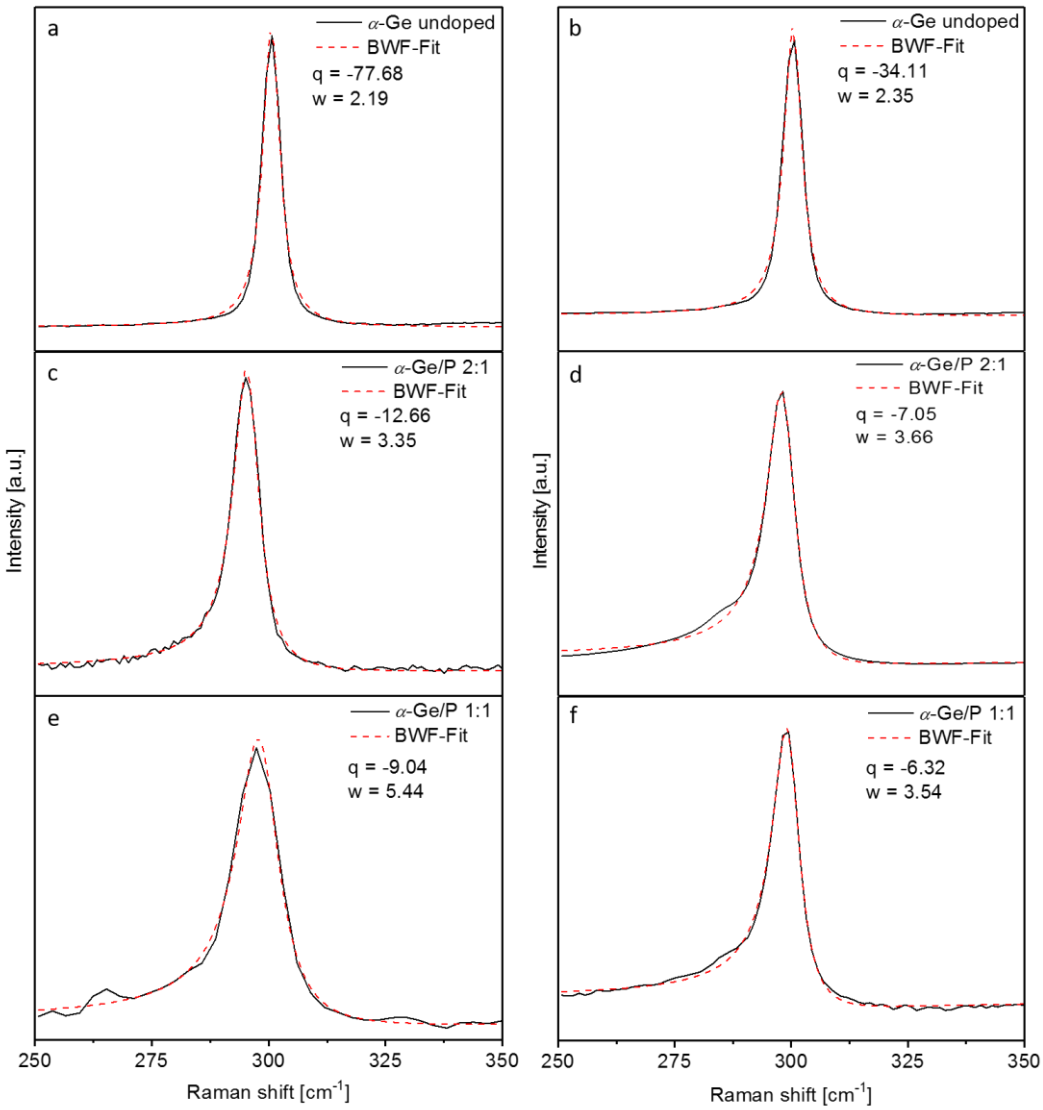

Figure 2.20. Raman spectra of inverse opal structured thin films on Si substrates for Fano effect determination. Shown spectra were measured for pure Ge films (a, b) and films prepared from mixed K_4Ge_9/PPh_3/*en* solutions (c-f). Spectra on the left hand side were measured at λ = 514 nm, spectra on the right hand side at λ = 633 nm.

Supplementary to XRD and Raman studies, XPS measurements of the obtained thin film were conducted. A molar ratio of Ge : P of 3:1 was used (0.06 mmol K_4Ge_9 / 0.18 mmol PPh_3 in 1 mL *en*). The thin film were not additionally crystallized at 600 °C. To avoid air exposure prior to the measurement, samples were transferred to the vacuum chamber under continuous nitrogen flow. The obtained spectra are depicted in Figure 2.21. As expected for samples without preliminary sputtering, the Ge 3d spectrum (Figure 2.21a) shows mainly Ge(0) and signals of Ge(II) and Ge(IV) with lower intensity. Phosphorus species are expected to be detected in the range of -128 eV up to -135 eV in the XPS spectrum of the P 2p signal (-128/129 eV for phosphides, -130 eV for P_{red}, -132/133 eV for phosphate, and -135 eV for oxides).[163] However, the spectrum in Figure 2.21b does not show any phosphorus signal, clearly indicating that no phosphorus is present on the film.

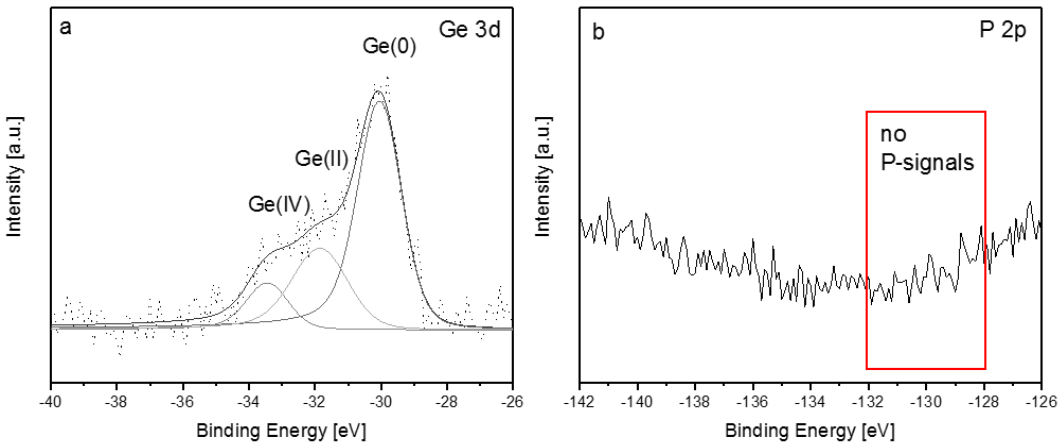

Figure 2.21. XPS spectra of an inverse opal structured thin film prepared from a mixed K_4Ge_9/PPh_3/*en* solution on Si substrates, Ge : P ratio 3:1. a) Ge 3d, b) P 2p. Spectra recorded without preliminary Ar^+ sputtering.

Conclusively it can be said that, even though thin film preparation using mixed K_4Ge_9/PPh_3/*en* solutions was successful, this is not a suitable method for phosphorus doping. The presented Raman and XRD results indicate that no reaction between the Zintl precursor K_4Ge_9 and the phosphorus source PPh_3 takes place. XPS studies further prove that no phosphorus insertion into the thin films happens using this method. Therefore no additional experiments utilizing PPh_3 were performed.

2.3.3 NaP_7 as phosphorus source

In the next step, NaP_7 was investigated regarding its suitability as phosphorus source. NaP_7 is a phosphorus-rich polyphosphide, featuring a helical polyphosphide substructure.[164] Synthesis was performed according to Nilges and coworkers (for details, see Chapter 4.3.6). NaP_7 shows good solubility in *en*, resulting in clear red solutions with concentrations of up to 180 µmol NaP_7 in 1 mL *en*. Similar to the aforementioned method utilizing PPh_3, it was taken advantage of this solubility by preparing mixed K_4Ge_9/NaP_7/*en* solutions with varying phosphorus concentration (for details in solution preparation see Chapter 4.3.9). The applied synthesis procedure did not include any additional cross-linking agents as e.g. $GeCl_4$ or PCl_3. SEM images of the resulting inverse opal structured thin films are presented in Figure 2.22 (Figure 2.22a: 100 mg/0.12 mmol K_4Ge_9, 20 mg/0.083 mmol NaP_7 in 2 mL *en*; Figure 2.22b: 50 mg/0.06 mmol K_4Ge_9, 19 mg/0.08 mmol NaP_7 in 1 mL *en*).

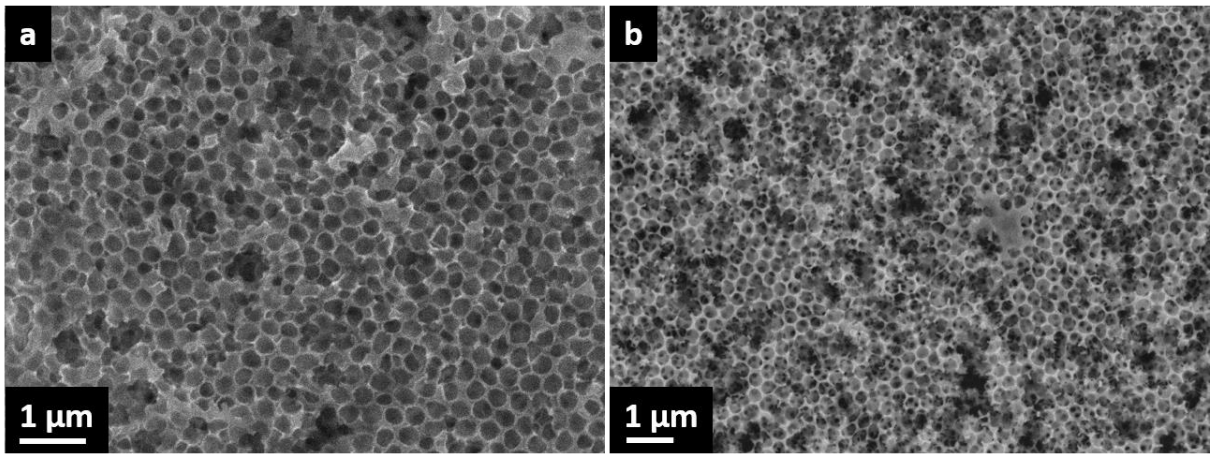

Figure 2.22. SEM images of inverse opal structured thin films prepared from a K_4Ge_9/NaP_7/en solutions. a) Film prepared on Si using a molar ratio of Ge : P of 1.86 : 1; 10000x magnification. b) Film prepared on Cu using a molar ratio of Ge : P of 2 : 1; 10000x magnification.

The desired inverse opal structure was successfully obtained. The SEM images show the characteristic honeycomb pattern over a large area of the substrate. Film thicknesses were determined by profilometry to be 2.5 µm. However, some inevitable cracks in the surface can also be observed.

Figure 2.23 shows Raman spectra of dried residues of a K_4Ge_9/*en* (Figure 2.23a) and a K_4Ge_9/NaP_7/*en* (Figure 2.23b) solution. The K_4Ge_9/NaP_7/*en* solution was prepared with a molar Ge : P ratio of 3:1 (0.12 mmol K_4Ge_9 / 0.053 mmol NaP_7 in 2 mL *en*). Analogue to Chapter 2.3.2, the solutions were filtrated under argon atmosphere and the solvent was removed under vacuum. To prevent air exposure, the remaining residues were filled into glass capillaries which were sealed in a glovebox.

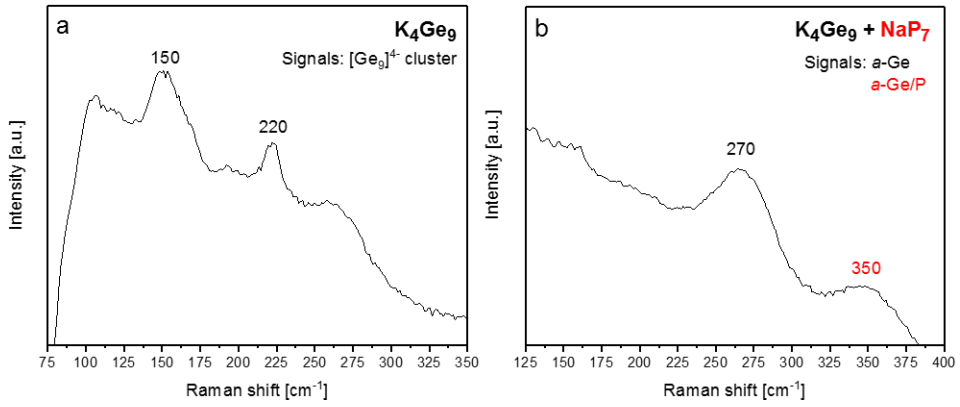

Figure 2.23. Raman spectra of dried residues of a) a K_4Ge_9/*en* solution and b) a K_4Ge_9/NaP_7/*en* solution. The K_4Ge_9/NaP_7/*en* solutions were prepared with a molar Ge/P ratio of 2:1.

Other than for PPh_3 as phosphorus source, no $[Ge_9]^{4-}$ cluster signals can be detected for the dried residue of the K_4Ge_9/NaP_7/*en* solution. The spectrum shows a broad signal of amorphous *a*-Ge at 270 cm^{-1} and a second signal at 350 cm^{-1}, indicating the presence of P in the inverse opal Ge thin film

structure. This is a first hint towards successful introduction of P, suggesting a reaction between the Zintl precursor K_4Ge_9 and the polyphosphide NaP_7 as the pure K_4Ge_9 sample still shows cluster signals after solvent removal.

Additionally to Raman measurements on dried residues, thin films prepared from pure K_4Ge_9/*en* and mixed K_4Ge_9/NaP_7/*en* (0.12 mmol K_4Ge_9 / 0.053 mmol NaP_7 in 2 mL *en*) solutions were measured after different steps in the synthesis procedure (after drying, after 100 °C, 500 °C, and 600 °C). The obtained spectra are shown in Figure 2.24.

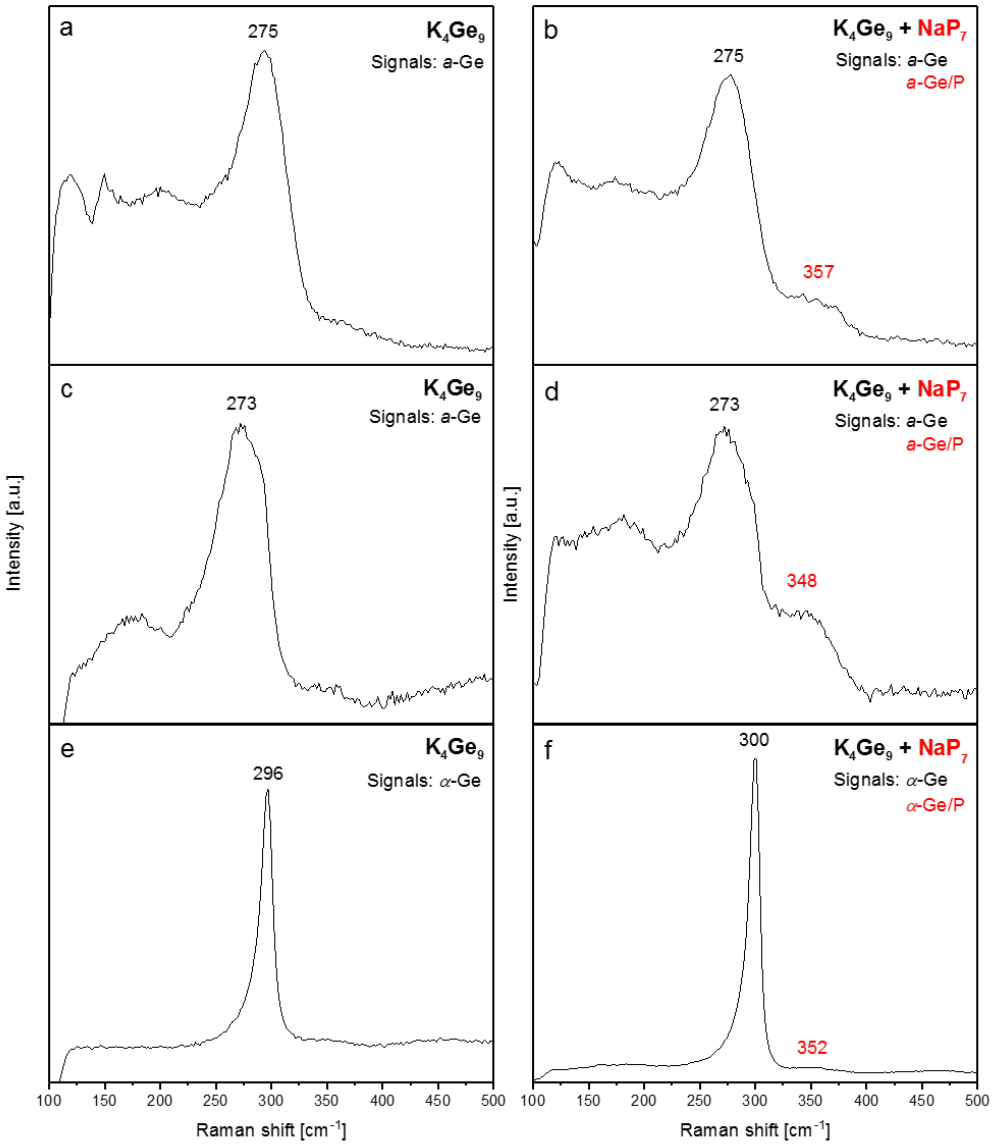

Figure 2.24. Raman spectra of thin films prepared from K_4Ge_9/*en* (a, c, e) and from K_4Ge_9/NaP_7/*en* (b, d, f) solutions. a) and b) thin films after drying under vacuum, c) and d) after 5 min at 500 °C under vacuum, e) and f) after 1 h at 600 °C under argon. The K_4Ge_9/NaP_7/*en* solutions were prepared with a molar Ge/P ratio of 3:1.

As expected and already reported by Fässler *et al.*,[139] the inverse opal structured Ge thin films prepared from pure K_4Ge_9/*en* solutions show amorphous *a*-Ge after drying and after 500 °C and

crystalline α-Ge after 1 h at 600 °C. On the contrary, films prepared from mixed K_4Ge_9/NaP_7/*en* solutions show additional signals at around 350 cm^{-1} throughout the whole experimental process. These signals again indicate the presence of P in the thin films and portend successful introduction of P into the Ge structure.

Supplementary PXRD investigations on dried residues of K_4Ge_9/NaP_7/*en* solutions (molar Ge : P ratio of 3:1; 0.12 mmol K_4Ge_9 / 0.053 mmol NaP_7 in 2 mL *en*) were performed, similar to the ones reported for PPh_3 in Chapter 2.3.2. Again, diffractograms were recorded after drying the residue, and after each individual heating step (100 °C, 500 °C, and 600 °C). The resulting diffractograms are depicted in Figure 2.25.

Solvent removal yields mostly amorphous residue, as can be seen in Figure 2.25a and Figure 2.25b. However, reflections can be assigned to K_4Ge_9 (Figure 2.25a), NaP_7 and traces of red P (Figure 2.25b). The red P could have either been introduced by impurities in the used NaP_7, even though that is not very likely since the purity of the starting material was checked by XRD, or it could be a possible product of an oxidation reaction that happened in solution or *via* solvent removal. After 1 h at 100 °C the powder pattern has not changed (Figures 2.25c and 2.25d). Similar to what could be observed in Chapter 2.3.2, after 5 min at 500 °C the intermetallic clathrate-I K_8Ge_{44} has formed (Figure 2.25e). Additionally, one peak at 32 °2θ can be observed. This peak cannot be assigned to any of the educts. After 1 h at 600 °C, crystalline α-Ge is obtained (Figure 2.25f). The reflections of crystalline α-Ge are not shifted towards higher or lower angles, indicating that no P got introduced into this phase. As already mentioned in the previous chapter, P inherits a smaller ionic radius than Ge, so a shift to lower angles due to an increase in lattice parameters should be detectable. A shift to higher angles could be explained by substitutional doping. In this case the lattice parameters would decrease due to the lower covalent radius of P compared to Ge.[156] Nilges *et al.* demonstrated that NaP_7 decomposes to Na_3P_{11} at 510 °C, to Na_3P_7 at 560 °C and into gaseous P and unspecified yellow solids at 568 °C.[164] None of these decomposition products can be detected in the diffractograms measured after 500 °C and 600 °C. One probability is that P evaporated after thermal decomposition of NaP_7 and therefore cannot anymore be found in the samples. The diffractograms in Figure 2.25a-e show an amorphous background which leads to the assumption that amorphous reaction products have been formed, possibly containing mixed Ge/P species. The diffractogram measured after the final heating step at 600 °C (Figure 2.25f) does not show any amorphous background, indicating that vaporization took place.

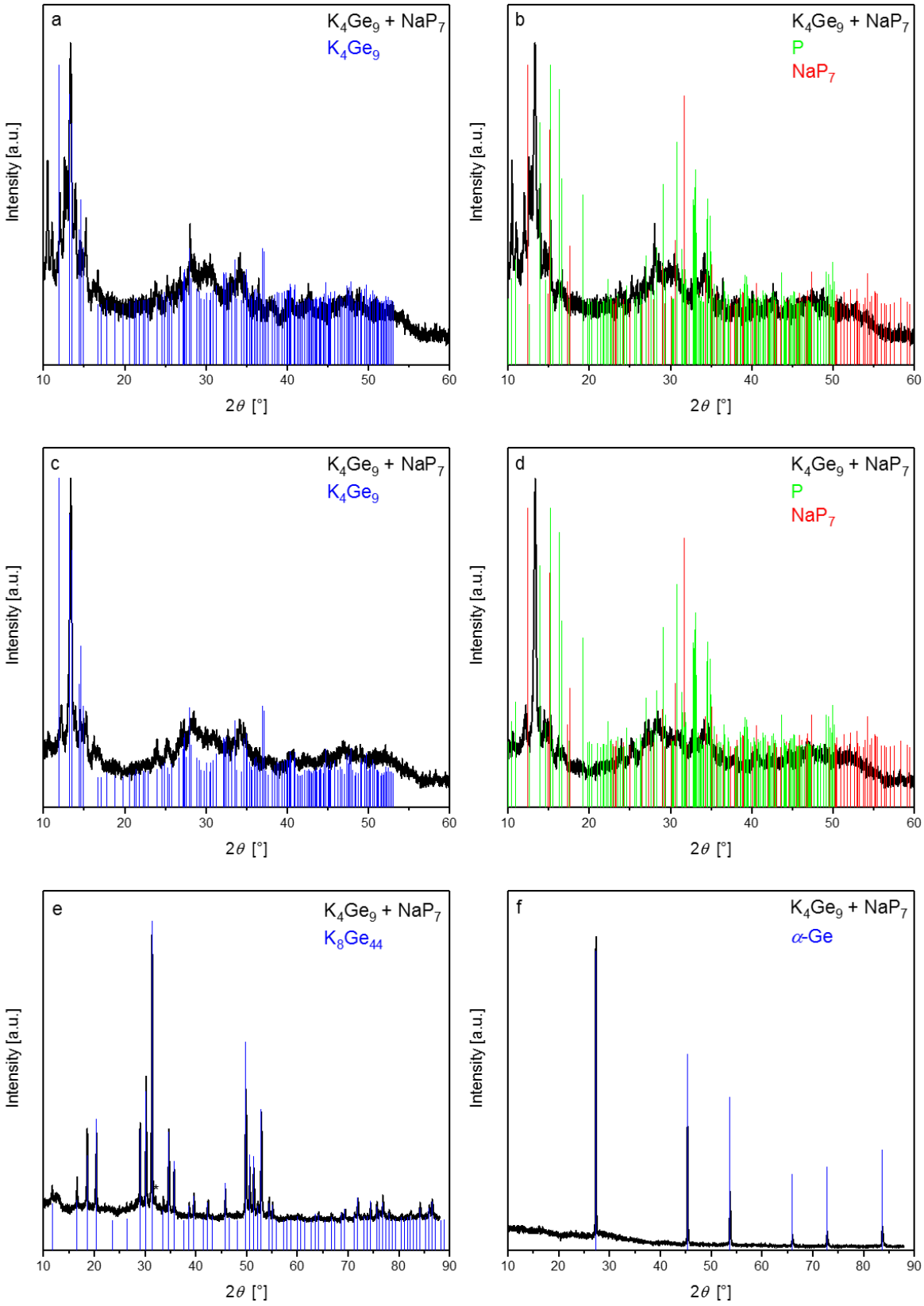

Figure 2.25. Powder X-ray diffractograms of dried residues of K_4Ge_9/NaP_7/*en* solutions (Ge : P 2:1) after different temperature treatments. a) And b) after solvent removal, c) and d) after 1 h at 100 °C under vacuum, e) after 5 min at 500 °C under vacuum, f) after 1 h at 600 °C under argon. The peak marked with an asterisk is an unknown impurity phase. The calculated diffractograms are based on single crystal data.[122b, 157b, 157c, 164-165] Diffractograms were measured using Cu-$K_{\alpha1}$ radiation.

Due to the fact that the aforementioned assumptions and hints for successful introduction of P are very vague, other analysis methods were needed. Figure 2.26 presents Raman spectra of measured thin films, prepared from pure K_4Ge_9/*en* and mixed K_4Ge_9/NaP_7/*en* solutions and crystallized applying temperature treatment at 600 °C. The mixed solutions featured molar ratios of Ge/P of 2:1 and 1:1. These measurements were conducted with the aim to detect a possible Fano effect, caused by phosphorus doping of the Ge thin films.

The measured samples show the expected trend for the BWF fit parameters $|q|$ and w and a significant asymmetric broadening of the signal of crystalline α-Ge can be observed. The absolute value of the inverse coupling strength $|q|$ is decreasing with increasing dopant concentration (77.68 > 10.24 > 7.72 for λ = 514 nm and 34.11 > 8.02 > 6.58 for λ = 633 nm) while the Fano line width w is increasing (2.19 < 5.07 < 5.72 for λ = 514 nm and 2.35 < 3.79 < 4.25 for λ = 633 nm). The samples in Figure 2.26 show no exceptions to this trend. Furthermore, Raman spectra of the thin films prepared from mixed K_4Ge_9/NaP_7/*en* solutions additionally show a weak signal at around 350 cm^{-1}, again indicating P in the Ge structure.

The clearly observable trend for the BWF fit parameters for two different laser wavelengths, being in good agreement with the assumptions made for impurity doping of Ge, and the aforementioned Ge/P signal at 350 cm^{-1} strongly suggest that phosphorus doping of the inverse opal structured Ge thin films was successfully performed utilizing NaP_7 as P source. Especially the presence of the literature reported Ge/P signal proves that P was introduced into the Ge films.

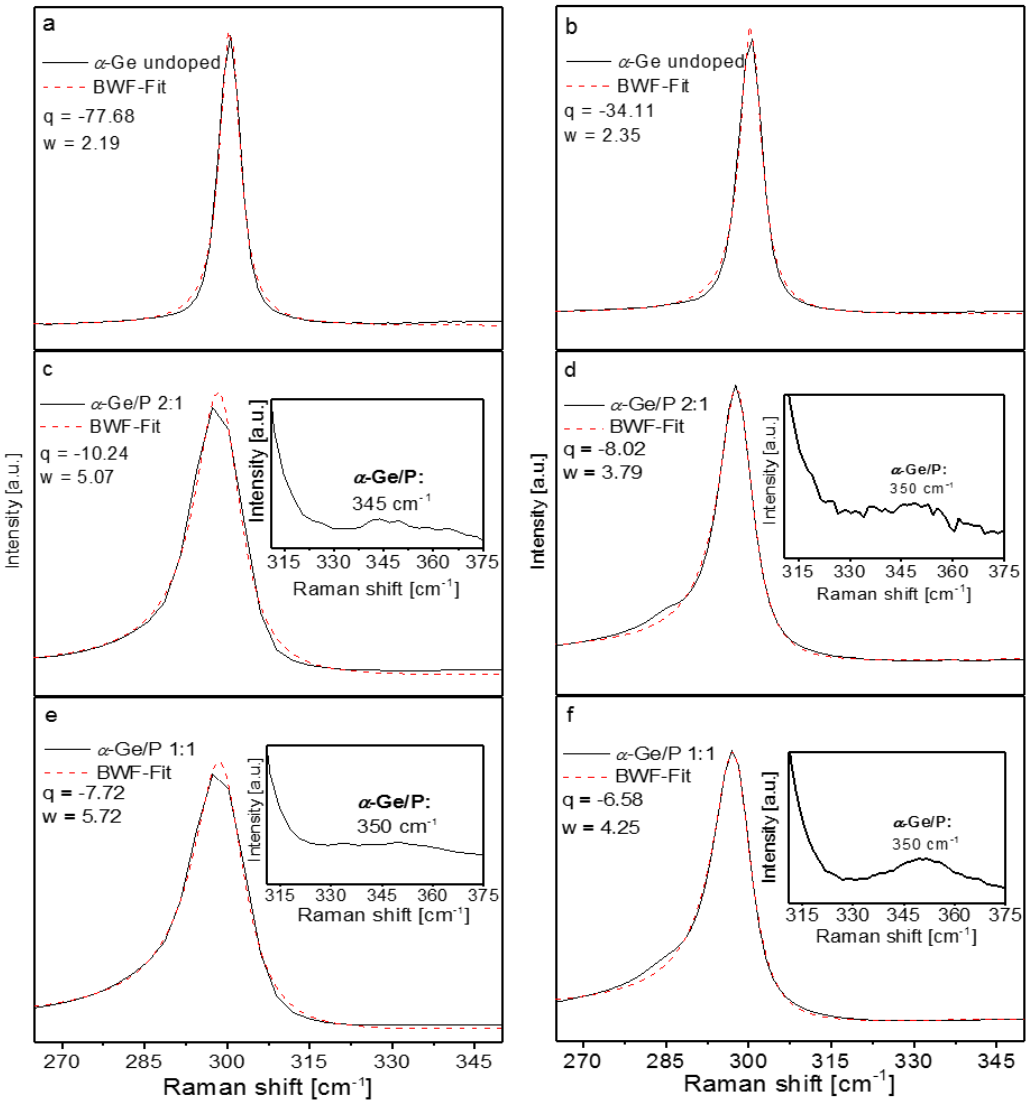

Figure 2.26. Raman spectra of inverse opal structured thin films for Fano effect determination. Shown spectra were measured for pure Ge films (a, b) and films prepared from mixed K_4Ge_9/NaP_7/*en* solutions (c-f). Spectra on the left hand side were measured at λ = 514 nm, spectra on the right hand side at λ = 633 nm.

However, to confirm the assumption of successful P introduction, XPS measurements on thin films were performed. For these experiments, thin films prepared from mixed K_4Ge_9/NaP_7/*en* solutions were used. The thin films were not additionally crystallized at 600 °C. The molar ratio of Ge/P in the mixed solutions was 3:1 (0.12 mmol K_4Ge_9 / 0.053 mmol NaP_7 in 2 mL *en*). Samples were measured without Ar^+ sputtering and after 10 min and 30 min sputter time. All samples were kept under argon atmosphere prior to the measurement. Nitrogen flow was applied while transferring the samples into the vacuum chamber of the XPS device. This was done to minimize air exposure during sample transfer, nevertheless air exposure could not be completely ruled out. Figure 2.27 shows the obtained spectra for Ge 3d (a, c, e) and P 2p (b, d, f).

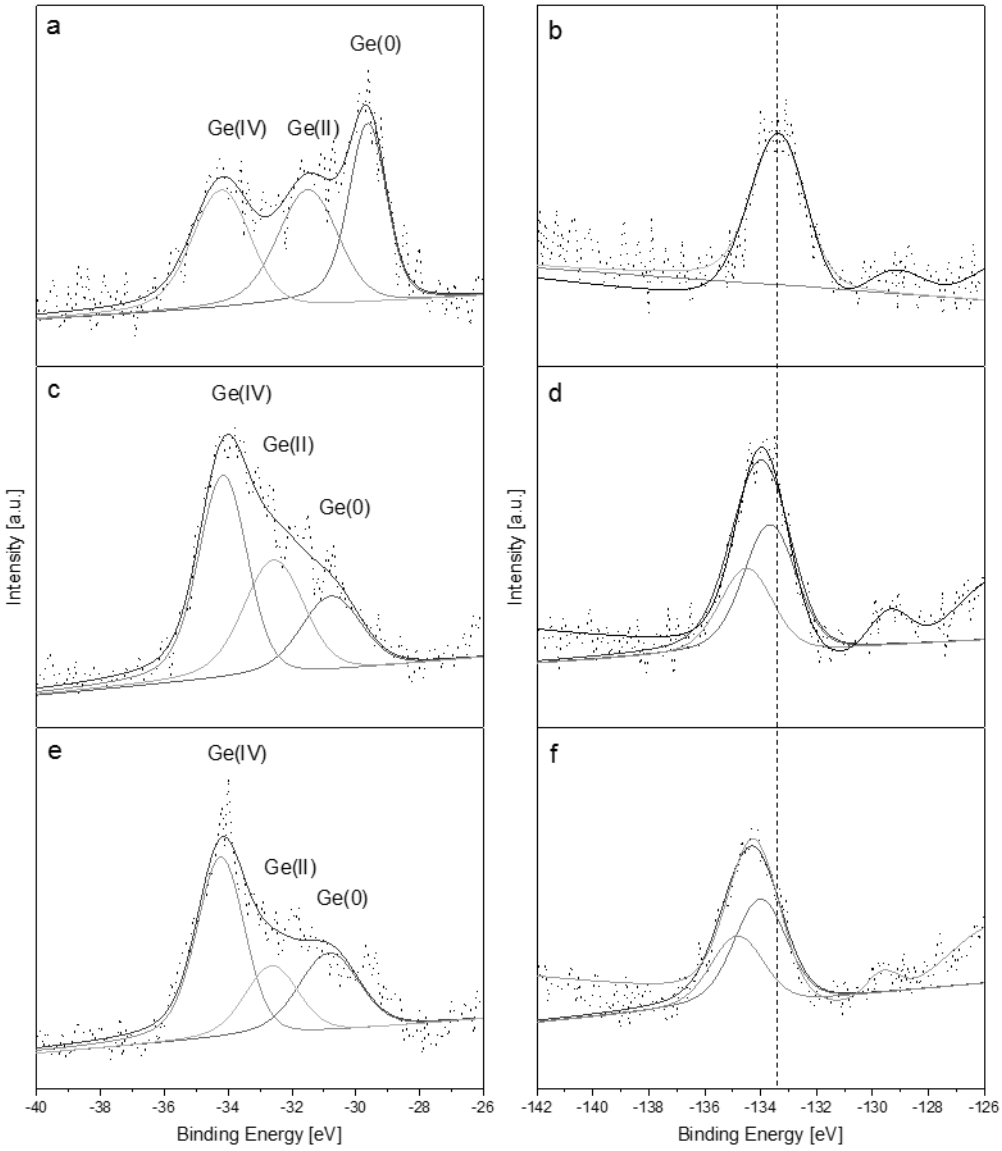

Figure 2.27. XPS spectra of thin films prepared from mixed K_4Ge_9/NaP_7/en solutions (Ge : P 3:1). Spectra are shown for Ge 3d (a, c, e) and P 2p (b, d, f). a) and b) spectra recorded without previous Ar^+ sputtering, c) and d) recorded after 10 min sputtering, e) and f) after 30 min sputtering.

Without Ar^+ sputtering, the Ge spectrum shows Ge(0) with highest intensity and peaks for Ge(II) and Ge(IV) with slightly lower intensities. This demonstrates that the surface composition of the measured thin film is dominated by Ge(0), even though the amount of oxidized Ge species is significantly higher than for undoped Ge thin films (see Figure 2.8). After sputtering for 10 min (Figure 2.27c) and 30 min (Figure 2.28e) the Ge(IV) signal shows the highest intensity while the intensity of the Ge(0) signal drastically decreased. This clearly showcases that deeper layers of the thin film mainly consist of Ge(IV), contrary to pure inverse opal structured Ge thin films where Ge(0) is the dominant Ge species after sputtering. Since the samples were kept under argon atmosphere and only got exposed to air for a very short period of time during the transfer process into the vacuum chamber, these results could

be a hint towards successful P introduction. Ge oxidation with only minimal air exposure indicates the formation of mixed Ge/P species which is in accordance with the previously presented Raman results.

The P spectrum measured prior to sputtering (Figure 2.27b) shows a signal at -129 eV and a signal at -133 eV. After sputtering (10 min: Figure 2.27d, 30 min: Figure 2.27f), the main signal gets slightly shifted towards -134/-135 eV, as shown by the dashed line. Literature known P 2p binding energies are listed in Table 2.4.

Table 2.4. P 2p binding energies of different phosphorus species.[163]

P species	**2p Binding energy [eV]**
Phosphides	-128/-129
P_{red}	-130
Phosphate	-132/-133
Oxides	-135

Comparing the here obtained results to 2p binding energies shown above, phosphides are present on the film surface as well as in deeper layers of the thin film. These could be mixed Ge/P products of reactions between the Zintl precursor K_4Ge_9 and the P source NaP_7. The phosphate and oxide signals are more likely to be products of air induced oxidation of the applied P species since oxidation of NaP_7 by $[Ge_9]^{4-}$ clusters is highly unlikely. Here the short period of air exposure could have been enough to oxidize the P species on the thin film. The film surface shows mainly phosphate while oxides can be found within deeper layers of the film. This can also be explained by air exposure of the oxidic species, leading to phosphate formation through air moisture.

Conclusively it can be said that introducing P in the inverse opal structured Ge thin films was successfully performed using NaP_7 as P source. All obtained results are in great accordance and indicate successful P introduction. Due to the high solubility of NaP_7 in *en*, this method allows for a simple wet-chemical doping procedure with easily adjustable P content.

2.3.4 Red P as phosphorus source

For a third strategy to introduce P, red P as a potential P source was investigated. Red P could be a suitable candidate for a wet-chemical doping route, similar to the aforementioned NaP_7, since it allows for mixed solutions of K_4Ge_9 and red P in *en*. For details on solution compositions see Chapter 4.3.9. The relatively good solubility of red P together with K_4Ge_9 (up to 17 mg red P and 50 mg K_4Ge_9 in 1 mL *en*) enables adjustable dopant concentrations in the Ge thin films to a certain degree. Film preparation

is described in Chapter 4.3.11. Figure 2.28 displays SEM images of the obtained thin films. The inverse opal structure was successfully achieved over a large surface area. The desired honeycomb structure is very homogenously distributed, no larger cracks or sintered particles can be observed. EDX measurements of the prepared film show a Ge : P ratio of 3:1 and remaining K (see Figure 5.2 in the Appendix Chapter 5.1).

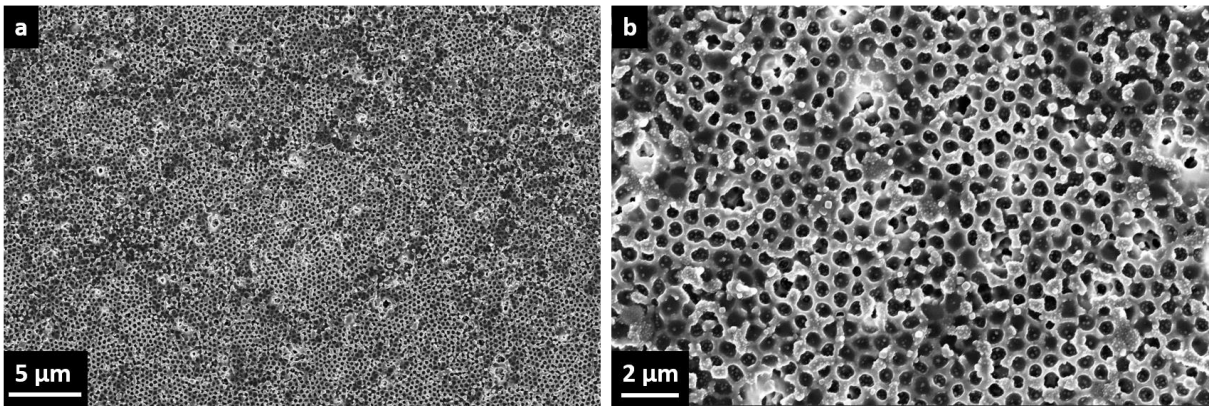

Figure 2.28. SEM images of an inverse opal structured thin film on a Si substrate, prepared from a K_4Ge_9/P_{red}/*en* solution (Ge : P 3:1). a) 5000x magnification, b) 20000x magnification.

Similar to before mentioned doping strategies, Raman measurements of dried residues of K_4Ge_9/P_{red}/*en* were performed and compared to pure Zintl precursor solutions. The obtained spectra are shown in Figure 2.29. The K_4Ge_9/P_{red}/*en* solution was prepared with a molar Ge : P ratio of 1:1 (0.12 mmol K_4Ge_9 / 1.00 mmol P_{red} in 2 mL *en*). The solutions were filtrated under argon atmosphere and the solvent was removed under vacuum. To prevent air exposure, the remaining residues were filled into glass capillaries which were sealed in a glovebox.

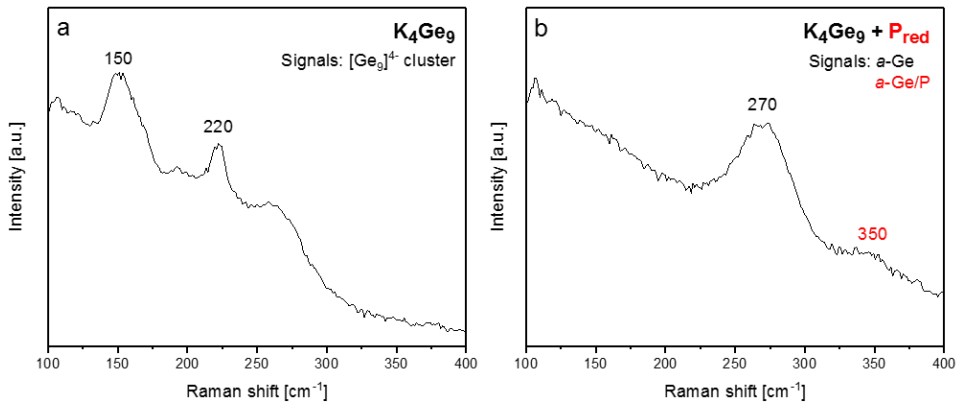

Figure 2.29. Raman spectra of dried residues of a) a K_4Ge_9/*en* solution and b) a K_4Ge_9/P_{red}/*en* solution. Molar ratios of Ge : P 1:1.

Analogue to Chapter 2.3.3, where phosphorus doping based on NaP_7 is presented, the spectrum in Figure 2.29b shows a signal of amorphous Ge at 270 cm^{-1} and an additional signal at 350 cm^{-1} which

can be assigned to P in the Ge environment, giving a first hint towards successful P introduction applying this method.

Similar Raman studies were performed on thin films. For comparison, films were prepared using K_4Ge_9/*en* and mixed K_4Ge_9/P_{red}/*en* solutions. The molar Ge/P ratio of the K_4Ge_9/P_{red}/*en* solution was 3:1 (0.12 mmol K_4Ge_9 / 0.36 mmol P_{red} in 2 mL *en*). Raman was measured after drying the films at room temperature, after 5 min at 500 °C and after 1 h at 600 °C. The resulting Raman spectra are presented in Figure 2.30.

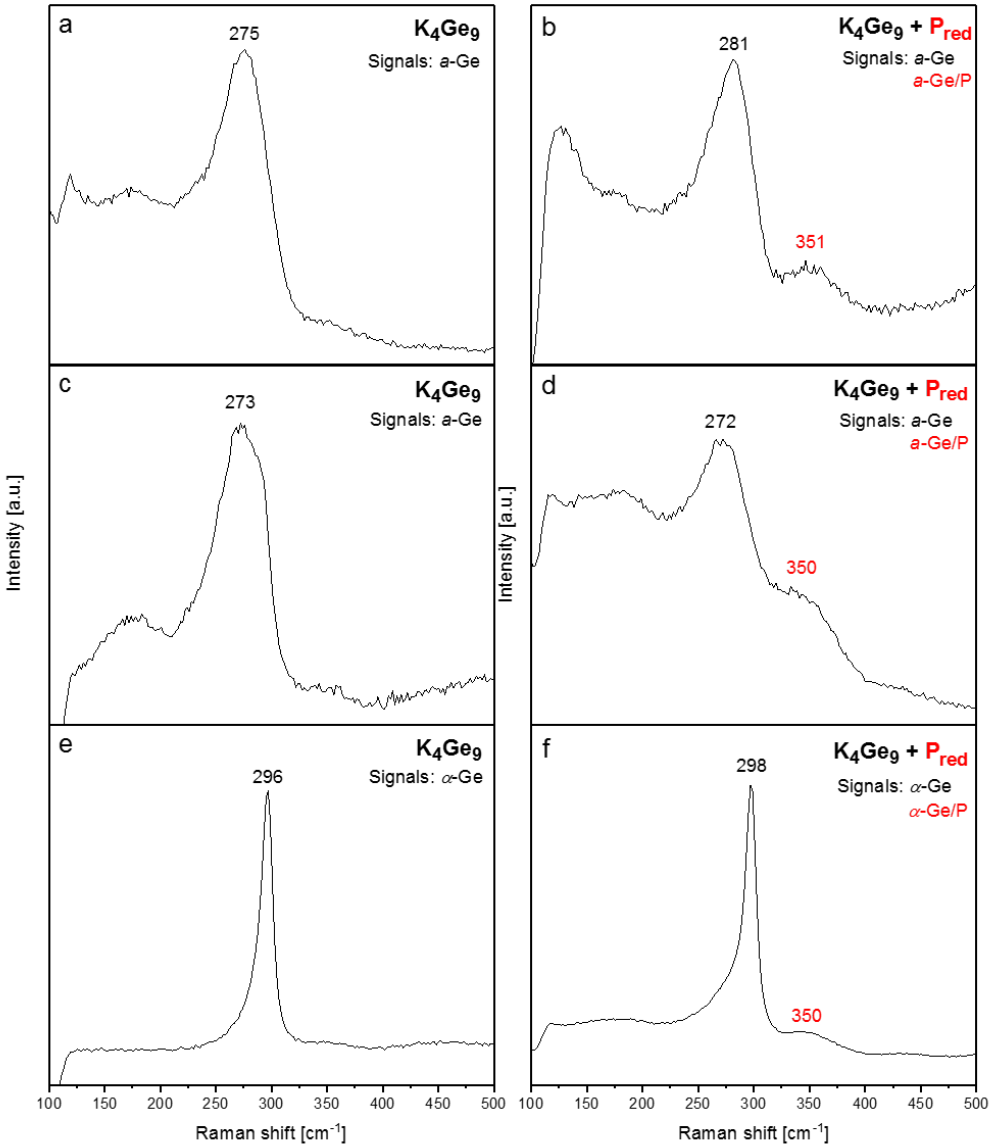

Figure 2.30. Raman spectra of thin films after different temperature treatments (Ge : P 3:1). a), c), and e) spectra of thin films prepared from K_4Ge_9/*en* solutions; b), d), and f) spectra of thin films prepared from K_4Ge_9/P_{red}/*en* solutions. Spectra a) and b) measured after drying at room temperature under vacuum, c) and d) after 5 min at 500 °C under vacuum, e) and f) after 1 h at 600 °C under argon.

Throughout all shown Raman spectra, the Ge signals of the films prepared from pure K_4Ge_9/*en* and mixed K_4Ge_9/P_{red}/*en* solutions are identical. After solvent removal under vaccum, amorphous Ge can be seen. Temperature treatment at 500 °C causes no changes in this Ge signal, and after 1 h at 600 °C crystalline α-Ge has expectably formed. The major difference between the spectra on the left hand side and the ones on the right hand side is the signal at 350 cm^{-1}, which can only be detected for the samples prepared from mixed K_4Ge_9/P_{red}/*en* solutions. As stated before, this signal shows P in the inverse opal structured Ge film. This demonstrates that P is not only present in the dried residues of the respective solutions but can also be found in the prepared thin films, even after temperature treatment.

XPS as another spectroscopic method was applied to check for the presence of P not only on the surface but also within deeper layers of the prepared films. For these experiments, thin films prepared from mixed K_4Ge_9/P_{red}/*en* solutions were used. The thin films were not additionally crystallized at 600 °C. The molar ratio of Ge : P in the mixed solutions was 3:1 (0.12 mmol K_4Ge_9 / 0.36 mmol P_{red} in 2 mL *en*). Samples were measured without Ar^+ sputtering and after 10 min sputter time. Prior to the measurement, all samples were kept under argon atmosphere. To minimize air exposure during sample transfer into the vacuum chamber of the XPS device, nitrogen flow was applied. Figure 2.31 shows the obtained spectra for Ge 3d (a, c) and P 2p (b, d).

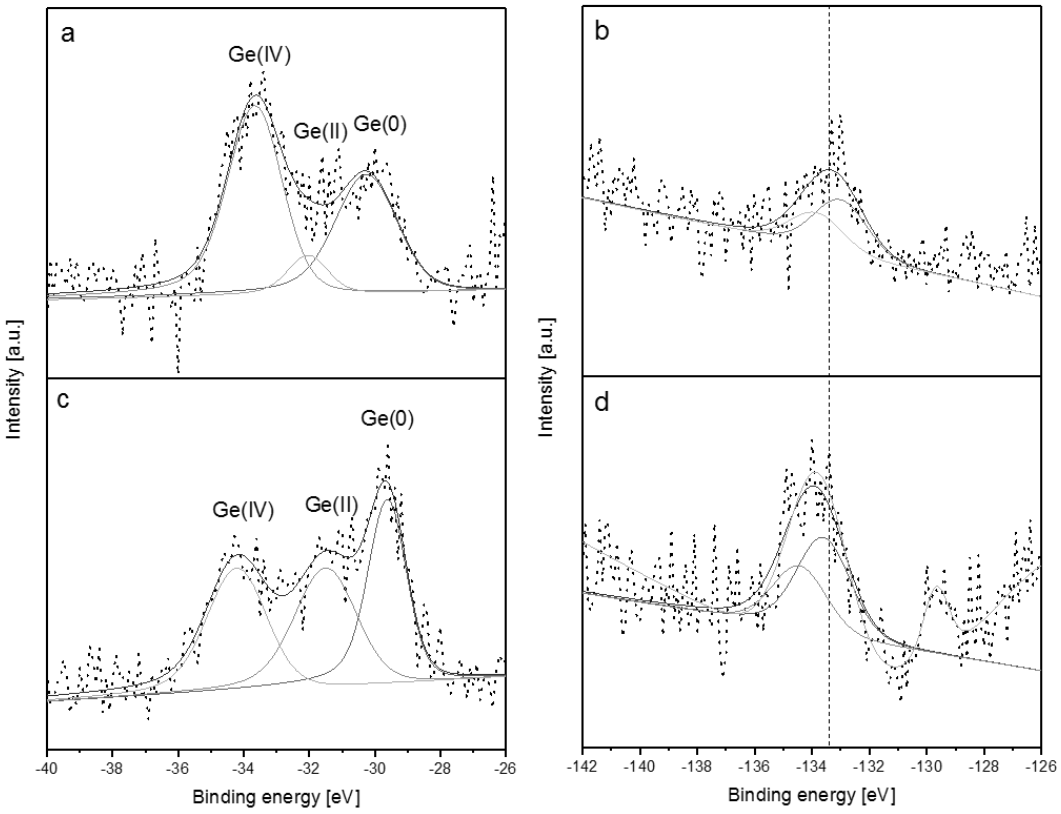

Figure 2.31. XPS spectra of thin films prepared from K_4Ge_9/*en* (a, c) and K_4Ge_9/P_{red}/*en* (b, d) solutions. Spectra a) and b) measured before Ar^+ sputtering, spectra c) and d) measured after 10 min sputter time.

The Ge 3d spectra (Figure 2.31a, c) show a large Ge(IV) signal before sputtering (a) and mainly Ge(0) after sputtering (c), indicating oxidized Ge on the film surface and mainly *a*-Ge in deeper layers within the porous film.

Looking at the P 2p spectra (Figure 2.31b, d), before Ar^+ sputtering exclusively phosphate or oxide signals from -132 eV to -136 eV can be detected on the surface (Figure 2.31b). After 10 min of sputtering, an additional signal at -129 eV can be seen, pointing out that phosphide is present within deeper layers of the thin film (Figure 2.31d). This is a sign that germanium phosphide species have formed in the film, matching the previously discussed Raman results. Similarly to what could be seen in Figure 2.27d/f, Chapter 2.3.3, the phosphate signal has shifted towards the region of oxidic signals, indicating a reaction of oxides while exposed to air moisture.

To conclude, the presented results prove that P was successfully introduced into the inverse opal structured Ge thin film. This strategy, utilizing red P as phosphorus source, allows for a simple wet-chemical synthesis route to phosphorus doped Ge films. Furthermore, the P content of the obtained thin films is easily controlled *via* varying the concentration of red P in the K_4Ge_9/P_{red}/*en* solution.

2.3.5 Strategies involving the ternary phases "$K_2Ge_2P_2$" and "$K_2Ge_7P_2$"

A different strategy to achieve mixed Ge/P thin films with inverse opal structure involved the use of ternary, Ge and P containing, Zintl phases. Dehnen *et al.* reported on the synthesis of "$K_2Ge_2P_2$" and crystallization of $(Ge_2P_2)^{2-}$ as well as $(Ge_7P_2)^{2-}$ from *en* solutions.[166] These results were promising for the production of phosphorus doped Ge films. In this work, synthesis of "$K_2Ge_2P_2$" as well as "$K_2Ge_7P_2$" was attempted (for details on synthesis see Chapters 4.3.4 and 4.3.5). Powder diffractograms of the reaction products are displayed in the Appendix Chapter 5.1 (Figures 5.29 & 5.30). Due to the lack of literature or single crystal data, it could not be further checked if the desired products were obtained by running the described synthesis programs.

Subsequently, the obtained powders were dissolved in *en* and thin films were prepared, applying the standard procedure for thin film preparation (solution concentrations: 0.12 mmol "$K_2Ge_7P_2$" in 2 mL *en*, 0.18 mmol "$K_2Ge_2P_2$" in 2 mL *en*; for details on preparation see Experimental Part Chapter 4.3.9 & 4.3.11). No crystallization step at 600 °C was applied. Figure 2.32 shows SEM images of the received films. Starting from "$K_2Ge_7P_2$", the inverse opal structure was successfully obtained over a large surface area. However, the pores are covered by a thin surface layer which is cracked open at some spots. The surface layer could be a hint towards excess of precursor solution, some further fine tuning may need to be done.

Using "$K_2Ge_2P_2$" as precursor, a porous structure was also obtained. Though, the resulting structure does not show the desired honeycomb pattern of the inverse opals. The pore walls are much thicker than expected. This could have been caused by swelling processes of the material during solvent removal. Nevertheless, the film exhibits a highly porous surface over a large area.

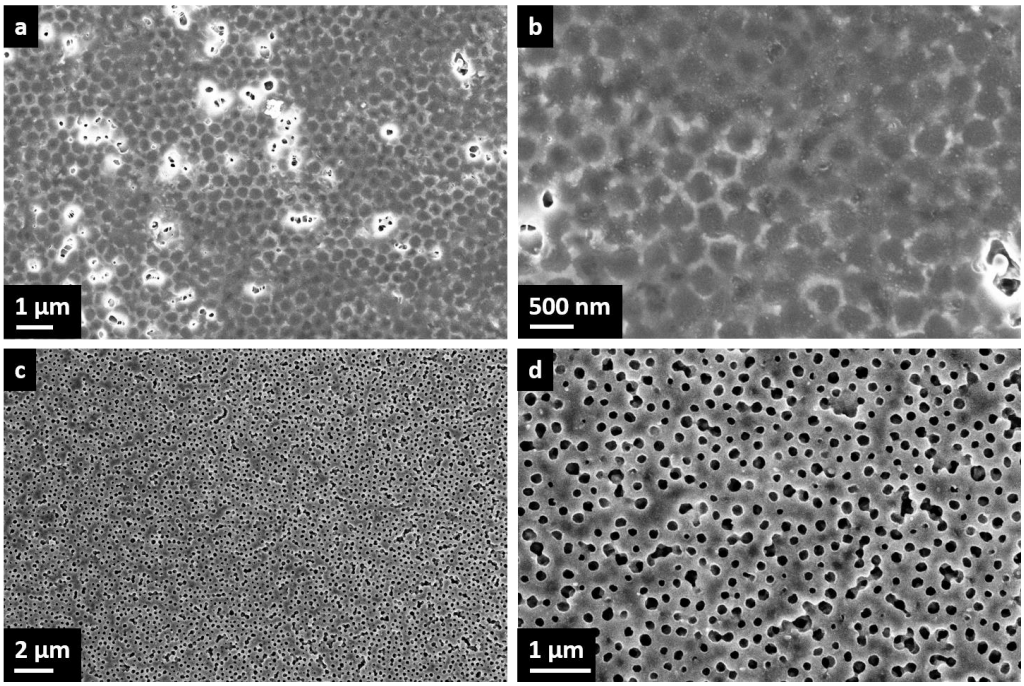

Figure 2.32. SEM images of inverse opal structured thin films on Si substrates. a) and b) prepared from a "$K_2Ge_7P_2$"/*en* solution, c) and d) prepared from a "$K_2Ge_2P_2$"/*en* solution. a) 15000x magnification, b) 36226x magnification, c) 8000x magnification, d) 25000x magnification.

Results of EDX measurements of the prepared thin films are given in Table 2.5, the spectra can be found in the Appendix Chapter 5 (Figures 5.3 & 5.4).

Table 2.5. EDX measurements of films prepared from "$K_2Ge_2P_2$"/*en* and "$K_2Ge_7P_2$"/*en* solutions.

Precursor	Ge	P
"$K_2Ge_7P_2$"	39.25	1
"$K_2Ge_2P_2$"	1	1.2

A Ge : P molar ratio of 39.25 : 1 was found on the film for "$K_2Ge_7P_2$". The Ge content is by far too high for what was expected for this precursor phase, clearly indicating that successful synthesis could not be performed. The XRD pattern of the obtained reaction product of the solid state synthesis shows reflections of $K_{12}Ge_{17}$ (see Appendix Chapter 5, Figure 5.30), which is soluble in *en*. This explains the high amount of Ge on the film. The very small amount of P can be caused by residual red P in the product mixture and its solubility in *en*.

On the other hand, the Ge : P molar ratio for "$K_2Ge_2P_2$" found on the film is very close to the expected value, hinting towards successful synthesis of the desired $K_2Ge_2P_2$ phase. However, yield of a phase pure reaction product by the solid state synthesis was definitely not the case, as a large amount of Ge can be detected by PXRD (see Appendix Chapter 5, Figure 5.29). Though, the obtained impurity phases seem not to be soluble in *en*, which explains why the Ge : P ratio on the thin film is so close to the expected composition for $K_2Ge_2P_2$.

For further investigation, Raman spectra of dried residues and thin films prepared from filtrated "$K_2Ge_7P_2$"/*en* and "$K_2Ge_2P_2$"/*en* solutions were measured (Figure 2.33). Solution concentrations were 0.12 mmol "$K_2Ge_7P_2$" in 2 mL *en* and 0.18 mmol "$K_2Ge_2P_2$" in 2 mL *en*. Spectra 2.33a and b were measured after solvent removal in vacuum, no additional heating steps were applied. To avoid air exposure, the dried residues were filled into glass capillaries inside a glovebox. The thin films shown in Figure 2.33c and d were prepared using $GeCl_4$ as cross-linking agent. After cross-linking, the samples were hold at 500 °C for 5 min under vacuum. No crystallization step at 600 °C was applied. Details on solution preparation can be found in Chapter 4.3.9.

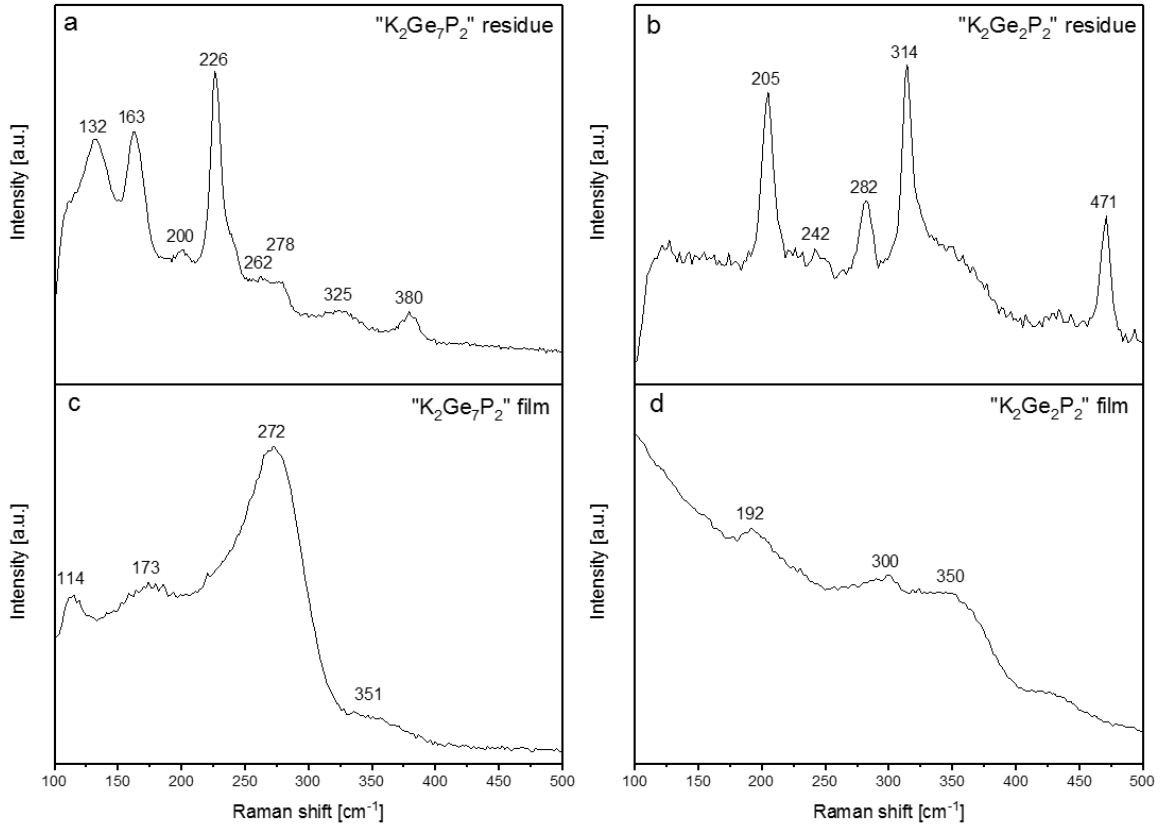

Figure 2.33. Raman spectra of dried residues (a, b) and thin films on Si substrates (c, d) prepared from "$K_2Ge_7P_2$"/*en* (a, c) and "$K_2Ge_2P_2$"/*en* (b, d) solutions.

Figure 2.33a shows the Raman spectrum of a dried residue of a "$K_2Ge_7P_2$"/*en* solution. The observed signals match the literature know signals of $K_{12}Ge_{17}$ very well.[122a] This confirms the results gained from

XRD measurements. However, two additional signals at 325 cm^{-1} and 380 cm^{-1} are depicted in the spectrum. While the signal at 380 cm^{-1} can be assigned to red P,[167] the signal at 325 cm^{-1} cannot be assigned to either any literature known Ge-clusters or P compound. Literature known potassium phosphides also show a clear frequency gap between 300 cm^{-1} and 340 cm^{-1}, meaning that those can also be excluded. This leads to the assumption that a Ge/P species could have been formed. The thin film prepared from this solution mainly shows amorphous *a*-Ge at 272 cm^{-1} (Figure 2.33c). A broad signal with low intensity at 351 cm^{-1} is hinting towards P in the porous Ge film.

Figure 2.33b shows the Raman spectrum of a dried residue of a "$K_2Ge_2P_2$"/*en* solution. The signals cannot be assigned to any literature known phase. Crystalline α-Ge, as found in the PXRD diffractrogram, cannot be detected in the Raman spectrum which can be explained by its insolubility in *en*. Combined with the results from the EDX measurements in Table 2.5, it can be assumed that the depicted signals in Figure 2.33b can be assigned to an unknown Ge/P species. The Raman spectrum of the prepared thin film in Figure 2.33d shows three signals at 192 cm^{-1}, 300 cm^{-1} and 350 cm^{-1}. As discussed before, the signal at 350 cm^{-1} can be associated with P in the inverse opal structured Ge thin film. A signal at 300 cm^{-1} in a Ge sample usually clearly indicates the presence of crystalline α-Ge. However, the signal for α-Ge should be very sharp and show much higher intensity. This and the unknown broad signal at 192 cm^{-1} give a hint that the measured thin film sample consists of an unknown amorphous phase.

As conclusion, it can be assumed that synthesis of $K_2Ge_7P_2$ could not be successfully performed, even though small amounts of P can be found on the obtained thin films. Synthesis of $K_2Ge_2P_2$, however, could have been successful. While a clear evidence for successful synthesis is missing due to the lack of a single crystal; Raman, PXRD, and EDX results definitely hint towards the synthesis of a new mixed Ge/P phase with a molar Ge : P ratio of 1 : 1. The obtained phase also shows good solubility in *en*, allowing for easy thin film preparation.

2.3.6 Electrochemical measurements

To check for the influence of P regarding electrochemical performance, cycling experiments were conducted. P exhibits a very high theoretical capacity of 2595 mAh g^{-1} in lithium ion batteries, forming Li_3P.[98a] Mixed Ge/P thin films should feature increased electric conductivity, compared to electrodes made of pure Ge. This would allow for higher *C*-rates during charging and discharging which is highly desirable for potential applications.

For the presented studies, inverse opal structured thin films were prepared on Cu substrates, starting from $K_4Ge_9/P_{red}/en$ and $K_4Ge_9/NaP_7/en$ solutions. Red P and NaP_7 were chosen as P sources since successful P introduction was demonstrated using these starting materials and they allow for adjustable solution compositions, contrary to "$K_2Ge_2P_2$". Two different molar Ge : P ratios were chosen for the electrochemical experiments. Samples with Ge/P ratios of 3 : 1 and 10 : 1 were prepared. For details on solution composition see Experimental Part Chapter 4.1.6, for details on sample preparation see Experimental Part Chapters 4.3.9 & 4.3.11. For easier comparison of the obtained cycling results with results gained from pure Ge electrodes, all capacity values as well as *C*-rates were calculated for Ge as active material. It could also not be guaranteed that the amount of P on the films was the same as the initial amount, therefore referring to Ge as active material was applied as the safer option. This should result in capacities higher than the theoretical capacity of 1385 mAh g^{-1} for $Li_{15}Ge_4$, if mixed Ge/P films were successfully cycled. The obtained results for electrochemical cycling experiments are shown in Figure 2.34.

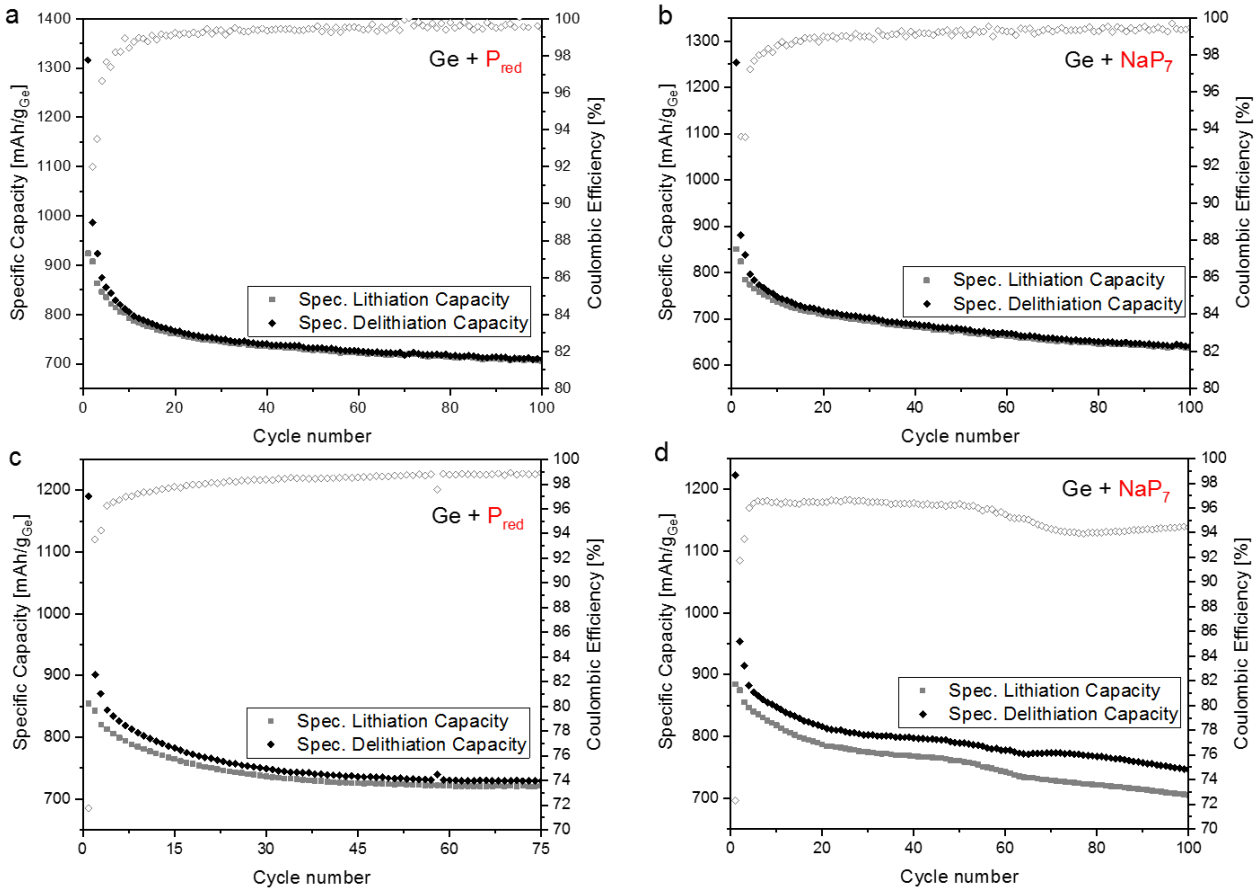

Figure 2.34. Specific capacities over extended cycling at a rate of 0.2*C* with the first two cycles at 0.1*C* of mixed Ge/P thin films. a) and c) thin films prepared from $K_4Ge_9/P_{red}/en$ solutions, b) and d) thin films prepared from $K_4Ge_9/NaP_7/en$ solutions. Molar Ge/P ratios of 3 : 1 for a) and b) and 10 : 1 for c) and d).

None of the electrodes presented in Figure 2.34 displays capacities higher than the pure Ge electrodes shown in Chapter 2.2.3. Capacity values and retentions are summarized in Table 2.6. Initial capacities are taken from the 4th cycle, after SEI formation has stabilized.

Table 2.6. Summary of electrochemical measurements on mixed Ge/P electrodes.

Electrode material [molar ratio]	**Loading**	**Specific delithiation capacity [mAh/g_{Ge}]**		**Capacity retention [%]**
		Initial (4th cycle)	**100th cycle**	
Ge	313 µg	1360	990	73
Ge + P_{red} 3 : 1	364 µg	875	709	81
Ge + P_{red} 10 : 1	173 µg	847	729 (75th cycle)	86 (75th cycle)
Ge + NaP_7 3 : 1	404 µg	791	641	81
Ge + NaP_7 10 : 1	246 µg	884	743	84

The lower overall capacities gained for the Ge/P electrodes are most likely caused by the higher mechanical stress compared to pure Ge electrodes, based on the two different reaction mechanisms (lithiation of Ge and lithiation of P). Nevertheless, the Ge/P electrodes show capacity retentions roughly 10% higher than pure Ge electrodes tested in this work. This proves the presumption that Ge/P electrodes could possibly be cycled at higher *C*-rates than pure Ge electrodes, with less capacity fading. However, even pure Ge electrodes proved to be very stable towards higher *C*-rates. As aforementioned, a more than ten times higher *C*-rate translates in a very low capacity loss of only 8.2%. Even taking this capacity loss into account, pure Ge electrodes still perform better in terms of absolute capacity than the mixed Ge/P electrodes shown in Figure 2.34. This means that even though higher capacity retentions could be achieved for Ge/P electrodes, pure Ge electrodes are still more attractive for actual battery applications. Ge/P electrodes could possibly find use in niche applications were very fast charging and discharging is desired with less focus on overall capacity.

2.4 Tin and Mixed Tin/Germanium Thin Films

The following chapter describes the transition to the heavier homologue tin, including synthesis and characterization of inverse opal structured thin films. Analytical methods applied to the samples in this chapter are summarized in Table 2.7.

Table 2.7. Analytical methods applied to Sn and mixed Sn/Ge samples.

Sample	SEM	EDX	Raman	XRD	XPS	Electrochemical methods
Sn film	x	x	x	-	x	x
$[Sn_9]^{4-}$ dried residue	-	-	x	x	-	-
$[Sn_9]^{4-}/[Ge_9]^{4-}$ film	x	x	x	-	x	x
$[Sn_9]^{4-}/[Ge_9]^{4-}$ dried residue	-	-	x	x	-	-
"$K_4Ge_5Sn_4$" film	x	x	x	-	x	x
"$K_4Ge_5Sn_4$" dried residue	-	-	x	x	-	-

2.4.1 Synthesis

Sevov *et al.* reported on mixtures of K_4Sn_9 and K_4Ge_9 in *en* and *dmf*. Using mass spectrometry, they found $[Sn_9]^{4-}$ and $[Ge_9]^{4-}$ clusters in *en* and mixed $Ge_{9-x}Sn_x$ (x = 1 – 9) clusters in *dmf*.[168] Based on their results, we tried to prepare inverse opal structured thin films from the described solutions. To fabricate Sn and mixed Sn/Ge thin films with inverse opal structure, the procedure described in Chapter 2.2.1 was slightly adjusted (see Figure 2.36). For pure Sn films, K_4Sn_9 was used as Zintl precursor and the clusters were linked by impregnation with $SnCl_4$ vapor. Mixed Sn/Ge films were prepared in two different ways. The first option involved a mixture of K_4Sn_9/*en* (0.10 mmol in 2 mL *en*) and K_4Ge_9/*en* (0.10 mmol in 2 mL *en*), while the second option utilized a "$K_4Ge_5Sn_4$"/*en* (0.05 mmol in 1 mL *en*) precursor solution (details on solution preparation can be found in Chapter 4.3.9). $GeCl_4$ was used for cluster cross-linking for both mixed film variants (see Chapter 4.3.11). Due to the low melting point of Sn at 231.9 °C, the temperature treatments were performed at lower temperatures than for pure Ge thin films. After infiltration by the respective precursor solution, the substrates were dried at 80 °C for 1 h under vacuum. Following cluster cross-linking, the samples were heated to 150 °C for 1 h under vacuum. In the final step, the films were washed with DMSO and THF for solvate assisted template and KCl removal. Details on film preparation can be found in the Experimental Part Chapter 4.3.11.

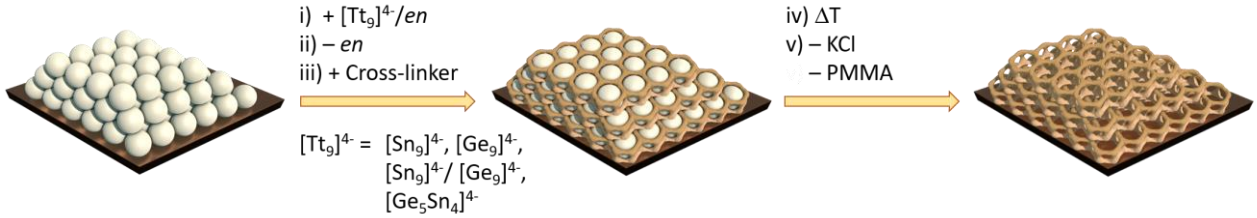

Figure 2.35. Wet-chemical synthesis of inverse opal structured Sn or Sn/Ge thin films using a PMMA template. i) Casting of a tetrel cluster solution in *en* on a PMMA template (grey spheres), ii) solvent removal by evaporation, iii) impregnation of a cross-linker ($GeCl_4$ or $SnCl_4$, depending on the desired film composition), iv) drying step under vacuum, v) removal of KCl and the PMMA template opals via washing with DMSO and THF resulting in an inverse opal structured Sn or mixed Sn/Ge thin film. Figure adapted from ref.[144]

The obtained thin films are depicted in Figure 2.36. The desired inverse opal structure could be achieved for all mentioned compositional variants. A characteristic red glimmer could be observed under light exposure (Figure 2.36e). Film thicknesses were determined to be 2.5 µm for pure Sn films and 2.5 – 3.0 µm for mixed Sn/Ge films (measured by profilometry). EDX measurements of pure Sn films only show Sn (see Appendix Chapter 5.1, Figure 5.5). EDX of mixed Sn/Ge films show a molar Ge : Sn ratio of 1.37:1 for the film in Figure 2.36c and a molar Ge : Sn ratio of 1.42:1 for the film in Figure 2.36d (see Appendix Chapter 5.1, Figure 5.6 & 5.7). These molar ratios are in good agreement with the expected results for the mixed Sn/Ge films.

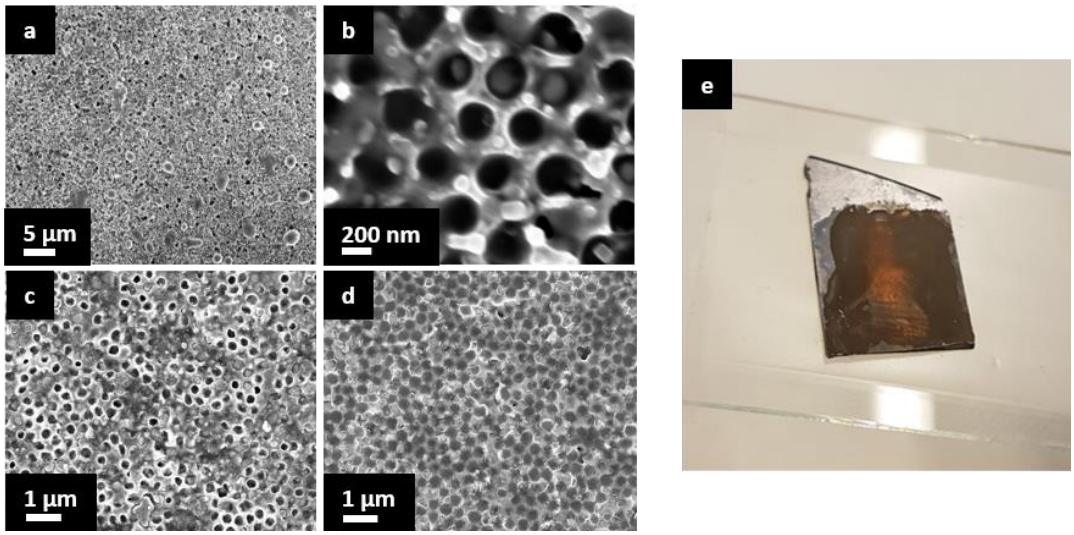

Figure 2.36. SEM images (a-d) and photo (e) of inverse opal structured thin films on Si substrates. Films prepared from *en* solutions. a) Sn thin film, 2000x magnification. b) Sn thin film, 85000x magnification. c) Mixed Sn/Ge film using K_4Sn_9 and K_4Ge_9 as precursors, 10000x magnification. d) Mixed Sn/Ge film using "$K_4Ge_5Sn_4$" as precursor, 10000x magnification. e) Photo of an inverse opal structured Sn thin film under illumination.

An approach analogous to the first method described was pursued with dimethylformamide (*dmf*) as solvent of choice. A mixture of K_4Sn_9/*dmf* (0.10 mmol in 2 mL *dmf*) and K_4Ge_9/*dmf* (0.10 mmol in 2 mL *dmf*) was used as precursor solution (see Chapter 4.3.9). However, the obtained green solution was not suitable for thin film preparation, no substrate coatings could be achieved.

2.4.2 Investigations of precursor solutions

To gain a better understanding of what is happening during the synthesis procedure, the precursor solutions were dried under vacuum and the obtained residues were investigated by Raman and XRD after completed solvent removal. Table 2.8 lists literature reported signals for relevant Zintl phases.

Table 2.8. Raman signals for K_4Sn_9, K_4Ge_9, $K_{12}Sn_{17}$, and $K_{12}Ge_{17}$.

	K_4Sn_9	**K_4Ge_9**	**$K_{12}Sn_{17}$**	**$K_{12}Ge_{17}$**
Literature reported Raman signals [cm^{-1}][122a]	99 146 (main)	104 125 147 164 188 220 (main) 241	93 110 152 (main) 190	85 126 160 199 224 (main) 278

Figure 2.37 depicts the Raman spectrum (Figure 2.37a) and powder X-Ray diffractogram (Figure 2.37b) of a dried residue of K_4Sn_9/*en* (0.05 mmol in 1 mL *en*). It is clearly demonstrated that the $[Sn_9]^{4-}$ clusters remain after solvent removal. No unwanted oxidation takes place as no β-Sn or Sn oxides can be detected. Von Schnering *et al.* reported Raman signals for K_4Sn_9 at 99 (weak) and 146 cm^{-1} (strong), however both reported signals were broad. Slavik *et al*. observed splitting of the signal at 99 cm^{-1} into two separate signals at 87 and 105 cm^{-1} and an additional shoulder signal at 128 cm^{-1} by achieving a higher resolution due to a newer Raman device.[169]

As already reported by Sevov *et al.*,[168] a mixture of K_4Ge_9/*en* (0.01 mmol in 2 mL *en*) and K_4Sn_9/*en* (0.01 mmol in 2 mL *en*) consists of both $[Ge_9]^{4-}$ and $[Sn_9]^{4-}$ clusters. Figure 2.38c shows that both clusters remain even after solvent removal. The Raman spectrum still shows the literature known main signals of $[Ge_9]^{4-}$ (222 cm^{-1}) and $[Sn_9]^{4-}$ (148 cm^{-1}) clusters.[122a] Additional literature reported weaker Raman signals of $[Ge_9]^{4-}$ at 104, 125, 147, 164, 188, and 241 cm^{-1} cannot be observed. The XRD pattern (Figure 2.37d) shows reflections of β-Sn, which indicate that the $[Sn_9]^{4-}$ clusters got partially oxidized (for more details see Figure 2.38a). The main Raman signal of β-Sn is expected to be at 127 cm^{-1}, therefore it could be overlaid by the broad signals in Figure 2.37c. In Figure 2.37e and 2.37f, a Raman spectrum and powder diffractogram of the dried residue of a "$K_4Ge_5Sn_4$"/*en* solution (0.05 mmol in 1 mL *en*) are presented. The Raman signals in Figure 2.37e are in the expected range for tetrel clusters but cannot be assigned to either $[Sn_9]^{4-}$ or $[Ge_9]^{4-}$. Signals of β-Sn would be expected at 127 cm^{-1},[170] while *a*-Ge shows a broad signal at 270 cm^{-1} whereas α-Ge exhibits a sharp signal at 300 cm^{-1}.[139, 156] This immediately suggests the assumption that the Raman spectrum in Figure 2.37e features signals of a mixed Sn/Ge cluster compound. This is in agreement with studies by Sevov and coworkers, who detected heteroatomic $Ge_{9-x}Sn_x$ Zintl ions in solutions of ternary precursors in *en*.[168] Figure 2.37f

shows powder X-ray diffractograms of the precursor "$K_4Ge_5Sn_4$" and the dried residue of "$K_4Ge_5Sn_4$"/*en*. After removing the solvent, the cluster reflections in the range of 10 – 15 °2θ have changed compared to the as-synthesized Zintl precursor phase and β-Sn can be detected as impurity phase, indicating partial oxidation (for more details on the starting phase see Figure 2.38b). It seems that the ternary precursor "$K_4Ge_5Sn_4$" cannot be obtained after solvent removal, even though there are reflections of supposedly mixed Sn/Ge clusters in the diffractogram which cannot be assigned to any literature known phases.

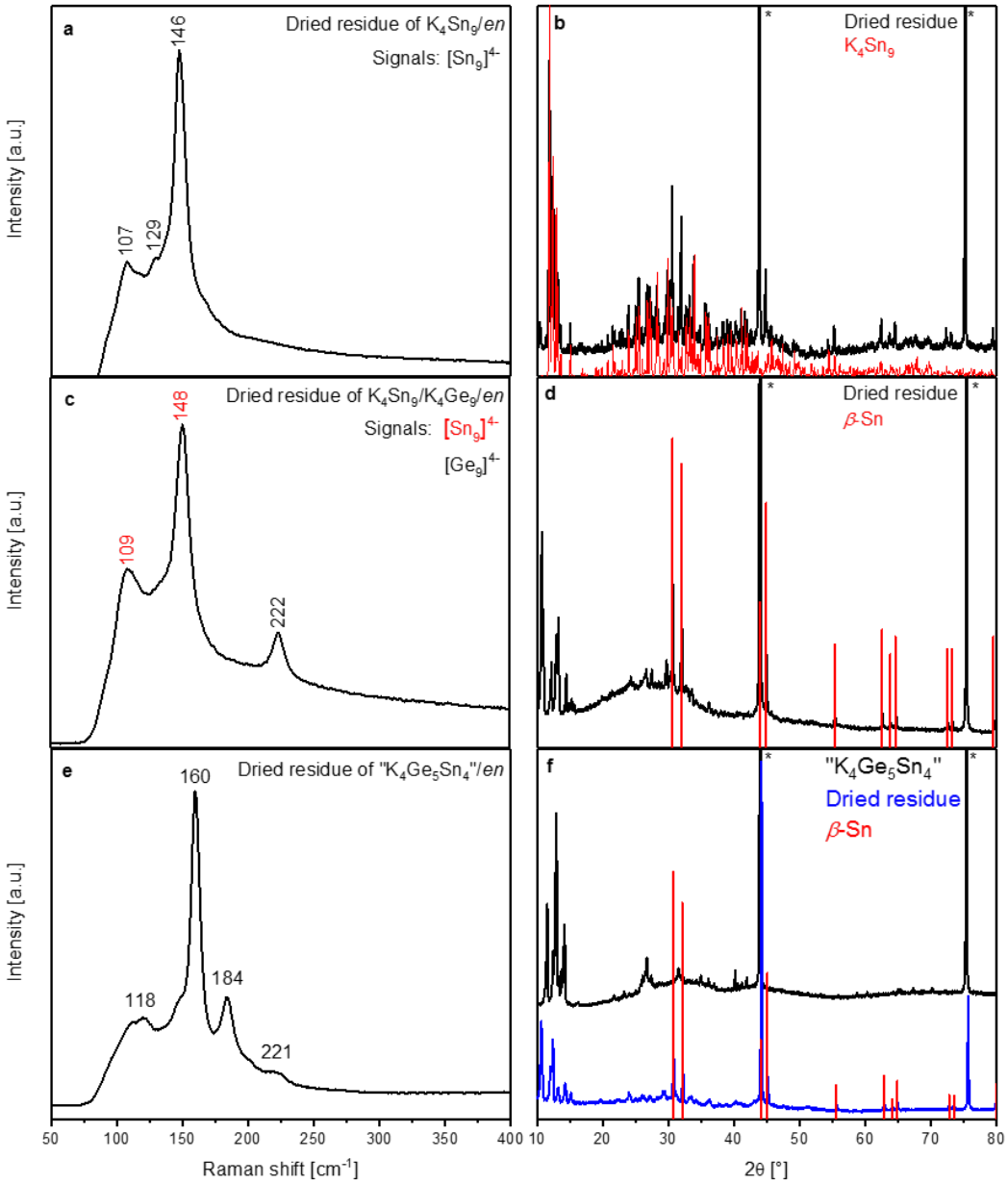

Figure 2.37. Raman spectra (left) and X-ray diffractograms (right) of dried residues. (a) Raman spectrum of the dried residue of a K_4Sn_9/*en* solution, (b) PXRD of the dried residue of a). (c) Raman spectrum of the dried residue of a mixture of K_4Sn_9/*en* and K_4Ge_9/*en*, (d) PXRD of the dried residue of c), (e) Raman spectrum of the dried residue of a "$K_4Ge_5Sn_4$"/*en* solution, (f) PXRD of the dried residue of e). Reflections marked with * can be assigned to diamond used as standard. The calculated diffractrograms are based on single crystal data.[171] Raman literature data is taken from ref.[122a] Diffractograms were measured using Cu-$K_{\alpha1}$ radiation.

Figure 2.38 shows X-ray diffractograms of the dried residues of a mixture of K_4Ge_9/*en* and K_4Sn_9/*en* (Figure 2.38a) and "$K_4Ge_5Sn_4$"/*en* (Figure 2.38b) in more detail. The reflections observed in Figure 2.38a can be compared to the known phase $Rb_4[Ge_9][en]$, but are shifted towards higher angles.[171b] This is expected when substituting Rb with the smaller K, leading to smaller cell parameters. Additionally, reflections can be compared to α-K_4Sn_9, a low temperature phase reported by Slavik *et al*.[169] Calculation of a theoretical pattern was not possible due to the lack of single crystal data. The reflections observed for the dried residue are matching to the ones of α-K_4Sn_9, however they are shifted towards higher angles. This could be explained by the substitution of Sn by Ge in the $[Tt_9]^{4-}$ cluster. The diffractogram also shows three reflections with low intensities (marked with *), which cannot be assigned to any literature known phase. However, this contradicts the observations of Sevov *et al.* who did not find mixed Ge/Sn clusters by performing ESI-MS measurements of mixtures of K_4Ge_9/*en* and K_4Sn_9/*en*.

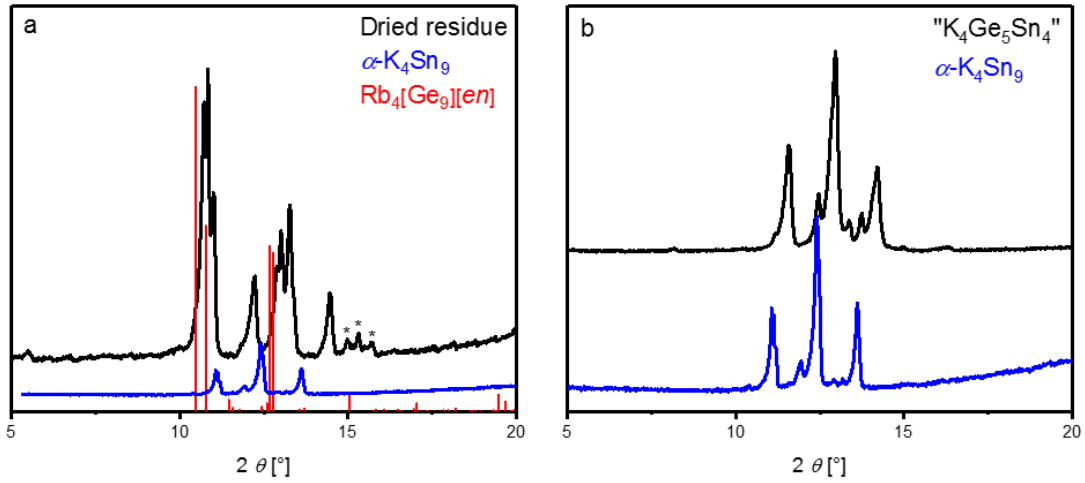

Figure 2.38. X-ray diffractograms of a) a dried residue of a mixture of K_4Sn_9/*en* and K_4Ge_9/*en*, and b) of "$K_4Ge_5Sn_4$". The calculated diffractogram of $Rb_4[Ge_9][en]$ is based on single crystal data.[171b] The diffractogram of α-K_4Sn_9 is taken from ref.[169] Reflections marked with * cannot be assigned to any literature known phase. Diffractograms were measured using Cu-$K_{\alpha1}$ radiation.

Figure 2.38b compares the prepared "$K_4Ge_5Sn_4$" with α-K_4Sn_9. The reflections observed for "$K_4Ge_5Sn_4$" are matching to the ones of α-K_4Sn_9, however they are also shifted towards higher angles, similar to what can be seen in Figure 2.38a. This can again be explained by the substitution of Sn by Ge in the $[Tt_9]^{4-}$ cluster, as it has already been observed by Sevov *et al.* for *en* solutions of mixed ternary phases.

Figure 2.39 presents a Raman spectrum (Figure 2.39a) and a powder X-ray diffractrogram (Figure 2.39b) of a dried residue of a mixture of K_4Sn_9/*dmf* and K_4Ge_9/*dmf* (0.10 mmol in 2 mL *dmf* each).

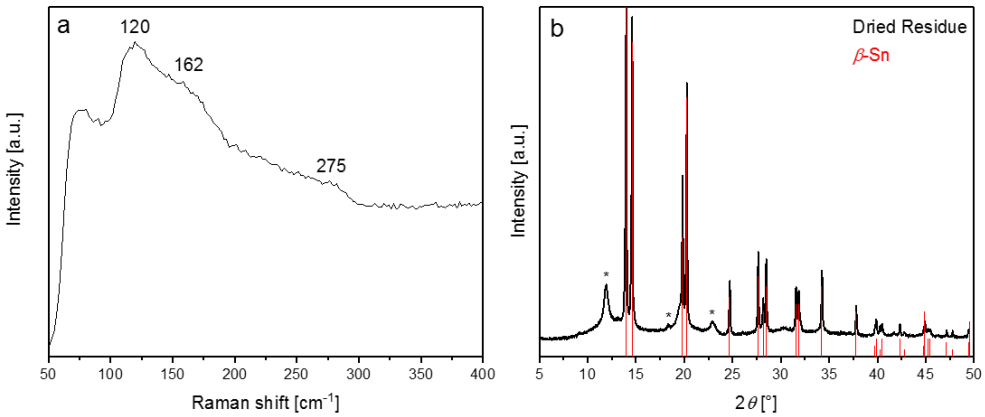

Figure 2.39. a) Raman spectrum of a dried residue of a mixture of K_4Sn_9/*dmf* and K_4Ge_9/*dmf*, b) powder diffractogram of the same residue. The calculated diffractrogram is based on single crystal data.[171a] The diffractrogram was measured using Mo-$K_{\alpha 1}$ radiation.

Sevov *et al.* reported that a mixture of K_4Sn_9/*dmf* and K_4Ge_9/*dmf* contains all possible mixed $Ge_{9-x}Sn_x$ (x = 1 – 9) clusters, contrary to mixed *en* solutions which only contain $[Sn_9]^{x-}$ and $[Ge_9]^{x-}$ species.[168] The Raman spectrum in Figure 2.39a shows very broad signals at 120, 162, and 275 cm^{-1} which could probably be assigned to mixed Sn/Ge compounds. The powder X-ray diffractogram in Figure 2.39b depicts reflections of β-Sn as main phase and additional reflections at 11.95, 18.38, and 22.90 °2θ, which cannot be assigned to known Sn or Ge phases. A mixed Sn/Ge phase has probably been formed as impurity phase. However, due to the fact that thin film preparation was not possible using *dmf* solutions, this route was not further pursued in this work.

2.4.3 Investigations of the obtained thin films

Similar Raman studies have been performed on thin films prepared by utilization of the before mentioned precursor solutions. Figure 2.40 shows Raman spectra of the different obtained inverse opal structured thin films.

In Figure 2.40a the Raman spectrum a thin film obtained from a K_4Sn_9/*en* precursor solution (0.05 mmol in 1 mL *en*) is shown. The spectrum was taken before applying $SnCl_4$ as cluster cross-linker and without performing the final washing steps mentioned in Chapter 2.4.1. Signals at 72, 87, 109, 124, 137, 164, and 203 cm^{-1} can be observed. The main signal at 164 cm^{-1} could possibly be assigned to a clathrate-I phase.[172] As mentioned in Chapter 2.3.2, Grin *et al.* also performed oxidation of M_4Ge_9 (M = Na, K) to Ge with clathrate-II structure and also oxidation of M_4Si_4 (M = Na, K) to clathrate-I compounds of the composition $M_{8-x}Si_{46}$.[155] However, there are only hints towards possible clathrate

formation. Von Schnering *et al.* report Raman signals for $K_{12}Sn_{17}$ at 93, 110, 152, and 190 cm^{-1}, which can also be compared to the signals in Figure 2.40a, even though the signals are shifted.[122a] The measured spectrum in Figure 2.40a most likely shows a mixture of different oxidized Sn species which cannot clearly be assigned to the observed signals. If oxidation would already take place during solvent removal, $[Sn_9]^{4-}$ cluster signals could not have been detected in Figure 2.37a. Taking this observation into account, it can be assumed that the $[Sn_9]^{4-}$ clusters get oxidized by casting onto the PMMA template. Following up with impregnation of the porous film with the cross-linking agent $SnCl_4$, signals at 125 cm^{-1} and 219 cm^{-1} can be observed (Figure 2.40c). The signal at 125 cm^{-1} can be assigned to β-Sn, while the signal at 219 cm^{-1} can be assigned to Sn-Cl bonds, originating from the used $SnCl_4$.[173] After washing the thin film with DMSO and THF in the final step, β-Sn (126 cm^{-1}) can be detected exclusively (Figure 2.40e). Thereby it is demonstrated that a controlled way to synthesize inverse opal structured Sn thin films was found.

Figure 2.40b shows the Raman spectrum of a porous thin film obtained from a mixture of the precursor solutions K_4Sn_9/*en* (0.01 mmol in 2 mL *en*) and K_4Ge_9/*en* (0.01 mmol in 2 mL *en*), before using a cross-linking agent and without applying any additional washing steps. Signals at 127 cm^{-1} and 275 cm^{-1} can be observed. Other than in Figure 2.37c where both $[Sn_9]^{4-}$ and $[Ge_9]^{4-}$ clusters can be seen under these conditions, the spectrum in Figure 2.40b shows β-Sn (127 cm^{-1}) and α-Ge (275 cm^{-1}). Similar to what could be seen for the pure Sn films, an oxidation process takes place when casting the precursor solution onto the substrate coated with the PMMA template. In the case of this mixed Sn/Ge film, other than for a pure Sn film, we directly end up with β-Sn and α-Ge, even without application of a cross-linker. Figure 2.40d shows the film of K_4Sn_9/K_4Ge_9 after impregnation of $GeCl_4$ and the final washing steps. There is still the large signal of α-Ge at 274 cm^{-1}, but it shows a shoulder signal at 245 cm^{-1}, which could also be seen in Figure 2.40b, even though the intensity was much weaker. The signal at 161 cm^{-1} is newly formed. The signals at 161 cm^{-1} and 245 cm^{-1} cannot be assigned to any literature known pure Sn or Ge phases, therefore it can be assumed that a mixed Sn/Ge phase has been formed on the substrate.

Figure 2.40f shows a thin film obtained from a "$K_4Ge_5Sn_4$"/*en* precursor solution, after cluster cross-linking and washing. The signals at 74 cm^{-1}, 116 cm^{-1} and 279 cm^{-1} are very broad and cannot be safely assigned to literature known Sn or Ge phases. Especially the area between 116 and 279 cm^{-1} looks like a very broad signal which covers the expected range of all known Sn and Ge cluster compounds. Preliminary measurements without cross-linking and washing did not result in any detectable signals so it was not possible to keep track of the different stages of the applied synthetic procedure. Though, as stated before in Figure 2.37e and 2.37f a mixed Sn/Ge cluster compound could be obtained after

solvent removal. Additionally, EDX measurements demonstrate the presence of both Sn and Ge, so it can be assumed that the obtained thin film consists of an amorphous mixed Sn/Ge phase.

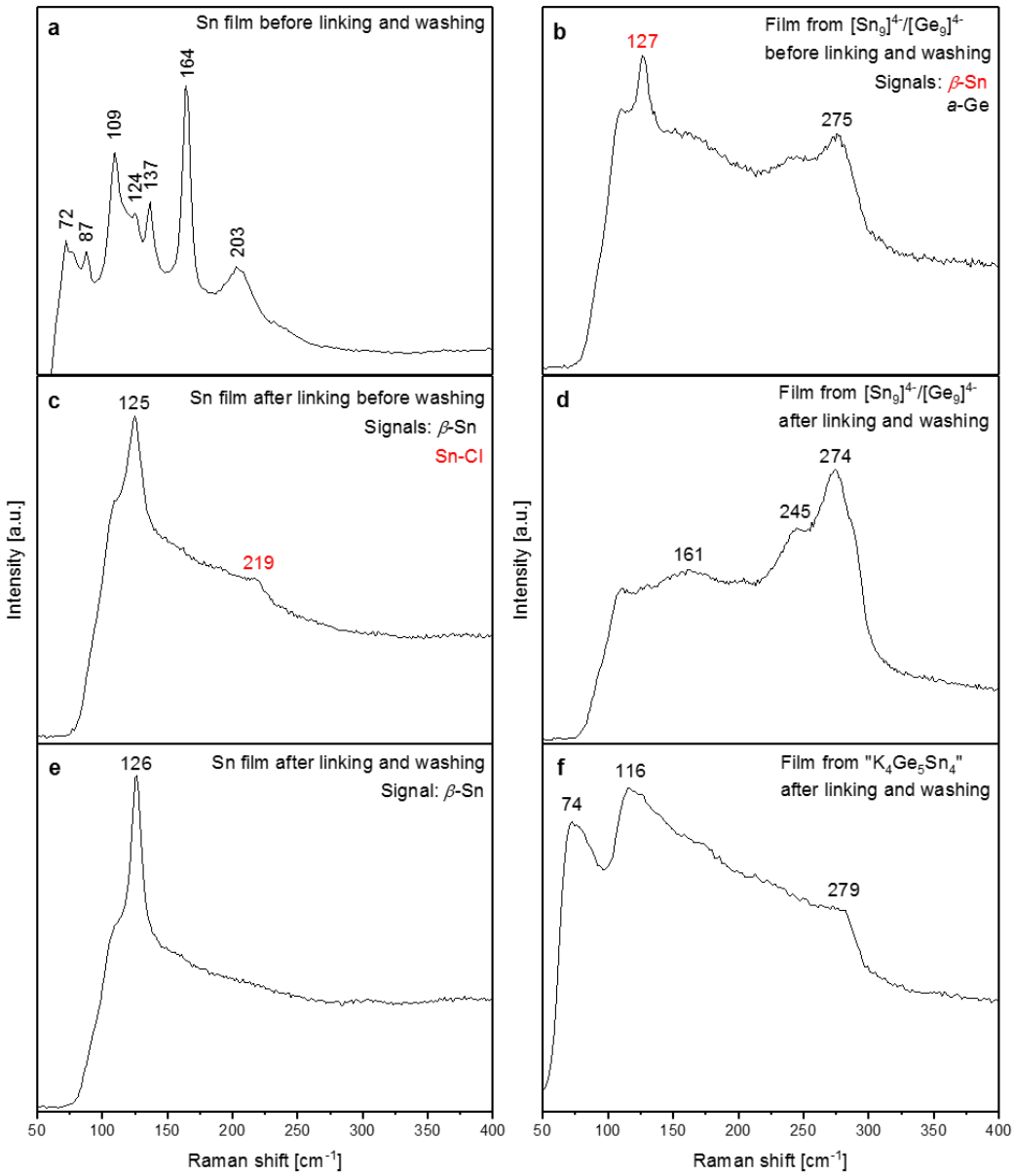

Figure 2.40. Raman spectra of inverse opal structured thin films. (a) Thin film obtained from K_4Sn_9/*en* as precursor solution, before applying $SnCl_4$ and following washing steps. (b) Thin film obtained from a mixture of K_4Sn_9/*en* and K_4Ge_9/*en*, before applying $GeCl_4$ and washing steps. (c) Sn film after cluster cross-linking via $SnCl_4$, without washing steps. (d) Thin film obtained from a mixture of K_4Sn_9/*en* and K_4Ge_9/*en* after using $GeCl_4$ and washing steps. (e) Sn film after cross-linking and washing. (f) Thin film obtained from "$K_4Ge_5Sn_4$"/*en*, after cross-linking and washing.

EDX measurements of the prepared thin films are shown in Table 2.9, the respective spectra are found in the Appendix Chapter 5.1 (Figures 5.8-5.11). The Ge : Sn ratios of all obtained thin films are according to the respective precursor solutions and cross-linking agents.

Table 2.9. Summary of the EDX results of thin films prepared *via* varying precursor/linker compositions.

Zintl Precursor	Linker	Ge/Sn Ratio
K_4Sn_9	$GeCl_4$	1.0/8.1
K_4Ge_9	$SnCl_4$	20/1.0
K_4Ge_9/K_4Sn_9	$GeCl_4$	1.4/1.0
„$K_4Ge_5Sn_4$“	$GeCl_4$	1.5/1.0

To check if the chosen strategy for cluster cross-linking could successfully be applied, two additional thin film variants were prepared. A film starting from a K_4Ge_9/*en* solution (0.06 mmol L^{-1}) was impregnated by $SnCl_4$, while a K_4Sn_9/*en* (0.05 mmol L^{-1}) based film was impregnated by $GeCl_4$. EDX shows that Sn as well as Ge could be found on the resulting thin films, indicating that introduction of the cross-linking agent was successful. Besides that, Raman spectra were recorded of the obtained thin films (Figure 2.41).

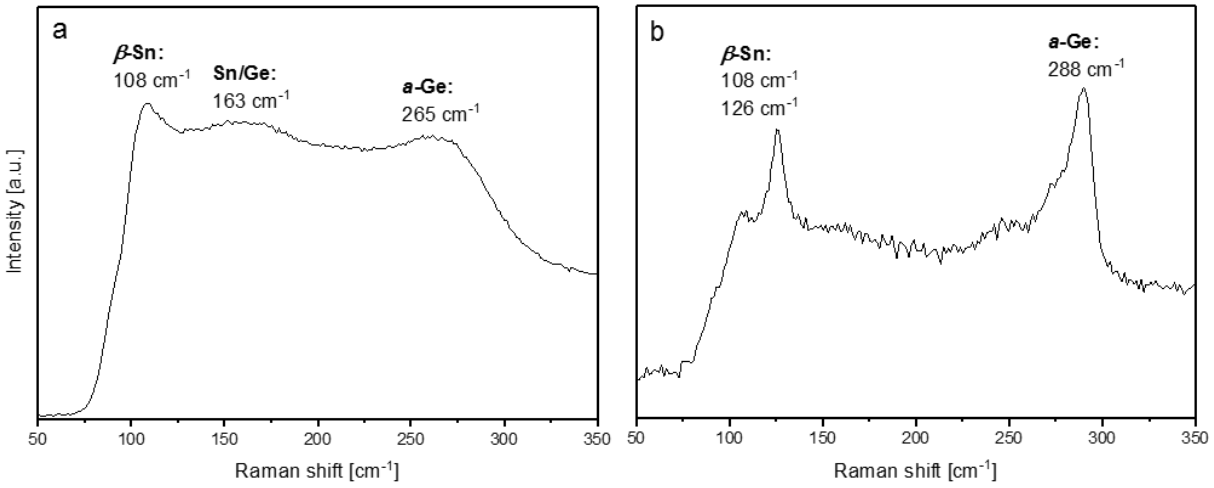

Figure 2.41. Raman spectra of (a) a Ge film linked by $SnCl_4$, and (b) a Sn film linked by $GeCl_4$. Films were prepared on Si substrates.

Both Raman spectra in Figure 2.41 show signals of *α*-Ge and *β*-Sn, further proving that cluster cross-linking was successfully performed by impregnation with the chosen linking agents.

Additionally, X-ray photoelectron spectra have been measured for inverse opal structured thin films, prepared on Si substrates using precursor solutions with compositions identical to the ones used in Figure 2.40. All samples have been cross-linked and washed as described in Chapter 2.4.1. To avoid air exposure, the samples were prepared in a glovebox under argon atmosphere and transferred into the vacuum chamber of the XPS device using a sealed transfer vessel. Prior to the measurements, the samples have been sputtered with Ar^+ ions for 90 min. Spectra were recorded for Sn $3d_{5/2}$ and Ge $2p_{3/2}$. The resulting spectra are shown in Figure 2.42.

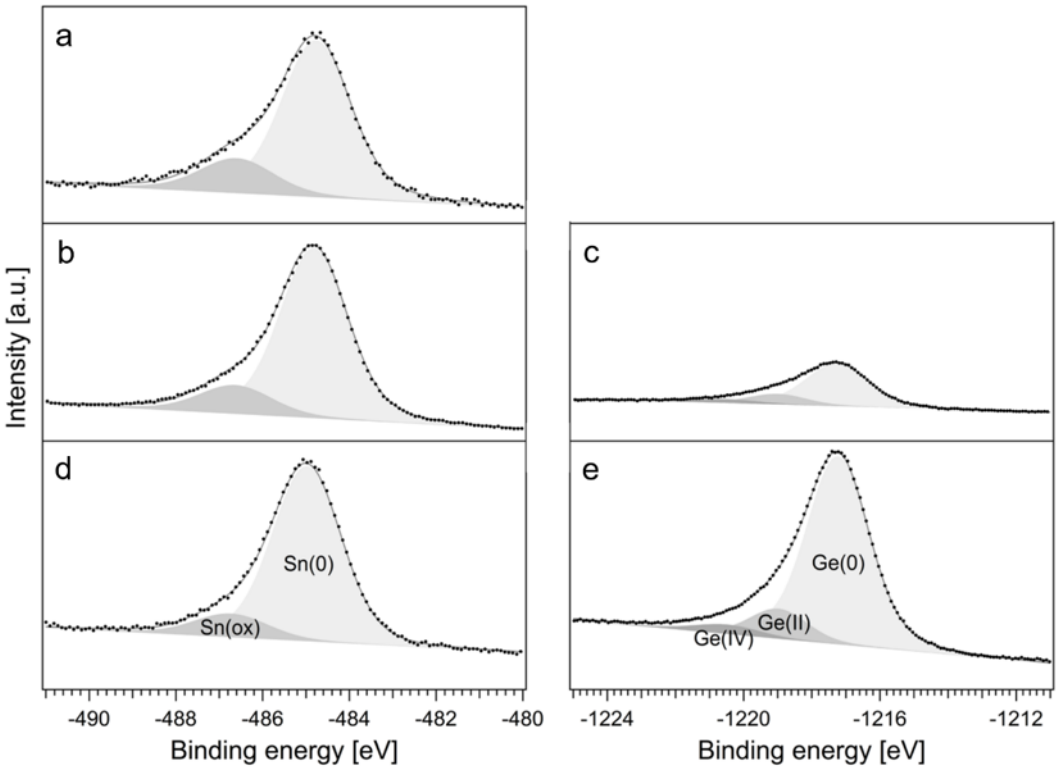

Figure 2.42. XPS spectra of measured thin films on Si substrates. Sn $3d_{5/2}$ on the left, Ge $2p_{3/2}$ on the right. (a) Thin film obtained from K_4Sn_9/*en* as precursor solution (see Figure 2.41e). (b) and (c) Thin film obtained from a mixture of K_4Sn_9/*en* and K_4Ge_9/*en* (see Figure 2.41d). (d) and (e) Thin film obtained from "$K_4Ge_5Sn_4$"/*en* (see Figure 2.41f).

The results of the XPS measurements are in good agreement with what has been proposed before. Each thin film sample mainly shows Sn(0) or Ge(0), only a small amount of oxides can be detected (for exact values, see Table 2.10). The fact that both variations of mixed Sn/Ge films mainly consist of non-oxidized species which are, according to the Raman results, not β-Sn and α-Ge supports the assumption that mixed Sn/Ge phases have been formed on the substrates.

Table 2.10. Quantification of the different oxidation states of Sn and Ge for the measured samples.

	K_4Sn_9	**K_4Ge_9/K_4Sn_9**	**„$K_4Ge_5Sn_4$“**
Sn(0)	80 ± 3	84 ± 3	87 ± 4
Sn(ox)	20 ± 4	16 ± 5	13 ± 5
Ge(0)		75 ± 6	83 ± 9
Ge(II)		17 ± 7	12 ± 7
Ge(IV)		8 ± 2	5 ± 2

2.4.4 Electrochemical measurements

Sn and mixed Sn/Ge thin films with inverse opal structure were prepared with the scope of building Li ion batteries, where the tetrel films should act as anodes, analogous to the Ge electrodes discussed in Chapter 2.2.3. Figure 2.43 shows specific capacities and coulombic efficiencies for pure Sn and mixed Sn/Ge electrodes over extended cycling. Details on the cycling procedures can be found in Chapter 4.2.10, while details on electrode preparation are given in Chapter 4.3.11. Loading determination and solution compositions are described in Chapter 4.1.6.

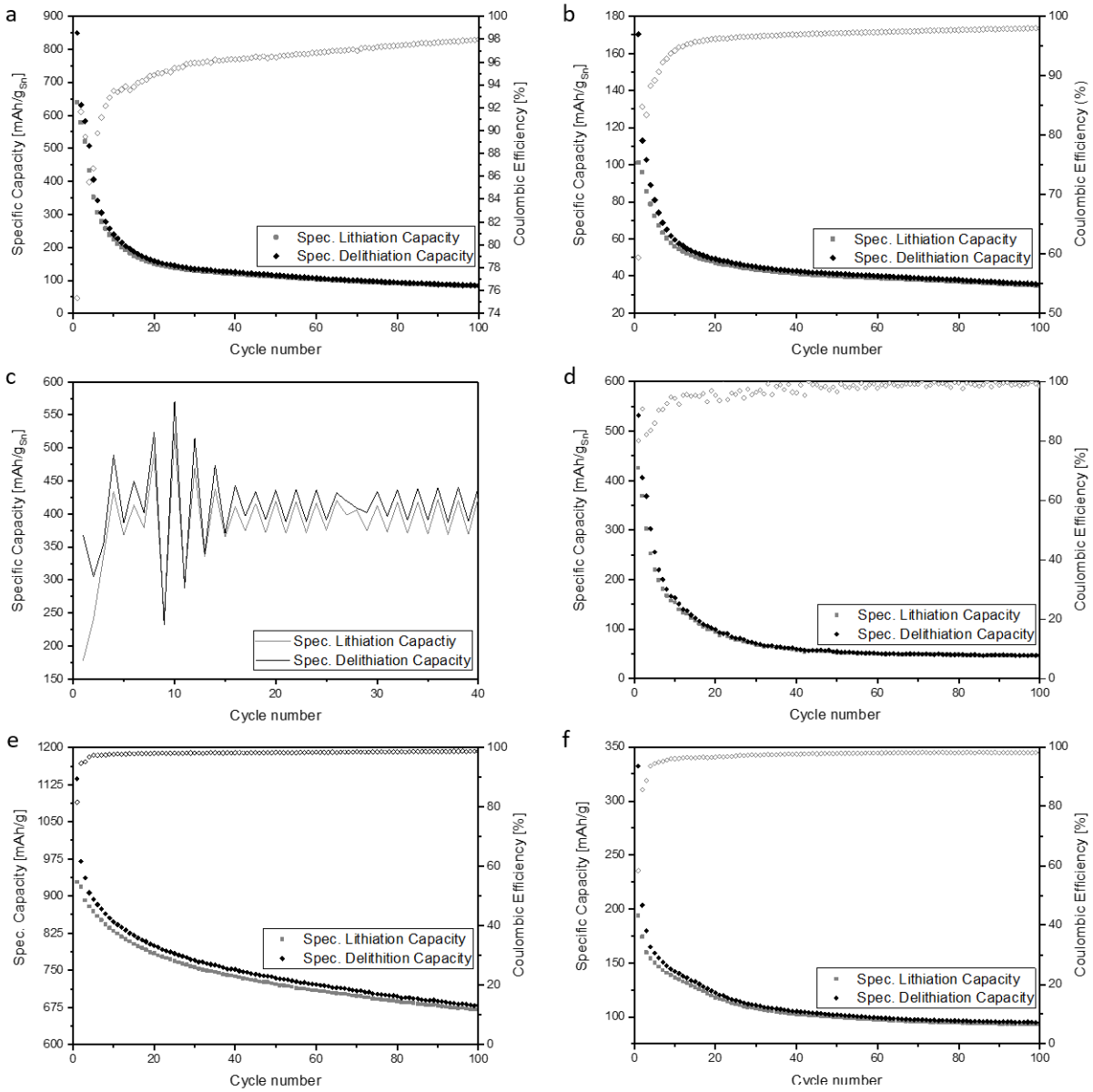

Figure 2.43. Specific capacities over extended cycling at a rate of 0.2*C* with the first two cycles at 0.1*C* of Sn and Sn/Ge thin films. a) Unstructured film prepared from K_4Sn_9/*en* without using a PMMA template. b) Inverse opal structured thin film prepared from K_4Sn_9/*en*. c) Film prepared from K_4Sn_9/*en* using an ink as template replacer. d) Film prepared from an ink including the $[Sn_9]^{4-}$ clusters. e) Mixed film prepared from "$K_4Ge_5Sn_4$" using a PMMA template. f) Mixed film prepared from K_4Sn_9/*en* and K_4Ge_9/*en* solutions using a PMMA template.

For reasons of clarity, Table 2.11 gives an overview of the measured electrodes.

Table 2.11. Overview of measured electrodes.

Film	Figure	Loading	Number
Unstructured Sn (K_4Sn_9/*en* + $SnCl_4$, no PMMA used)	2.43a	311 µg	1
Inverse opal structured Sn (K_4Sn_9/*en* + $SnCl_4$, PMMA used)	2.43b	510 µg	2
Sn on ink (K_4Sn_9/*en* casted onto ink)	2.43c	355 µg	3
Sn/Ink (K_4Sn_9 mixed together with ink)	2.43d	3.11 mg	4
Sn/Ge film ("$K_4Ge_5Sn_4$"/*en* + $GeCl_4$, PMMA used)	2.43e	637 µg	5
Sn/Ge film (K_4Sn_9/*en* + K_4Ge_9/*en* + $GeCl_4$, PMMA used)	2.43f	654 µg	6

Figure 2.43a shows specific capacities and coulombic efficiencies of electrode **1**. The Zintl precursor solution (122 mg/0.10 mmol K_4Sn_9 in 2 mL *en*) was directly drop-casted onto a Cu substrate. Drying, cross-linking (using ($SnCl_4$), and washing steps were performed following the standard procedure described in Chapter 2.4.1. The presented electrode exhibits an initial delithiation capacity of 849 mAh g^{-1} and an initial lithiation capacity of 640 mAh g^{-1}, resulting in a coulombic efficiency of 75% for the first cycle. The initial capacities are lower than the theoretical gravimetric capacity of 991 mAh g^{-1} for $Li_{4.4}Sn$ which is most likely due to connectivity issues of the inhomogeneous electrode surface. However, the obtained initial capacity values are somewhat close to the theoretical values, indicating that indeed Sn and not any unwanted species were cycled in this experiment. After only 20 cycles though, the delithiation capacity dropped down to 159 mAh g^{-1} and the lithiation capacity to 151 mAh g^{-1}. This rapid decrease in capacity retention was expected and can be explained by the massive volume changes alloy-based anodes undergo during electrochemical cycling. These volume changes lead to a loss of contact and therefore to drastic capacity losses during cycling.

Preparation of inverse opal structured electrodes, as described in this work, is one possible way to overcome the issue of volume changes. Figure 2.43b presents specific capacities and coulombic efficiencies for the 100 charge-discharge cycles of electrode **2** (prepared with 122 mg/0.10 mmol K_4Sn_9 in 2 mL *en*). Similar to what has been shown for Ge electrodes in Chapter 2.2.3, the resulting honeycomb structure should provide sufficient flexibility and mechanical stability to act as a buffer for the inevitable volume changes during cycling. Electrode **2** shows an initial delithiation capacity of 170 mAh g^{-1} and an initial lithiation capacity of 101 mAh g^{-1}, achieving a coulombic efficiency of 59% for the first cycle. While the coulombic efficiency goes up after SEI formation and reaches more than 96% after 20 cycles, the capacities decrease to 49.1 mAh g^{-1} and 47.2 mAh g^{-1} after 20 cycles and 35.6 mAh g^{-1} and 34.8 mAh g^{-1} after 100 cycles. These values are much lower than what could be expected for Sn as electrode material and even lower than the capacities of the electrode **1**. One

possible explanation for these results could be an insulating layer of residual PMMA placed between the Cu substrate and the Sn thin film. Other than for Ge films, the PMMA substrate cannot be thermally removed due to the low melting point of Sn. The solvent assisted template removal might not be sufficient to completely remove the PMMA template from deeper layers within the Sn film. That could result in cycling residual species of the template rather than the actual active material Sn, leading to much lower capacities.

Figure 2.43c shows capacities of an electrode prepared from a K_4Sn_9/*en* solution (122 mg/0.10 mmol in 2 mL *en*), using a conventional ink containing C65, polyvinylidene fluoride, and N-methyl-2-pyrrolidone (NMP) as replacer for the PMMA template (electrode **3**). For details on ink preparation see Chapter 4.3.10. The Zintl precursor solution was drop-casted on the ink coated Cu substrate. The obtained capacities for electrode **3** show a rather unorthodox behavior. This behavior is most likely caused by the aforementioned volume changes this electrode undergoes during cycling. Due to these volume changes, the electrode seems to alternatingly loose and regain contact during cycling, resulting in the capacities increasing and decreasing.

Electrode **4**, which capacity is shown in Figure 2.43d, was also prepared including an ink, but here the ink already contained the $[Sn_9]^{4-}$ clusters (see Chapter 4.1.6, Table 4.2). An initial delithiation capacity of 532 mAh g^{-1} and an initial lithiation capacity of 426 mAh g^{-1} was achieved, resulting in a coulombic efficiency of 80% after the first cycle. After 20 cycles, 98.8 mAh g^{-1} and 94.4 mAh g^{-1} with a coulombic efficiency of 95% were retained. After 100 charge-discharge cycles, the electrode showed capacities of 46.9 mAh g^{-1} for delithiation and 46.2 mAh g^{-1} for lithiation. The initial capacity values are significantly lower than for $Li_{4.4}Sn$ but much higher than for electrode **2**. Comparing the capacities of the fourth cycle, where SEI formation should mostly be completed, with the ones obtained after 20 cycles, a capacity retention of only 33% was achieved. This capacity retention is still very low and indicates significant contact losses due to volume changes during cycling.

Figure 2.43e shows the capacities of an inverse opal structured electrode prepared from a $K_4Ge_5Sn_4$/*en* solution, using $GeCl_4$ as linker (electrode **5**). A theoretical gravimetric capacity of 1229 mAh g^{-1} was calculated for this material composition. The electrode shows an initial delithiation capacity of 1137 mAh g^{-1} and an initial lithiation capacity of 929 mAh g^{-1}, resulting in a coulombic efficiency of 82% after the first cycle. The capacities decrease to 800 mAh g^{-1} for delithiation and 785 mAh g^{-1} for lithiation after 20 cycles, achieving a coulombic efficiency of 98%. After 100 cycles, 679 mAh g^{-1} and 671 mAh g^{-1} could be obtained for delithiation and lithiation, with a coulombic efficiency of 99%. These capacities translate to a capacity retention of 88% after 20 cycles and 75% after 100 cycles, when compared to the capacities after the fourth cycle (907 mAh g^{-1} for delithiation and 879 mAh g^{-1} for lithiation). The initial capacities are close to the calculated theoretical value of this mixed Sn/Ge

electrode material. The capacity retentions are very similar to the ones obtained for pure Ge electrodes shown in Chapter 2.2.3.

Figure 2.43f shows capacities of electrode **6**. The theoretical gravimetric capacity for this material composition was calculated to be 1209 mAh g^{-1}. The initial delithiation capacity of this electrode was 332 mAh g^{-1}, the initial lithiation capacity 194 mAh g^{-1}. These capacities result in a coulombic efficiency of 58% after the first cycle. After 20 cycles, capacities of 122 mAh g^{-1} for delithiation and 118 mAh g^{-1} for lithiation were obtained, with a coulombic efficiency of 97%. After 100 cycles, the electrode delivered a delithiation capacity of 94.9 mAh g^{-1} and a lithiation capacity of 93.1 mAh g^{-1}, resulting in a coulombic efficiency of 98%. The initial capacities as well as the capacities obtained after cycling are much lower than what could be theoretically expected for this material composition. It seems that the electrode shown here had similar connectivity issues as electrode **2**. Its electrochemical performance was much worse than the one of electrode **5** and also much worse than the performance of pure Ge electrodes presented in Chapter 2.2.3.

Literature data for Sn and Sn/Ge electrodes can be found in Table 1.3 in the Introduction Chapter 1.3.3. In the following, the here measured electrodes will be compared in more detail to the most relevant literature reports.

Zhang *et al*. tested pure Sn film electrodes prepared by thermal evaporation which exhibited an initial delithiation capacity of 756 mAh g^{-1} and a low capacity retention of only 158 mAh g^{-1} after 30 cycles.[91] Their material morphology is comparable to electrode **1** and their cycling results match very well with the capacities measured for electrode **1** in this work.

Wang *et al.* used 3D porous Sn thin films as anodes in LIBs. Other than the inverse opal structured electrode **2**, they achieved a random porous structure but featuring much higher capacities. An initial lithiation capacity of 676 mAh g^{-1} was obtained and after 100 cycles, a capacity retention of 46% was achieved.[93] Electrode **2** in this work can hardly be compared to literature data since, as already mentioned before, almost no capacity could be observed.

Electrode **4** has to be compared to Sn-C composite materials. They are summarized in Table 1.3 in the Introduction Chapter 1.3.3. All electrodes shown in Table 1.3 achieve much higher initial capacities and capacity retention than electrode **4**. As already discussed, significant contact losses during cycling could be responsible for the comparably bad cycling performance of electrode **4**. The low initial capacity of electrode **4** also hints towards contacting issues.

Electrodes **5** and **6** are mixed Sn/Ge electrodes and therefore have to be compared to mixed Sn/Ge systems in the literature. As they are not already mentioned in the Introduction Chapter 1, they will be discussed in more detail in the following.

Jiang *et al.* synthesized and cycled Sn-Ge composite powder. Starting from ethanolic solutions of $SnCl_2$ and $GeCl_4$ they precipitated $SnGeO_3$, which was then reduced to the desired Sn-Ge powder by H_2-flow at 450 °C for 4 h. They achieved initial capacities of 625 mAh g^{-1} and 590 mAh g^{-1} with a coulombic efficiency of 94%. After 20 cycles, a capacity retention of 88% and a coulombic efficiency of 96% were obtained.[174] The initial capacity values are significantly lower than the ones of electrode **5** while the capacity retention was identical to the one of the here presented electrode. Cho *et al.* synthesized a nanocomposite consisting of amorphous Ge and Sn nanoparticles by thermal annealing of a mixture of butyl-capped Ge gels and $SnP_{0.94}$ nanoparticles at 400 °C *in vacuo*. They measured initial capacities of 1638 and 1078 mAh g^{-1}. The large first delithiation capacity of 1638 mAh g^{-1} was caused by side reactions with the electrolyte which happened due to the large active surface area. Also oxide formation was considered as one of the reasons for the large irreversible capacity. After 50 cycles, a capacity retention of 66% was achieved. They also studied a mixture of physically blended Sn and Ge nanoparticles. For this mixture they could only obtain 28% of the first lithiation capacity after 22 cycles. Cho *et al.* assumed that Sn particles within a cluster became electrically isolated and therefore inactive as lithium metal alloy material, while the Ge phase still provided conduction paths.[175] These observations could be transferable to electrode **6** which shows better performance than electrode **2** but much worse cycling performance than pure Ge electrodes presented in Chapter 2.2.3. W. I. Cho *et al.* prepared $Ge_{1-x}Sn_x$ nanocrystals by a gas-phase laser photolysis reaction of $Ge(CH_3)_4$ and $Sn(CH_3)_4$. A $Ge_{0.95}Sn_{0.05}$ electrode showed initial capacities of 1470 and 990 mAh g^{-1}, resulting in an initial coulombic efficiency of 67%. A reversible capacity of 1010 mAh g^{-1} could be achieved after 50 cycles for $Ge_{0.95}Sn_{0.05}$. Increasing the Sn amount to 10% lead to a reversible capacity of 815 mAh g^{-1} after 50 cycles. Coulombic efficiencies of 97% were achieved in both cases.[176] However, the theoretical gravimetric capacities were calculated based on the capacity of $Li_{22}Ge_5$, which lead to an overestimation of the measured capacities. Referring to the theoretical capacity of $Li_{15}Ge_4$ (1385 mAh g^{-1}), initial capacities of 1257 and 846 mAh g^{-1} and a reversible capacity of 863 mAh g^{-1} were obtained for $Ge_{0.95}Sn_{0.05}$, while $Ge_{0.9}Sn_{0.1}$ showed a reversible capacity of 697 mAh g^{-1}. These capacity values are very close to the ones achieved for electrode **5**.

Conclusively it can be said that the electrodes presented in Figure 2.43 are outperformed by literature reported electrode systems based on Sn-C composite materials. However, observations made for pure Sn electrodes in this work can be validated when comparing to literature. Furthermore, electrode **5** can compete with previously reported mixed Sn/Ge electrodes for lithium ion batteries.

2.5 Tin/Selenium, Tin/Tellurium and Tin/Phosphorus Mixed Films

The following chapter describes synthetic strategies to generate both group IV-VI semiconductors consisting of Sn/Se and Sn/Te and mixed Sn/P films as well as spectroscopic methods performed to characterize the obtained thin films and reaction products. Analytical methods applied to the samples in this chapter are summarized in Table 2.12.

Table 2.12. Analytic methods applied to Sn/Se, Sn/Te, and Sn/P samples.

Sample	REM	EDX	Raman	XRD
$[Sn_9]^{4-}$/*en* + Se/*en* film	x	x	x	-
$[Sn_9]^{4-}$/*en* + Se/*en* dried residue	-	x	x	x
K/Se/*en* + $[Sn_9]^{4-}$/*en* dried residue	-	x	x	-
Se/$[Sn_9]^{4-}$/*en* film	-	x	x	-
Se/$[Sn_9]^{4-}$/*en* dried residue	-	x	x	x
Sn/Te film	x	x	x	-
Sn/Te dried residue	-	x	x	x
K_3P_7/K_4Sn_9/*en* film	x	x	x	-
K_3P_7/K_4Sn_9/*en* dried residue	-	x	x	-

2.5.1 Sn/Se thin films

With the scope to create group IV-VI semiconductors with interesting properties for e.g. optical components, the preparation of mixed Sn/Se films with inverse opal structure was investigated. Several different synthetic approaches were performed, they are described in the following.

Two-step strategy involving Se/*en* and K_4Sn_9/*en*

In the first step, a solution of Se in *en* was prepared, which was then dropwise added to a solution of K_4Sn_9/*en*. Se was directly dissolved in *en* by stirring at room temperature for 24 h, resulting in a clear yellow-green solution, shown in Figure 2.44a. Concentrations of up to 0.50 mmol Se in 1 mL *en* could be achieved this way. Dropwise addition of Se/*en* to K_4Sn_9/*en* resulted in red solutions and a black precipitate. After filtration, clear, red solutions were obtained which were then used for thin film preparation. Details about the preparation of the solutions can be found in Chapter 4.3.9. An obtained film, prior to any additional washing steps, can be seen in Figure 2.44b. The concentration of the solution in Figure 2.44a was 7.90 mg/0.10 mmol Se in 1 mL *en*, the concentrations in Figure 2.44b were 31.6 mg/0.4 mmol Se in 1 mL *en* and 244 mg/0.20 mmol K_4Sn_9 in 3 mL *en*.

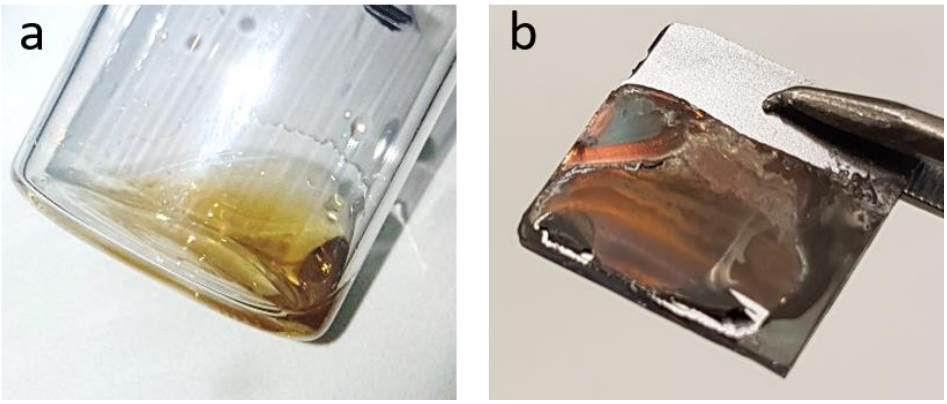

Figure 2.44. Photos of a Se/*en* solution (a) and an unwashed thin film prepared on a Si substrate from a mixture of Se/*en* and K_4Sn_9/*en* (Sn : Se 4.5:1) (b).

SEM images of the thin film in Figure 2.44b are shown in Figure 2.45. Temperature treatment and washing steps were applied to the film, according to the standard procedure for Sn films described in Chapter 2.4.1. No cross-linking agent such as $SnCl_4$ was used. As depicted in the SEM images, the desired inverse opal structure could not be obtained. It seems that the film still consists of encapsulated PMMA spheres which could not be removed by washing due to the fact that they seem to be covered with shells of material. Figure 2.45b also shows several smaller grains on the film surface. The honeycomb structure which has been reported for Ge, Sn, and Sn/Ge films cannot be observed. EDX measurements of the thin film only show Sn, but no Se (see Appendix Chapter 5.1, Figure 5.12). This leads to the assumption that Se did not get introduced into the Sn film and probably got washed out by the washing solvents. Another possibility would be that Se was not present in the mixed, red K_4Sn_9/Se/*en* solutions but rather in the before mentioned black precipitate.

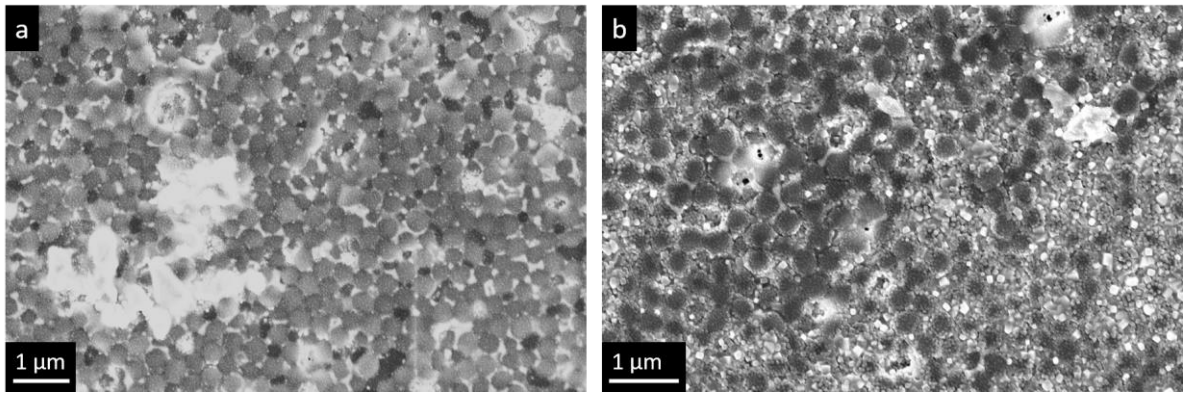

Figure 2.45. SEM images of a thin film obtained from a mixture of Se/*en* and K_4Sn_9/*en* (Sn : Se 4.5:1). a) 20000x magnification, b) 25000x magnification.

Raman measurements of a thin film prepared from a mixture of a Se/*en* and a K_4Sn_9/*en* solution were conducted to examine if any Se can be observed by Raman analysis (Figure 2.46). The solution

compositions for thin film preparation were 31.6 mg/0.4 mmol Se in 1 mL *en* and 54.4 mg/0.04 mmol K_4Sn_9 in 1 mL *en*. The spectrum of the resulting thin film only shows one signal at 125 cm^{-1} which can be assigned to β-Sn. No other signals can be observed, matching the results of the EDX measurements described before (see Appendix Chapter 5.1, Figure 5.12), clearly indicating that no Se is present in the film.

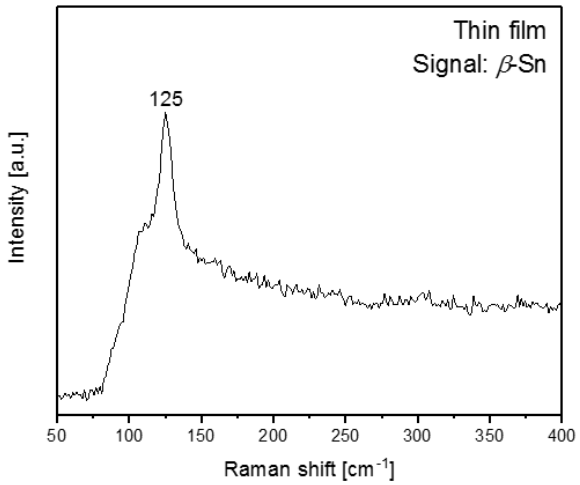

Figure 2.46. Raman spectrum of a thin film prepared from a mixture of Se/en and K_4Sn_9/en (Sn : Se 4.5:1), after temperature treatment and washing.

To get insights of about the composition of the described red mixed Se/K_4Sn_9/*en* solution, Raman and XRD studies of dried residues were performed. Additionally, due to the lack of literature data, Raman spectra of pure Se were measured at different laser wavelengths (λ = 532 nm and λ = 785 nm). The measured spectra and diffractogram are presented in Figure 2.47. The spectrum in Figure 2.47a shows a dried residue of a mixture of Se/*en* and K_4Sn_9/*en* (31.6 mg/0.4 mmol Se in 1 mL *en* and 244 mg/0.20 mmol K_4Sn_9 in 3 mL *en*). Prior to the measurement, the red solution was filtrated and dried at room temperature under vacuum. The spectrum shows signals at 107 and 151 cm^{-1}, the characteristic signals of $[Sn_9]^{x-}$ clusters. No additional Se signals can be detected as the spectrum is identical to the one obtained from a residue of a pure K_4Sn_9/*en* solution. The term $[Sn_9]^{x-}$ is chosen since it cannot be distinguished between $[Sn_9]^{4-}$ and $[Sn_9]^{3-}$ and partial oxidation may have happened due to the addition of the Se/*en* solution. Since no Se can be seen in the spectrum of the dried residue, it can be assumed that Se is not present in the mixture of Se/*en* and K_4Sn_9/*en* solutions and most likely can be found in the precipitate which formed during dropwise addition of Se/*en* to K_4Sn_9/*en*. Note that the Raman spectrum of the film in Figure 2.46 was measured at a laser wavelength of λ = 785 nm where a sharp Se signal with high intensity at 235 cm^{-1} (Figure 2.47d) should also be detected in case of Se presence in the film and therefore in the mixed precursor solution.

A powder X-ray diffractogram of the same dried residue as in Figure 2.47a was measured and compared with literature data to check for Se in the residue of the mixture. The obtained diffractrogram is shown in Figure 2.47b.

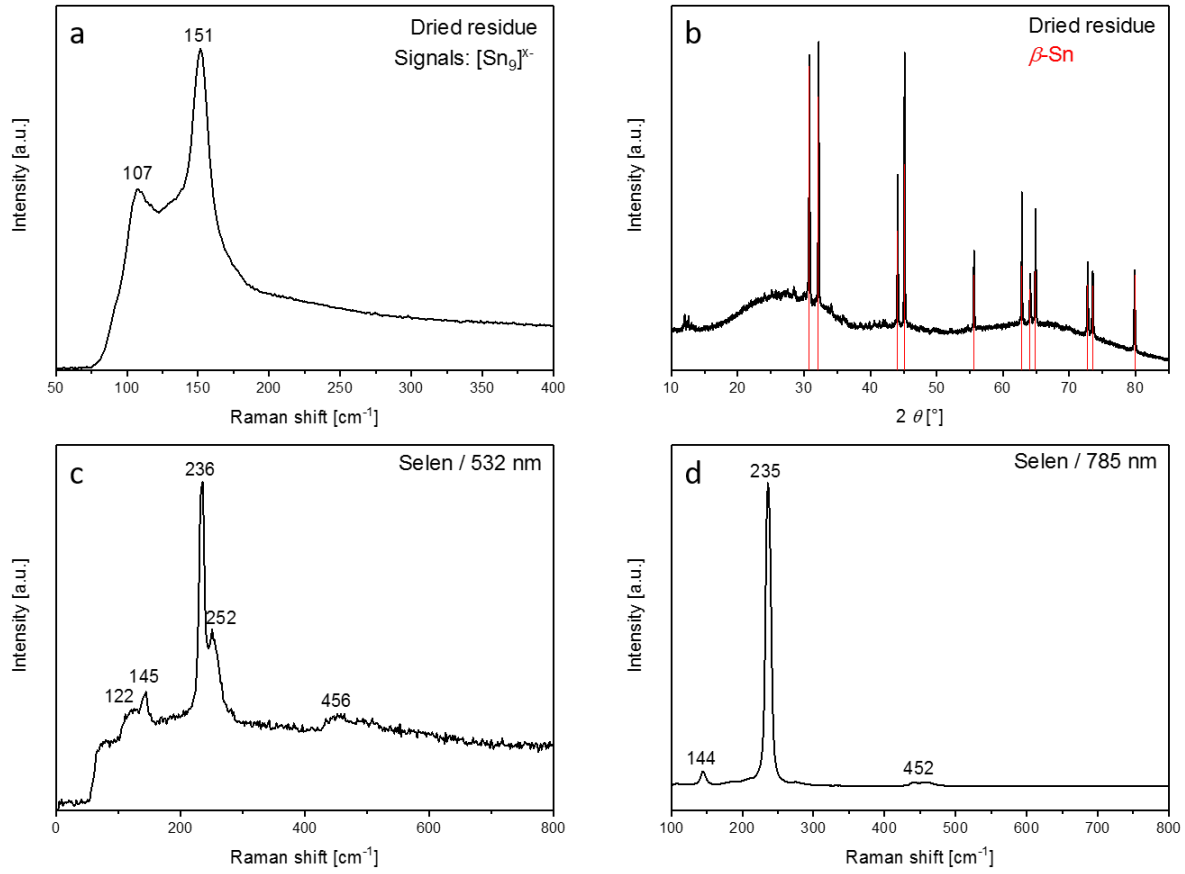

Figure 2.47. a) Raman spectrum of a dried residue of a mixture of Se/*en* and K_4Sn_9/*en* (Sn : Se 4.5:1), b) diffractogram of the same residue, c) Raman spectrum of a pure Se sample measured at λ = 532 nm, d) Raman spectrum of a pure Se sample measured at λ = 785 nm. The calculated diffractrogram is based on single crystal data.[171a] The diffractogram was measured using Mo-$K_{\alpha 1}$ radiation.

The diffractogram mostly shows reflections of β-Sn and a large amorphous background. The characteristic main reflections of the $[Sn_9]^{x-}$ clusters can be seen in the range between 10 – 15 °2θ. The fact that, other than in the Raman spectrum in Figure 2.47a, mainly β-Sn and not cluster reflections can be seen could be due to the much higher intensity of $[Sn_9]^{x-}$ cluster signals in Raman spectroscopy compared to signals of β-Sn. The cluster signals in Figure 2.47a overlap with the signals of β-Sn, so that the latter cannot be seen in the spectrum. Again, no Se can be seen in the residue.

The obtained results clearly show that this strategy to prepare mixed Sn/Se thin films was not successful. It was not possible to create the desired inverse opal structure and Se could not be found on the films or in the dried residues of the mixed precursor solutions, rendering this method not practically applicable to prepare mixed Sn/Se films.

Two-step strategy involving K/Se/*en* and K_4Sn_9/*en*

In order to achieve higher concentrations of Se in *en*, a strategy where K and Se were placed together in a glass flask followed by addition of *en* was investigated. A molar ratio of K : Se of 1 : 10 was chosen (10 mg/0.25 mmol K and 197 mg/2.50 mmol Se in 10 mL *en*). The mixture was stirred for 3 d at room temperature. After filtration, a dark green solution was obtained. 2 mL of this solution were dropwise added to a K_4Sn_9/*en* solution (61.2 mg/0.05 mmol in 1 mL *en*), leading to immediate precipitation of a dark solid, most likely elemental Sn. Filtration of the remaining solution yielded a clear, amber-colored solution. More details about the preparation of the solutions can be found in Chapter 4.3.9. The solution was filtrated and Raman spectroscopy was performed on the dried residue of the obtained solution. The spectrum is shown in Figure 2.48.

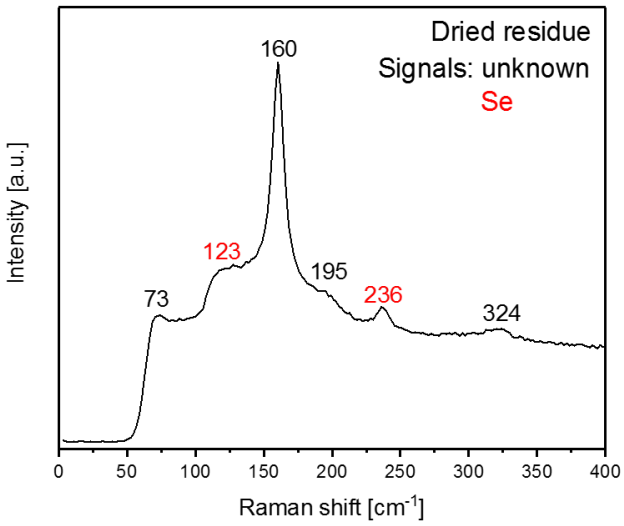

Figure 2.48. Raman spectrum of a dried residue of a mixture of K/Se/*en* and K_4Sn_9/*en*, with a molar K : Se ratio of 1 : 10 and a Sn : Se ratio of 9:10.

The Raman spectrum shows signals of Se (see Figure 2.47c) and signals at 73, 160, 195, and 324 cm^{-1}. The main signal at 160 cm^{-1} could possibly be assigned to Sn in the clathrate-I structure, comparably to what has been observed in Figure 2.40a. However, the other reported signals for the clathrate-I structure cannot be observed. The signals cannot be clearly assigned to any literature known Sn species. No $[Sn_9]^{4-}$ cluster signals can be seen anymore, which leads to the assumption that partial oxidation of the $[Sn_9]^{4-}$ clusters took place.

EDX measurements of the dried residue of the filtrated solution were also performed. The recorded spectrum can be found in the Appendix Chapter 5.1, Figure 5.13. K, Sn, and Se could be found in the residue, in a molar ratio of Sn : Se 1:2.7, which is higher than the starting ratio. This goes hand in hand with the assumption that the dark precipitate, which is formed by adding the K/Se/*en* solution to the K_4Sn_9/*en* solution, consists of elemental Sn.

After successfully detecting Se in the residue of a mixed K/Se/K_4Sn_9/*en* solution, thin film preparation with identical solution composition was performed, according to the standard procedure for Sn films described in Chapter 2.4.1. However, no cross-linker was used. The resulting films were extremely thin and washing was not possible, the films completely dissolved in the washing solvents, leaving slightly yellow colored washing solvents. Due to this issue, template removal could not be performed. EDX measurements were carried out on unwashed films, a recorded spectrum can be found in the Appendix Chapter 5.1, Figure 5.14. Both Sn and Se were found on the thin film, with a molar ratio of Sn : Se of 1:1.4. Raman studies on the unwashed thin films could not be performed, the films were not stable towards the laser beam and immediately evaporated.

Due to the fact that thin film preparation was not possible following this approach, this synthetic strategy was not further pursued.

One-step strategy involving Se/K_4Sn_9/*en*

Here, Se and K_4Sn_9 were directly together filled into a glass flask (122 mg/0.10 mmol K_4Sn_9 and 8.00 mg/101 µmol Se in 2 mL *en*; Sn : Se 9:1) and *en* was added (details can be found in Chapter 4.3.9). After stirring, a dark red solution and dark precipitate were obtained. Filtration resulted in a clear, dark red solution. This solution was then used for thin film preparation (according to the standard procedure in Chapter 2.4.1, but without cross-linker). However, the obtained thin films did not show any form of ordered structure and were extremely thin and inhomogeneous. EDX measurements were performed on the achieved films, a recorded spectrum is shown in the Appendix Chapter 5.1, Figure 5.15. No Se was found on the film. EDX was also measured of the dried residue of a Se/K_4Sn_9/*en* solution, the spectrum is shown in the Appendix Chapter 5.1, Figure 5.16. Again, no Se could be detected. The fact that no Se could be found in the EDX spectra leads to the assumption that the dark precipitate described above consisted of elemental Se. This is in agreement with what has been found for the two-step strategy involving Se/*en* and K_4Sn_9/*en*, where also no Se could be found in dried residues of the combined solution after removing a black precipitate.

Additionally, Raman and PXRD measurements of dried residues of Se/K_4Sn_9/*en* solutions (Sn : Se 9:1) were conducted. The spectrum and powder pattern are given in Figures 2.49a and 2.49b.

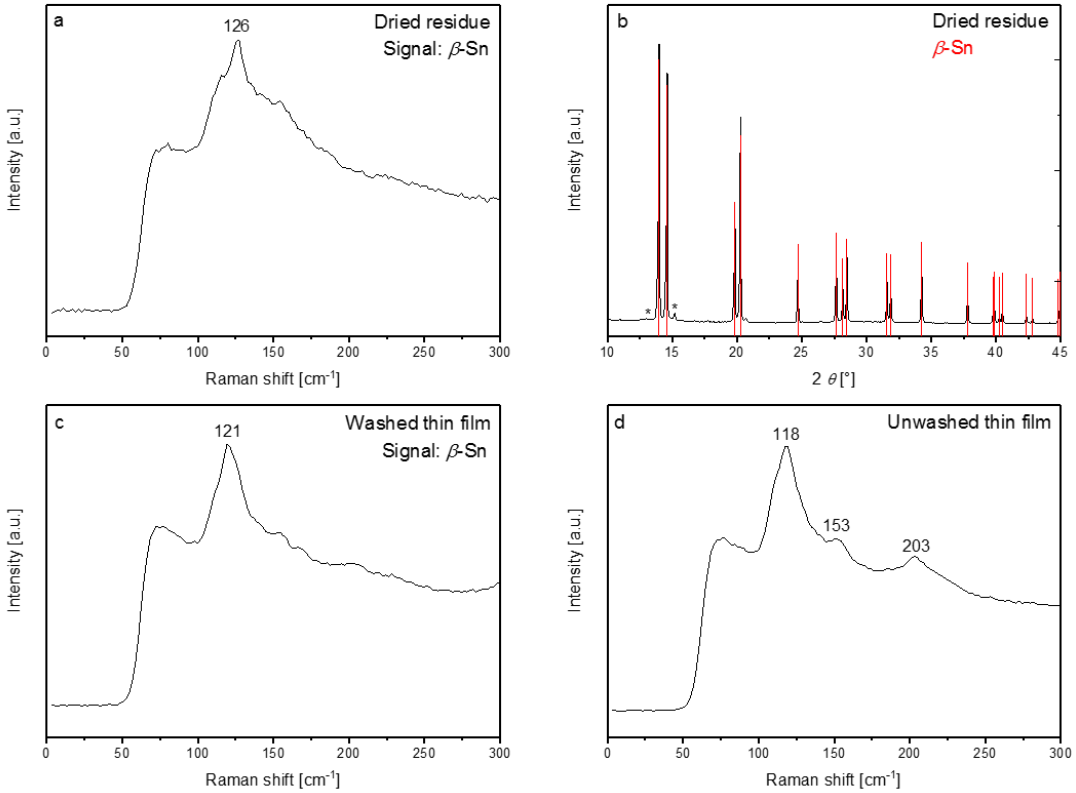

Figure 2.49. a) Raman spectrum of a dried residue of a Se/K_4Sn_9/*en* solution, b) powder X-ray diffractogram of the same residue, c) Raman spectrum of a washed thin film prepared from a Se/K_4Sn_9/*en* solution, d) Raman spectrum of an unwashed thin film prepared from a Se/K_4Sn_9/*en* solution. Reflections marked with an asterisk are an unknown impurity phase. The calculated diffractogram is based on single crystal data.[171a] The diffractogram was measured using Mo-$K_{\alpha 1}$ radiation.

The Raman spectrum of the dried residue in Figure 2.49 exclusively shows β-Sn (126 cm^{-1}), no Se signals can be seen. The powder diffractogram of the same residue in Figure 2.49b also shows β-Sn as main phase, but there are two very weak reflections at 13.13 and 15.16 °2θ which cannot be assigned to any known phase consisting of K, Sn, Se, or a mixture of these elements.

Figures 2.49c and 2.49d depict Raman spectra of thin films prepared from Se/K_4Sn_9/*en* solutions (Sn : Se 10:1). The spectrum in Figure 2.49c of a washed film shows β-Sn, but no Se signals are visible. However, the unwashed film in Figure 2.49d shows signals at 118, 153, and 203 cm^{-1}. The signal at 118 cm^{-1} could be assigned to β-Sn, even though its peak position is slightly more shifted from the literature reported value of 127 cm^{-1}. The signal at 203 cm^{-1} could possibly be assigned to a Sn clathrate, but this would lead to the question why the main signal of this compound at 160 cm^{-1} cannot be observed. It could possibly be found at 153 cm^{-1}, however, that would be a rather strong shift regarding the sharpness of that signal. Yet none of these signals can be assigned to Se or any known Sn-Se vibrations.

To conclude the chapter of mixed Sn/Se films, it must be said that none of the performed experiments lead to the desired result, an inverse opal structured mixed Sn/Se film, suitable for applications where group IV-VI semiconductors are needed. The characteristic honeycomb structure could not be obtained and Se cannot be reliably detected in any of the produced thin film samples.

2.5.2 Sn/Te thin films

Another promising candidate to achieve group IV-VI semiconductors is Te. The following chapter describes applied synthetic and spectroscopic methods which were performed with the aim to create inverse opal structured mixed Sn/Te thin films.

Mixed Sn/Te films were prepared by a two-step synthesis. In the first step, K and Te were filled into a glass tube with a molar ratio of 2 : 1 and *en* was added. After stirring and filtration, a clear solution was obtained (Figure 2.50a, 0.10 mmol mL^{-1}; a low concentration was chosen in order to make it easier to observe the coloring of the solution). This solution was then dropwise added to a K_4Sn_9/*en* solution (68.0 mg/0.06 mmol K_4Sn_9 in 2 mL *en* and 51.4 mg/0.25 mmol K_2Te in 3 mL *en*, Sn : Te 2:1), resulting in a dark red solution (Figure 2.50b). The combined K_2Te/K_4Sn_9/*en* solution was used for thin film preparation (according to the standard procedure in Chapter 2.4.1, but without cross-linker). Figure 2.50c shows photos of the obtained thin films.

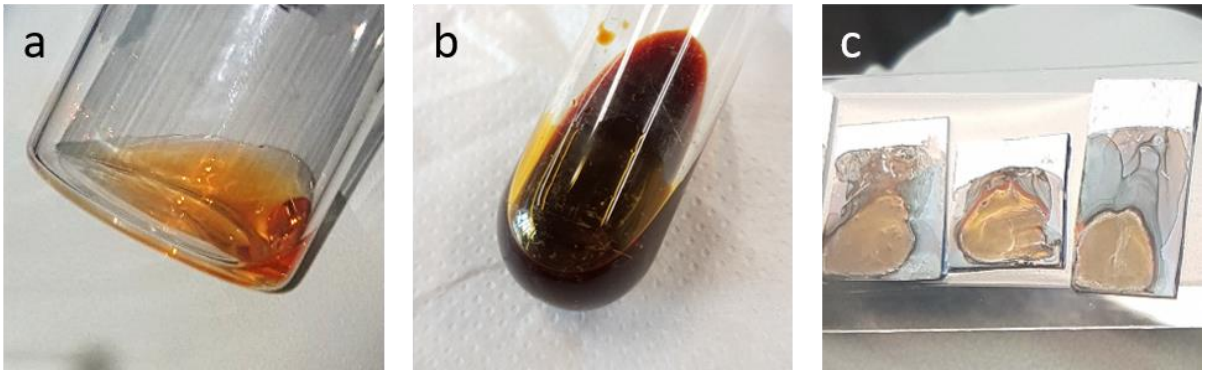

Figure 2.50. Photos of a) a K_2Te/*en* solution, b) a K_2Te/K_4Sn_9/*en* solution (Sn : Te 2:1), c) thin films prepared on Si substrates from a mixed K_2Te/K_4Sn_9/*en* solution (Sn : Te 2:1).

Figure 2.51 presents SEM images of obtained thin films. Figure 2.51a shows a film after the final washing steps, Figure 2.51b before washing.

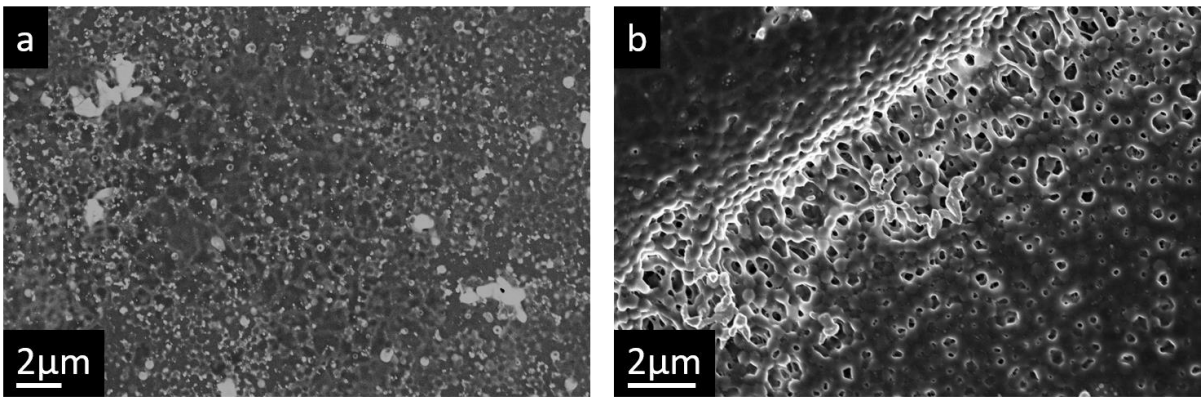

Figure 2.51. SEM images of a) a washed film prepared from a K_2Te/K_4Sn_9/*en* solution, 8000x magnification, b) an unwashed film prepared from a K_2Te/K_4Sn_9/*en* solution, 12000x magnification. Films were prepared on Si substrates. Molar ratios of Sn : Te 2:1.

As can be seen in Figure 2.51a, the desired inverse opal structure could not be achieved. The resulting films are extremely thin. While some pores of the honeycomb structure are visible in the SEM image, there are also grains and larger particles on the substrate. A main issue of these films was that the material was not stable towards the electron beam during SEM measurements, which lead to uncovered areas of blank substrate in Figure 2.51a. The unwashed film in Figure 2.51b was stable during the measurements, here the PMMA template covered in a thick layer of material can be observed. EDX measurements show that no Te seems to be present on the washed films, while the amount of Te on the unwashed films was determined to be 1.47at.% compared to the amount of Sn (for EDX spectra see Appendix Chapter 5.1, Figures 5.17 & 5.18). Due to the instability towards the electron beam, it cannot safely be said if Te got washed out during the washing steps or if the combined K_2Te/K_4Sn_9/*en* solution already contained very little Te.

To get more insights about what happened to the Te during the synthesis procedure, Raman and PXRD measurements of dried residues of K_2Te/K_4Sn_9/*en* solutions (68.0 mg/0.06 mmol K_4Sn_9 in 2 mL *en* and 112 mg/0.50 mmol K_2Te in 4 mL *en*, Sn : Te 1:1) as well as Raman measurements of prepared thin films were conducted. The resulting spectra and the diffractogram are presented in Figure 2.52.

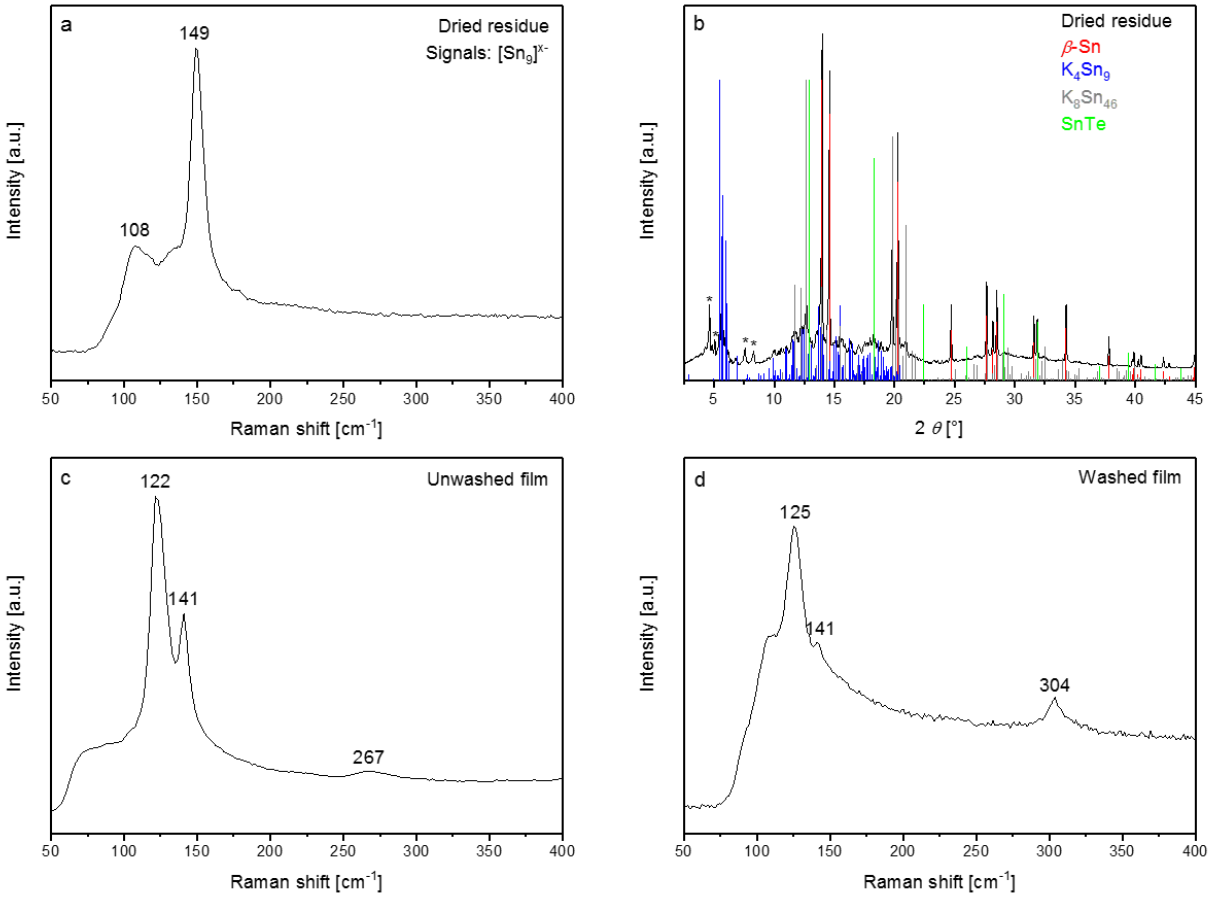

Figure 2.52. a) Raman spectrum of a dried residue of a K_2Te/K_4Sn_9/*en* solution, b) PXRD of the same residue, c) Raman spectrum of a washed film prepared from a K_2Te/K_4Sn_9/*en* solution, d) Raman spectrum of an unwashed film prepared from a K_2Te/K_4Sn_9/*en* solution. Reflections marked with an asterisk are an unknown impurity phase. The calculated diffractograms are based on single crystal data.[122f, 171a, 177] The diffractogram was measured using Mo-$K_{\alpha1}$ radiation. Molar ratios of Sn : Te 1:1.

The Raman spectrum in Figure 2.52a shows signals at 108 and 149 cm^{-1}, they can be assigned to $[Sn_9]^{x-}$ clusters. However, the main signal at 149 cm^{-1} exhibits a broad shoulder towards lower wavenumbers, possibly indicating Sn-Te vibrations. The powder X-ray diffractogram in Figure 2.52b is very hard to interpret. Reflections of β-Sn, K_4Sn_9, and K_8Sn_{46} can be detected, as well as reflections of SnTe and additional reflections marked with an asterisk which cannot be assigned to literature known compounds, probably originating from newly formed Sn/Te compounds. For reasons of clarity, Figure 2.52b is additionally shown in the Appendix Chapter 5.1, divided in two separate Figures (5.32a and 5.32b). The Raman spectrum in Figure 2.52c of a washed thin film shows signals at 122, 141, and 267 cm^{-1}, while the unwashed film exhibits signals at 125, 141, and 304 cm^{-1} (Figure 2.52d). The signals at 122/125 and 141 cm^{-1} could be assigned to Te, according to literature.[178] Very little can be found about Sn-Te vibrations in the literature. The polyanionic K_4SnTe_4 synthesized by Haushalter *et al.* shows Raman signals at 130 and 180 cm^{-1}.[179] SnTe exhibits Raman signals at 106, 130, and 147 cm^{-1} according to Kawamura *et al.*, though the spectrum was measured at 21 K.[180] Burstein *et al.* observed a signal

at 133 cm^{-1} for SnTe at 4 K.[181] Due to lack of comparable Raman data for SnTe at room temperature, the phase was synthesized according to a synthesis protocol reported by Ando *et al*.[182] The powder X-ray diffractogram of the phase pure reaction product can be found in the Appendix Chapter 5.1, Figure 5.33. A Raman spectrum was measured of the prepared SnTe, it is shown in Figure 2.53.

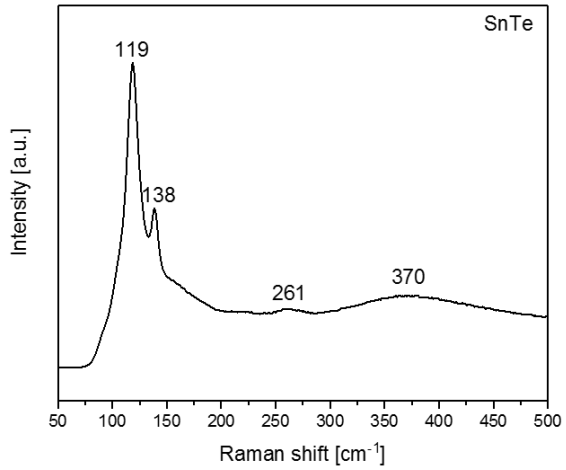

Figure 2.53. Raman spectrum of the prepared SnTe, measured at room temperature.

The synthesized SnTe shows Raman signals at 119, 138, 261, and 370 cm^{-1}. Comparing this spectrum to the literature known spectrum of Te and the spectra of the thin films in Figure 2.52, it cannot safely be said if Te or SnTe was detected on the films. Te as well as SnTe show intense Raman signals at about 120 and 140 cm^{-1}. The broad signal at 267 cm^{-1} in Figure 2.52c hints towards the presence of SnTe on the washed film. The additional signal at 304 cm^{-1} of the unwashed thin film in Figure 2.52d cannot be assigned to any literature known Sn or Sn-Te vibrations. However, the presence of at least one Te species on the films has been proven by Raman spectroscopy which is a promising result with respect to the scope of preparing mixed Sn/Te films.

Additionally, EDX was measured of dried residues of K_2Te/K_4Sn_9/*en* solutions. A higher concentration of the solution was chosen with the scope of staying above the detection level of the EDX device. The solution composition was 68.0 mg/0.06 mmol K_4Sn_9 in 1 mL *en* and 112 mg/0.50 mmol K_2Te in 3 mL *en*, resulting in a molar Sn : Te ratio of 1:1. The obtained spectra can be found in the Appendix Chapter 5.1, Figure 5.19. A molar Sn : Te ratio of 15:1 was detected. Even though the compositions of the starting solutions were chosen to contain a Sn : Te ratio of 1:1, the EDX results prove the presence of Te in the dried residue of the mixed solution.

To conclude the chapter about mixed Sn/Te films it has to be noted that thin film preparation was successful. However, it cannot be checked by means of SEM if the desired inverse opal structure was obtained due to instability of the thin films towards the electron beam. The Raman spectrum in Figure

2.52c shows that the films consist of SnTe and probably other Sn, Te or Sn/Te species which cannot safely be detected.

2.5.3 Sn/P thin films

Additionally to the aforementioned experiments to create thin films consisting of group IV-VI semiconductors, an approach to achieve mixed Sn/P film was pursued. A similar synthetic strategy as described for Sn/Te films was applied. In a first step, K and P were filled into a glass flask in a molar ratio of 3 : 7 and *en* was added. A second solution of K_4Sn_9/*en* was prepared and after filtration, the K_3P_7/*en* solution was dropwise added to the K_4Sn_9/*en* solution. A molar ratio of Sn : P of 2.2:1 was chosen (122 mg/0.10 mmol K_4Sn_9 in 2 mL *en* and 21.5 mg/0.06 mmol K_3P_7 in 1 mL *en*). The resulting red solution was used for film preparation (details can be found in Chapter 4.3.9 & 4.3.11). No cross-linker was used. Figure 2.54 shows SEM images of the obtained thin films.

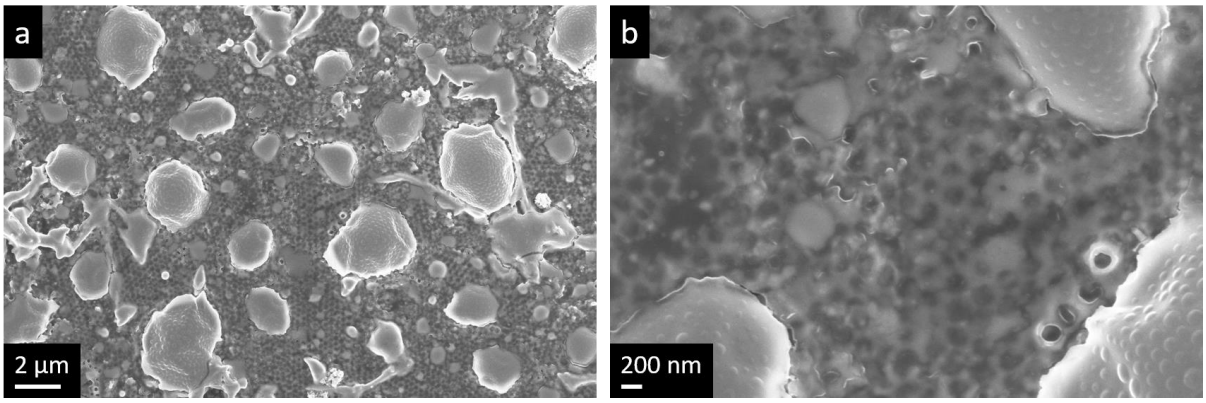

Figure 2.54. SEM images of a thin film prepared from a K_3P_7/K_4Sn_9/*en* solution (Sn : P 2.2:1) on a Si substrate. a) 8000x magnification, b) 35721x magnification.

The desired inverse opal structure could partially be obtained. The honeycomb structure is covered with a thin film of excessive material as can be seen in Figure 2.54b. Furthermore, larger particles can be found on the thin film. EDX measurements of the thin films were conducted at different magnifications, giving different results (EDX spectra can be found in the Appendix Chapter 5.1, Figures 5.20 & 5.21). For the image taken with 8000x magnification (Figure 2.54a), a molar ratio of Sn : P of 1.18:1 was found. EDX of the section shown in Figure 2.54b depicts a Sn : P ratio of 1.64:1. This indicates that P is in higher concentration in the large particles seen in Figure 2.54a than in the covered inverse opal structure seen in Figure 2.54b.

In addition to that, Raman spectra of dried residues and prepared thin films were measured. The obtained spectra are shown in Figure 2.55. Note that the spectra in Figure 2.55a, b, and c were all measured from different spots of the same dried residue of a mixed K_3P_7/K_4Sn_9/*en* solution (Sn : P 2.2:1).

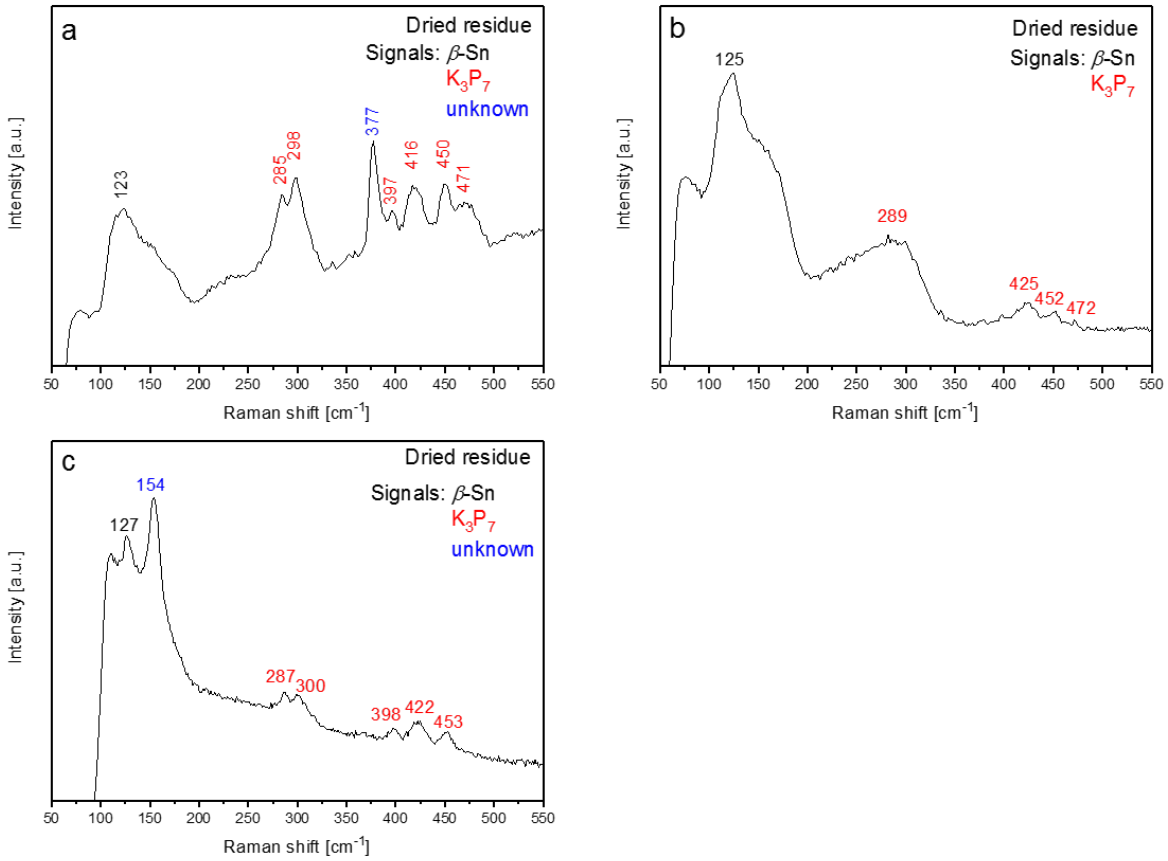

Figure 2.55. Raman spectra of a), b), and c) dried residue of a K_3P_7/K_4Sn_9/*en* solution, d) of a washed thin film prepared from such as solution.

Table 2.13 shows literature reported Raman signals for K_3P_7.[183] Raman signals for Sn-P are not reported in literature thus far, therefore comparison with literature data was not possible during this work.

Table 2.13. Literature reported Raman frequencies for K_3P_7.

Compound	**Raman frequencies [cm^{-1}]**
K_3P_7	70, 227, 308, 393, 425, 453, 467

The spectra of the dried residue all show signals of β-Sn and K_3P_7,[183] with varying intensity and resolution, as expected when measuring three different spots of the same sample. However, the Raman spectra in Figure 2.55a and c depict additional signals at 377 and 154 cm^{-1} which cannot be

assigned to the educts or any known Sn or P species. These signals could probably indicate newly formed Sn-P compounds in the dried residue.

Figure 2.56 shows a Raman spectrum of an obtained thin film after temperature treatment and solvent assisted template removal. The film was prepared from a mixed K_3P_7/K_4Sn_9/*en* solution (122 mg/0.10 mmol K_4Sn_9 in 2 mL *en* and 21.5 mg/0.06 mmol K_3P_7 in 1 mL *en*).

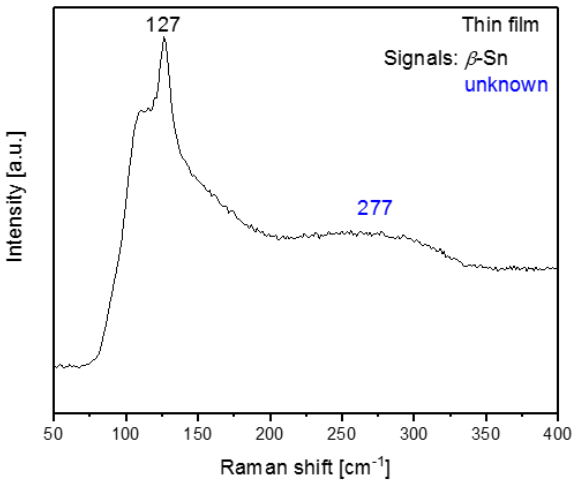

Figure 2.56. Raman spectrum of a washed thin film prepared on a Si substrate from a K_3P_7/K_4Sn_9/*en* solution (Sn : P 2.2:1).

The Raman spectrum of the thin film in Figure 2.56 also shows a signal at 127 cm^{-1}, which can be assigned to β-Sn, and an additional, very broad signal at 277 cm^{-1} which cannot be assigned to a known compound. Signals of K_3P_7 cannot be detected anymore on the film. Due to the fact that EDX measurements clearly demonstrated the presence of P on the film (see Appendix Chapter 5.1, Figures 5.20 & 5.21), it can be assumed that the unknown signal is caused by Sn-P vibrations of a most likely amorphous compound.

To draw a conclusion, by application of the here presented experimental strategy inverse opal structured thin films could be achieved, even though the films show a covering layer and some inhomogeneously distributed larger particles. Sn and P could both be positively detected on the resulting films. However, some more investigations seem to be needed to fully characterize the films and achieve a better homogeneity of the desired structure.

2.6 Phosphorus thin films

This chapter describes preparation and characterization of pure P thin films as well as first attempts to achieve doped P films. Analytical methods applied to the samples in this chapter are summarized in Table 2.14.

Table 2.14. Analytical methods applied to P thin films.

Sample	REM	EDX	Raman	Electrochemical methods
P + PCl_3 film	x	-	x	x
P + PCl_3 dried residue	-	-	x	-
P + $GeCl_4$ film	x	x	-	-
P + $SnCl_4$ film	x	x	-	-
P + $SiCl_4$ film	x	x	-	-

2.6.1 Synthesis

Synthesis of P thin films followed a similar strategy as described in the previous Chapter 2.4.3. An *en* solution containing a 3 : 7 molar mixture of K and P was prepared and the resulting dark red solution was used for thin film preparation (details can be found in Chapter 4.3.9 & 4.3.11). PCl_3 was utilized as cross-linking agent. Figure 2.57 shows a photo of an obtained thin film on a Si substrate. The film was prepared using 13.5 mg/0.35 mmol K and 25.0 mg/0.81 mmol P_{red} in 2 mL *en*. EDX measurements of the film show P and K and in a molar ratio of P : K 1:1.35 (see Appendix Chapter 5.1, Figure 5.22).

Figure 2.57. Photo of a P thin film on a Si substrate, prepared using a K_3P_7/*en* solution.

Figure 2.58 shows SEM images of thin films prepared from a solution of 54 mg/1.38 mmol K and 100 mg/3.23 mmol P_{red} in 2 mL *en*. A high solution concentration was chosen to obtain films of high thickness.

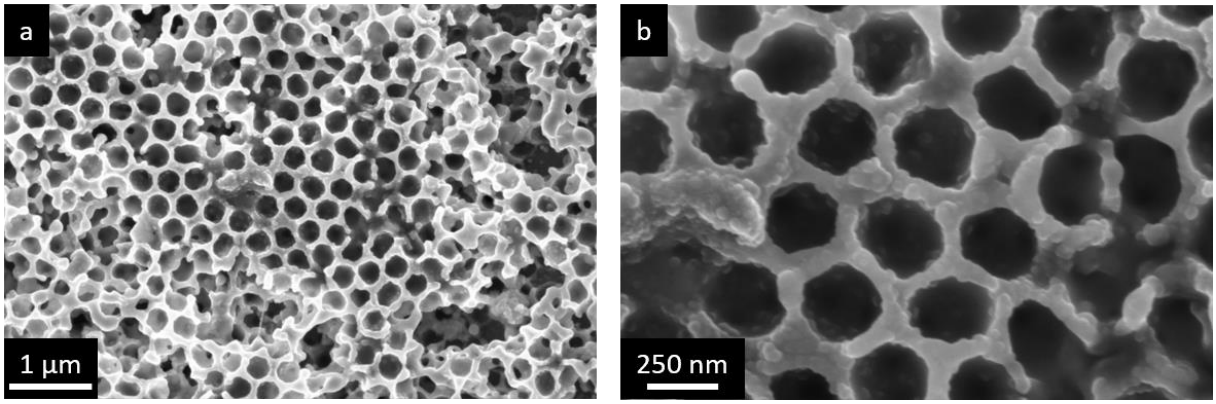

Figure 2.58. SEM images of a P thin film prepared from a K_3P_7/*en* solution on a Si substrate. a) 28873x magnification, b) 100000x magnification.

As can be seen, the desired inverse opal structure was successfully obtained. Smaller cracks in the surface are visible, but nevertheless, the honeycomb structure was homogeneously achieved over a large surface area. No larger sintered particles are present on the film. The achieved film thickness was 2.5 µm (determined by profilometry).

Variation of the cross-linking agent opened up new possibilities to create doped P thin films. Figure 2.59 shows SEM images of films prepared by utilizing $GeCl_4$ (a), $SnCl_4$ (b), and $SiCl_4$ (c) as linking agents.

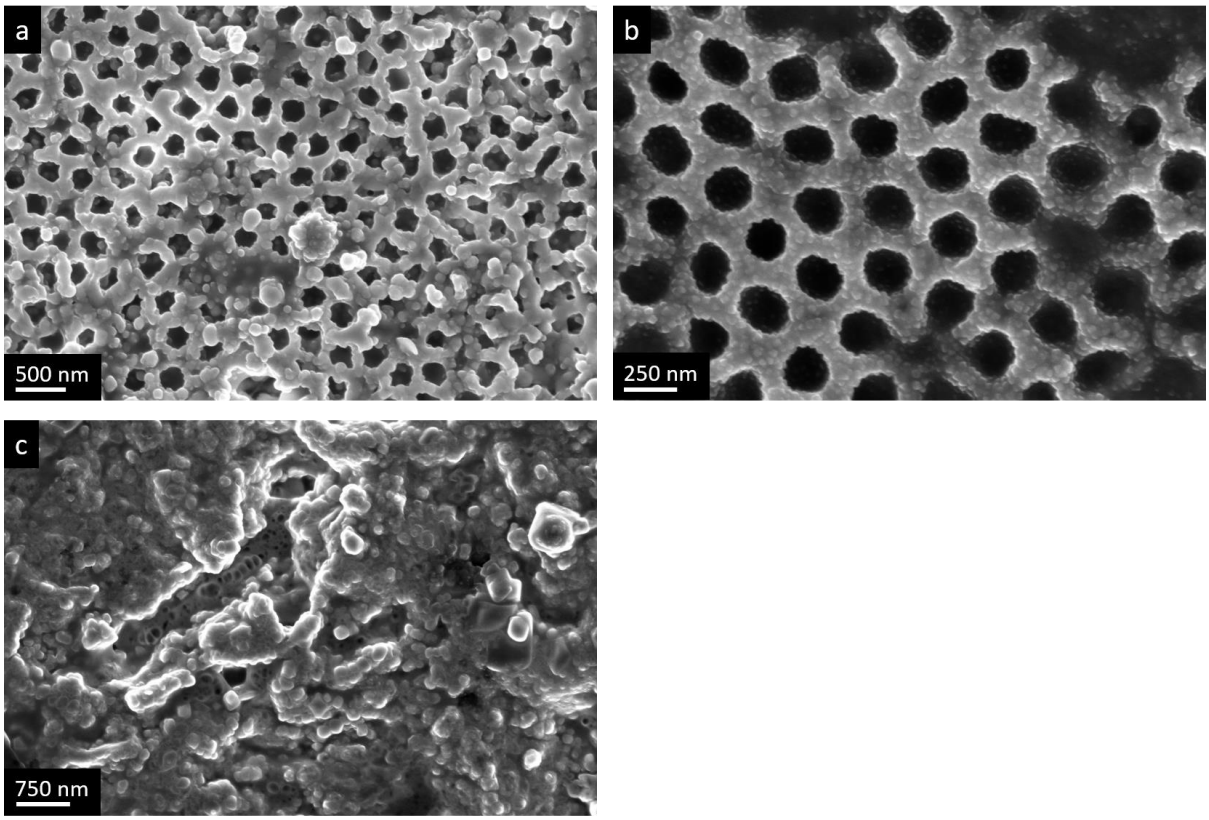

Figure 2.59. SEM images of P films prepared utilizing different cross-linking agents. a) $GeCl_4$ as linker, 35000x magnification; b) $SnCl_4$ as linker, 75167x magnification; c) $SiCl_4$ as linker, 25000x magnification. Film using $GeCl_4$ and $SnCl_4$ were prepared on Si substrates, the film using $SiCl_4$ was prepared on a Cu substrate.

For $GeCl_4$ (Figure 2.59a) and $SnCl_4$ (Figure 2.59b) as cross-linkers, the inverse opal structure could successfully be obtained. Especially the film linked with $SnCl_4$ shows a very homogeneous honeycomb structure. The film linked by $SiCl_4$ in Figure 2.59c does not exhibit any features of the desired structure. The film consists of large, sintered particles. No characteristic porosity can be observed. It is not clear why this was the case, further studies need to be conducted. EDX measurements were performed to investigate if Ge, Sn, or Si got successfully introduced into the structures. The spectra can be found in the Appendix Chapter 5.1 (Figures 5.23, 5.24, 5.25). Table 2.15 sums up the results of the EDX measurements.

Table 2.15. Summary of the EDX measurements of P thin films linked with different cross-linkers.

Linker	**Molar ratio**
$GeCl_4$	P : Ge 1:0
$SnCl_4$	P : Sn 49 : 1
$SiCl_4$	P : Si 46 : 1

As can be seen, introduction of Ge by using $GeCl_4$ as linking agent was not successful, no Ge could be found on the obtained film by EDX. For $SnCl_4$ and $SiCl_4$ very low amounts of Sn and Si could be found. However, due to the low percentages of Sn and Si it cannot safely be assumed that doping was successful by applying this strategy. The measured Sn and Si amounts are so low that they are at the border of the detection level of the EDX device, so that definite statements about the absolute numbers cannot be made. Nevertheless, Sn and Si were undeniably found on the films, indicating that introduction of dopants could be successfully performed by this method.

2.6.2 Raman characterization and electrochemical measurements

Since EDX results of films linked with various cross-linkers were not very promising, Raman measurements of a dried residue (Figure 2.60a) and a thin film prepared (Figure 2.60b) were performed to investigate the influence of the linking agent. The dried residue was obtained from a solution containing 54.0 mg/1.38 mmol K and 100 mg/3.23 mmol P_{red} in 2 mL *en*, while the thin film was prepared using a solution containing 13.5 mg/0.35 mmol K and 25.0 mg/0.81 mmol P_{red} in 2 mL *en*. The dried residue in Figure 2.60a was not exposed to any cross-linking agent, while the thin film in Figure 2.60b was infiltrated by PCl_3 vapor. This way the differences between linked and unlinked samples should be observable.

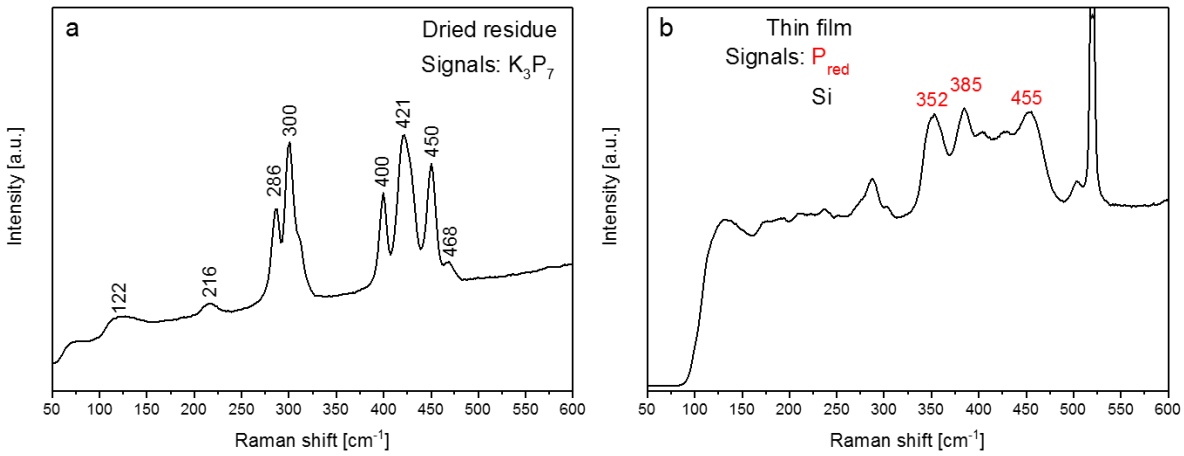

Figure 2.60. Raman spectra of a) the dried residue of a K_3P_7/*en* solution, b) a thin film prepared from a K_3P_7/*en* solution, after cross-linking with PCl_3. The Si signal is caused by the Si substrate, due to the extremely high laser power (250 mW) which was needed for the measurement.

The spectrum in Figure 2.60a clearly shows K_3P_7 (see Table 2.13), no other signals are visible. This means that solvent removal has no influence on the material and without cross-linking K_3P_7 is obtained. The spectrum in Figure 2.60b on the other hand shows the characteristic signals of red P.[167] Similar to Ge or Sn films, where $[Tt_9]^{x-}$ cluster signals can be detected before cross-linking and *α*-Ge or *β*-Sn after cross-linking, P samples show K_3P_7 before and P_{red} after linking. This proves that cross-linking was successful, and the desired P thin films with inverse opal structure were obtained.

Additionally, electrochemical charge-discharge cycling experiments were conducted with P films, prepared from a K_3P_7/*en* solution (19.25 mg/0.525 mmol in 1 mL *en*). Figure 2.61 shows the cycling performance (a) and voltage profile (b) of the binder-free P thin film electrodes. All measurements were performed referring to a theoretical gravimetric capacity of 2596 mAh g^{-1} for Li_3P.[98b, 184] For details on electrode preparation, see Chapters 4.1.6 and 4.3.11.

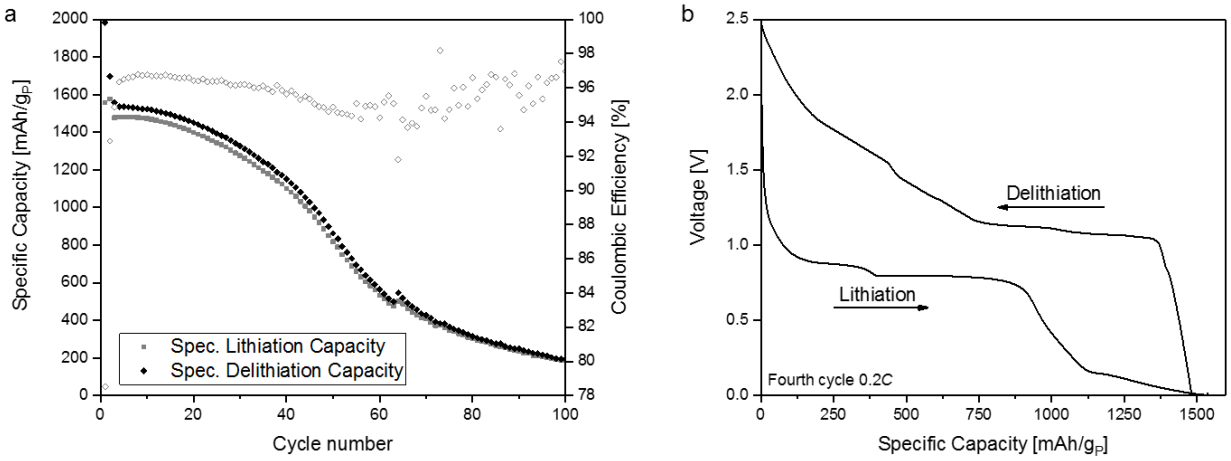

Figure 2.61. a) Specific delithiation capacity over extended cycling at a rate of 0.2*C* with the first two cycles at 0.1*C* of an electrode prepared from a K_3P_7/*en* solution (loading: 151 µg, see Chapter 4.1.6 & 4.3.11). b) Voltage profile of the fourth cycle of the same electrode.

The electrode which capacities are presented in Figure 2.61a shows an initial delithiation capacity of 1988 mAh g^{-1} and an initial lithiation capacity of 1559 mAh g^{-1}, with a coulombic efficiency of 78% for the first cycle. For the fourth cycle, where SEI formation should be completed, the electrode exhibits a delithiation capacity of 1538 mAh g^{-1} and a lithiation capacity of 1478 mAh g^{-1}, corresponding to a coulombic efficiency of 96%. After 20 cycles, capacities of 1454 mAh g^{-1} and 1398 mAh g^{-1} can be observed. However, from the 20th cycle onwards a rapid capacity fading takes place and after 100 cycles, the electrode only shows capacities of 194 mAh g^{-1} and 184 mAh g^{-1}. From the 60th cycle on, the coulombic efficiency shows a rather unstable trend, fluctuating between 92% and 98%. The electrodes measured in this work do not reach the theoretical capacity of 2596 mAh g^{-1}, most likely due to connectivity issues. However, they still show initially high capacities and good capacity retention during the first cycles. They do not seem to be suitable for long-lifetime applications, since the capacity decreases rapidly with increasing cycle number.

The voltage profile in Figure 2.61b shows voltage plateaus for the lithiation process at 0.88 V, 0.80 V, and 0.14 V and for the delithiation process at 1.06 V, 1.20 – 1.42 V, and 1.60 V. These plateaus correlate very well with the assumed stepwise lithiation of P to Li_3P and delithiation back to P.

Red P as electrode material for Li ion batteries has been reported literature before. An overview about the most recent work can be found in Table 1.3 in Chapter 1 Introduction.

Compared to literature data, the here presented electrodes perform much worse regarding cycling stability. However, all materials reported in the literature are composite materials, mostly involving porous C species to stabilize the red P towards volume expansion and shrinkage. This seems to be necessary to overcome the problem of volume changes during cycling and therefore to prevent significant connectivity issues. No reports on pure, binder-free red P electrodes can be found.

3. Conclusion

With increasing interest in renewable energies and electromobility, new storage materials with higher capacities and energy densities are needed. Especially Li ion batteries drew a lot of attention in recent years as desired storage technology. However, they suffer from strict limitations of the current generation of electrode materials. This work took place with the scope to design new, alloy-based electrodes with high capacities and capacity retentions, utilizing a simple wet-chemical process starting from Zintl ions as precursors.

This wet-chemical process involved preparation of inverse opal structured thin films. Therefore, a suitable template coating technique had to be found in the first step. Dip-coating, spin-coating, vertical deposition, and spray-coating have been investigated regarding their specific advantages and disadvantages. Dip-coating turned out to be the most versatile and well suited method for the desired applications in this work. The other mentioned coating techniques also find application for fabrication of thinner films for *e.g.* solar cells. Especially spray-coating is a promising method when it comes to up-scaling and automatization of the whole process. Furthermore, size variation of the PMMA template opals has been done to enable the possibility of pore size variation.

Various different material compositions were used to prepare thin films. Table 3.1 lists all used starting materials and summarizes if the desired inverse opal structure was successfully obtained. SEM was used to investigate the morphology of the prepared thin films. Film compositions determined by EDX measurements are also given in Table 3.1.

XRD and Raman studies were performed on dried residues of the respective precursor solutions. It was found that $[Tt_9]^{4-}$ (Tt = Ge, Sn) clusters remain after solvent removal, even from mixed solutions. Raman studies on thin films were conducted to examine the influence of cross-linkers. The effect of cross-linkers was demonstrated and it was shown that application of different cross-linkers allows for preparation of films with mixed elemental compositions. It was also found by means of Raman, EDX, and XPS that films with mixed compositions could be synthesized successfully by variation of the used starting materials.

Table 3.1. Summary of films and film compositions prepared from different starting materials.

Starting material	Cross-linker	Inverse opal structure	Film composition [molar ratio]
K_4Ge_9	$GeCl_4$	x	Ge
$K_4Ge_9 + PPh_3$	-	x	n.a.
$K_4Ge_9 + NaP_7$	-	x	n.a.
$K_4Ge_9 + P_{red}$	-	x	Ge/P 3 : 1
"$K_2Ge_2P_2$"	$GeCl_4$	-	Ge/P 1 : 1.2
"$K_2Ge_7P_2$"	$GeCl_4$	x	Ge/P 39 : 1
K_4Sn_9	$SnCl_4$	x	Sn
$K_4Sn_9 + K_4Ge_9$	$GeCl_4$	x	Ge/Sn 1.4 : 1
"$K_4Ge_5Sn_4$"	$GeCl_4$	x	Ge/Sn 1.4 : 1
$K_4Sn_9 + Se$	-	-	Sn/Se 1 : 1.4
$K_4Sn_9 + K_2Te$	-	-	Sn/Te 68 : 1
$K_4Sn_9 + K_3P_7$	-	-	Sn/P 1.6 : 1
K_3P_7	PCl_3	x	P
K_3P_7	$GeCl_4$	x	P/Ge no Ge found
K_3P_7	$SnCl_4$	x	P/Sn 49 : 1
K_3P_7	$SiCl_4$	-	P/Si 46 : 1

Electrochemical cycling experiments were performed on prepared thin films. Table 3.2 summarizes the used electrodes and their electrochemical performance regarding capacity and capacity retention. Inverse opal structured Ge electrodes (see Chapter 2.2.3) showed the overall best performance of all tested electrodes. Ge electrodes with higher loading or without the inverse opal structure performed worse, due to the lack of a mechanically stable and flexible structure, allowing for compensation of the massive volume changes during lithiation and delithiation. Mixed Ge/P electrodes delivered good capacity retentions but lower overall capacities than pure Ge electrodes. Pure Sn electrodes only achieved extremely low capacity retentions, not suitable for any application. Mixed Ge/Sn electrodes prepared from "$K_4Ge_5Sn_4$" showed high capacities and capacity retentions but worse overall performance than inverse opal structured Ge electrodes. Experiments including conventional inks did not succeed, almost no capacity could be observed after 100 charge-discharge-cycles. Inverse opal structured P_{red} electrodes achieved high capacities compared to Ge or Sn electrodes, but they were still significantly lower than the theoretical capacity. After 20 cycles, a rapid decrease in capacities could be observed.

Table 3.2. Summary of electrochemical performances of electrodes with different compositions.

Electrode composition	**Electrochemical performance**	
	4th cycle delithiation capacity [mAh g^{-1}]	**Capacity retention [% after X cycles]**
Inverse opal structured Ge	1360	71 after 100
Porous Ge with high loading	555	66 after 100
Unstructed Ge	617	42 after 100
Ge on ink	237	78 after 100
Ge/Ink	975	17 after 100
Ge + P_{red} 3:1	875	81 after 100
Ge + P_{red} 10:1	847	86 after 75
Ge + NaP_7 3:1	791	81 after 100
Ge + NaP_7 10:1	884	84 after 100
Unstructured Sn	507	31 after 20
Inverse opal structured Sn	89	40 after 100
Sn on ink	n.a.	n.a.
Sn/Ink	303	15 after 100
Sn/Ge ("$K_4Ge_5Sn_4$")	907	75 after 100
Sn/Ge (K_4Sn_9 + K_4Ge_9)	165	58 after 100
Inverse opal structured P_{red}	1538	13 after 100

Conclusively it can be said that the developed wet-chemical synthesis route allows for easy and potentially up-scalable production of inverse opal structured thin films starting from different Zintl tetrel cluster solutions. Preparation of films with mixed elemental compositions was investigated and successfully performed. The prepared Ge electrodes show high capacities and good capacity retentions. First experiments regarding Sn and P electrodes for Li ion batteries were performed. More experiments regarding fine-tuning these materials have to be conducted. Due to the accessibility of Si-Ge mixed clusters,[132] a transfer to an alloyed $Si_{1-x}Ge_x$ material could be investigated in the future.

4. Experimental Part

In this part, experimental techniques, syntheses and characterization methods are described.

4.1 Experimental Techniques

In this section details on the applied experimental techniques and used chemicals are reported.

4.1.1 Working under inert gas conditions

The used precursor Zintl phases as well as the prepared thin films are highly sensitive towards water and oxygen. For this reason all experiments, either synthesis or characterization, are carried out under inert gas atmosphere. All used glass equipment gets cleaned via potassium hydroxide and isopropanol and washed with deionized water. Glassware is stored in a dry oven at 120 °C. Experiments are performed using Schlenk technique. Prior to use, glass equipment is additionally baked out via heating up to 630 °C using a heat gun (Steinel HG 2120 E) and applying vacuum. For this step, a vacuum apparatus connected to a vacuum pump (VACUUBRAND GmbH & Co. KG, $p < 10^{-3}$ mbar) and argon gas (Argon 4.8, WESTFALEN AG, 99.998 vol.%) is used. The applied argon gas is further dried by a BTS-catalyst, molecular sieve and P_4O_{10}. Sample preparation is carried out in a glovebox (MBRAUN Inertgas-Systeme GmbH; $H_2O < 0.1$ ppm, $O_2 < 0.1$ ppm) under argon atmosphere. The glovebox is equipped with a BTS-catalyst, a molecular sieve and an activated carbon filter.

4.1.2 Solid state synthesis

Binary Zintl phases K_4Tt_9 (*Tt* = Ge, Sn) are synthesized in stainless steel tubes (size inner tube: 7.0 x 1.5 cm; outer tube: 9.0 x 2.5 cm) under argon atmosphere. Prior to use, the tubes are cleaned with deionized water and dried at 120 °C overnight. The stainless steel tubes are filled inside a glovebox and placed in an argon-filled corundum tube, closed with a balloon for pressure equalization (see Figure 4.1).

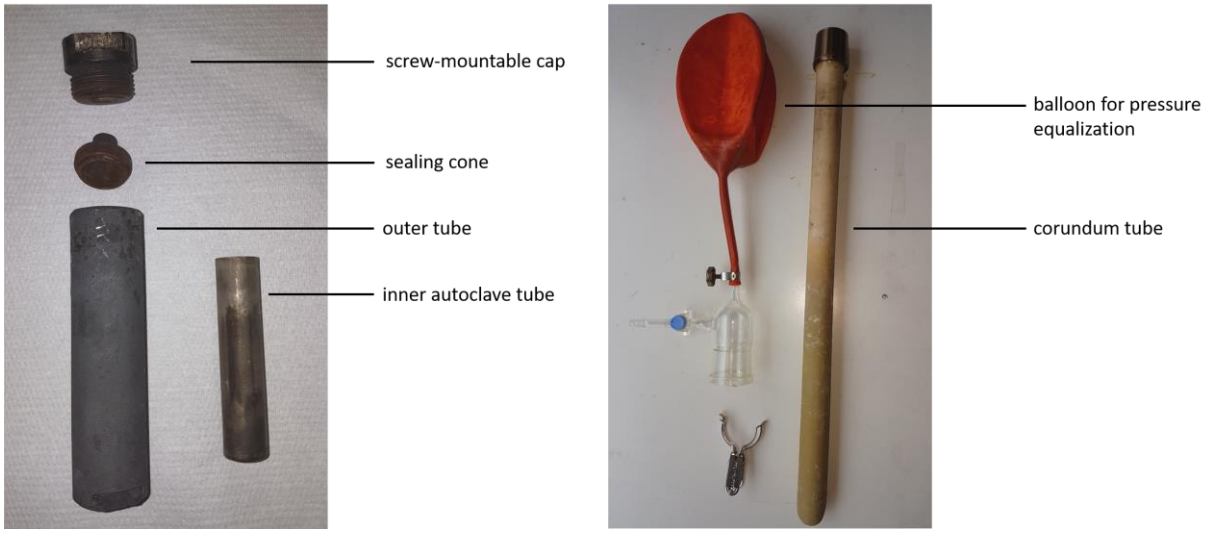

Figure 4.1. Stainless stell tube and corundum tube including the balloon for pressure equalization.

Ternary Zintl phases $K_4Ge_5Sn_4$, $K_2Ge_2P_2$ and $K_2Ge_7P_2$ and the phase SnTe are synthesized in tantalum ampoules (diameter 10 mm, length 50 mm). Before usage, the ampoules get cleaned in acetone and acetic acid and subsequently dried at 120 °C. One end of the ampoules is closed by pressing a cap on it using a hydraulic press inside a glovebox. The caps are sealed by an electric arc furnace (Edmund Bühler GmbH). After filling in a glovebox, the ampoules are sealed using an electric arc furnace and placed in a fused silica tube. The fused silica tube is evacuated and vertically placed in a tubular oven (Loba 1200-400-600, HTM Reetz GmbH) for temperature treatment. The temperature program is controlled by a temperature controller (Invensys Systems GmbH, Eurotherm Deutschland GmbH).

The binary phase NaP_7 is synthesized under vacuum in a fused silica-glass ampoule (diameter 8 mm, length 100 mm). The ampoules are prepared from fused silica-glass tubes (> 99.99%, ilmasil® PN fused quartz, QSIL GmbH) using a H_2/O_2 flame. The ampoules are cleaned with acetone and deionized water and dried at 120 °C overnight. After cleaning and prior to use, the ampoules are graphitized. This is done by filling the ampoules with 3 - 5 mL of acetone and evaporating the acetone using a H_2/O_2 flame. When this process is finished, the ampoules are again cleaned and stored as before mentioned. After filling with the educts inside a glovebox, the ampoule is closed with an airtight quickfit® tube-hose connection piece and evacuated to a pressure of 10^{-3} bar. The ampoule is sealed under vacuum using a H_2/O_2 flame. The sealed ampoule is placed in a muffle furnace (Nabertherm P330).

4.1.3 PMMA dip-coating

PMMA spheres are applied to various substrates by dip-coating a solution of 15 wt.% PMMA (particle size 250 -300 nm) in water. The sample is attached to a movable sample holder, powered by an electric engine (Figure 4.2). Sample movement takes place at a constant speed to guarantee a homogenous coating onto the substrate. Prior to usage, the PMMA suspension is kept in an ultrasonic cleaner (EMMI 120 HC, EMAG) for 2 d. After dip-coating, the substrates are dried at 100 °C under vacuum for 4 h.

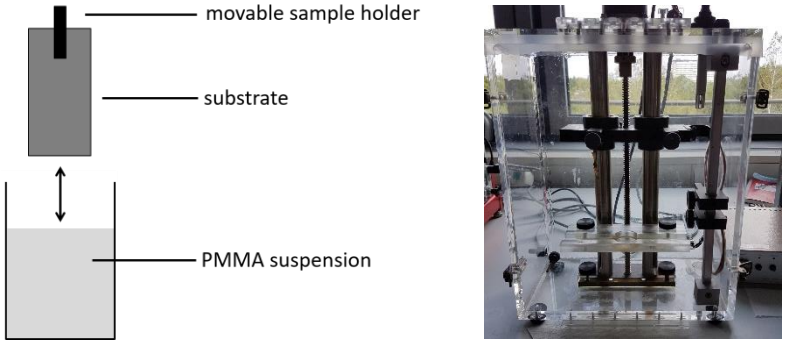

Figure 4.2. Schematic depiction of the PMMA dip-coating process and photo of the home-built dip-coater.

4.1.4 Drop-casting of precursor solutions

Zintl precursor solutions are drop-casted onto the PMMA coated substrates. The drop-casting procedure is shown in Figure 4.3. The substrates are slightly tilted during the casting process which allows for a homogenous coating without creating areas of too high concentration. For battery applications, the tilt angle is removed and the substrates are placed on a flat surface to ensure that no active material is lost during the casting step, otherwise a reliable capacity determination would not be possible.

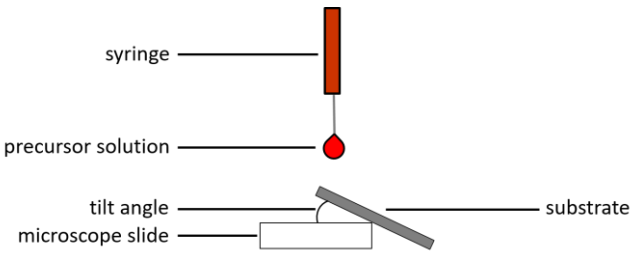

Figure 4.3. Schematic depiction of the drop-casting process of a Zintl precursor solution.

4.1.5 Substrate preparation

Silicon (Siegert Wafer), sapphire (Siegert Wafer) and glass substrates (1.0 x 1.5 cm) are cleaned by ultrasonication in three different solvents for 15 min each. The solvents are, in this order, an Extran® solution (Merck Millipore), ethanol and acetone. After the final ultrasonication step, the substrates are held in an O_2-Plasma oven (Electronic Diener, Femto) for 10 min. After cleaning, the substrates are kept under argon atmosphere inside a glovebox.

For electrochemical measurements copper substrates (diameter 10 mm) are used. They are punched out of copper foil with 0.2 mm thickness (Advent, 99.9%). The substrates are cleaned in two steps. Firstly, they are given into an ammoniacal hydrogen peroxide solution (H_2O_2 (30%) + NH_3 (conc.) in H_2O (1.3 : 2.2 : 100 wt%)) and ultrasonicated for 2 min at 30 °C. In the second step, ultrasonication is repeated in diluted hydrochloric acid (HCl in H_2O (1 : 100 wt%)). After cleaning with water, the substrates are dried under vacuum and stored in a glovebox.

4.1.6 Cell preparation

All electrochemical measurements in this work are carried out using Swagelok T-cells. Two glass fiber separators (glass microfiber filter, 691, VWR, diameter 11 mm) are used between working and counter electrode (metallic lithium; thickness 0.45 mm, diameter 10 mm, battery grade foil, 99.9%, Rockwood Lithium). 80 µL of LP57 electrolyte (1 M LiPF6 in EC:EMC 3:7 wt.%, < 20 ppm H_2O, BASF) or LP57 with the addition of 5 wt.% FEC are used. Preparation of the different working electrodes is described in the respective Chapters 4.3.10 and 4.3.11.

Due to the drop-casting process during electrode preparation, minor losses of active material are inevitable. Determination of the mass loading is performed by three different methods: Weighing with a Sartorius M2P microscale (accuracy ≤ 1 µg for a total weight up to 500 mg), using the concentration of the solution, and the film thickness. Utilizing the film thickness, the loading is calculated as follows:

$$V = \pi \times r^2 \times h \times (1 - 0.74) \quad (2)$$

Where *V* is the volume, *r* the radius, *h* the height, and where the term between parentheses describes the spherical packing of the inverse opal structure, assuming an hcp packing of the PMMA opals.

This calculation under the assumption of an averaged and homogenous film thickness is in good agreement with the maximum loading. Experiments with different Ge loadings were performed to compare the discrepancy of the mentioned methods. According to that, for Ge electrodes used in Figures 2.11, 2.12, and 2.13 a loading of 313 µg (282 µg of Ge from K_4Ge_9 + 31 µg of Ge by addition of

$GeCl_4$) is calculated utilizing the concentration of the solution. This is in good agreement with the calculation according to Formula 2, which gives a loading of 300 µg for an average film thickness of 2.75 µm. Ge electrodes used in Figure 2.14 and 2.15 feature loadings of 5.5 mg (2.14) and 1.7 mg (2.15), determined by the microscale. The loadings of the electrodes in Figure 2.16a (321 µg) and Figure 2.16b (2.35 mg) are determined by the microscale.

Loadings of the Ge/P electrodes used in Figure 2.34 are determined by calculation based on the solution concentration (Table 4.1) and by using the microscale. Loadings determined by the microscale are used for data evaluation since minimal losses of active mass during the heating process cannot be avoided and it could also not safely be assumed that the amount of P on the films was the same as the initial amount, lowering the reliability of the calculation based method.

Table 4.1. Solutions used for Ge/P electrodes in Figure 2.34.

Figure	**K_4Ge_9**	**P species**	***en***
2.34a	100 mg / 0.12 mmol	11 mg / 0.36 mmol P_{red}	2 mL
2.34b	100 mg / 0.12 mmol	12.7 mg / 0.053 mmol NaP_7	2 mL
2.34c	100 mg / 0.12 mmol	3.44 mg / 0.11 mmol P_{red}	2 mL
2.34d	100 mg / 0.12 mmol	3.8 mg / 0.016 mmol NaP_7	2 mL

Loadings of Sn and mixed Sn/Ge electrodes used in Figure 2.43 are determined by the microscale (Figures 2.43a, b, and d; due to minor losses during the synthesis) or by calculation based on the solvent concentration (Figures 2.43c, e, and f). For the mixed Sn/Ge electrodes, calculation based on the solvent concentration is used to get a more precise result regarding the Sn and Ge fractions of the loading.

Table 4.2. Solutions used for Sn and Sn/Ge electrodes in Figure 2.43.

Figure	**K_4Sn_9**	**K_4Ge_9**	**"$K_4Ge_5Sn_4$"**	**Solvent**
2.43a	122 mg / 0.12 mmol	-	-	*en* 2 mL
2.43b	122 mg / 0.12 mmol	-	-	*en* 2 mL
2.43c	122 mg / 0.12 mmol	-	-	*en* 2 mL
2.43d	600 mg / 490 mmol	-	-	Toluene 3 g
2.43e	-	-	99.4 mg / 0.1 mmol	*en* 1 mL
2.43f	122 mg / 0.12 mmol	81 mg / 0.10 mmol	-	*en* 4 mL

For the P electrodes prepared from 19.25 mg/0.525 mmol K_3P_7 in 1 mL *en* shown in Figure 2.61 in Chapter 2.5.2, the loading determined by the microscale is used for data evaluation since minor losses of active mass during the heating process cannot be avoided.

4.1.7 List of used materials

Materials used for synthesis are listed in Table 4.3. Solvents were either taken from a SPS station or dried over calcium hydride under reflux conditions. The water content of ethylene diamine was monitored according to Fässler *et al*.[139]. Deuterated solvents for NMR studies are stored in a glovebox over molecular sieve (3 Å). Specifications of materials used for characterization (*e.g.* T-cell material) are given in the respective chapters. Synthesis of precursor materials is also described in the respective chapters.

Table 4.3. List of used materials.

Compound	**Shape**	**Producer**	**Purity**	**Storage**
Acetone	Liquid	Merck	Analysis grade	Lab
Acetonitrile	Liquid	VWR	SPS	Lab
Acetonitrile-d3	Liquid	Deutero GmbH	Mole Sieve 4 Å	Glovebox
Benzo-12-crown-4	Solid	Molekula	96%	Glovebox
Bis(trimethylsilyl)silane	Powder	Sigma-Aldrich	98%	Glovebox
Calcium hydride	Pieces	Merck	Synthesis grade	Lab
Chloroform-d1	Liquid	Deutero GmbH	Mole Sieve 4 Å	Glovebox
Carbon black	Powder	TIMCAL	99.99%	Glovebox
Copper	Foil, thickness 12 µm	Advent	99.9%	Lab
Copper	Foil, thickness 0.2 mm	Advent	99.9%	Glovebox
Copper(II)chloride	Powder	Alfa Aesar	>98%	Glovebox
Dimethylformamide	Liquid		Stored over CaH_2	Lab
Dimethyl sulfoxide	Liquid	Sigma-Aldrich	H_2O < 0.005%	Glovebox
Ethanol	Liquid	VWR	Synthesis grade	Lab
Ethylene diamine	Liquid	Alfa Aesar	Stored over CaH_2	Lab
Extran®	Liquid	Merck Millipore		Lab
Fluoroethylene carbonate	Liquid	Sigma-Aldrich	99%	Glovebox
Germanium	Pieces	ChemPur	99.9999+	Glovebox
Germanium tetrachloride	Liquid	Sigma-Aldrich	99.999%	Glovebox
Glass microfiber filter	Sheets	VWR		Lab

Hydrochloric acid	Liquid	Merck		Lab
Hydrogen peroxide	Liquid	Merck		Lab
Lithium	Foil	Rockwood Lithium	Battery grade	Glovebox
LP57	Liquid	BASF	< 20 ppm H_2O	Glovebox
Methyl methacrylate	Powder	VWR	>99.5%	Lab
N-Methyl-2-pyrrolidone	Liquid	VWR	>99.5%	Glovebox
Poly ethylenoxide	Powder	Merck Millipore	>99%	Lab
Polyvinylidene fluoride	Liquid	Kynar	99.99%	Glovebox
Phosphorus (red)	Powder	Sigma-Aldrich	98%	Glovebox
Phosphorus trichloride	Liquid	Merck	>99%	Glovebox
Potassium	Pieces	Merck	99%	Glovebox
Potassium persulfate	Powder	VWR	>98%	Lab
Selen	Pieces	ChemPur	99.99%	Glovebox
Sodium	Pieces	Sigma-Aldrich	>99%	Glovebox
Sodium dodecyl sulfate	Powder	Merck	Synthesis grade	Lab
Silicon tetrachloride	Liquid	Sigma-Aldrich	99.999%	Glovebox
Tellurium	Pieces	Alfa Aesar	99.99%	Glovebox
Tetrahydrofuran	Liquid	Merck	SPS	Lab
Tin	Powder	ChemPur	99.9999+	Glovebox
Tin tetrachloride	Liquid	Sigma-Aldrich	99.999%	Glovebox
Triphenylphosphine	Pieces	Merck	>98%	Glovebox
Toluene	Liquid	Merck	SPS	Lab

4.2 Analytical Methods

The following section describes the analytical methods used for sample characterization.

4.2.1 Raman spectroscopy

Raman spectroscopy was performed using a Renishaw inVia Raman microscope equipped with a CCD detector and three different lasers (λ = 532 nm, 633 nm, and 785 nm) with a maximum power of 500 mW. For operating the device, the software WiRe 4.2 (build 5037, Renishaw, 2002) was used. Sample preparation for characterization of dried residues of the Zintl precursor solutions is done by solvent removal under vacuum at room temperature. Inside a glovebox, the resulting powders are filled into glass capillaries (diameter 0.3 mm, Hilgenberg GmbH) which are sealed afterwards using wax. Spectra of thin film samples were recorded directly on the respective films.

Raman spectra of the Ge electrodes in Figure 2.10, Chapter 2.2.3 were measured on a LabRAM HR UV-vis (HORIBA JOBIN YVON) Raman microscope (OLYMPUS BX41) with a SYMPHONY CCD detector and a He-Ne laser, with λ = 633 nm.

4.2.2 Fano-effect determination

Raman spectroscopy for determination of the Fano-effect is performed using a confocal LabRAM HR UV/VIS (HORIBA JobinYvon) Raman microscope (Olympus BX 41) equipped with a SYMPHONY CCD detector and two different lasers (λ = 514 nm and 644 nm, maximum power 17 mW). Measurements are performed at 1.7 mW to avoid sample heating.

To successfully prove for phosphorus doping, crystallized thin film samples are used. Inside a glovebox, the films are given into a Schlenk glass tube and then transferred to an oven (Losa 600-40-180, HTM Reetz GmbH) and subsequently heated at 600 °C for 1 h under argon atmosphere.

4.2.3 X-Ray powder diffraction

X-ray powder diffraction (XRD) is performed on a STOE STADI P device (Cu-$K_{\alpha1}$ radiation, Ge monochromator, detector: IP-PSD) in transmission mode. Samples with higher tin content are measured at a STOE STADI P diffractometer with a Ge(111) monochromatized Mo-$K_{\alpha1}$ radiation coupled to a Mythen 1K detector.

Sample preparation for measurements of dried residues is done as described for Raman spectroscopy in Chapter 4.2.1.

4.2.4 X-ray photoelectron spectroscopy

X-ray photoelectron spectra are recorded on a Leybold-Heraeus LHS 10 spectrometer using a non-monochromatized Al-K_α source (1486.7 eV). All thin film samples are cleaned by argon sputtering (E = 2 keV, 90 min). The analyzer is operated at a constant pass energy of 100 eV leading to an energy resolution with a full width at half-maximum (fwhm) of ~1.2 eV. The C 1s (284.5 eV) peak corresponding to adventitious carbon is used as energy reference to compensate energy shifts due to charging. The oxidation state of the main Ge, Sn, and P fraction is determined by the binding energies of the Ge $2p_{3/2}$, the Ge 3d, the Sn $3d_{5/2}$, and the P 2p signal, respectively, by comparing with literature values.[163] The oxidation states of germanium are additionally confirmed by the Auger parameter ($a' = E_{kin}\,(L_3M_{45}M_{45}) + E_b\,(2p_{3/2}) = 2362.4$ eV for Ge(0)).[185] All spectra are recorded in an ultra-high vacuum chamber at a pressure below 5×10^{-8} mbar. Core level spectra are deconvoluted by using Voigt functions and linear background subtraction. Oxidation states are identified by deconvolution of the P 2p, Sn $3d_{5/2}$, Ge 3d, and Ge $2p_{3/2}$ peaks, respectively. Quantification is accomplished by comparison of the peak areas of the respective deconvoluted P, Sn, and Ge species. The derived peak area fractions depend sensitively on the energy reference. The precision of the energy referencing of $\pm$0.1 eV influences the outcome of the peak deconvolution and, thus, introduces the given errors of about 5% for each P, Sn, and Ge fraction.

4.2.5 Scanning electron microscopy

Scanning electron microscopy (SEM) is performed using a FEI Helios NanoLab G3 UC scanning electron microscope equipped with a field emission gun operated at 3 - 5 kV. Substrates for SEM analysis are glued onto an aluminum sample holder using silver lacquer (ACHSEON 1415, Plano). SEM images of cycled electrodes are recorded with a FEI Helios NanoLab G3 UC scanning electron microscope equipped with a field emission gun operated at 3 - 5 kV.

4.2.6 Energy dispersive X-ray spectroscopy

EDX measurements of thin films are performed at an operating voltage of 20 kV with an X-MaxN Silicon Drift Detector with 80 mm² detector area (OXFORD INSTRUMENTS) and AZTec acquisition software (OXFORD INSTRUMENTS). Sample preparation is done as described in Chapter 4.2.5.

EDX measurements of dried residues are carried out using a Hitachi TM-1000 tabletop microscope device. Data evaluation is performed using the SWIFT-ED-TM program (OXFORD INSTRUMENTS: INCA System Software).

4.2.7 Nuclear magnetic resonance spectroscopy

NMR-spectroscopy is carried out on a BRUKER GmbH Ultrashield400 spectrometer. The air sensitive sample solutions are filled inside a glovebox into Norell® glass tubes (DEUTERO, outer diameter 0.3 mm) which are closed using plastic caps. A Norell® tube is then placed in a NMR tube (inner diameter 0.4 mm) which is filled with the deuterated solvent.

4.2.8 Dynamic light scattering

Dynamic light scattering for PMMA particle size determination is performed on a Malvern Zetasizer.

4.2.9 Profilometry

Film roughness and thickness of all prepared thin film samples is by default determined with a Veeco Dektak profilometer.

4.2.10 Electrochemical measurements

Electrochemical measurements are performed in a climate chamber (Binder, Germany) at 25 °C using a battery cycler (Series 4000, Maccor).

Electrodes prepared from K_4Ge_9/*en* solutions are cycled at a *C*-rate of 0.11 *C* during the first two cycles and at 0.23 *C* during the other cycles. Measurements are stopped after 100 charge-discharge-cycles. Rate tests are performed at 0.23 *C*, 0.38 *C*, 0.56 *C*, 1.13 *C*, and 2.23 *C* after the first 20 cycles (two cycles

at 0.11 *C*, 18 cycles at 0.23 *C*). This is done to prevent a strong overlap of the capacity fading during the first 20 cycles with the rate test. Three cycles are done at every rate.

Germanium electrodes prepared from slurries and Ge/P electrodes are cycled at *C*-rates of 0.1 *C* during the first two cycles and at 0.2 *C* during the other cycles. For all Ge and Ge/P electrodes, independent of the preparation procedure, lithiation is either done in constant current mode (CC) or in constant current-constant voltage mode (CCCV) with a current limitation corresponding to 0.05 *C*, while delithiation is done in CC mode. The voltage range is always 0.02 – 2 V vs. Li/Li^+.

Tin and mixed Ge/Sn electrodes are cycled in a voltage range of 0.01 – 2 V vs. Li/Li^+ at *C*-rates of 0.1 *C* during the first two cycles and at 0.2 *C* during the other cycles. Sn electrodes are referenced to the theoretical capacity of 994 mAh g^{-1} of $Li_{4.4}Sn$, while Ge/Sn electrodes are referenced to the theoretical capacity according to the exact composition of the precursor material. All measurements are carried out in CCCV mode for lithiation and CC mode for delithiation.

P electrodes are cycled in a voltage range of 0.001 – 2.5 V vs. Li/Li^+ at *C*-rates of 0.1 *C* during the first two cycles and at 0.2 *C* during the other cycles. The electrodes are referenced to the theoretical gravimetric capacity of 2596 mAh g^{-1} of Li_3P. All measurements are carried out in CCCV mode for lithiation and CC mode for delithiation.

4.3 Syntheses

The following chapter describes the synthesis of solid state phases, the preparation of Zintl solutions as well as thin film and electrode preparation. Powder X-ray diffactograms of the synthesized phases are presented in the Appendix Chapter 5.1 (Figures 5.26 – 5.33).

4.3.1 Synthesis of K_4Ge_9

Synthesis of K_4Ge_9 is performed according to Fässler *et al*.[122g] Inside a glovebox, 1.07 g (27.4 mmol) potassium and 4.03 g (55.5 mmol) germanium are filled into a stainless steel autoclave (see Chapter 5.1.2), which is then sealed by a screw cap. The autoclave is transferred to an argon filled corundum tube. The mixture is then heated to 650 °C with a heating rate of 2 °C min^{-1}. After 46 h at 650 °C, it gets cooled down to room temperature at a rate of 1 °C min^{-1}.

4.3.2 Synthesis of K_4Sn_9

The synthesis of K_4Sn_9 is performed analogously to the synthesis of K_4Ge_9. Inside a glovebox, 1.07 g (27.4 mmol) potassium and 6.59 g (55.5 mmol) tin are filled into a stainless steel autoclave which is then is transferred to an argon filled corundum tube. The mixture is heated to 950 °C with a heating rate of 2 °C min^{-1}. After 46 h at 950 °C, it is cooled down to room temperature at a rate of 1 °C min^{-1}.

4.3.3 Synthesis of "$K_4Ge_5Sn_4$"

Inside a glovebox, 157.27 mg (4.022 mmol) potassium, 365.23 mg (5.028 mmol) germanium, and 477.50 mg (4.022 mmol) tin are filled into a tantalum ampoule (for details on ampoule preparation see Chapter 5.1.2). The ampoule gets sealed using an electric arc furnace and put into a fused silica glass tube. After evacuating, the glass tube is transferred to an oven and heated to 950 °C with a heating rate of 2 °C min^{-1}. After 48 h at 950 °C it is cooled to room temperature at a rate of 1 °C min^{-1}.

4.3.4 Synthesis of "$K_2Ge_2P_2$"

269 mg (6.88 mmol) potassium, 500 mg (6.88 mmol) germanium, and 213 mg (6.88 mmol) red phosphorus are filled into a tantalum ampoule inside a glovebox. After sealing the ampoule is transferred to a fused silica glass tube, which is then evacuated. The mixture is then heated to 650 °C with a heating rate of 2 °C min^{-1}. After 48 h at 650 °C it is cooled to room temperature at a rate of 1 °C min^{-1}.

4.3.5 Synthesis of "$K_2Ge_7P_2$"

60 mg (15.34 mmol) potassium, 392 mg (53.69 mmol) germanium, and 48 mg (15.34 mmol) red phosphorus are filled into a tantalum ampoule inside a glovebox. After sealing the ampoule is transferred to a fused silica glass tube, which is then evacuated. The mixture is then heated to 950 °C with a heating rate of 2 °C min^{-1}. After 48 h at 950 °C it is cooled to room temperature at a rate of 1 °C min^{-1}.

4.3.6 Synthesis of NaP_7

Synthesis of NaP_7 is performed according to Nilges *et al*.[164] 47.93 mg (2.085 mmol) sodium, 452.1 mg (14.60 mmol) red phosphorus and 10.00 mg (0.074 mmol) copper(II)chloride are filled into a graphitized fused silica glass ampoule. The ampoule is sealed under dynamic vacuum, provided by a Schlenk apparatus. The sealed ampoule is placed in a muffle furnace and heated to 550 °C with a heating rate of 55 °C h^{-1}. After 7 d at 950 °C, the ampoule is cooled down to room temperature at a rate of 22 °C h^{-1}.

4.3.7 Synthesis of SnTe

492.2 mg (mmol) tin and 510.4 mg (mmol) tellurium are filled into a graphitized fused silica glass ampoule. The ampoule is sealed under dynamic vacuum, provided by a Schlenk apparatus. The sealed ampoule is placed in a muffle furnace and heated to 990 °C with a heating rate of 55 °C h^{-1}. After 2 d at 950 °C, the ampoule is cooled down to 770 °C at a rate of 2 °C h^{-1}. After 1 d at 770 °C, the ampoule is taken out of the muffle furnace and put into cold water to rapidly cool it down.

4.3.8 Synthesis of poly(methyl methacrylate) opals

The PMMA opals are prepared by emulsion polymerization as described by Smarsly *et al.*[143] 35.5 g (355 mmol) MMA and 5.00 mg (17.3 µmol) SDS (for 250 nm particle size) are added under stirring into water (98.0 mL). Beforehand, the water has been purged with nitrogen under reflux conditions for 0.5 h. 56.0 mg (207 µmol) potassium persulfate, solved in 2 mL water are added after stirring at 90 °C for 1 h. After stirring for additional 2.5 h at 90 °C the reaction is stopped by ice cooling and further stirred at room temperature overnight. The product is filtered and washed by several centrifugation and redispersion steps. Particle size can be controlled by the amount of SDS added to the reaction mixture, with a higher amount of SDS resulting in smaller PMMA particles (24.5 mg, 84.8 µmol SDS are used for PMMA particles with 125 nm particle size).

4.3.9 Preparation of precursor solutions

Precursor solutions are prepared in Schlenk glass tubes which have been baked out prior to use. Due to the sensitivity towards oxygen and water, all preparations are performed in a glovebox. The used solvents ethylene diamine and dimethylformamide are dried over calcium hydride under reflux conditions before usage. The compositions of the different precursor solutions are summarized in Table 4.4. For reasons of clarity, information about what solution composition is used for which experiment is given directly in the respective chapters.

Table 4.4. Compositions of the prepared precursor solutions.

Compound A	**Compound B**	**Solvent**	**Molar ratio**
K_4Ge_9 (50 mg, 0.06 mmol)	-	*en* (1 mL)	-
K_4Ge_9 (100 mg, 0.12 mmol)	-	*dmf* (2 mL)	-
K_4Ge_9 (100 mg, 0.12 mmol)	PPh_3 (1.00 mg, 3.81 µmol)	*en* (2 mL)	Ge >> P
K_4Ge_9 (25.0 mg, 0.03 mmol)	PPh_3 (73.0 mg, 0.30 mmol)	*en* (1 mL)	Ge : P 1:1
K_4Ge_9 (25.0 mg, 0.03 mmol)	PPh_3 (36.0 mg, 0.15 mmol)	*en* (1 mL)	Ge : P 2:1
K_4Ge_9 (50.0 mg, 0.06 mmol)	PPh_3 (48.3 mg, 0.18 mmol)	*en* (1 mL)	Ge : P 2.7:1
K_4Ge_9 (100 mg, 0.12 mmol)	NaP_7 (12.7 mg, 0.05 mmol)	*en* (2 mL)	Ge : P 3:1
K_4Ge_9 (50 mg, 0.06 mmol)	NaP_7 (9.5 mg, 0.04 mmol)	*en* (1 mL)	Ge : P 2:1
K_4Ge_9 (100 mg, 0.12 mmol)	P_{red} (34.0 mg, 1.00 mmol)	*en* (2 mL)	Ge : P 1:1
K_4Ge_9 (100 mg, 0.12 mmol)	P_{red} (11.0 mg, 0.36 mmol)	*en* (2 mL)	Ge : P 3:1
K_4Ge_9 (100 mg, 0.12 mmol)	P_{red} (3.44 mg, 0.11 mmol)	*en* (2 mL)	Ge : P 10:1
$K_2Ge_2P_2$ (51.0 mg, 0.18 mmol)	-	*en* (2 mL)	-
$K_2Ge_7P_2$ (80.0 mg, 0.12 mmol)	-	*en* (2 mL)	-
K_4Sn_9 (61.0 mg, 0.05 mmol)	-	*en* (1 mL)	-
K_4Sn_9 (122 mg, 0.10 mmol)	-	*dmf* (2 mL)	-
$K_4Ge_5Sn_4$ (50.0 mg, 0.05 mmol)	-	*en* (1 mL)	-
$K_4Ge_5Sn_4$ (99.0 mg, 0.10 mmol)	-	*en* (2 mL)	-
K_4Ge_9 (81.0 mg, 0.10 mmol)	K_4Sn_9 (122 mg, 0.10 mmol)	*en* (4 mL)	Ge : Sn 1:1
K_4Ge_9 (81.0 mg, 0.10 mmol)	K_4Sn_9 (122 mg, 0.10 mmol)	*dmf* (4 mL)	Ge : Sn 1:1
Se (36.6 mg, 0.40 mmol)	-	*en* (1 mL)	-
Se (39.5 mg, 0.50 mmol)	-	*en* (1 mL)	-
Se (7.90 mg, 0.10 mmol)	-	*en* (1 mL)	-
K (10.0 mg, 0.25mmol)	Se (197 mg, 2.50 mmol)	*en* (10 mL)	K : Se 1:10
K_4Sn_9 (244 mg, 0.20 mmol)	Se (31.6 mg, 0.40 mmol)	*en* (4 mL)	Sn : Se 4.5:1

K_4Sn_9 (68.0 mg, 0.06 mmol)	Se (39.5 mg, 0.50 mmol)	*en* (2 mL)	Sn : Se 1:1
K_4Sn_9 (54.4 mg, 0.04 mmol)	Se (31.6 mg, 0.40 mmol)	*en* (2 mL)	Sn : Se 1:1
K_4Sn_9 (122 mg, 0.10 mmol)	Se (8.00 mg, 101 µmol)	*en* (2 mL)	Sn : Se 9:1
K (19.5 mg, 0.50 mmol)	Te (31.9 mg, 0.25 mmol)	*en* (3 mL)	K : Te 2:1
K_4Sn_9 (68.0 mg, 0.06 mmol)	K_2Te (103 mg, 0.50 mmol)	*en* (6 mL)	Sn : Te 1:1
K_4Sn_9 (68.0 mg, 0.06 mmol)	K_2Te (103 mg, 0.50 mmol)	*en* (4 mL)	Sn : Te 1:1
K_4Sn_9 (68.0 mg, 0.06 mmol)	K_2Te (51.4 mg, 0.25 mmol)	*en* (5 mL)	Sn : Te 2:1
K_4Sn_9 (122 mg, 0.10 mmol)	K_3P_7 (21.5 mg, 0.06 mmol)	*en* (3 mL)	Sn : P 2.2:1
K (54.0 mg, 1.38 mmol)	P_{red} (100 mg, 3.23 mmol)	*en* (2 mL)	K : P 3:7
K (13.5 mg, 0.35 mmol)	P_{red} (25.0 mg, 0.81 mmol)	*en* (2 mL)	K : P 3:7

Preparation of K_4Ge_9/*en* and K_4Sn_9/*en* and the respective *dmf* solutions

The respective solid state compound is filled into a baked out Schlenk glass tube inside a glovebox. The solvent *en* (or dmf, respectively) is added dropwise and the mixture is stirred at room temperature for a certain time (3 h for K_4Ge_9, 15 min for K_4Sn_9). In both cases, a clear, red solution is formed. Formation of a green solution indicates cluster oxidation and thus the solvent has to be further dried. The solution is filtered into a baked out Schlenk glass tube using a glass fiber filter inside a glovebox.

Preparation of K_4Ge_9/PPh_3/*en*

K_4Ge_9 and PPh_3 are given together into a baked out Schlenk glass tube inside a glovebox. The solvent *en* is added dropwise and the mixture is stirred at room temperature for 1 h time. Stirring for 3 h results in a dark brown-black precipitation. The green solution is filtered into a baked out Schlenk glass tube using a glass fiber filter inside a glovebox.

Preparation of K_4Ge_9/NaP_7/*en*

K_4Ge_9 and NaP_7 are given together into a baked out Schlenk glass tube inside a glovebox. The solvent *en* is added dropwise and the solution is stirred at room temperature for 3 h. The red solution is filtered into a baked out Schlenk glass tube using a glass fiber filter inside a glovebox.

Preparation of K_4Ge_9/P_{red}/*en*

K_4Ge_9 and P_{red} are given together into a baked out Schlenk glass tube inside a glovebox. The solvent *en* is added dropwise and the solution is stirred at room temperature for 24 h. The red solution is filtered into a baked out Schlenk glass tube using a glass fiber filter inside a glovebox.

Preparation of $K_2Ge_2P_2$/*en* and $K_2Ge_7P_2$/*en*

The respective solid state compound is filled into a baked out Schlenk glass tube inside a glovebox. The solvent *en* is added dropwise and the mixture is stirred at room temperature for a certain time (4 h for $K_2Ge_2P_2$, 1.5 h for $K_2Ge_7P_2$). In both cases, a clear, red solution is formed. The solution is filtered into a baked out Schlenk glass tube using a glass fiber filter inside a glovebox.

Preparation of a mixed K_4Ge_9/*en* and K_4Sn_9/*en* solution

The respective solid state compound is filled into a baked out Schlenk glass tube inside a glovebox. The solvent *en* or *dmf* is added dropwise (2 mL each) and the mixture is stirred at room temperature for a certain time (3 h for K_4Ge_9, 15 min for K_4Sn_9). In both cases, a clear, red solution is formed. The solutions are filtered into two separate baked out Schlenk glass tubes using a glass fiber filter inside a glovebox. Again inside a glovebox, the K_4Sn_9/*en* solution is dropwise added to the K_4Ge_9/*en* solution. The mixed red solution is stirred for another 45 min at room temperature and then filtrated using a glass fiber filter inside a glovebox.

Preparation of "$K_4Ge_5Sn_4$"/*en*

"$K_4Ge_5Sn_4$" is given into a baked out Schlenk glass tube inside a glovebox. The solvent *en* is added dropwise and the mixture is stirred at room temperature for 15 min. A clear, red solution is formed. The solution is filtered into a baked out Schlenk glass tube using a glass fiber filter inside a glovebox.

Preparation of a mixture of Se/*en* and K_4Sn_9/*en*

Se is given into a baked out Schlenk glass tube inside a glovebox. The solvent *en* is dropwise added and the solution is stirred at room temperature for 24 h. The yellow-green solution is filtrated into a baked out Schlenk glass tube using a glass fiber filter inside a glovebox. K_4Sn_9 is given into a separate baked out Schlenk glass tube inside a glovebox and stirred at room temperature for 15 min after *en* addition.

The red solution is filtered into a baked out Schlenk glass tube using a glass fiber filter inside a glovebox. The Se/*en* solution is then dropwise added to the K_4Sn_9/*en* solution and the resulting red solution is stirred for another 15 min at room temperature. A black precipitation can be observed. Stirring for 1 h instead of 15 min results in precipitation of elemental Sn. After stirring, the mixed solution is again filtrated using a glass fiber filter inside a glovebox and a clear, red solution is obtained.

Preparation of a mixture of K/Se/*en* and K_4Sn_9/*en*

K and Se are given into a baked out Schlenk glass tube inside a glovebox. The solvent *en* is dropwise added. The mixture is then stirred at room temperature for 3 d, resulting in a dark-green solution. The solution is filtrated into a baked out Schlenk glass tube using a glass fiber filter inside a glovebox. K_4Sn_9 is given into a separate baked out Schlenk glass tube inside a glovebox and stirred at room temperature for 15 min after *en* addition. The red solution is filtered into a baked out Schlenk glass tube using a glass fiber filter inside a glovebox. 2 mL of the K/Se/*en* solution are then dropwise added to the K_4Sn_9/*en* solution, resulting in an immediate precipitation of a dark solid. Filtration of the remaining solution using a glass fiber filter gives a clear, amber-colored solution.

Preparation of Se/K_4Sn_9/*en*

K_4Sn_9 and Se are given together into a baked out Schlenk glass tube inside a glovebox. The solvent *en* is added dropwise and the solution is stirred at room temperature for 15 min (for molar ratios of Sn : Se up to 4.5:1; molar ratios of Sn : Se 9:1 are stirred for 2 h). The dark red solution is filtered into a baked out Schlenk glass tube using a glass fiber filter inside a glovebox.

Preparation of K_2Te/K_4Sn_9/*en*

K and Te are given into a baked out Schlenk glass tube inside a glovebox. The solvent *en* is dropwise added. The mixture is then stirred at room temperature for 24 h. The solution is filtrated into a baked out Schlenk glass tube using a glass fiber filter inside a glovebox. K_4Sn_9 is given into a separate baked out Schlenk glass tube inside a glovebox and stirred at room temperature for 15 min after *en* addition. The red solution is filtered into a baked out Schlenk glass tube using a glass fiber filter inside a glovebox. The K_2Te/*en* solution is then dropwise added to the K_4Sn_9/*en* solution and the resulting dark red solution is stirred for another 15 min. The solution is filtered into a baked out Schlenk glass tube using a glass fiber filter inside a glovebox.

Preparation of K_3P_7/*en*

K and P_{red} are given into a baked out Schlenk glass tube inside a glovebox. The solvent *en* is dropwise added. The mixture is then stirred at room temperature for 24 h. The dark red solution solution is filtrated into a baked out Schlenk glass tube using a glass fiber filter inside a glovebox.

Preparation of a mixture of K_3P_7/*en* and K_4Sn_9/*en*

A solution of K_3P_7/*en* is prepared as described above. A separate solution of K_4Sn_9/*en* is prepared as mentioned before. Both solutions are filtrated into two separate baked out Schlenk glass tubes inside a glovebox using glass fiber filters. The filtered K_3P_7/*en* solution is dropwise added to the filtered K_4Sn_9/*en* solution and the resulting solution is stirred at room temperature for a maximum of 5 min. The solution is filtered into a baked out Schlenk glass tube using a glass fiber filter inside a glovebox.

4.3.10 Ink preparation

Ink for measuring cells with germanium and tin anodes is prepared in two different ways. Firstly, ink not containing the active material is prepared as follows. Inside a glovebox, 400 mg C65, 400 mg polyvinylidene fluoride, and 5 mL NMP are filled into a glass vessel which has been dried at 120 °C for 24 h. The mixture is stirred at 2000 rpm for 5 min using a planetary mixer. Another 3 mL of NMP are added and the mixture is again stirred at 2000 rpm for 5 min. A viscous slurry is obtained.

Inks containing the active materials germanium or tin are prepared as following. Inside a glovebox, 600 mg of active material (either K_4Ge_9 or K_4Sn_9), 75 mg C65, and 75 mg PEO) are filled into a glass vessel which has been dried at 120 °C for 24 h. 3 g toluene are added and the mixture is stirred at 60 °C for 20 min. A viscous slurry is obtained.

4.3.11 Thin film preparation

Thin film preparations are performed inside a glovebox under argon atmosphere. If not stated differently in the respective chapter, all films are prepared using PMMA opals with a size of 250 – 300 nm.

Preparation of inverse opal structured Ge and Ge/P thin films

Inverse opal structured germanium thin films are prepared as follows. A K_4Ge_9/*en* solution with a concentration of 50 mg (0.06 mmol) K_4Ge_9 in 1 mL *en* is prepared as described in chapter 5.3.9. After filtration over a glass fiber filter, the solution is drop-casted onto a PMMA coated substrate (see Chapter 4.1.4). After drying at room temperature under argon atmosphere, the substrate is transferred to a Schlenk glass tube. The glass tube is evacuated to a pressure of $<10^{-3}$ mbar using a Schlenk apparatus and held in an oven (Losa 600-40-180, HTM Reetz GmbH) at 100 °C for 1 h under dynamic vacuum. Following this drying step, 20 µL of a cross-linker ($GeCl_4$, $SnCl_4$ or PCl_3) are filled into the Schlenk tube, but without direct contact to the substrate. This is done by filling the cross-linker in a small snap cover glass (glass volume 3 mL) which is then inserted into the vertically held Schlenk glass tube. The substrate is held in this cross-linker saturated atmosphere. After 3 d, the cross-linker containing glass is removed and the substrate is heated up to 500 °C for 5 min under dynamic vacuum. An additional crystallization step at 600 °C for 1 h under argon atmosphere can be performed. Finally, the substrate is washed by placing it in a snap cover glass (glass volume 3 mL) filled with DMSO for 1 h and in a snap cover glass filled with THF for additional 0.5 h and dried under vacuum.

Mixed Ge/P films are prepared similarly, using the respective Ge/P solutions as described in Chapter 4.3.9. No cross-linkers are used for Ge/P films prepared using PPh_3, NaP_7, and P_{red}. Film preparation based on "$K_2Ge_2P_2$"/*en* and "$K_2Ge_7P_2$"/*en* is conducted using $GeCl_4$ as cross-linker.

Preparation of inverse opal structured Sn and Sn/Ge thin films

Sn thin films are prepared analogous to Ge thin films (with concentrations of 61 mg/0.05 mmol of K_4Sn_9 in 1 mL *en*), but at different temperatures. The first drying step is performed at 80 °C (1 h) and the second temperature treatment is carried out at 150 °C for 1h , opposing to the 100 °C (1 h) and 500 °C (5 min) for Ge. $SnCl_4$ is used as cross-linker (20 µL per substrate). Washing with DMSO and THF is performed as before mentioned for Ge films.

Mixed Sn/Ge thin films are prepared analogous to pure Sn films, utilizing the precursor solutions mentioned in Chapter 4.3.9. $GeCl_4$ is used as cross-linker (20 µL per substrate).

Preparation of inverse opal structured Sn/Se, Sn/Te, and Sn/P films

Mixed Sn/Se, Sn/Te, and Sn/P films are prepared analogous to pure Sn films, applying the same temperature treatment and washing steps. Solutions used for film preparation are given in the respective chapters and summarized in Table 4.2. No cross-linkers are used for these mixed films.

Preparation of P thin films

P thin films are prepared using K_3P_7/*en* solutions as described in Chapter 4.3.9. The procedure is performed analogous to the one described for inverse opal structured Ge thin films. After drop-casting the solution, a temperature treatment at 100 °C for 1 h under dynamic vacuum is performed. Cross-linking is done in the same way as for Ge films, but by using PCl_3. Doping experiments are performed utilizing $GeCl_4$, $SiCl_4$, or $SnCl_4$ as cross-linkers. After cross-linking, a temperature treatment at 500 °C for 5 min under dynamic vacuum is applied. Washing is performed using THF. DMSO dissolves the films and therefore is not used here.

Preparation of inverse opal structured thin films as electrodes for LIBs

Inverse opal structured thin films used as electrodes for lithium ion batteries are prepared similarly as the before mentioned films. As described in Chapter 4.1.4 there is a difference in the drop-casting process of the precursor solution, the tilt angle is removed to make sure that the loss of active material during the casting process is at an absolute minimum. Another difference is that Cu substrates with a diameter of 1.0 cm and a thickness of 0.2 mm are used instead of the standard Si substrates. The third difference is regarding the amount of solution used. While this is decided individually for thin films which are not used for electrodes, it is always held constant at 7 µL (of Zintl precursor in *en*, 50 mg/0.06 mmol K_4Ge_9 in 1 mL *en,* 122 mg/0.12 mmol of K_4Sn_9 in 2 mL *en*, and 99.4 mg/0.1 mmol "$K_4Ge_5Sn_4$" in 1 mL *en*) per Cu substrate. P electrodes shown in Figure 2.61 (Chapter 2.6.2) are prepared by drop-casting 5.5 µL of a K_3P_7/*en* solution (19.25 mg/0.525 mmol in 1 mL *en*). More details about the solutions used for electrochemical measurements are given in Chapter 4.1.6. This allows for proper determination of the mass loading which is necessary for electrochemical measurements.

Ink coating

Inks (Ge: Chapter 2.2.3; Sn: Chapter 2.4.4), prepared as mentioned in Chapter 4.3.10, are coated differently. Inside a glovebox, the slurries are coated on thin Cu foil (thickness 12 µm, diameter 14 mm)

using Mayer rods, providing different film thicknesses. After coating, the electrodes are dried at room temperature under vacuum overnight.

Inks without active material are coated on copper foil (thickness 0.2 mm, diameter 10 mm) with a film thickness of 60 µm. The active material is then added by drop-casting 6 µL of a K_4Ge_9/*en* (Chapter 2.2.3) or K_4Sn_9/*en* solution (Chapter 2.4.4) with given concentration (0.06 mmol mL^{-1} for Ge, 0.05 mmol mL^{-1} for Sn) onto the coated copper foil. Cross-linking, temperature treatment and washing is then performed as described above.

Inks containing Ge (Chapter 2.2.3) or Se (Chapter 2.4.4) are coated with 150 µm film thickness. After coating, the electrodes are dried inside a glovebox at room temperature overnight. No further cross-linking, temperature treatment or washing steps are added. For ink composition see Chapter 4.3.10.

5. Appendix

5.1 Recorded spectra and diffractograms

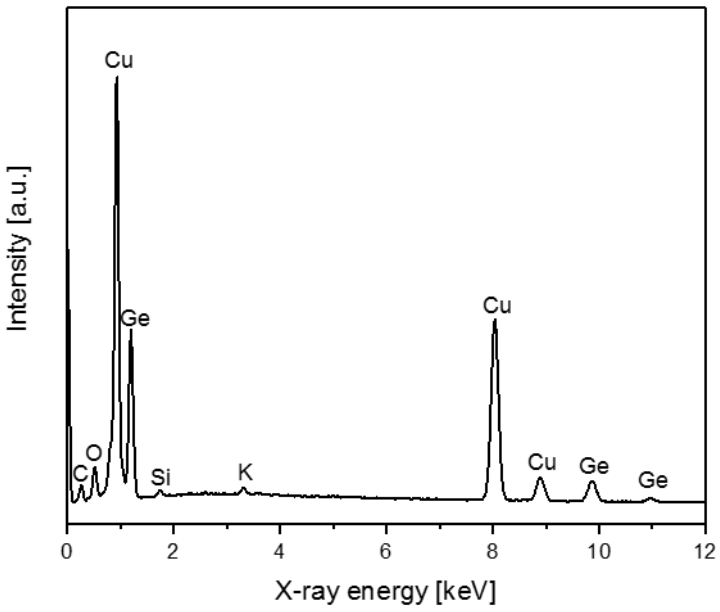

Figure 5.1. EDX spectrum of an *α*-Ge film on a copper substrate.

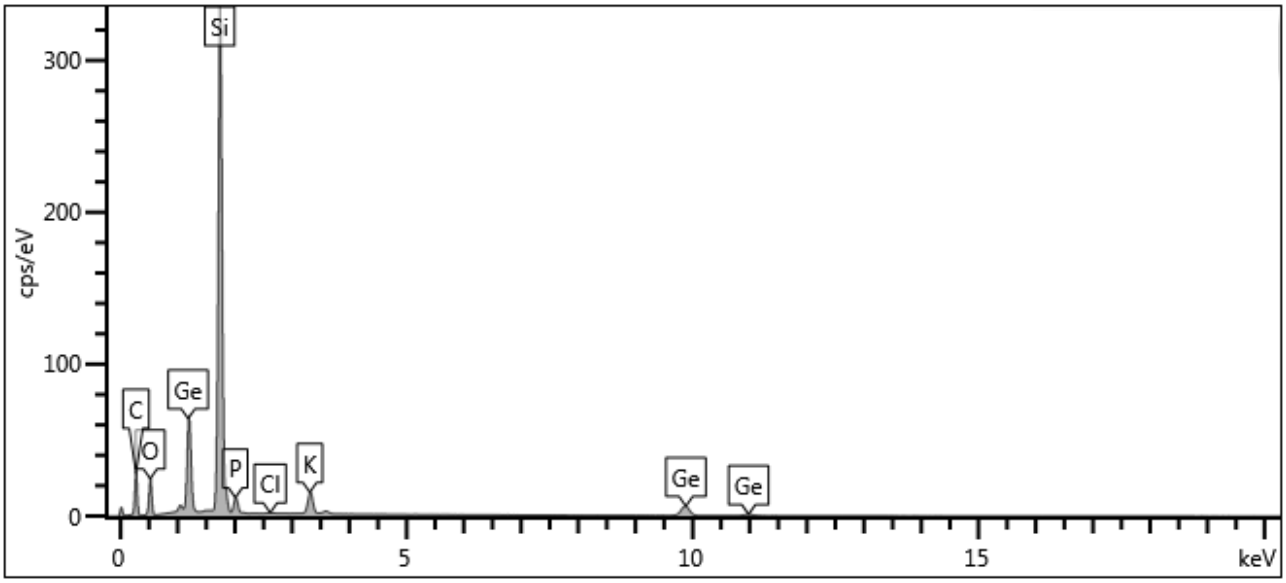

Figure 5.2. EDX spectrum of a thin film prepared from a K_4Ge_9/P_{red}/*en* solution.

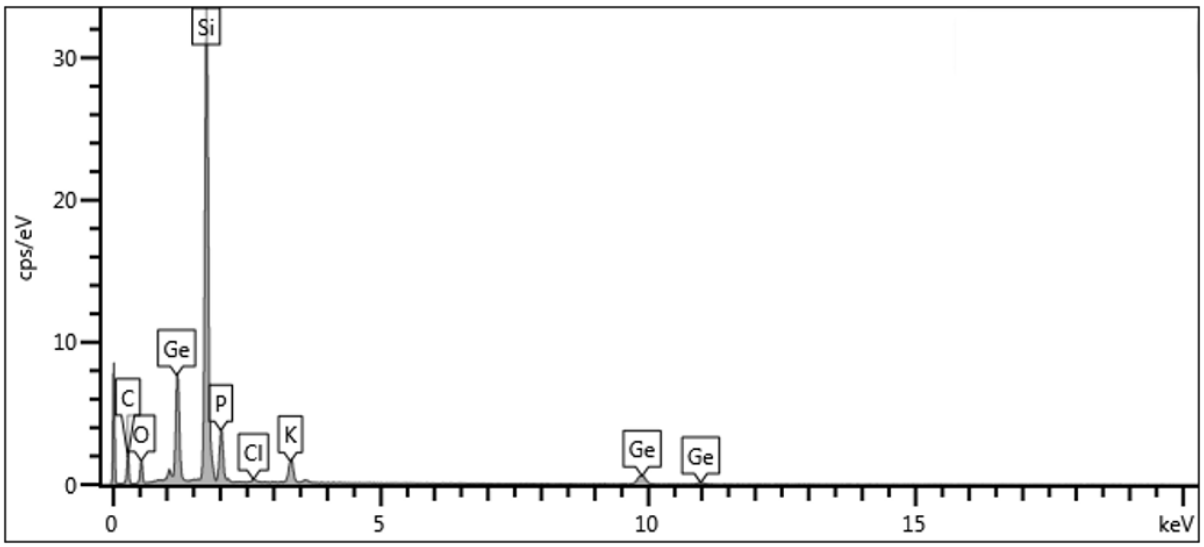

Figure 5.3. EDX spectrum of a thin film prepared from a $K_2Ge_2P_2$/*en* solution.

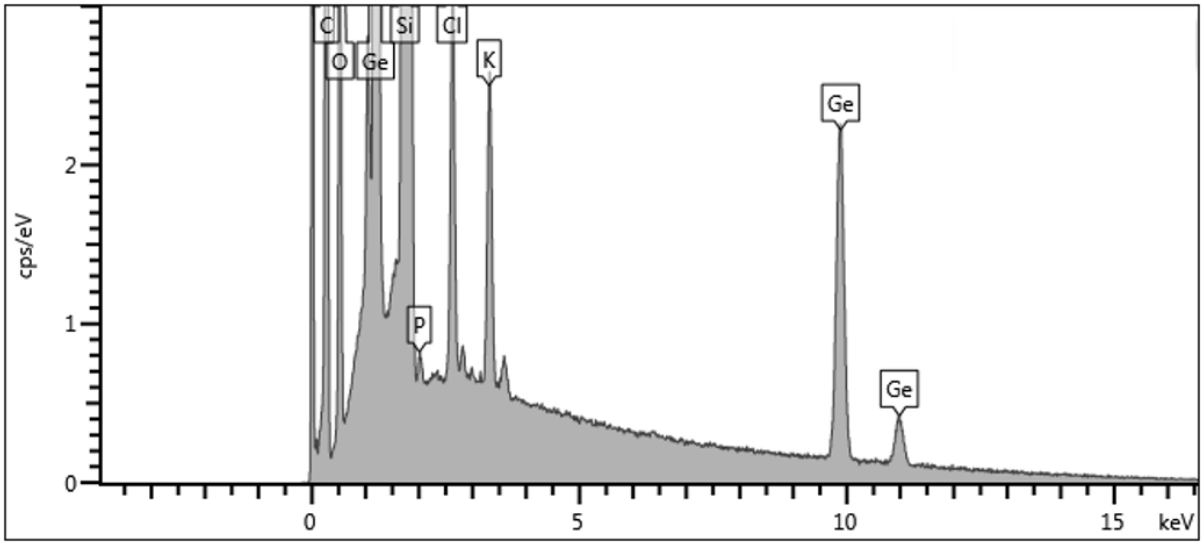

Figure 5.4. EDX spectrum of a thin film prepared from a $K_2Ge_7P_2$/*en* solution.

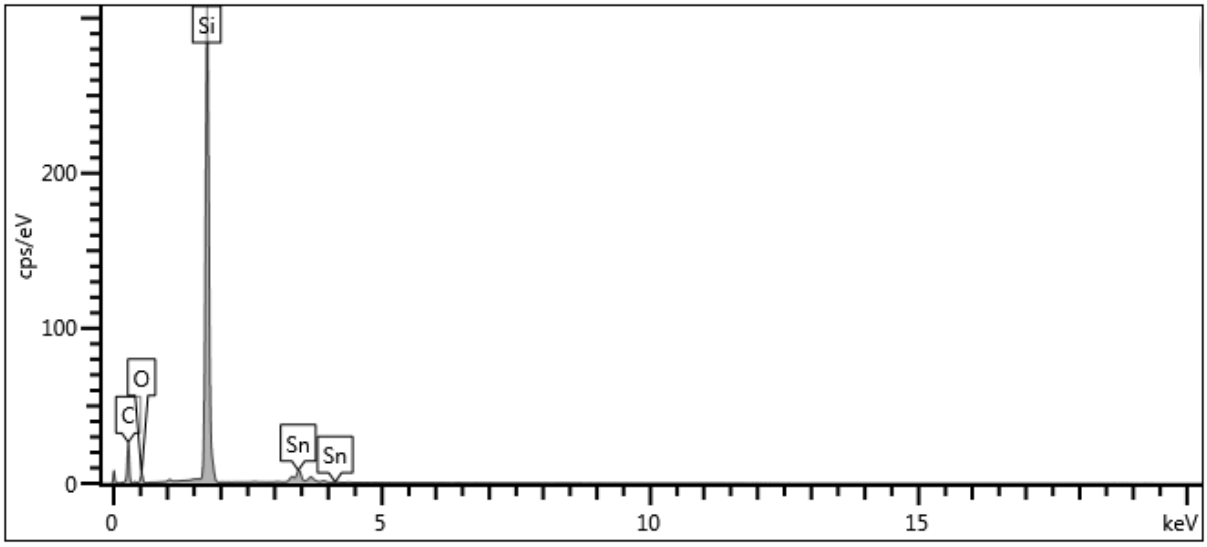

Figure 5.5. EDX spectrum of a Sn thin film prepared from a K_4Sn_9/*en* solution.

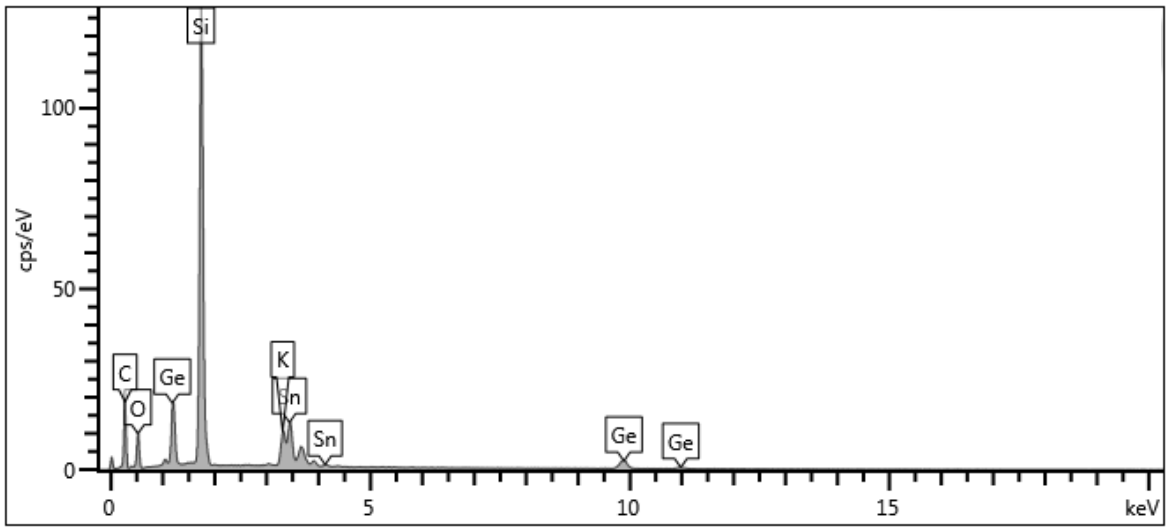

Figure 5.6. EDX spectrum of a thin film prepared using K_4Sn_9 and K_4Ge_9 in *en* as precursors.

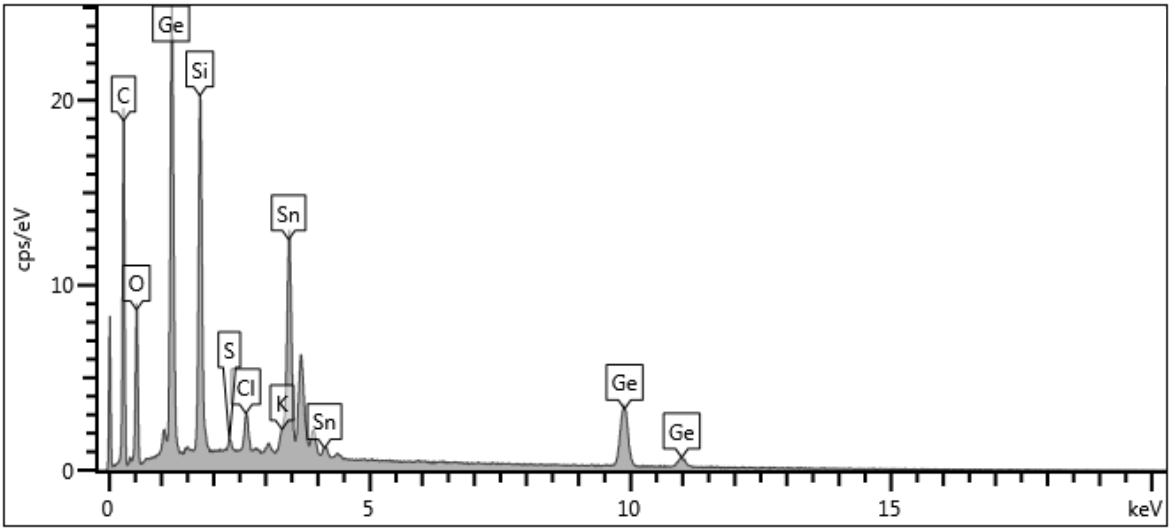

Figure 5.7. EDX spectrum of a thin film prepared from a "$K_4Ge_5Sn_4$"/*en* solution.

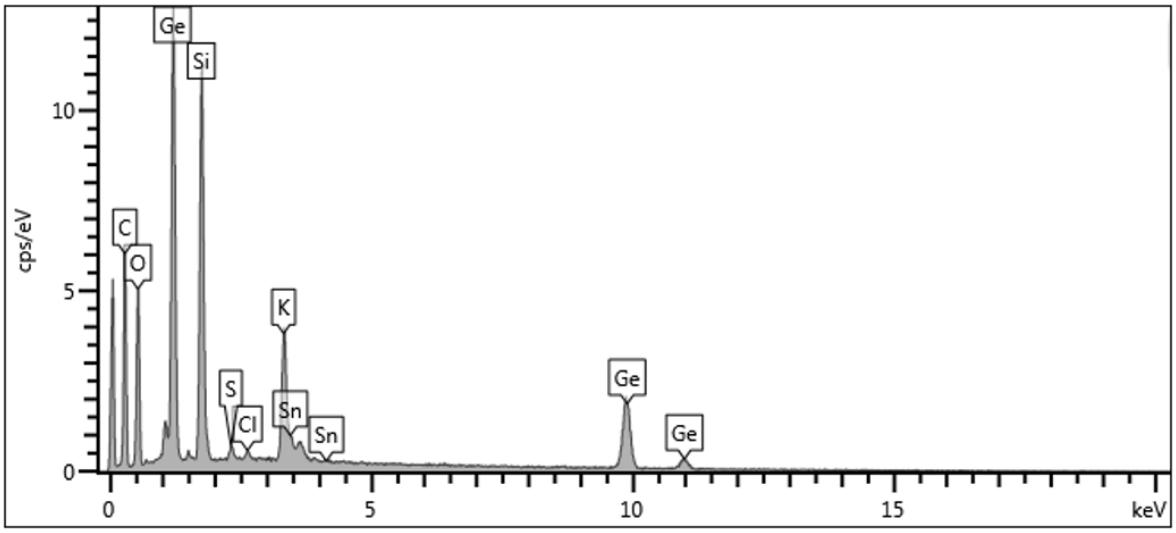

Figure 5.8. EDX spectrum of a Ge thin film linked by $SnCl_4$.

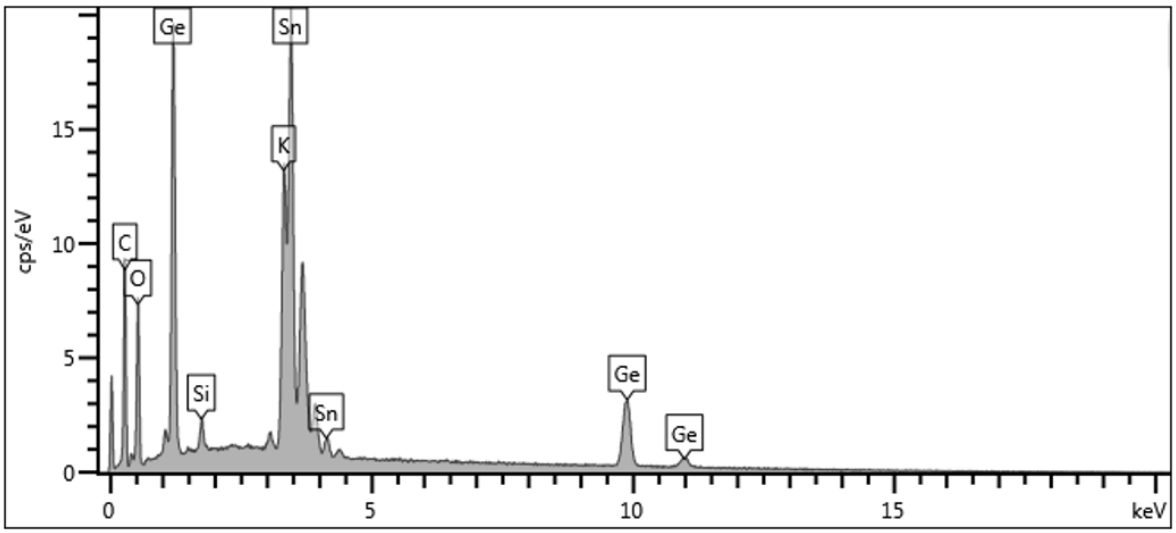

Figure 5.9. EDX spectrum of a Sn thin film linked by $GeCl_4$.

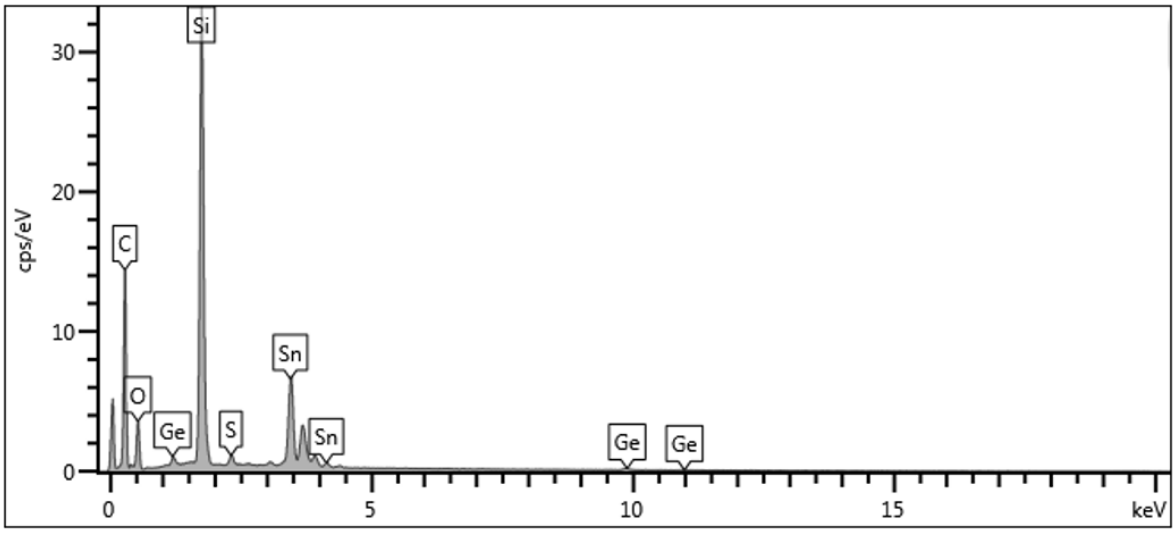

Figure 5.10. EDX spectrum of a mixed Sn/Ge thin film prepared from $K_4Ge_5Sn_4$/*en*.

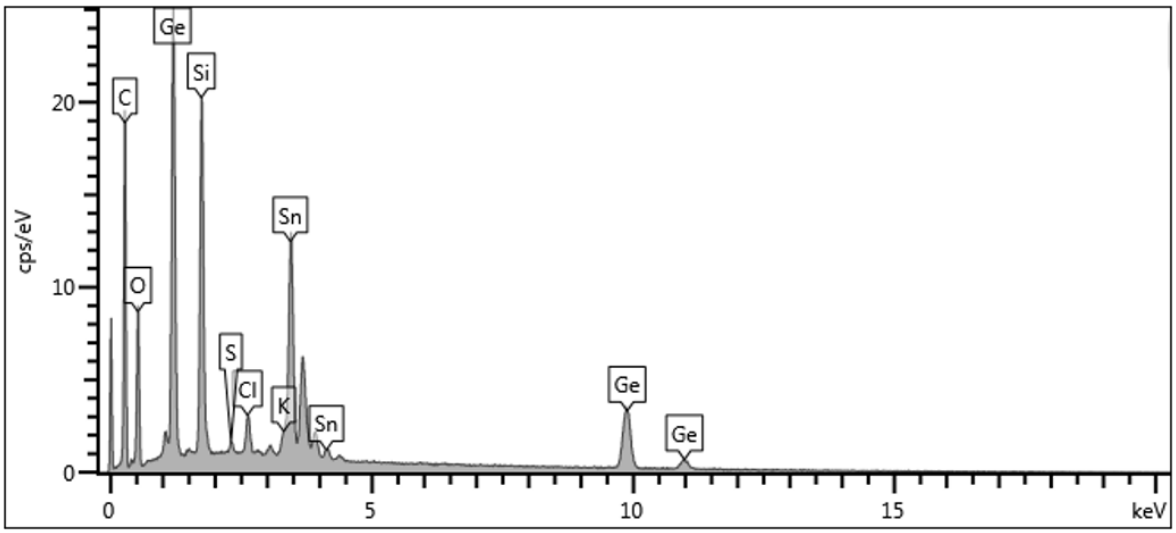

Figure 5.11. EDX spectrum of a mixed Sn/Ge thin film prepared from K_4Sn_9/*en* and K_4Ge_9/*en* solutions.

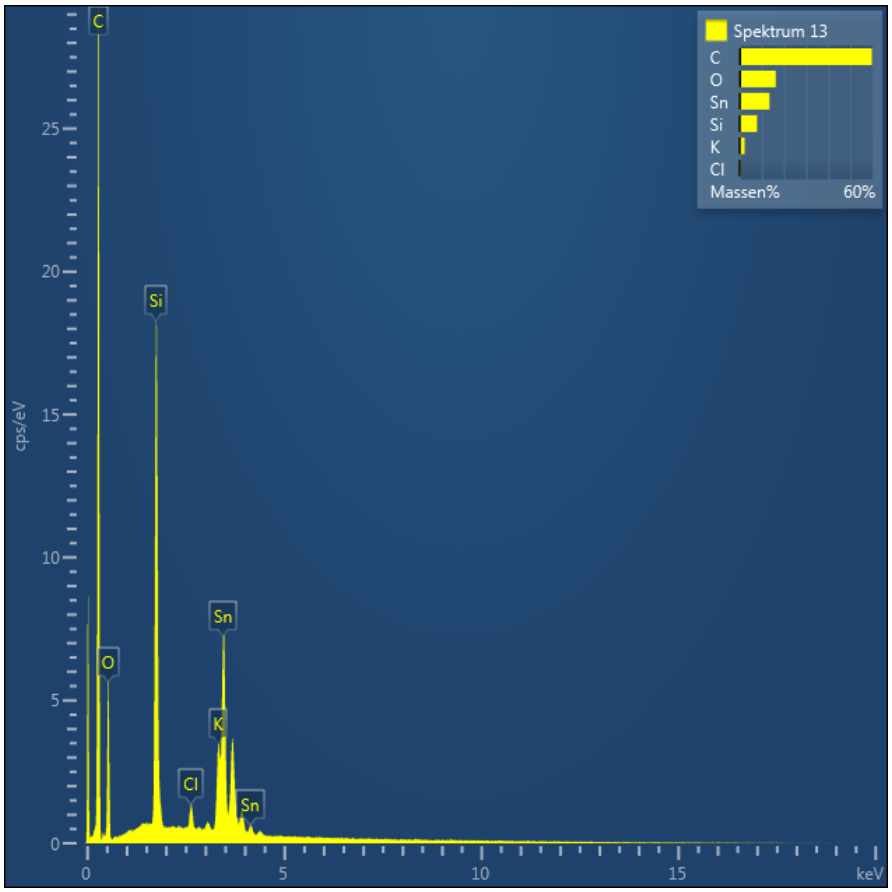

Figure 5.12. EDX spectrum of a Sn/Se film prepared from a mixture of Se/*en* and K_4Sn_9/*en* (Sn : Se 4.5:1).

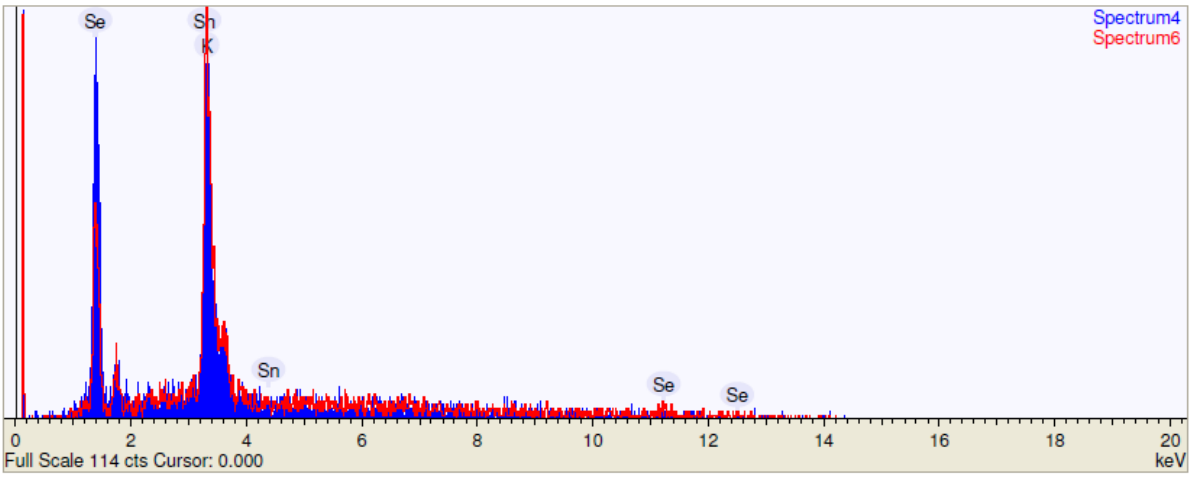

Figure 5.13. EDX spectrum of a dried residue of a mixture of K/Se/*en* and K_4Sn_9/*en*, with a molar K : Se ratio of 1 : 10 and a Sn : Se ratio of 9:10.

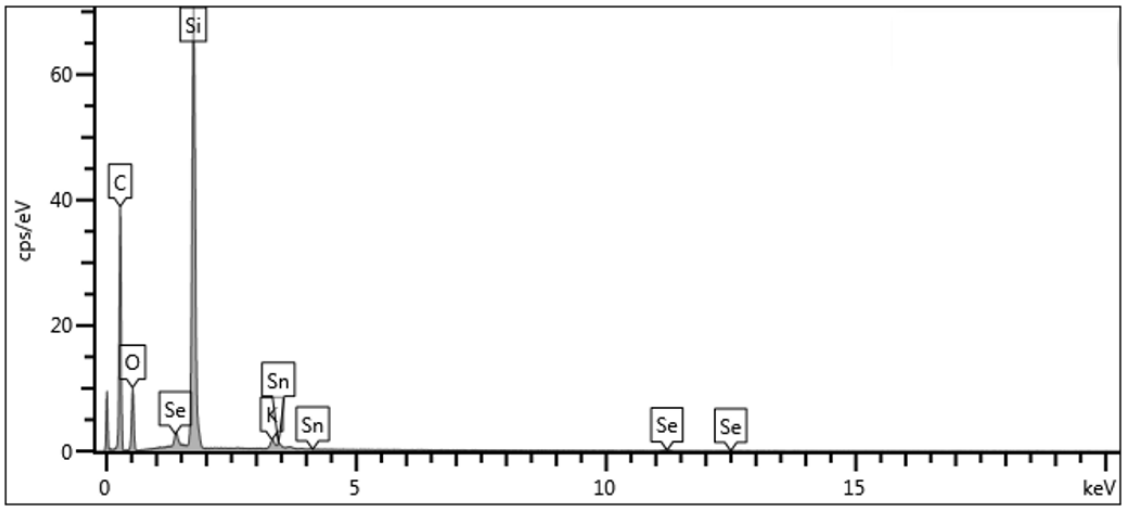

Figure 5.14. EDX spectrum of an unwashed film prepared from a mixture of K/Se/*en* and K_4Sn_9/*en* with a molar ratio of Sn : Se of 9 : 10.

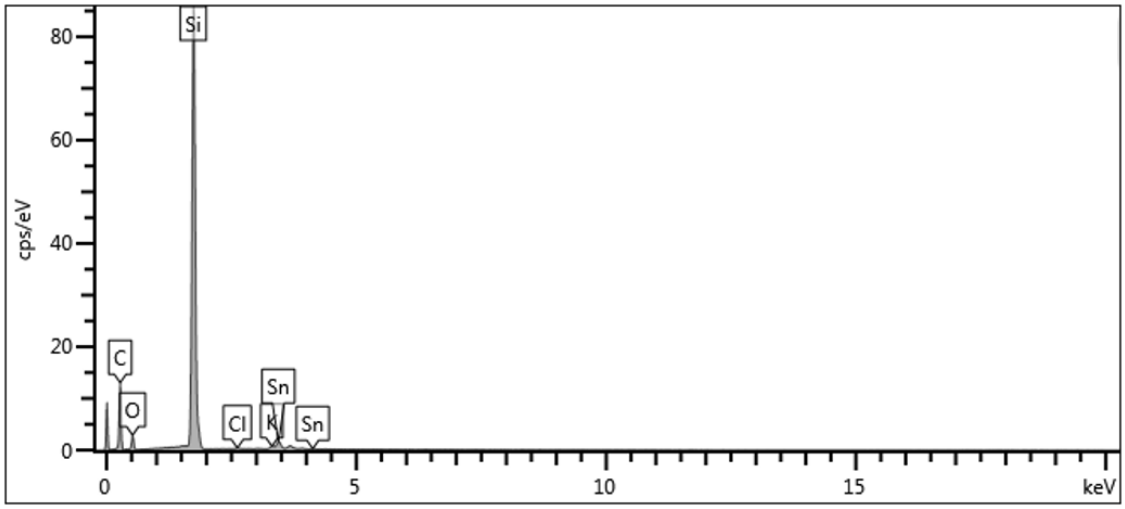

Figure 5.15. EDX spectrum of an unwashed film prepared from a Se/K_4Sn_9/*en* solution.

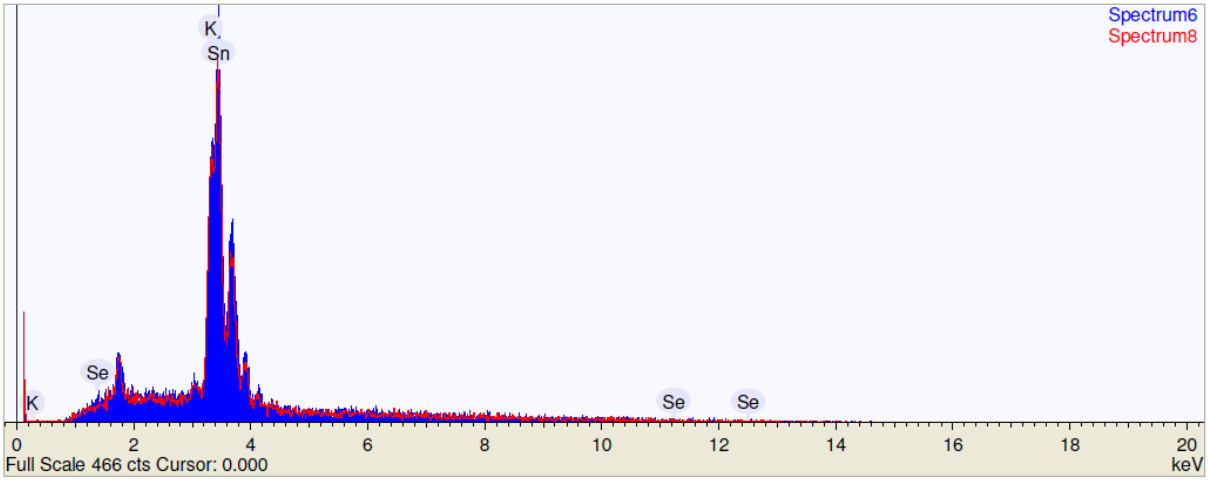

Figure 5.16. EDX spectra of a dried residue of a Se/K_4Sn_9/*en* solution. Se was manually included in the wt.% calculation but could not be detected.

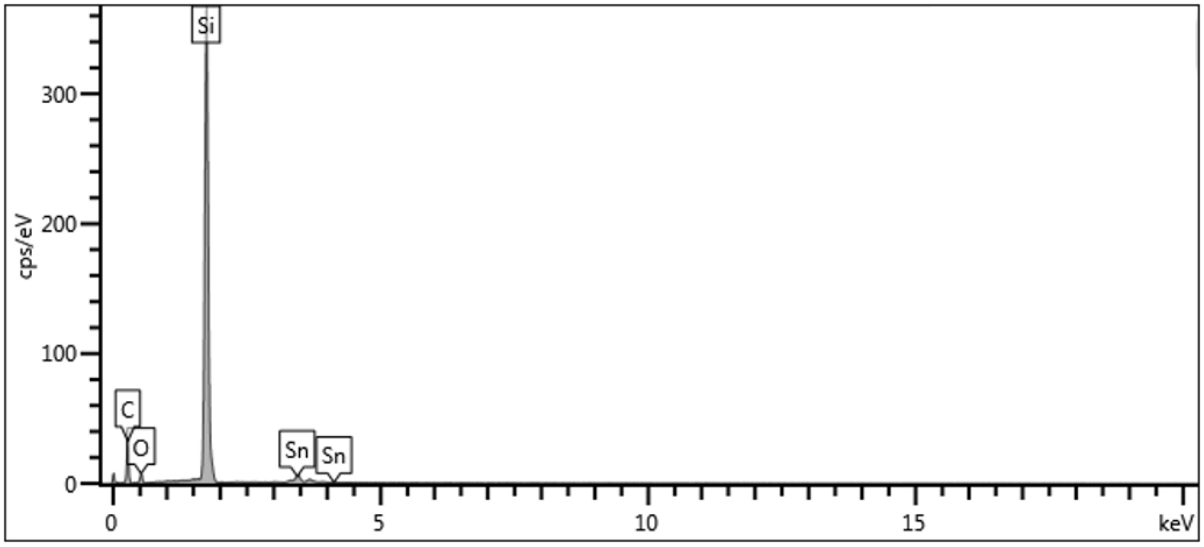

Figure 5.17. EDX spectrum of a washed film prepared from a K_2Te/K_4Sn_9/*en* solution.

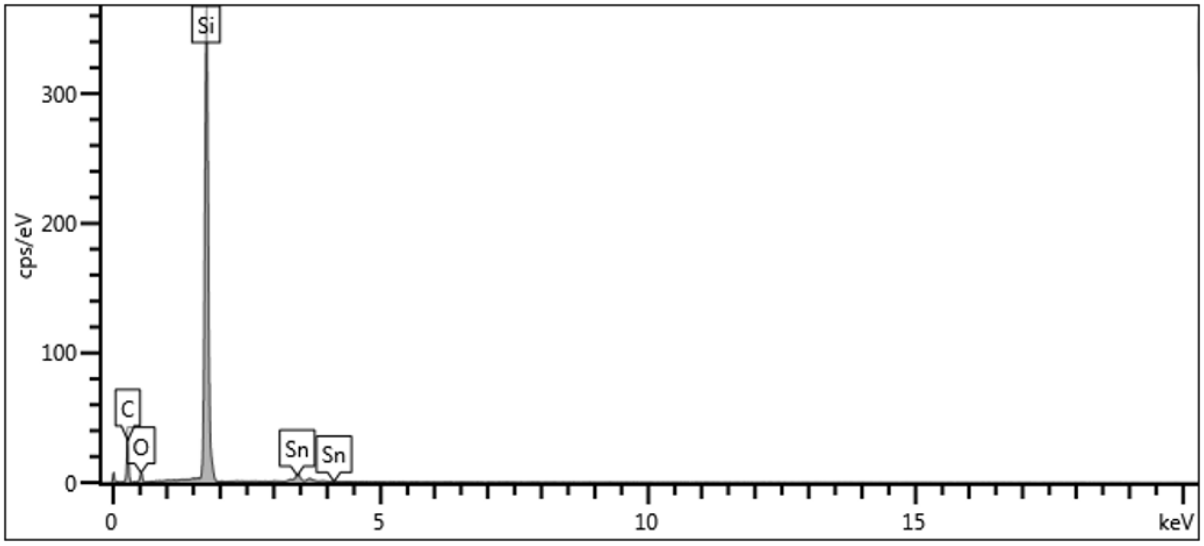

Figure 5.18. EDX spectrum of an unwashed film prepared from a K_2Te/K_4Sn_9/*en* solution.

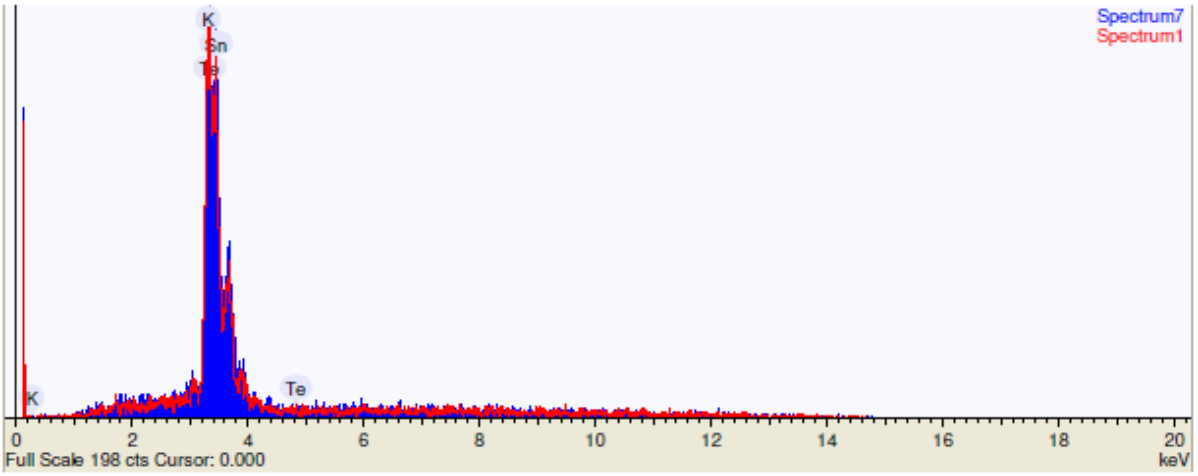

Figure 5.19. EDX spetra of dried residues of a K_2Te/K_4Sn_9/*en* solution.

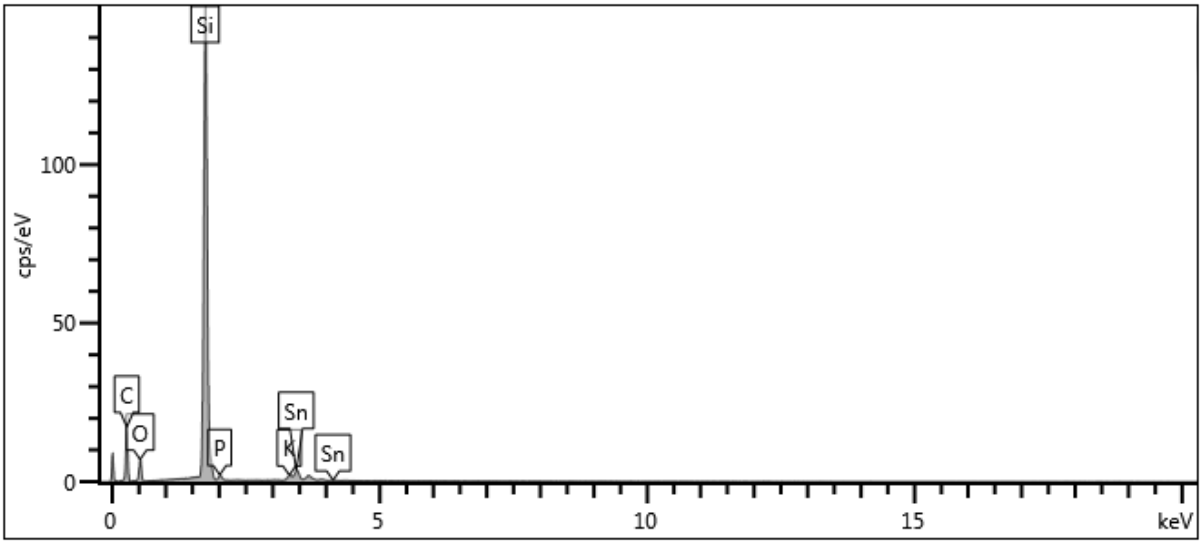

Figure 5.20. EDX spectrum of a thin film prepared from a K_3P_7/K_4Sn_9/*en* solution, measured with 8000x magnification.

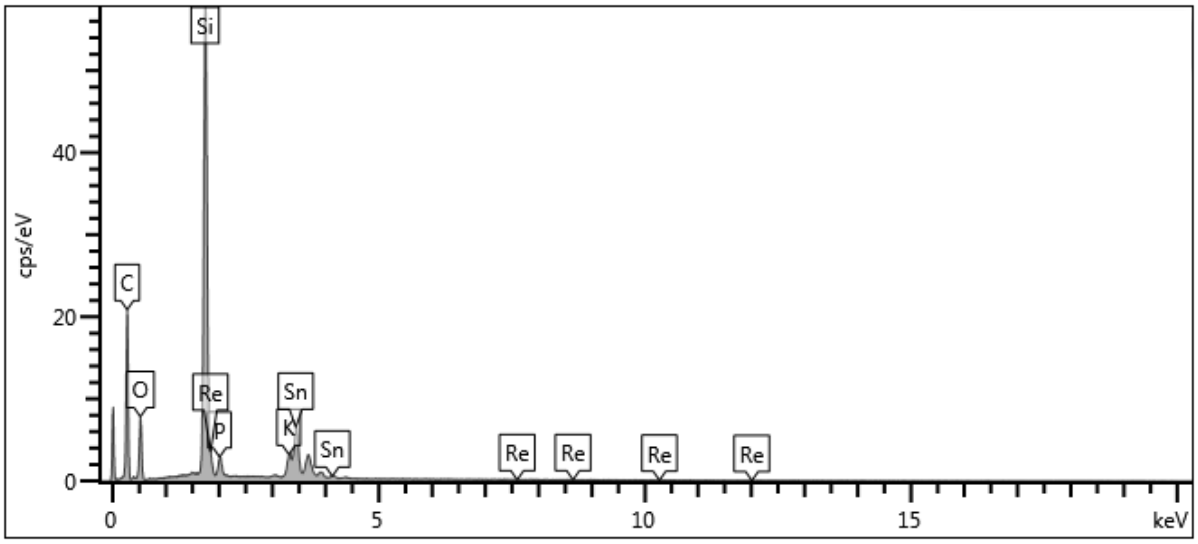

Figure 5.21. EDX spectrum of a thin film prepared from a K_3P_7/K_4Sn_9/*en* solution, measured with 35721x magnification.

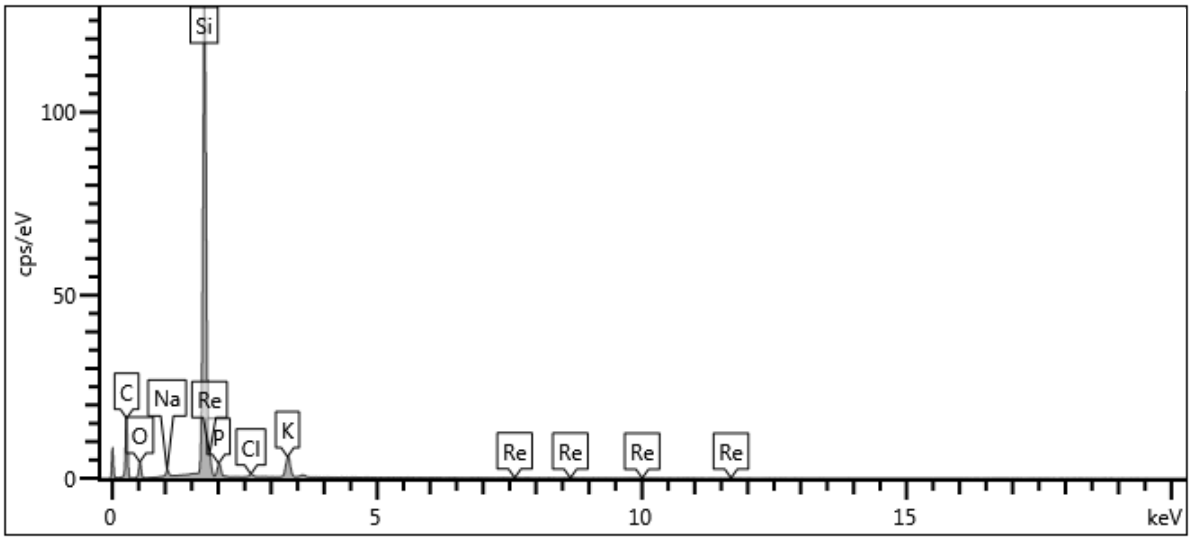

Figure 5.22. EDX spectrum of a film prepared on a Si substrate using 13.5 mg/0.35 mmol K and 25.0 mg/0.81 mmol P_{red} in 2 mL *en*.

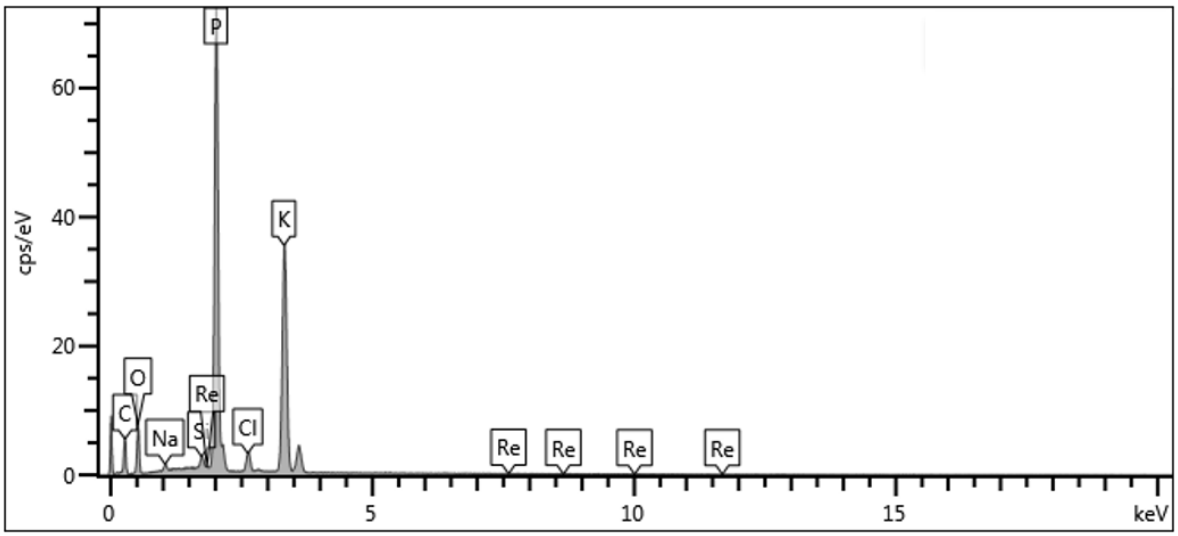

Figure 5.23. EDX spectrum of a thin film prepared from a K_3P_7/*en* solution, linked with $GeCl_4$.

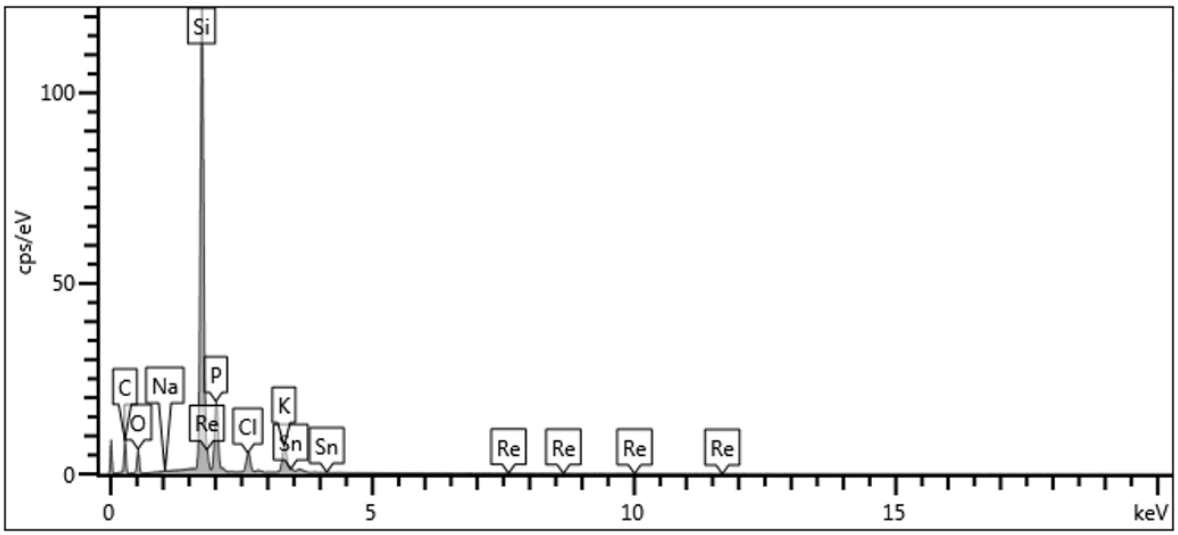

Figure 5.24. EDX spectrum of a thin film prepared from a K_3P_7/*en* solution, linked with $SnCl_4$.

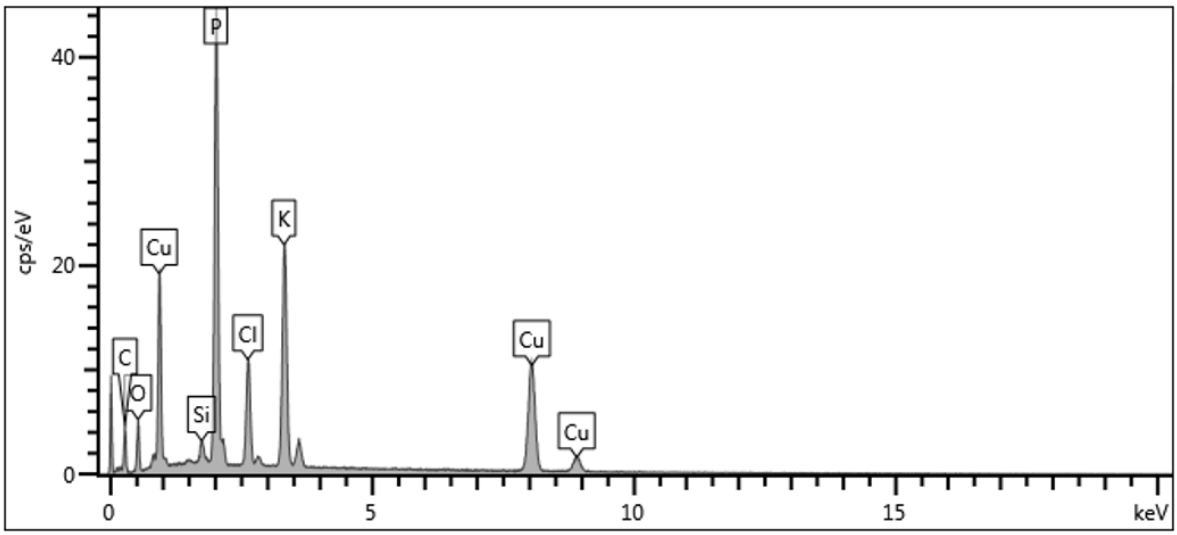

Figure 5.25. EDX spectrum of a thin film prepared from a K_3P_7/*en* solution, linked with $SiCl_4$.

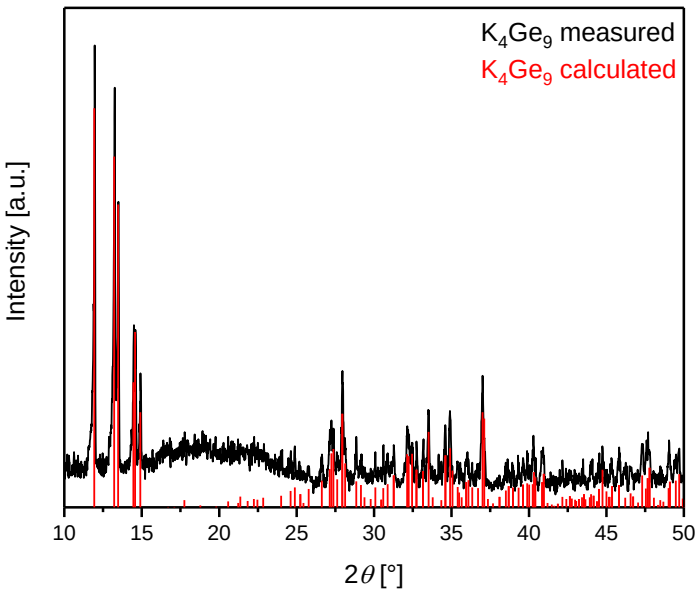

Figure 5.26. X-ray powder diffractogram of measured (black) and calculated (red) K_4Ge_9. The calculated diffractogram is based on single crystal data.[122b] The diffractogram was measured using Cu-$K_{\alpha1}$ radiation.

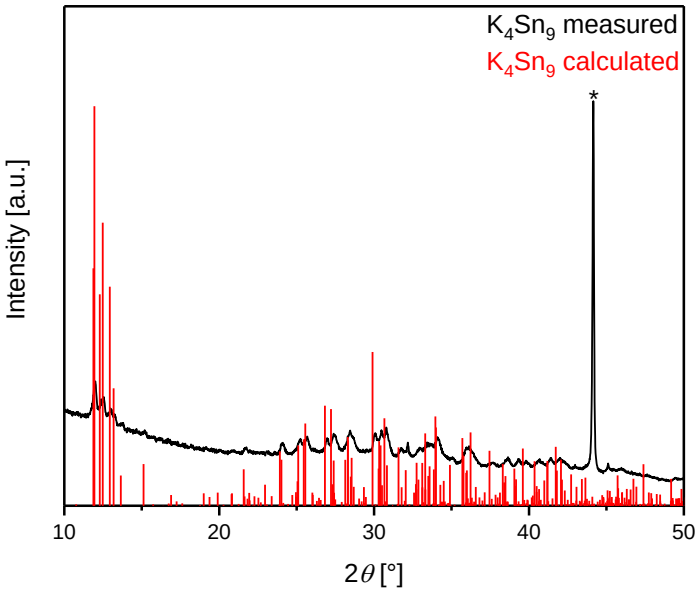

Figure 5.27. X-ray powder diffractogram of measured (black) and calculated (red) K_4Sn_9. The reflex marked with an asterisk is diamond. The calculated diffractogram is based on single crystal data.[122f] The diffractogram was measured using Mo-$K_{\alpha1}$ radiation.

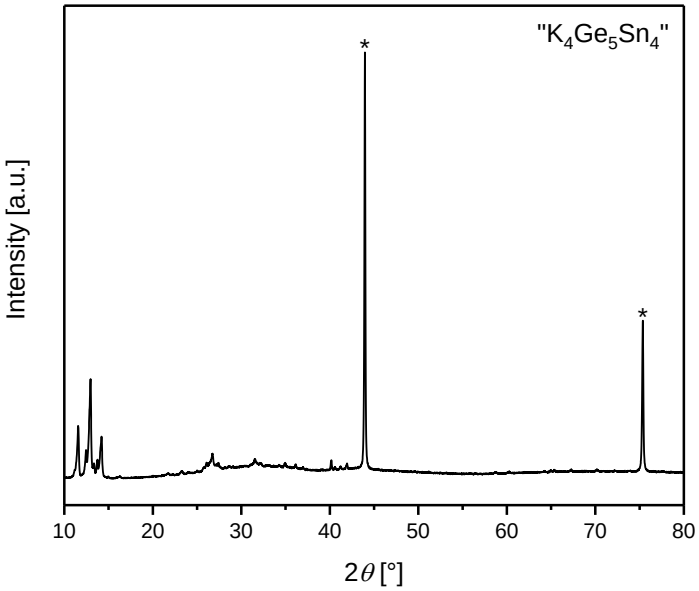

Figure 5.28. X-ray powder diffractogram of synthesized „$K_4Ge_5Sn_4$“. Peaks marked with an asterisk are diamond. The diffractogram was measured using Cu-$K_{\alpha1}$ radiation.

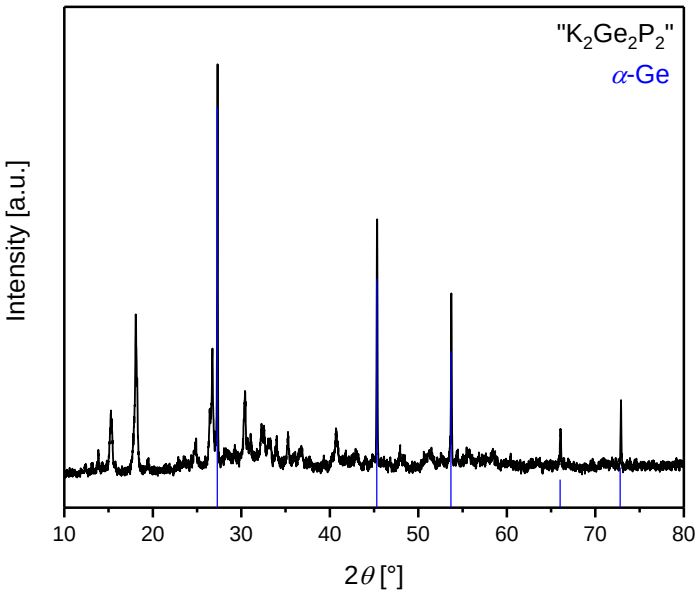

Figure 5.29. X-ray powder diffractogram of synthesized „$K_2Ge_2P_2$”. The calculated diffractogram of α-Ge is based on single crystal data.[157c] The diffractogram was measured using Cu-$K_{\alpha1}$ radiation.

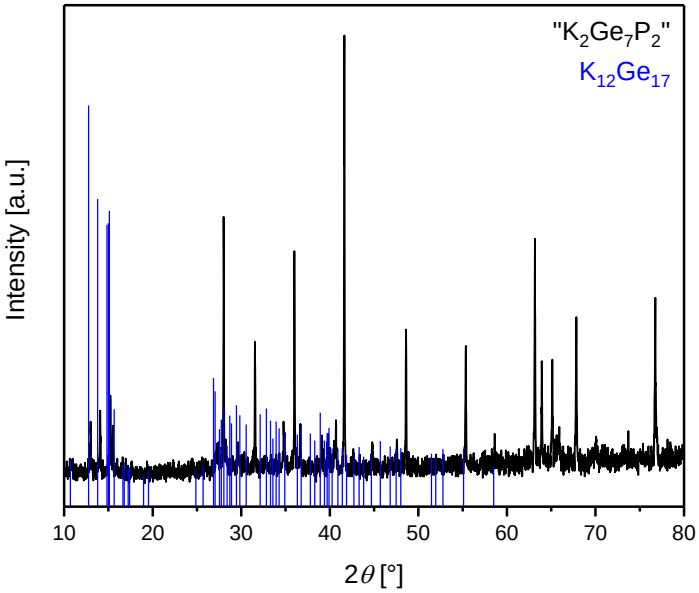

Figure 5.30. X-ray powder diffractogram of synthesized „$K_2Ge_7P_2$". The calculated diffractogram of $K_{12}Ge_{17}$ is based on single crystal data.[186] The diffractogram was measured using Cu-$K_{\alpha1}$ radiation.

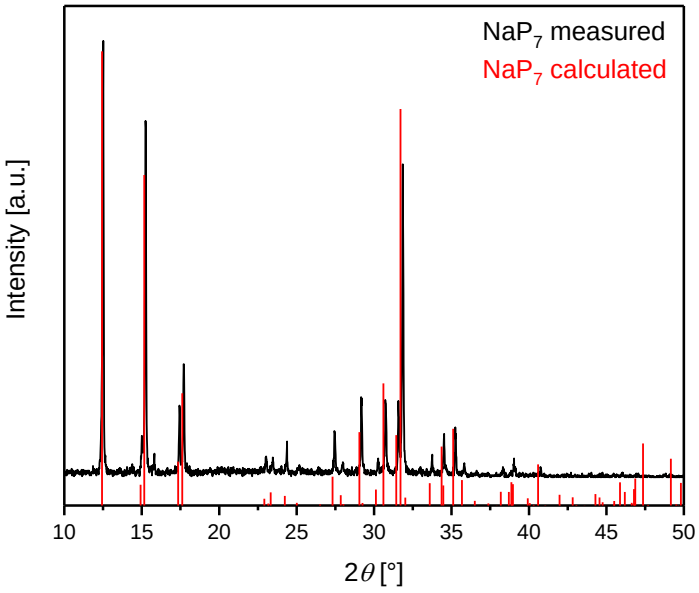

Figure 5.31. X-ray powder diffractogram of measured (black) and calculated (red) NaP_7. The calculated diffractogram is based on single crystal data.[164] The diffractogram was measured using Cu-$K_{\alpha1}$ radiation.

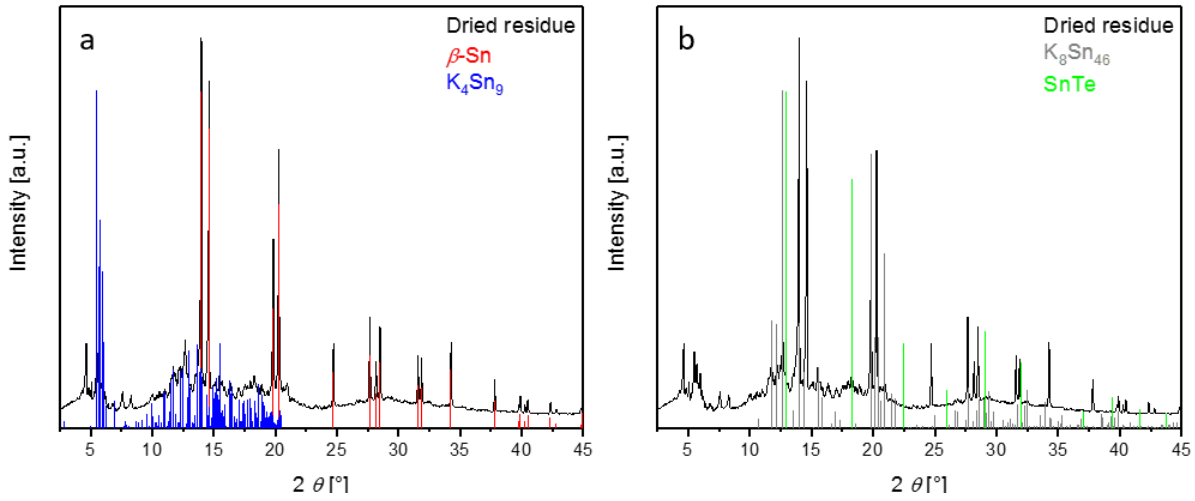

Figure 5.32. PXRDs of a dried residue of a K_2Te/K_4Sn_9/*en* solution, divided in two separate figures. a) Comparison with literature data for β-Sn and K_4Sn_9, b) comparison with literature data from K_8Sn_{46} and SnTe. The diffractograms were measured using Mo-$K_{\alpha1}$ radiation.

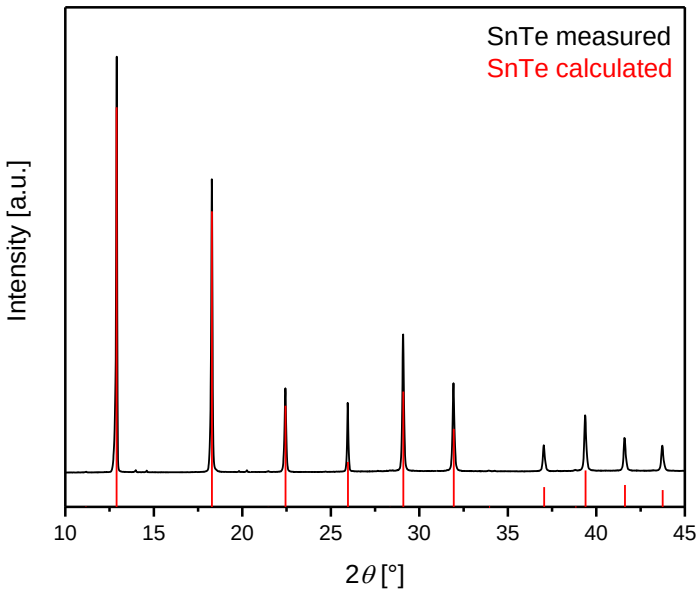

Figure 5.33. X-ray powder diffractogram of measured (black) and calculated (red) SnTe. The calculated diffraktogram is based on single crystal data.[177b] The diffractogram was measured using Mo-$K_{\alpha1}$ radiation.

5.2 References

[1] T. Nagaura, *Progress in Batteries & Solar Cells* **1990**, *9*, 209.

[2] a) B. Dunn, H. Kamath, J. M. Tarascon, *Science* **2011**, *334*, 928-935; b) D. Andre, S.-J. Kim, P. Lamp, S. F. Lux, F. Maglia, O. Paschos, B. Stiaszny, *Journal of Materials Chemistry A* **2015**, *3*, 6709-6732; c) M. Winter, R. J. Brodd, *Chemical Reviews* **2005**, *105*, 1021-1021.

[3] a) R. Agrawal, G. Pandey, *Journal of Physics D: Applied Physics* **2008**, *41*, 223001; b) J. F. Oudenhoven, L. Baggetto, P. H. Notten, *Advanced Energy Materials* **2011**, *1*, 10-33.

[4] S. Goriparti, E. Miele, F. De Angelis, E. Di Fabrizio, R. Proietti Zaccaria, C. Capiglia, *Journal of Power Sources* **2014**, *257*, 421-443.

[5] a) M. Wagemaker, F. M. Mulder, *Accounts of Chemical Research* **2012**, *46*, 1206-1215; b) A. Moretti, G.-T. Kim, D. Bresser, K. Renger, E. Paillard, R. Marassi, M. Winter, S. Passerini, *Journal of Power Sources* **2013**, *221*, 419-426; c) Z. Chen, I. Belharouak, Y. K. Sun, K. Amine, *Advanced Functional Materials* **2013**, *23*, 959-969.

[6] D. Deng, M. G. Kim, J. Y. Lee, J. Cho, *Energy & Environmental Science* **2009**, *2*, 818-837.

[7] N.-S. Choi, J.-S. Kim, R.-Z. Yin, S.-S. Kim, *Materials Chemistry and Physics* **2009**, *116*, 603-606.

[8] J. H. Song, H. J. Park, K. J. Kim, Y. N. Jo, J.-S. Kim, Y. U. Jeong, Y. J. Kim, *Journal of Power Sources* **2010**, *195*, 6157-6161.

[9] D. McNulty, G. Collins, C. O'Dwyer, *Journal of Materials Chemistry A* **2018**, *6*, 18103-18115.

[10] A. R. Armstrong, C. Lyness, P. M. Panchmatia, M. S. Islam, P. G. Bruce, *Nature Materials* **2011**, *10*, 223-229.

[11] J. R. Dahn, W. R. McKinnon, *Solid State Ionics* **1987**, *23*, 1-7.

[12] U. K. Sen, A. Shaligram, S. Mitra, *ACS Applied Materials & Interfaces* **2014**, *6*, 14311-14319.

[13] B. Chen, Y. Meng, F. He, E. Liu, C. Shi, C. He, L. Ma, Q. Li, J. Li, N. Zhao, *Nano Energy* **2017**, *41*, 154-163.

[14] Z. Liao, Q. Li, J. Zhang, J. Xu, B. Gao, P. K. Chu, K. Huo, *ChemElectroChem* **2018**, *5*, 1350-1356.

[15] J. S. Xu, Y. J. Zhu, *ACS Applied Materials & Interfaces* **2012**, *4*, 4752-4757.

[16] S. Kanzaki, T. Inada, T. Matsumura, N. Sonoyama, A. Yamada, M. Takano, R. Kanno, *Journal of Power Sources* **2005**, *146*, 323-326.

[17] X. Xu, R. Cao, S. Jeong, J. Cho, *Nano Letters* **2012**, *12*, 4988-4991.

[18] a) D. Barreca, M. Cruz-Yusta, A. Gasparotto, C. Maccato, J. Morales, A. Pozza, C. Sada, L. Sánchez, E. Tondello, *The Journal of Physical Chemistry C* **2010**, *114*, 10054-10060; b) L. Zhang, P. Hu, X. Zhao, R. Tian, R. Zou, D. Xia, *Journal of Materials Chemistry* **2011**, *21*.

[19] Y. Sun, X. Hu, W. Luo, Y. Huang, *The Journal of Physical Chemistry C* **2012**, *116*, 20794-20799.

[20] D. McNulty, H. Geaney, E. Carroll, S. Garvey, A. Lonergan, C. O'Dwyer, *Materials Research Express* **2017**, *4*, 025011.

[21] a) V. Aravindan, P. S. Kumar, J. Sundaramurthy, W. C. Ling, S. Ramakrishna, S. Madhavi, *Journal of Power Sources* **2013**, *227*, 284-290; b) J. Li, S. Xiong, X. Li, Y. Qian, *Nanoscale* **2013**, *5*, 2045-2054; c) S. Grugeon, S. Laruelle, R. Herrera-Urbina, L. Dupont, P. Poizot, J. Tarascon, *Journal of The Electrochemical Society* **2001**, *148*, A285-A292; d) A. Paolella, R. Brescia, M. Prato, M. Povia, S. Marras, L. De Trizio, A. Falqui, L. Manna, C. George, *ACS Applied Materials & Interfaces* **2013**, *5*, 2745-2751; e) P. Poizot, S. Laruelle, S. Grugeon, L. Dupont, J. Tarascon, *Nature* **2000**, *407*, 496; f) H. Liu, X. Du, X. Xing, G. Wang, S. Z. Qiao, *Chemical Communications* **2012**, *48*, 865-867; g) Y. Ma, Y. Ma, G. Giuli, T. Diemant, R. J. Behm, D. Geiger, U. Kaiser, U. Ulissi, S. Passerini, D. Bresser, *Sustainable Energy & Fuels* **2018**.

[22] J. W. Hall, N. Membreno, J. Wu, H. Celio, R. A. Jones, K. J. Stevenson, *Journal of the American Chemical Society* **2012**, *134*, 5532-5535.

[23] Y.-M. Chun, H.-C. Shin, *Electrochimica Acta* **2016**, *209*, 369-378.

[24] D. Yang, J. Zhu, X. Rui, H. Tan, R. Cai, H. E. Hoster, D. Y. Yu, H. H. Hng, Q. Yan, *ACS Applied Materials & Interfaces* **2013**, *5*, 1093-1099.

[25] A. Hayashi, A. Inoue, M. Tatsumisago, *Journal of Power Sources* **2009**, *189*, 669-671.

[26] P. Lou, Z. Cui, Z. Jia, J. Sun, Y. Tan, X. Guo, *ACS Nano* **2017**, *11*, 3705-3715.
[27] L. De Trizio, A. Figuerola, L. Manna, A. Genovese, C. George, R. Brescia, Z. Saghi, R. Simonutti, M. Van Huis, A. Falqui, *ACS Nano* **2012**, *6*, 32-41.
[28] S. Liu, C. Liu, J. Guo, W. Yan, *Journal of The Electrochemical Society* **2017**, *164*, A2390-A2397.
[29] V. Yarmiayev, Y. Miroshnikov, G. Gershinsky, V. Shokhen, D. Zitoun, *Electrochimica Acta* **2018**, *292*, 846-854.
[30] W. Li, H. Li, Z. Lu, L. Gan, L. Ke, T. Zhai, H. Zhou, *Energy & Environmental Science* **2015**, *8*, 3629-3636.
[31] K.-W. Tseng, S.-B. Huang, W.-C. Chang, H.-Y. Tuan, *Chemistry of Materials* **2018**, *30*, 4440-4447.
[32] J.-J. Wu, Z.-W. Fu, *Journal of The Electrochemical Society* **2009**, *156*, A22-A26.
[33] J. W. Park, C. M. Park, *Science Reports* **2016**, *6*, 35980.
[34] S. Liu, H. Zhang, L. Xu, L. Ma, X. Chen, *Journal of Power Sources* **2016**, *304*, 346-353.
[35] a) L. Ji, Z. Lin, M. Alcoutlabi, X. Zhang, *Energy & Environmental Science* **2011**, *4*; b) J. Cabana, C. M. Ionica-Bousquet, C. P. Grey, M. R. Palacín, *Electrochemistry Communications* **2010**, *12*, 315-318; c) K. Aso, A. Hayashi, M. Tatsumisago, *Electrochimica Acta* **2012**, *83*, 448-453; d) A. Paolella, C. George, M. Povia, Y. Zhang, R. Krahne, M. Gich, A. Genovese, A. Falqui, M. Longobardi, P. Guardia, T. Pellegrino, L. Manna, *Chemistry of Materials* **2011**, *23*, 3762-3768; e) Y. Wang, J. Wu, Y. Tang, X. Lu, C. Yang, M. Qin, F. Huang, X. Li, X. Zhang, *ACS Applied Materials & Interfaces* **2012**, *4*, 4246-4250; f) Y. Wang, L. Yu, X. W. Lou, *Angewandte Chemie International Edition* **2016**, *55*, 7423-7426; g) T. Wang, S. Chen, H. Pang, H. Xue, Y. Yu, *Advanced Science* **2017**, *4*, 1600289; h) Q. Pan, F. Zheng, Y. Wu, X. Ou, C. Yang, X. Xiong, M. Liu, *Journal of Materials Chemistry A* **2018**, *6*, 592-598; i) Q. Lian, G. Zhou, J. Liu, C. Wu, W. Wei, L. Chen, C. Li, *Journal of Power Sources* **2017**, *366*, 1-8.
[36] a) N. Pereira, L. Dupont, J. Tarascon, L. Klein, G. Amatucci, *Journal of The Electrochemical Society* **2003**, *150*, A1273-A1280; b) Q. Sun, Z.-W. Fu, *Electrochimica Acta* **2008**, *54*, 403-409; c) B. Das, M. V. Reddy, P. Malar, T. Osipowicz, G. V. Subba Rao, B. V. R. Chowdari, *Solid State Ionics* **2009**, *180*, 1061-1068; d) Q. Sun, W.-J. Li, Z.-W. Fu, *Solid State Sciences* **2010**, *12*, 397-403; e) N. Emery, E. Panabière, O. Crosnier, S. Bach, T. Brousse, P. Willmann, J.-P. Pereira-Ramos, *Journal of Power Sources* **2014**, *247*, 402-405; f) Y. Dong, B. Wang, K. Zhao, Y. Yu, X. Wang, L. Mai, S. Jin, *Nano Letters* **2017**, *17*, 5740-5746; g) F. Gillot, J. Oró-Solé, M. R. Palacín, *Journal of Materials Chemistry* **2011**, *21*; h) A. Ulvestad, J. P. Mæhlen, M. Kirkengen, *Journal of Power Sources* **2018**, *399*, 414-421.
[37] a) N. Berti, E. Hadjixenophontos, F. Cuevas, J. Zhang, A. Lacoste, P. Dubot, G. Schmitz, M. Latroche, *Journal of Power Sources* **2018**, *402*, 99-106; b) A. El Kharbachi, Y. Hu, M. H. Sørby, P. E. Vullum, J. P. Mæhlen, H. Fjellvåg, B. C. Hauback, *The Journal of Physical Chemistry C* **2018**, *122*, 8750-8759.
[38] M. Pramanik, Y. Tsujimoto, V. Malgras, S. X. Dou, J. H. Kim, Y. Yamauchi, *Chemistry of Materials* **2015**, *27*, 1082-1089.
[39] S. Schmidt, S. Sallard, C. Borca, T. Huthwelker, P. Novak, C. Villevieille, *Chemical Communications* **2018**, *54*, 4939-4942.
[40] a) L. Beaulieu, K. Eberman, R. Turner, L. Krause, J. Dahn, *Electrochemical and Solid-State Letters* **2001**, *4*, A137-A140; b) M. N. Obrovac, V. L. Chevrier, *Chemical Reviews* **2014**, *114*, 11444-11502.
[41] a) M. Obrovac, L. Christensen, *Electrochemical and Solid-State Letters* **2004**, *7*, A93-A96; b) M. Winter, J. O. Besenhard, M. E. Spahr, P. Novák, *Advanced Materials* **1998**, *10*, 725-763.
[42] a) J. Y. Kwon, J. H. Ryu, S. M. Oh, *Electrochim. Acta* **2010**, *55*, 8051-8055; b) M. Zeilinger, V. Baran, L. van Wüllen, U. Häussermann, T. F. Fässler, *Chemistry of Materials* **2013**, *25*, 4113-4121; c) M. Zeilinger, D. Benson, U. Häussermann, T. F. Fässler, *Chemistry of Materials* **2013**, *25*, 1960-1967.
[43] a) T. D. Hatchard, J. R. Dahn, *Journal of The Electrochemical Society* **2004**, *151*; b) J. Li, J. Dahn, *Journal of The Electrochemical Society* **2007**, *154*, A156-A161.

[44] B. Key, R. Bhattacharyya, M. Morcrette, V. Seznec, J.-M. Tarascon, C. P. Grey, *Journal of the American Chemical Society* **2009**, *131*, 9239-9249.

[45] a) B. Philippe, R. Dedryvère, J. Allouche, F. Lindgren, M. Gorgoi, H. Rensmo, D. Gonbeau, K. Edström, *Chemistry of Materials* **2012**, *24*, 1107-1115; b) M. Nie, D. P. Abraham, Y. Chen, A. Bose, B. L. Lucht, *The Journal of Physical Chemistry C* **2013**, *117*, 13403-13412.

[46] Y. Yao, M. T. McDowell, I. Ryu, H. Wu, N. Liu, L. Hu, W. D. Nix, Y. Cui, *Nano Letters* **2011**, *11*, 2949-2954.

[47] D. Chen, X. Mei, G. Ji, M. Lu, J. Xie, J. Lu, J. Y. Lee, *Angewandte Chemie International Edition in English* **2012**, *51*, 2409-2413.

[48] R. Batmaz, F. M. Hassan, D. Higgins, Z. P. Cano, X. Xiao, Z. Chen, *Journal of Power Sources* **2018**, *407*, 84-91.

[49] T. Shen, X.-h. Xia, D. Xie, Z.-j. Yao, Y. Zhong, J.-y. Zhan, D.-h. Wang, J.-b. Wu, X.-l. Wang, J.-p. Tu, *Journal of Materials Chemistry A* **2017**, *5*, 11197-11203.

[50] H. Ma, F. Cheng, J. Y. Chen, J. Z. Zhao, C. S. Li, Z. L. Tao, J. Liang, *Advanced Materials* **2007**, *19*, 4067-4070.

[51] Q. Xu, J. Y. Li, J. K. Sun, Y. X. Yin, L. J. Wan, Y. G. Guo, *Advanced Energy Materials* **2017**, *7*, 1601481.

[52] A. M. Morales, C. M. Lieber, *Science* **1998**, *279*, 208-211.

[53] C. K. Chan, H. Peng, G. Liu, K. McIlwrath, X. F. Zhang, R. A. Huggins, Y. Cui, *Nature Nanotechnology* **2008**, *3*, 31-35.

[54] H. Kim, B. Han, J. Choo, J. Cho, *Angewandte Chemie International Edition in English* **2008**, *47*, 10151-10154.

[55] J. Graetz, C. Ahn, R. Yazami, B. Fultz, *Electrochemical and Solid-State Letters* **2003**, *6*, A194-A197.

[56] A. Esmanski, G. A. Ozin, *Advanced Functional Materials* **2009**, *19*, 1999-2010.

[57] a) G. W. Brady, *The Journal of Physical Chemistry* **1959**, *63*, 1119-1120; b) A. Hohl, T. Wieder, P. A. van Aken, T. E. Weirich, G. Denninger, M. Vidal, S. Oswald, C. Deneke, J. Mayer, H. Fuess, *Journal of Non-Crystalline Solids* **2003**, *320*, 255-280.

[58] a) T. Kim, S. Park, S. M. Oh, *Journal of The Electrochemical Society* **2007**, *154*, A1112-A1117; b) Y. Nagao, H. Sakaguchi, H. Honda, T. Fukunaga, T. Esaka, *Journal of The Electrochemical Society* **2004**, *151*, A1572-A1575.

[59] Y. Yamada, Y. Iriyama, T. Abe, Z. Ogumi, *Journal of The Electrochemical Society* **2010**, *157*, A26-A30.

[60] a) G. Jeong, J.-H. Kim, Y.-U. Kim, Y.-J. Kim, *Journal of Materials Chemistry* **2012**, *22*; b) M. Zhou, M. L. Gordin, S. Chen, T. Xu, J. Song, D. Lv, D. Wang, *Electrochemistry Communications* **2013**, *28*, 79-82; c) J.-H. Kim, H.-J. Sohn, H. Kim, G. Jeong, W. Choi, *Journal of Power Sources* **2007**, *170*, 456-459; d) D. J. Lee, M.-H. Ryou, J.-N. Lee, B. G. Kim, Y. M. Lee, H.-W. Kim, B.-S. Kong, J.-K. Park, J. W. Choi, *Electrochemistry Communications* **2013**, *34*, 98-101; e) M. Yamada, A. Inaba, A. Ueda, K. Matsumoto, T. Iwasaki, T. Ohzuku, *Journal of the Electrochemical Society* **2012**, *159*, A1630-A1635; f) Y. Sun, K. Liu, Y. Zhu, *Journal of Nanomaterials* **2017**, *2017*; g) X. Zuo, J. Zhu, P. Müller-Buschbaum, Y.-J. Cheng, *Nano Energy* **2017**, *31*, 113-143.

[61] H. Jung, P. K. Allan, Y.-Y. Hu, O. J. Borkiewicz, X.-L. Wang, W.-Q. Han, L.-S. Du, C. J. Pickard, P. J. Chupas, K. W. Chapman, A. J. Morris, C. P. Grey, *Chemistry of Materials* **2015**, *27*, 1031-1041.

[62] X. H. Liu, S. Huang, S. T. Picraux, J. Li, T. Zhu, J. Y. Huang, *Nano Letters* **2011**, *11*, 3991-3997.

[63] a) J. Graetz, C. C. Ahn, R. Yazami, B. Fultz, *Journal of The Electrochemical Society* **2004**, *151*, A698; b) C. Fuller, J. Severiens, *Physical Review* **1954**, *96*, 21.

[64] X. Xiao, X. Li, S. Zheng, J. Shao, H. Xue, H. Pang, *Advanced Materials Interfaces* **2017**, *4*, 1600798.

[65] B. Farbod, K. Cui, M. Kupsta, W. P. Kalisvaart, E. Memarzadeh, A. Kohandehghan, B. Zahiri, D. Mitlin, *Journal of Materials Chemistry A* **2014**, *2*, 16770-16785.

[66] F.-W. Yuan, H.-J. Yang, H.-Y. Tuan, *Acs Nano* **2012**, *6*, 9932-9942.

[67] A. M. Chockla, M. G. Panthani, V. C. Holmberg, C. M. Hessel, D. K. Reid, T. D. Bogart, J. T. Harris, C. B. Mullins, B. A. Korgel, *The Journal of Physical Chemistry C* **2012**, *116*, 11917-11923.
[68] S. Fang, L. Shen, H. Zheng, X. Zhang, *Journal of Materials Chemistry A* **2015**, *3*, 1498-1503.
[69] R. A. DiLeo, S. Frisco, M. J. Ganter, R. E. Rogers, R. P. Raffaelle, B. J. Landi, *The Journal of Physical Chemistry C* **2011**, *115*, 22609-22614.
[70] G. Cui, L. Gu, L. Zhi, N. Kaskhedikar, P. A. van Aken, K. Müllen, J. Maier, *Advanced Materials* **2008**, *20*, 3079-3083.
[71] F. S. Ke, K. Mishra, L. Jamison, X. X. Peng, S. G. Ma, L. Huang, S. G. Sun, X. D. Zhou, *Chemical Communications* **2014**, *50*, 3713-3715.
[72] K. C. Klavetter, S. M. Wood, Y.-M. Lin, J. L. Snider, N. C. Davy, A. M. Chockla, D. K. Romanovicz, B. A. Korgel, J.-W. Lee, A. Heller, *Journal of Power Sources* **2013**, *238*, 123-136.
[73] H. Lee, M. G. Kim, C. H. Choi, Y.-K. Sun, C. S. Yoon, J. Cho, *The Journal of Physical Chemistry B* **2005**, *109*, 20719-20723.
[74] Y. Xu, X. Zhu, X. Zhou, X. Liu, Y. Liu, Z. Dai, J. Bao, *The Journal of Physical Chemistry C* **2014**, *118*, 28502-28508.
[75] M. Pelosi, M. Tillard, D. Zitoun, *Journal of Nanoparticle Research* **2013**, *15*.
[76] L. Yang, Q. Gao, L. Li, Y. Tang, Y. Wu, *Electrochemistry Communications* **2010**, *12*, 418-421.
[77] H. Jia, R. Kloepsch, X. He, J. P. Badillo, P. Gao, O. Fromm, T. Placke, M. Winter, *Chemistry of Materials* **2014**, *26*, 5683-5688.
[78] S. Choi, Y. G. Cho, J. Kim, N. S. Choi, H. K. Song, G. Wang, S. Park, *Small* **2017**, *13*, 1603045.
[79] T. Song, Y. Jeon, M. Samal, H. Han, H. Park, J. Ha, D. K. Yi, J.-M. Choi, H. Chang, Y.-M. Choi, U. Paik, *Energy & Environmental Science* **2012**, *5*, 9028.
[80] K. H. Seng, M. H. Park, Z. P. Guo, H. K. Liu, J. Cho, *Nano Letters* **2013**, *13*, 1230-1236.
[81] J. Hwang, C. Jo, M. G. Kim, J. Chun, E. Lim, S. Kim, S. Jeong, Y. Kim, J. Lee, *ACS Nano* **2015**, *9*, 5299-5309.
[82] A. G. Medvedev, A. A. Mikhaylov, D. A. Grishanov, D. Y. Yu, J. Gun, S. Sladkevich, O. Lev, P. V. Prikhodchenko, *ACS Applied Materials & Interfaces* **2017**, *9*, 9152-9160.
[83] a) R. A. Huggins, *Journal of Power Sources* **1999**, *81*, 13-19; b) N. Wiberg, E. Wiberg, A. Holleman, de Gruyter, Berlin, **2007**.
[84] K. Kravchyk, L. Protesescu, M. I. Bodnarchuk, F. Krumeich, M. Yarema, M. Walter, C. Guntlin, M. V. Kovalenko, *Journal of the American Chemical Society* **2013**, *135*, 4199-4202.
[85] Y. Wang, B. Li, C. Zhang, H. Tao, S. Kang, S. Jiang, X. Li, *Journal of Power Sources* **2012**, *219*, 89-93.
[86] Z. Tan, Z. Sun, H. Wang, Q. Guo, D. Su, *Journal of Materials Chemistry A* **2013**, *1*, 9462.
[87] Y. Yu, L. Gu, C. Zhu, P. A. Van Aken, J. Maier, *Journal of the American Chemical Society* **2009**, *131*, 15984-15985.
[88] Y. Yu, L. Gu, C. Wang, A. Dhanabalan, P. A. van Aken, J. Maier, *Angewandte Chemie International Edition in English* **2009**, *48*, 6485-6489.
[89] D. Zhou, W.-L. Song, X. Li, L.-Z. Fan, Y. Deng, *Journal of Alloys and Compounds* **2017**, *699*, 730-737.
[90] X. Bai, B. Wang, H. Wang, J. Jiang, *Journal of Alloys and Compounds* **2015**, *628*, 407-412.
[91] L. Ji, Z. Tan, T. Kuykendall, E. J. An, Y. Fu, V. Battaglia, Y. Zhang, *Energy & Environmental Science* **2011**, *4*.
[92] C. H. Jian Qin, Naiqin Zhao, ZhiyuanWang, Chunsheng Shi, En-Zuo Liu and Jiajun Li, *ACS Nano* **2014**, *8*, 1728-1738.
[93] Q. Li, S. Hu, H. Wang, F. Wang, X. Zhong, X. Wang, *Electrochimica Acta* **2009**, *54*, 5884-5888.
[94] K. Zhuo, M.-G. Jeong, C.-H. Chung, *Journal of Power Sources* **2013**, *244*, 601-605.
[95] Y. Idota, T. Kubota, A. Matsufuji, Y. Maekawa, T. Miyasaka, *Science* **1997**, *276*, 1395-1397.
[96] a) I. A. Courtney, *Journal of The Electrochemical Society* **1997**, *144*; b) I. A. Courtney, *Journal of The Electrochemical Society* **1997**, *144*.
[97] a) Y. Wang, H. C. Zeng, J. Y. Lee, *Advanced Materials* **2006**, *18*, 645-649; b) M. S. Park, G. X. Wang, Y. M. Kang, D. Wexler, S. X. Dou, H. K. Liu, *Angewandte Chemie International Edition in*

English **2007**, *46*, 750-753; c) H. Kim, J. Cho, *Journal of Materials Chemistry* **2008**, *18*; d) J. Liu, Y. Li, X. Huang, R. Ding, Y. Hu, J. Jiang, L. Liao, *Journal of Materials Chemistry* **2009**, *19*; e) L. Noerochim, J.-Z. Wang, S.-L. Chou, H.-J. Li, H.-K. Liu, *Electrochimica Acta* **2010**, *56*, 314-320; f) Z. Wang, D. Luan, F. Y. Boey, X. W. Lou, *Journal of the American Chemical Society* **2011**, *133*, 4738-4741; g) Y. Jiang, T. Yuan, W. Sun, M. Yan, *ACS Applied Materials & Interfaces* **2012**, *4*, 6216-6220; h) X. W. Guo, X. P. Fang, Y. Sun, L. Y. Shen, Z. X. Wang, L. Q. Chen, *Journal of Power Sources* **2013**, *226*, 75-81; i) C. Heubner, T. Liebmann, K. Voigt, M. Weiser, B. Matthey, N. Junker, C. Laemmel, M. Schneider, A. Michaelis, *ACS Applied Materials & Interfaces* **2018**; j) W. Dong, J. Xu, C. Wang, Y. Lu, X. Liu, X. Wang, X. Yuan, Z. Wang, T. Lin, M. Sui, *Advanced Materials* **2017**, *29*, 1700136; k) B. Jiang, Y. He, B. Li, S. Zhao, S. Wang, Y. B. He, Z. Lin, *Angewandte Chemie International Edition in English* **2017**, *56*, 1869-1872.

[98] a) J. Qian, D. Qiao, X. Ai, Y. Cao, H. Yang, *Chemical Communications* **2012**, *48*, 8931-8933; b) C. M. Park, H. J. Sohn, *Adv. Mater.* **2007**, *19*, 2465-2468.

[99] A. E. Del Rio Castillo, V. Pellegrini, H. Sun, J. Buha, D. A. Dinh, E. Lago, A. Ansaldo, A. Capasso, L. Manna, F. Bonaccorso, *Chemistry of Materials* **2018**, *30*, 506-516.

[100] Q. Jiang, J. Li, N. Yuan, Z. Wu, J. Tang, *Electrochimica Acta* **2018**, *263*, 272-276.

[101] J. Zhou, X. Liu, W. Cai, Y. Zhu, J. Liang, K. Zhang, Y. Lan, Z. Jiang, G. Wang, Y. Qian, *Advanced Materials* **2017**, *29*.

[102] W. C. Chang, K. W. Tseng, H. Y. Tuan, *Nano Letters* **2017**, *17*, 1240-1247.

[103] Q. Wang, P. Lian, B. Wang, Y. Tang, H. Liu, Y. Mei, *Ionics* **2018**.

[104] L. Sun, Y. Zhang, D. Zhang, J. Liu, Y. Zhang, *Nano Research* **2018**, *11*, 2733-2745.

[105] T. Tojo, S. Yamaguchi, Y. Furukawa, K. Aoyanagi, K. Umezaki, R. Inada, Y. Sakurai, *Journal of The Electrochemical Society* **2018**, *165*, A1231-A1237.

[106] W. Li, Z. Yang, M. Li, Y. Jiang, X. Wei, X. Zhong, L. Gu, Y. Yu, *Nano Letters* **2016**, *16*, 1546-1553.

[107] Z. Yu, J. Song, M. L. Gordin, R. Yi, D. Tang, D. Wang, *Advanced Science* **2015**, *2*, 1400020.

[108] Y. Du, Y. Tang, C. Chang, *Journal of The Electrochemical Society* **2016**, *163*, A2938-A2942.

[109] J. Ruan, T. Yuan, Y. Pang, X. Xu, J. Yang, W. Hu, C. Zhong, Z. F. Ma, X. Bi, S. Zheng, *ACS Applied Materials & Interfaces* **2017**, *9*, 36261-36268.

[110] Z. Xu, Y. Zeng, L. Wang, N. Li, C. Chen, C. Li, J. Li, H. Lv, L. Kuang, X. Tian, *Journal of Power Sources* **2017**, *356*, 18-26.

[111] H. Yang, Y. Li, P. Long, J. Han, C. Cao, F. Yao, W. Feng, *RSC Advances* **2018**, *8*, 17325-17333.

[112] D. C. Souza, V. Pralong, A. J. Jacobson, L. F. Nazar, *Science* **2002**, *296*, 2012-2015.

[113] Y.-U. Kim, B. W. Cho, H.-J. Sohn, *Journal of The Electrochemical Society* **2005**, *152*, A1475-A1478.

[114] a) C.-M. Park, Y.-U. Kim, H.-J. Sohn, *Chemistry of Materials* **2009**, *21*, 5566-5568; b) F. Gillot, M. Ménétrier, E. Bekaert, L. Dupont, M. Morcrette, L. Monconduit, J. M. Tarascon, *Journal of Power Sources* **2007**, *172*, 877-885.

[115] G. R. Goward, N. J. Taylor, D. C. S. Souza, L. F. Nazar, *Journal of Alloys and Compounds* **2001**, *329*, 82-91.

[116] F. Laves, *Die Naturwissenschaften*, Springer, **1941**, 244-256.

[117] C. E. Housecroft, A. G. Sharpe, A. Rompel, *Anorganische Chemie*, Pearson Studium München, Germany, **2006**.

[118] E. Zintl, *Angewandte Chemie International Edition in English* **1939**, *52*, 1-6.

[119] E. Busmann, S. Lohmeyer, *Zeitschrift für anorganische und allgemeine Chemie* **1961**, *312*, 53-59.

[120] a) C. Hoch, M. Wendorff, C. Röhr, *Journal of Alloys and Compounds* **2003**, *361*, 206-221; b) S. C. Sevov, J. M. Goicoechea, *Organometallics* **2006**, *25*, 5678-5692; c) S. Scharfe, F. Kraus, S. Stegmaier, A. Schier, T. F. Fassler, *Angewandte Chemie International Edition in English* **2011**, *50*, 3630-3670.

[121] a) E. Busmann, *Zeitschrift für anorganische und allgemeine Chemie* **1961**, *313*, 90-106; b) W. Klemm, E. Busmann, *Zeitschrift für anorganische und allgemeine Chemie* **1963**, *319*, 297-311; c) H. von Schnering, M. Schwarz, J.-H. Chang, K. Peters, E.-M. Peters, R. Nesper, *Zeitschrift für*

Kristallographie-New Crystal Structures **2005**, *220*, 525-527; d) J. Witte, H. v. Schnering, W. Klemm, *Zeitschrift für anorganische und allgemeine Chemie* **1964**, *327*, 260-273.

[122] a) H. von Schnering, U. Bolle, W. Carrillo-Cabrera, J. Curda, Y. Grin, F. Heinemann, J. Llanos,, A. S. K. Peters, and M. Somer, *Zeitschrift für anorganische und allgemeine Chemie* **1997**, *623*, 1037-1039; b) S. Ponou, T. F. Fässler, *Zeitschrift für anorganische und allgemeine Chemie* **2007**, *633*, 393-397; c) V. Queneau, S. C. Sevov, *Angewandte Chemie International Edition in English* **1997**, *36*, 1754-1756; d) V. Queneau, S. C. Sevov, *Inorganic Chemistry* **1998**, *37*, 1358-1360; e) E. Todorov, S. C. Sevov, *Inorganic Chemistry* **1998**, *37*, 3889-3891; f) C. Hoch, M. Wendorff, C. Röhr, *Acta Crystallographica Section C Crystal Structure Communications* **2002**, *58*, i45-i46; g) T. F. Fässler, *Coordination Chemistry Reviews* **2001**, *215*, 347-377.

[123] K. Wade, *Inorganic and Nuclear Chemistry Letters* **1972**, *8*, 559-562.

[124] H. von Schnering, J. Llanos, J.-H. Chang, K. Peters, E.-M. Peters, R. Nesper, *Zeitschrift für Kristallographie-New Crystal Structures* **2005**, *220*, 324-326.

[125] J. Åkerstedt, S. Ponou, L. Kloo, S. Lidin, *European Journal of Inorganic Chemistry* **2011**, *2011*, 3999-4005.

[126] a) J. D. Corbett, D. G. Adolphson, D. J. Merryman, P. A. Edwards, F. J. Armatis, *Journal of the American Chemical Society* **1975**, *97*, 6267-6268; b) T. F. Fässler, R. Hoffmann, *Angewandte Chemie International Edition in English* **1999**, *38*, 543-546.

[127] a) T. F. Fässler, L. Schiegerl, A. Karttunen, J. Tillmann, S. Geier, G. Raudaschl-Sieber, M. Waibel, *Angewandte Chemie International Edition in English* **2018**; b) C. B. Benda, T. Henneberger, W. Klein, T. F. Fässler, *Zeitschrift für anorganische und allgemeine Chemie* **2017**, *643*, 146-148; c) S. Joseph, C. Suchentrunk, N. Korber, *Zeitschrift für Naturforschung B* **2010**, *65*, 1059-1065; d) S. Joseph, C. Suchentrunk, F. Kraus, N. Korber, *European Journal of Inorganic Chemistry* **2009**, *2009*, 4641-4647.

[128] X. Meng, R. Al-Salman, J. Zhao, N. Borissenko, Y. Li, F. Endres, *Angewandte Chemie International Edition in English* **2009**, *48*, 2703-2707.

[129] a) X. Liu, J. Zhao, Y. Zhang, X. An, Y. Ding, Y. Zhang, Y. Li, F. Endres, *Zeitschrift für Physikalische Chemie* **2013**, *227*; b) J. Z. Wuhong Xin, Dengteng Ge, Yanbo Ding, Yao Li, and, F. Endres, *Physical Chemistry Chemical Physics* **2013**, *15*, 2421-2426.

[130] E. C. H. Miguez, F. Garcia-Santamaria, M. Ibisate, S. John, C. Lopez, F. Meseguer, J. P. Mondia, G. A. Ozin, O. Toader, H. M. van Driel, *Advanced Materials* **2001**, *13*, 1634-1637.

[131] F. M. H. Miguez, C. Lopez, A. Mifsud, M. Holgado, G. Andreasen, and V. Forne, *Langmuir* **2000**, *16*, 4405-4408.

[132] a) M. Waibel, C. B. Benda, B. Wahl, T. F. Fässler, *Chemistry - A European Journal* **2011**, *17*, 12928-12931; b) M. Waibel, T. F. Fässler, *Inorganic Chemistry* **2013**, *52*, 5861-5866.

[133] K. K. Rangan, P. N. Trikalitis, M. G. Kanatzidis, *Journal of the American Chemical Society* **2000**, *122*, 10230-10231.

[134] P. N. Trikalitis, K. K. Rangan, T. Bakas, M. G. Kanatzidis, *Nature* **2001**, *410*, 671.

[135] M. G. Kanatzidis, *Advanced Materials* **2007**, *19*, 1165-1181.

[136] S. D. Korlann, Bradley L. Kirsch, B. S. Mun, S. H. Tolbert, *Journal of the American Chemical Society* **2005**, *127*, 12516-12527.

[137] a) A. E. Riley, S. D. Korlann, E. K. Richman, S. H. Tolbert, *Angewandte Chemie International Edition in English* **2005**, *45*, 235-241; b) S. D. Korlann, B. S. Mun, S. H. Tolbert, *Journal of Physical Chemistry C* **2009**, *113*, 7697–7705.

[138] a) N. Chandrasekharan, S. C. Sevov, *Journal of The Electrochemical Society* **2010**, *157*, C140-C145; b) N. Chandrasekharan, S. C. Sevov, *Journal of The Electrochemical Society* **2010**, *157*, C419-C423.

[139] M. M. Bentlohner, M. Waibel, P. Zeller, K. Sarkar, P. Müller-Buschbaum, D. Fattakhova-Rohlfing, T. F. Fässler, *Angew. Chem. Int. Ed. Engl.* **2016**, *128*, 2487-2491.

[140] M. Mizuhata, Y. Kida, S. Deki, *Journal of the Ceramic Society of Japan* **2007**, *115*, 724-728.

[141] J. Xiao, Q. Huang, J. Xu, C. Li, G. Chen, Y. Luo, D. Li, Q. Meng, *The Journal of Physical Chemistry C* **2014**, *118*, 4007-4015.

[142] a) J. Wang, Y. Xu, W. Xu, M. Zhang, X. Chen, *Microporous and Mesoporous Materials* **2015**, *208*, 93-97; b) F. Liu, B. Shan, S. Zhang, B. Tang, *Langmuir* **2018**, *34*, 3918-3924.
[143] T. Wang, O. Sel, I. Djerdj, B. Smarsly, *Colloid and Polymer Science* **2006**, *285*, 1-9.
[144] S. Geier, R. Jung, K. Peters, H. A. Gasteiger, D. Fattakhova-Rohlfing, T. F. Fässler, *Sustainable Energy & Fuels* **2018**, *2*, 85-90.
[145] L. Baggetto, E. J. Hensen, P. H. Notten, *Electrochimica Acta* **2010**, *55*, 7074-7079.
[146] M. Zeilinger, T. F. Fässler, *Dalton Transactions* **2014**, *43*, 14959-14970.
[147] a) V. Etacheri, O. Haik, Y. Goffer, G. A. Roberts, I. C. Stefan, R. Fasching, D. Aurbach, *Langmuir* **2012**, *28*, 965-976; b) R. Jung, M. Metzger, D. Haering, S. Solchenbach, C. Marino, N. Tsiouvaras, C. Stinner, H. A. Gasteiger, *Journal of The Electrochemical Society* **2016**, *163*, A1705-A1716.
[148] D. Sun, A. E. Riley, A. J. Cadby, E. K. Richman, S. D. Korlann, S. H. Tolbert, *Nature* **2006**, *441*, 1126-1130.
[149] a) G. S. Armatas, M. G. Kanatzidis, *Science* **2006**, *313*, 817-820; b) S. D. Korlann, A. E. Riley, B. L. Kirsch, B. S. Mun, S. H. Tolbert, *Journal of the American Chemical Society* **2005**, *127*, 12516-12527.
[150] Y. Xiao, M. Cao, *ACS Applied Materials & Interfaces* **2014**, *6*, 12922-12930.
[151] B. Wang, Z. Wen, J. Jin, X. Hong, S. Zhang, K. Rui, *Journal of Power Sources* **2017**, *342*, 521-528.
[152] M. M. Gillett-Kunnath, A. G. Oliver, S. C. Sevov, *Journal of the American Chemical Society* **2011**, *133*, 6560-6562.
[153] R. J. Clark, C. D. Flint, A. J. Hempleman, *Spectrochimica Acta Part A: Molecular Spectroscopy* **1987**, *43*, 805-816.
[154] N. Fukata, K. Sato, M. Mitome, Y. Bando, T. Sekiguchi, M. Kirkham, J.-i. Hong, Z. L. Wang, R. L. Snyder, *ACS Nano* **2010**, *4*, 3807-3816.
[155] a) A. M. Guloy, R. Ramlau, Z. Tang, W. Schnelle, M. Baitinger, Y. Grin, *Nature* **2006**, *443*, 320-323; b) B. Böhme, A. Guloy, Z. Tang, W. Schnelle, U. Burkhardt, M. Baitinger, Y. Grin, *Journal of the American Chemical Society* **2007**, *129*, 5348-5349; c) A. M. Guloy, Z. Tang, R. Ramlau, B. Böhme, M. Baitinger, Y. Grin, *European Journal of Inorganic Chemistry* **2009**, *2009*, 2455-2458.
[156] G. Contreras, L. Tapfer, A. K. Sood, A. M. Cardona, *Physica Status Solidi* **1985**, *131*, 475-487.
[157] a) J. Daly, *Journal of the Chemical Society (Resumed)* **1964**, 3799-3810; b) H. von Schnering, J. Llanos, K. Peters, M. Baitinger, Y. Grin, R. Nesper, *Zeitschrift für Kristallographie-New Crystal Structures* **2011**, *226*, 9-10; c) H. Bouderba, Y. Djaballah, A. Belgacem-Bouzida, R. Beddiaf, *Physica B: Condensed Matter* **2011**, *406*, 2601-2609.
[158] F. Cerdeira, M. Cardona, *Physical Review B* **1972**, *5*, 1440-1454.
[159] U. Fano, *Physical Review* **1961**, *124*, 1866-1878.
[160] B. G. Burke, J. Chan, K. A. Williams, Z. Wu, A. A. Puretzky, D. B. Geohegan, *Journal of Raman Spectroscopy* **2010**, *41*, 1759-1764.
[161] P. L. N. H. Nickel, I. Sieber, *Physical Review B* **2000**, *61*, 15558-15561.
[162] F. Cerdeira, T. Fjeldly, M. Cardona, *Physical Review B* **1974**, *9*, 4344-4350.
[163] J. Chastain, R. C. King, J. Moulder, *Handbook of X-ray photoelectron spectroscopy: a reference book of standard spectra for identification and interpretation of XPS data*, Physical Electronics Division, Perkin-Elmer Corporation Eden Prairie, Minnesota, **1992**.
[164] C. Grotz, M. Köpf, M. Baumgartner, L.-A. Jantke, G. Raudaschl-Sieber, T. F. Fässler, T. Nilges, *Zeitschrift für anorganische und allgemeine Chemie* **2015**, *641*, 1395-1399.
[165] M. Ruck, D. Hoppe, B. Wahl, P. Simon, Y. Wang, G. Seifert, *Angewandte Chemie International Edition in English* **2005**, *117*, 7788-7792.
[166] S. Mitzinger, J. Bandemehr, K. Reiter, J. Scott McIndoe, X. Xie, F. Weigend, J. F. Corrigan, S. Dehnen, *Chemical Communications* **2018**, *54*, 1421-1424.
[167] D. J. Olego, J. A. Baumann, M. A. Kuck, R. Schachter, C. G. Michel, P. M. Raccah, *Solid State Communications* **1984**, *52*, 311-314.
[168] M. M. Gillett-Kunnath, I. Petrov, S. C. Sevov, *Inorganic Chemistry* **2010**, *49*, 721-729.

[169] H. Slavik, *Synthese und Charakterisierung von Doppelsazlen mit Clustern der Tetrelelemente*, Dissertation, Technische Universtität München, München, **2017**.
[170] H. Olijnyk, *Physical Review B* **1992**, *46*, 6589-6591.
[171] a) E. R. Jette, F. Foote, *The Journal of Chemical Physics* **1935**, *3*, 605-616; b) M. Somer, W. Carrillo-Cabrera, E. M. Peters, K. Peters, H. v. Schnering, *Zeitschrift für anorganische und allgemeine Chemie* **1998**, *624*, 1915-1921.
[172] a) C. W. Myles, J. Dong, O. F. Sankey, C. Kendziora, G. Nolas, *Physical Review B* **2002**, *65*, 235208; b) H. Shimizu, T. Imai, T. Kume, S. Sasaki, A. Kaltzoglou, T. F. Fässler, *Chemical Physics Letters* **2008**, *464*, 54-57; cG. S. Nolas, C. A. Kendziora, *Physical Review B* **2000**, *62*, 7157-7161.
[173] a) J. Creighton, J. Green, *Journal of the Chemical Society A: Inorganic, Physical, Theoretical* **1968**, 808-813; b) R. Clark, B. Hunter, D. Rippon, *Inorganic Chemistry* **1972**, *11*, 56-61; c) W. Brockner, A. Demiray.
[174] C. X. Lv, X. K. Gai, R. Q. Yang, J. Z. Wang, H. Z. Jiang, *Advanced Materials Research* **2014**, *953-954*, 1082-1086.
[175] M. G. Kim, J. Cho, *Journal of The Electrochemical Society* **2009**, *156*, A277-A282.
[176] Y. J. Cho, C. H. Kim, H. S. Im, Y. Myung, H. S. Kim, S. H. Back, Y. R. Lim, C. S. Jung, D. M. Jang, J. Park, S. H. Lim, E. H. Cha, K. Y. Bae, M. S. Song, W. I. Cho, *Physical Chemistry Chemical Physics* **2013**, *15*, 11691-11695.
[177] a) J. Gallmeier, H. Schäfer, A. Weiss, *Zeitschrift für Naturforschung B* **1969**, *24*, 665-671; b) N. Dzyubenko, E. Rogacheva, G. Gorne, N. Zhigarev, A. Ivanova*, Interaction in the Systems SnTe-InTe and SnTn-In_2Tn_3*, Maik Nauka/Interperiodica C/O Plenum/Consultants Bureau 233 Spring St., New York, **1988**, 1486-1488.
[178] A. S. Pine, G. Dresselhaus, *Physical Review B* **1971**, *4*, 356-371.
[179] J. Huffman, J. Haushalter, A. Umarji, G. Shenoy, R. Haushalter, *Inorganic Chemistry* **1984**, *23*, 2312-2315.
[180] S. Sugai, K. Murase, H. Kawamura, *Solid State Communications* **1977**, *23*, 127-129.
[181] L. J. Brillson, E. Burstein, L. Muldawer, *Physical Review B* **1974**, *9*, 1547-1551.
[182] Y. Tanaka, Z. Ren, T. Sato, K. Nakayama, S. Souma, T. Takahashi, K. Segawa, Y. Ando, *Nature Physics* **2012**, *8*, 800-803.
[183] F. Bolduan, W. Hönle, H. Hochheimer, W. Henkel, *Physica Status Solidi (b)* **1985**, *132*, 41-50.
[184] C. M. Park, J. H. Kim, H. Kim, H. J. Sohn, *Chemical Society Reviews* **2010**, *39*, 3115-3141.
[185] C. Wagner, *Faraday Discussions of the Chemical Society* **1975**, *60*, 291-300.
[186] P. Villars, K. Cenzual, *PAULING FILE Multinaries Edition – 2012*, SpringerMaterials, Berlin Heidelberg, **2012**.